

Diss. ETH No. 25626

**Modeling and Design of
Medium-Frequency Transformers
for Future Medium-Voltage
Power Electronics Interfaces**

A thesis submitted to attain the degree of

DOCTOR OF SCIENCES of ETH ZURICH
(Dr. sc. ETH Zurich)

presented by

THOMAS PAUL HENRI GUILLOD

MSc ETH

born on 09.09.1989

citizen of Bas-Vully, Switzerland

accepted on the recommendation of

Prof. Dr. Johann W. Kolar, examiner

Prof. Dr. Dražen Dujčić, co-examiner

2018

ETH Zurich
Power Electronic Systems Laboratory
Physikstrasse 3 | ETL H23
8092 Zurich | Switzerland

<http://www.pes.ee.ethz.ch>

© 2018-2019, Thomas Guillod

Dans la vie, rien n'est à craindre, tout est à comprendre.
– Marie Curie

As long as one keeps searching, the answers will come.
– Joan Baez

Acknowledgments

FIRST and foremost, I would like to thank Prof. Dr. Johann W. Kolar for giving me the opportunity to conduct my Ph.D. studies at the Power Electronic Systems Laboratory (PES) of ETH Zurich. He was always available to share his extensive scientific expertise, provide valuable inputs, and discuss new challenges. I am particularly grateful for the great scientific freedom he gave me but also for his rigorous guidance. Furthermore, I would like to thank Prof. Dr. Dražen Dujčić for his interest in my work and for being part of the examination committee.

Many thanks are further directed to the High Voltage Laboratory (HVL) of ETH Zurich and more particularly to Prof. Dr. Christian M. Franck and Raphael Färber for the fruitful collaboration. Their broad knowledge of high voltage engineering and material science was extremely helpful. Besides the exchange of ideas, the sharing of our infrastructures has also been a key factor for the success of the work.

Special thanks are due to Dr. Florian Krismer, Dr. Dominik Bortis, and Dr. Gabriel Ortiz for the supporting supervision concerning different parts of my thesis. The Solid-State Transformer team of PES, namely Jonas Huber, Daniel Rothmund, and Piotr Czyz, helped me a lot with the discussions related to medium-voltage converters. Daniel Rothmund occupies a very special place in this project. The collaboration between our respective projects allowed the realization of a complete Solid-State Transformer demonstrator. The hundreds (or thousands) of hours spend together discussing, complaining, simulating, laughing, constructing, traveling, and measuring remain great memories.

Furthermore, I acknowledge the Swiss Competence Centers for Energy Research (SCCER) initiative for their funding of this project, through the Swiss federal agency Innosuisse. In particular, Prof. Dr. Patrick Favre-Perrod, our work package leader, organized the different meetings, took care of the project reporting and, therefore, kept the project on track.

I was very lucky to count on the help of the administrative and technical staff of PES, namely Monica Kohn-Müller, Roswitha Coccia, Prisca Maurantonio, Yvonne Schnyder-Lieberherr, Damaris Egger, Peter Seitz, Peter Albrecht, Marina Eisenstat, and Claudia Stucki. Without their reliable and careful support, this project would not have been possible. The same applies to Martin Vogt, from the D-ITET workshop, who manufactured the mechanical parts for my prototypes with incredible care.

I also thank all the students who contributed, directly or indirectly, to this project during their Semester or Master projects: Roger Stark, Dominik Neumayr, Andrew Morrison, Mingkun Liu, and Daifei Zhang. During my

Ph.D., I was also lucky to be a teaching assistant for many lectures, giving me the possibility to interact with hundreds of students.

Since the beginning of my work at PES, I had the privilege to share the office with Gabriel Ortiz, Oliver Knecht, Daniel Rothmund, and more recently, with Pantelis Papamanolis. This Chilean Spanish, Swiss German, German, Greek, and Swiss French speaking office was leading to lively (technical and non-technical) discussions and endless fun. Special thanks go to Oliver Knecht, who was always ready to help, with his impressive knowledge ranging from flawed PCB design tools to femtosecond lasers. I want to thank Pantelis Papamanolis for the support, the interesting discussions about magnetics, and the great time we had in the office.

This unforgettable time at PES was enriched by many activities such as ski-weekends, hikes, barbecues, and fondues. The different international conferences offered me the possibility to travel, with different colleagues, through North America and Japan, with few intermediate stops in bQm. Therefore, many thanks go to my colleagues for their support and friendship: Toke Andersen, Michael Antivachis, Jon Azurza, Julian Böhler, David Boillat, Dominik Bortis, Roman Bosshard, Ralph Burkart, Patricio Cortés, Piotr Czyz, Michael Flankl, Christoph Gammeter, Mattia Guacci, Michael Haider, Morris Heller, Thomas Holenstein, Jonas Huber, Emanuel Hubmann, Matthias Kasper, Oliver Knecht, Florian Krismer, Gustavo Knabben, Pedro Bezerra, Michael Leibl, Yanick Lobsiger, David Menzi, Spasoje Miric, Andreas Müsing, Dominik Neumayr, Pascal Niklaus, Gabriel Ortiz, Panteleimon Papamanolis, Pascal Püntener, Daniel Rothmund, Jannik Schäfer, Marcel Schuck, Daniel Steinert, Arda Tüysüz, Hirofumi Uemura, and Tobias Wellerdieck.

Finally, I thank all my friends in Zurich and elsewhere. They are one of the reasons why I stayed in Zurich much longer than originally planned. I express my thanks for my loving parents, Sylvie and François, and for my brother, Julien, for their encouraging support during this thesis. They, definitely, carry a heavy responsibility for my interest in science and engineering. Without all of you, this work would not have been possible.

Zurich, October 2018

Thomas Guillod

Abstract

NEWLY available fast-switching Medium-Voltage (MV) Silicon-Carbide (SiC) semiconductors are setting new limits for the design space of MV converters. Unprecedented blocking voltages (up to 15 kV), higher switching frequencies (up to 200 kHz), higher commutation speeds (up to 100 kV/ μ s), and high temperature operation can be reached. These semiconductors feature reduced switching and conduction losses and, therefore, allow for the realization of extremely efficient and compact MV converters. Moreover, the increased blocking voltage allows the usage of simple single-cell topologies for MV converters instead of complex multi-cell systems. Hence, the MV SiC semiconductors are interesting for many applications such as locomotive traction chains, datacenter power supply chains, collecting grids for renewable energies, high power electric vehicle chargers, and more-electric aircraft.

Most of these applications require an isolated DC-DC converter for providing voltage scaling and galvanic isolation. However, the increased voltages and frequencies allowed by MV SiC semiconductors create new challenges for the design of Medium-Frequency (MF) transformers, which start to become the bottleneck of isolated DC-DC converters in terms of power density and efficiency. More specifically, the winding losses (due to skin and proximity effects) and the core losses (due to eddy currents and hysteresis) are rapidly increasing and mitigate the advantages (e.g., the reduced volt-second product applied to the magnetic core) obtained with the increased operating frequencies. Moreover, the MV/MF PWM voltages with fast switching transitions are also particularly critical for the insulation of MF transformers and can lead to additional losses, thermal breakdowns, and partial discharge induced breakdowns. Finally, the MF transformers of DC-DC converters should feature reduced losses (efficiencies above 99.5 %) in order to match the performance offered by the MV SiC semiconductors.

The main focus of this thesis is, thus, set on the design of highly efficient MV/MF transformers employed in isolated DC-DC converters. First, a theoretical analysis of MF transformers is conducted in order to extract the fundamental performance limitations of such devices. The nature of the optimal designs is examined with analytical models, scaling laws, and numerical optimizations. Afterwards, several points are identified as critical and are studied in more detail.

First, the impact of model uncertainties and parameter tolerances on MF transformers is examined with statistical methods in order to highlight the achievable modeling accuracy. Then, a 2.5D numerical field simulation method is presented for assessing the impact of non-idealities on the losses produced

by litz wire windings (e.g., twisting scheme and pitch length). Afterwards, the impact of MV/MF PWM voltages with fast switching transitions on the insulation is examined. The electric field pattern is analyzed inside, at the surface, and outside the insulation and shielding methods are proposed. Finally, the dielectric loss mechanisms of dry-type insulation materials under PWM voltages is examined in detail. Different analytical expressions are proposed for extracting the insulation losses and it is found that the dielectric losses can be significant for MV/MF transformers operated with MV SiC semiconductors. Design guidelines are proposed for the selection of appropriate insulation materials for MV/MF applications and silicone elastomer is identified as an interesting choice. All the presented results are verified with measurements conducted on different MF transformer prototypes.

The derived models and results are applied to a MV isolated DC-DC converter, which is part of a MV AC (3.8 kV, phase-to-neutral RMS voltage) to LV DC (400 V) Solid-State Transformer (SST) demonstrator. This SST is aimed to supply future datacenters directly from the MV grid. The considered 25 kW DC-DC converter operates between a 7 kV DC bus and a 400 V DC bus. The usage of 10 kV SiC MOSFETs allows for the realization of the converter with a single-cell DC-DC Series-Resonant Converter (SRC). The DC-DC SRC is operated at 48 kHz as a DC Transformer (DCX) and the modulation scheme, which allows for Zero-Voltage Switching (ZVS) of all semiconductors, is examined in detail. The realized MV/MF transformer prototype features a power density of 7.4 kW/l (121 kW/in³, 4.0 kW/kg, and 1.8 kW/lb) and achieves a full-load efficiency of 99.65 %. The complete DC-DC converter achieves an efficiency of 99.0 % between 50 % and 100 % load with a power density of 3.8 kW/l (62 W/in³, 2.9 kW/kg, and 1.3 kW/lb). The results obtained with the constructed DC-DC converter, which are significantly beyond the state-of-the-art, demonstrate that MV/MF transformers can utilize the possibilities offered by the new MV SiC semiconductors.

Kurzfassung

MODERNSTE Silizium-Karbid (SiC) Halbleitertechnologie ermöglicht die Realisierung von Transistoren mit bisher unerreichten Sperrspannungen (bis zu 15 kV) und hohen Änderungsraten der geschalteten Spannung (bis zu 100 kV/ μ s), welche sich für hohe Betriebstemperaturen und, aufgrund geringer Leit- und Schaltverluste, für Anwendungen mit hohen Leistungen und hohen Schaltfrequenzen (bis zu 200 kHz) eignen. Entsprechend hat die Verfügbarkeit solcher SiC Transistoren signifikante Auswirkungen auf die limitierenden Grössen im Zusammenhang mit dem Entwurf von Mittelspannungskonvertern. Insbesondere lassen sich, im Vergleich zum Einsatz herkömmlicher Silizium-Technologien (MOSFETs, IGBTs, GTOs), sehr kompakte Mittelspannungskonverter mit extrem hoher Effizienz realisieren. Hinzu kommt, dass sich, aufgrund der hohen Sperrspannungsfestigkeit, komplexe Multizellensysteme durch Schaltungstopologien geringerer Komplexität ersetzen lassen. Entsprechend eignen sich SiC Halbleiterelemente für Traktionsanwendungen und, im Zusammenhang mit More-Electric-Aircraft-Konzepten für Flugzeuganwendungen, für Anwendungen in Verteilnetzen (v.a. im Zusammenhang mit der Erschliessung erneuerbarer Energiequellen und den damit einhergehenden zusätzlichen Anforderungen an das Verteilnetz) und für Anwendungen in Hochleistungsladegeräten für Elektrofahrzeuge.

Häufig kommen in den oben genannten Anwendungen, zur Spannungsübersetzung bzw. Anpassung der Ausgangsspannung an ein vorgegebenes Spannungsniveau und für eine galvanische Trennung, isolierte Gleichspannungs-Gleichspannungskonverter mit Mittelspannungs- und Mittelfrequenztransformatoren (MV/MF Transformatoren) zum Einsatz. Jedoch stellen die mit SiC Transistoren möglichen hohen Betriebsspannungen und Schaltfrequenzen, aufgrund erhöhter Wirbelstromverluste in den Wicklungen (Skin- und Proximityeffekt) und erhöhter Kernverluste (Wirbelstrom- und Hystereseverluste), neue Herausforderungen an den Transformator-entwurf welche sich negativ auf die erwarteten Vorteile hinsichtlich Wirkungsgrad und Bauvolumen auswirken. Im Zusammenhang mit dem Betrieb mit pulsbreitenmodulierten Spannungen kommt hinzu, dass mit zunehmenden Schaltfrequenzen und Spannungsänderungsraten auch erhöhte Beanspruchungen in den in MV/MF Transformatoren verwendeten Isolationsmaterialien resultieren, welche zusätzliche Verluste und letztlich Beschädigungen verursachen können, z.B. aufgrund von Teilentladungen oder thermischer Überlastung. Ziel des Transformator-entwurfs ist es, einen hohen Wirkungsgrad von mehr als 99.5 % zu erreichen, womit eine Anpassung an die SiC

Transistoren erzielbaren niedrigen Halbleiterverluste und damit ein hoher Gesamtwirkungsgrad des Konvertersystems erreichbar wird.

Der Fokus der vorliegenden Dissertation richtet sich daher auf den Entwurf hocheffizienter MV/MF Transformatoren, wie sie in potentialgetrennten Gleichspannungs-Gleichspannungskonvertern verwendet werden. Im Rahmen einer theoretischen Analyse erfolgt in einem ersten Schritt die Identifikation grundsätzlich vorliegender Einschränkungen/Limitierungen von MV/MF Transformatoren, z.B. der bei gegebenem Volumen minimal möglichen Verluste, und die Untersuchung wesentlicher Eigenschaften optimaler Entwurfsergebnisse mittels analytischer Modelle, Skalierungsgesetze und numerischer Methoden. Im Anschluss daran erfolgt eine detaillierte Erörterung einzelner ausgewählter Entwurfsergebnisse.

Nachfolgend wird auf Basis einer, unter Verwendung statistischer Methoden durchgeführten Untersuchung der Einfluss verschiedener Parameter-toleranzen bzw. Unsicherheiten der Modellierung auf die resultierenden Kennwerte von MV/MF Transformatoren analysiert und damit die erreichbare Genauigkeit der verwendeten Modelle bestimmt. Daran anschliessend erfolgt, unter Verwendung einer 2.5-dimensionalen numerischen Feldsimulation, eine Analyse der Verluste in Hochfrequenzlitzendrähten unter Berücksichtigung nichtidealer Eigenschaften (z.B. aufgrund nichtidealer Verflechtung oder der Schlaglänge) sowie die Untersuchung der Einflüsse pulsbreitenmodulierter MV/MF Spannungen mit hohen Änderungsraten auf die in MV/MF Transformatoren verwendeten Isolationsmaterialien. In diesem Zusammenhang werden die dielektrischen Verlustmechanismen von Isolationsmaterialien, wie in Trockentransformatoren verwendet, im Detail untersucht und die elektrischen Felder in unmittelbarer Nähe der Isolation bestimmt. Die Auswertung verschiedener analytischer, im Zuge dieser Dissertation zusammengefasster bzw. ermittelter Formeln zur Berechnung der Verluste in den Isolationsmaterialien zeigt, dass dielektrische Verluste in mit SiC Transistoren betriebenen MV/MF Transformatoren signifikante Werte annehmen können. Im weiteren Verlauf werden Entwurfsrichtlinien für die Auswahl von, für MV/MF Anwendungen geeigneten Isolationsmaterialien vorgeschlagen, wobei sich Silikonelastomer als interessante Wahl herausstellt. Die theoretisch ermittelten Ergebnisse werden anhand von Messungen, an verschiedenen Prototypen von MF Transformatoren, experimentell verifiziert.

Die entwickelten Modelle und Ergebnisse dienen als Basis für den Entwurf eines isolierten MV-Gleichspannungs-Gleichspannungskonverters (MV-DC-DC-Konverters). Der realisierte Konverter bildet die Kernkomponente eines Demonstrators für einen Solid-State-Transformator (SST), welcher sinusför-

mige Phasenspannungen mit Effektivwerten bis zu 3.8 kV in eine Gleichspannung von 400 V umwandelt. Anwendung finden solche SSTs beispielsweise in zukünftigen Rechenzentren, da hiermit eine direkte Versorgung der 400 V Gleichspannungsschiene aus dem MV-Netz möglich ist. Der betrachtete MV-DC-DC-Konverters ist für eine Nennleistung von 25 kW ausgelegt und wird auf der Mittelspannungsseite mit einer Gleichspannung von 7 kV gespeist. Durch den Einsatz hochsperrender SiC MOSFETs mit einer Sperrspannungsfestigkeit von 10 kV sind für die Realisierung des Konverters keine komplexen Multizellenstrukturen erforderlich. Der Konverter lässt sich somit mit einem einzigen DC-DC Serienresonanzkonverter (SRC) realisieren. Das im Zuge der Entwicklung des DC-DC SRC implementierte Steuerverfahren ermöglicht Schaltvorgänge mit geringen Schaltverlusten (Zero Voltage Switching, ZVS), womit sich der DC-DC SRC, trotz der sehr hohen geschalteten Spannungen, mit einer hohen Schaltfrequenz von 48 kHz betreiben lässt. Der realisierte Prototyp des MV/MF Transformators erzielt eine Leistungsdichte von 7.4 kW/l (121 kW/in^3 , 4.0 kW/kg und 1.8 kW/lb) und bei Vollast einen Wirkungsgrad von 99.65 %. Der Gesamtwirkungsgrad des MV-DC-DC-Konverters beträgt 99.0 % (in einem Lastbereich zwischen 12 kW und 25 kW) bei einer Leistungsdichte von 3.8 kW/l (62 W/in^3 , 2.9 kW/kg und 1.3 kW/lb). Die mit dem realisierten Konverter erzielten Ergebnisse liegen wesentlich über dem Stand der Technik und zeigen auf, dass sich mit geeigneten Konvertertopologien die besonderen Schalteigenschaften hochsperrender SiC-MOSFETs sehr gut nutzen lassen.

Abbreviations

| | |
|---------|---|
| AC | Alternating Current |
| CM | Common-Mode |
| DC | Direct Current |
| DCX | DC Transformer |
| DAB | Dual Active Bridge |
| DOF | Degree Of Freedom |
| DM | Differential-Mode |
| EMI | Electromagnetic Interference |
| FEM | Finite Element Method |
| FLOP | Floating Point Operation |
| GaN | Gallium Nitride |
| GSE | Generalized Steinmetz Equation |
| GTO | Gate Turn-Off Thyristor |
| HEMT | High-Electron-Mobility Transistor |
| HF | High-Frequency |
| HV | High-Voltage |
| IGBT | Insulated-Gate Bipolar Transistor |
| iGSE | Improved Generalized Steinmetz Equation |
| ISOP | Input Series Output Parallel |
| ISOS | Input Series Output Series |
| LF | Low-Frequency |
| LV | Low-Voltage |
| MCS-ZVS | Magnetizing Current Splitting ZVS |
| MF | Medium-Frequency |
| MMLC | Modular Multi-Level Converter |
| MV | Medium-Voltage |
| MOSFET | Metal-Oxide-Semiconductor Field-Effect Transistor |
| PEEC | Partial Element Equivalent Circuit |
| PWM | Pulse-Width Modulation |
| RMS | Root Mean Square |
| Si | Silicon |
| SiC | Silicon Carbide |
| SRC | Series Resonant Converter |
| SST | Solid-State Transformer |
| ZCS | Zero Current Switching |
| ZVS | Zero Voltage Switching |

Contents

| | |
|---|-------------|
| Acknowledgments | v |
| Abstract | vii |
| Kurzfassung | ix |
| Abbreviations | xiii |
| 1 Introduction | 1 |
| 1.1 Power Transformer Development | 1 |
| 1.2 Power Transformer Limitations | 3 |
| 1.3 Power Electronics Development | 7 |
| 1.4 MV/MF Transformer Applications | 10 |
| 1.5 MV DC-DC Converters | 11 |
| 1.6 MV/MF Transformer Technologies | 14 |
| 1.7 Aims and Contributions | 18 |
| 1.7.1 Scientific Contributions | 18 |
| 1.7.2 DC-DC Demonstrator System | 21 |
| 1.7.3 Performance Benchmark | 25 |
| 1.8 List of Publications | 27 |
| 1.8.1 Journal Papers | 28 |
| 1.8.2 Conference Papers | 28 |
| 1.8.3 Workshops and Seminars | 29 |
| 1.8.4 Further Scientific Contributions | 30 |
| 1.9 Thesis Outline | 31 |
| 2 MF Transformer Scaling Laws | 33 |
| 2.1 Introduction | 33 |
| 2.2 Full-Analytical Modeling | 36 |
| 2.2.1 Geometry and Operating Conditions | 36 |
| 2.2.2 Core and Winding Losses | 40 |
| 2.2.3 Thermal Modeling | 42 |
| 2.3 Optimization and Scaling Laws | 42 |
| 2.3.1 Area Product | 42 |
| 2.3.2 Optimal MF Design | 43 |
| 2.3.3 Frequency Diversity | 45 |
| 2.3.4 Scaling Laws | 47 |
| 2.4 Analytical Results | 52 |

| | | |
|----------|---|-----------|
| 2.4.1 | Considered Parameters | 53 |
| 2.4.2 | Optimal Design | 53 |
| 2.4.3 | Frequency Diversity | 55 |
| 2.4.4 | Scaling Laws | 55 |
| 2.4.5 | Core Material and Winding Stranding | 58 |
| 2.5 | Numerical Verification | 59 |
| 2.5.1 | Semi-Numerical Model | 59 |
| 2.5.2 | Scaling Laws | 60 |
| 2.5.3 | Design Space Diversity | 64 |
| 2.6 | Critical Analysis | 67 |
| 2.7 | Summary | 68 |
| 3 | MF Transformer Equivalent Circuit | 71 |
| 3.1 | Introduction | 71 |
| 3.2 | Considered Transformer | 74 |
| 3.3 | Analytical Methods | 77 |
| 3.3.1 | Open-Circuit | 77 |
| 3.3.2 | Short-Circuit | 78 |
| 3.3.3 | Circuit Extraction | 80 |
| 3.4 | FEM Simulations | 80 |
| 3.4.1 | Circuit Extraction | 80 |
| 3.4.2 | 2D Modeling | 80 |
| 3.4.3 | 3D Modeling | 82 |
| 3.5 | Statistical Analysis | 82 |
| 3.5.1 | Considered Parameters | 82 |
| 3.5.2 | Worst-Case Analysis | 84 |
| 3.5.3 | Normal Distribution Analysis | 87 |
| 3.6 | Results | 88 |
| 3.6.1 | Measurements | 88 |
| 3.6.2 | Computations | 91 |
| 3.6.3 | Comparison: Measurements and Computations | 92 |
| 3.7 | Summary | 97 |
| 4 | Litz Wire Losses | 99 |
| 4.1 | Introduction | 99 |
| 4.2 | Perfect Twisting | 102 |
| 4.3 | Twisting Imperfections | 105 |
| 4.3.1 | Computation Method | 105 |
| 4.3.2 | Considered Twisting Imperfections | 109 |
| 4.3.3 | Simulation: Twisting Schemes | 110 |

| | | |
|----------|--|------------|
| 4.3.4 | Simulation: Number of Pitches | 112 |
| 4.3.5 | Analytical Approximations | 113 |
| 4.4 | Measurements of Twisting Imperfections | 116 |
| 4.5 | Summary | 120 |
| 5 | MV/MF Transformer Prototype | 123 |
| 5.1 | Introduction | 123 |
| 5.2 | Optimization | 125 |
| 5.2.1 | Design Space Restrictions | 125 |
| 5.2.2 | Optimization Results | 126 |
| 5.2.3 | Design Selection | 129 |
| 5.3 | Design and Construction | 131 |
| 5.3.1 | Transformer Design | 131 |
| 5.3.2 | Insulation Capabilities | 137 |
| 5.3.3 | Construction and Vacuum Potting | 139 |
| 5.4 | Experimental Testing | 145 |
| 5.4.1 | Short-Circuit and Saturation | 145 |
| 5.4.2 | Impedance Measurements | 146 |
| 5.4.3 | Resonances | 147 |
| 5.4.4 | Insulation Testing | 152 |
| 5.4.5 | Thermal Model | 153 |
| 5.5 | Losses Measurements | 155 |
| 5.5.1 | Winding Losses | 156 |
| 5.5.2 | Core Losses | 157 |
| 5.5.3 | Other Losses | 161 |
| 5.5.4 | Efficiency | 162 |
| 5.6 | Summary | 165 |
| 6 | MV/MF Transformer Shielding | 167 |
| 6.1 | Introduction | 167 |
| 6.2 | MV/MF Transformer | 168 |
| 6.3 | Magnetic and Electric Field Analysis | 171 |
| 6.4 | Electrical Shielding | 176 |
| 6.4.1 | Shielding Methods | 176 |
| 6.4.2 | Resistive Shielding | 177 |
| 6.4.3 | Shield Functional Principle | 179 |
| 6.4.4 | Optimal Shield Conductivity | 182 |
| 6.4.5 | Shielding Effects | 184 |
| 6.4.6 | Experimental Verification | 187 |
| 6.5 | Summary | 188 |

| | | |
|----------|--|------------|
| 7 | Dielectric Losses with PWM | 191 |
| 7.1 | Introduction | 191 |
| 7.2 | Dielectric Polarization Losses | 193 |
| 7.2.1 | Time Domain | 193 |
| 7.2.2 | Frequency Domain | 197 |
| 7.2.3 | Loss Computation | 199 |
| 7.3 | Dielectric Losses with PWM Voltages | 201 |
| 7.3.1 | PWM with Frequency-Independent Materials | 201 |
| 7.3.2 | Frequency-Dependent Materials | 205 |
| 7.3.3 | Upper Bound on the Dielectric Losses | 206 |
| 7.3.4 | PWM with Frequency-Dependent Materials | 208 |
| 7.4 | Case Study: MV/MF Transformer | 210 |
| 7.4.1 | Transformer Design | 210 |
| 7.4.2 | Transformer Simulation | 213 |
| 7.4.3 | Epoxy Resin Insulation | 213 |
| 7.4.4 | Silicone Elastomer Insulation | 215 |
| 7.4.5 | Dielectric Loss Measurements | 218 |
| 7.5 | Design Guidelines | 221 |
| 7.6 | Summary | 224 |
| | | |
| 8 | MV DC-DC Converter Prototype | 227 |
| 8.1 | Introduction | 227 |
| 8.2 | Considered SRC-DCX | 229 |
| 8.3 | Passive Rectifier | 232 |
| 8.3.1 | Operating Principle | 232 |
| 8.3.2 | Simulated Waveforms | 236 |
| 8.3.3 | Partial-Load Operation | 238 |
| 8.4 | Active Rectifier / Analytical Model | 240 |
| 8.4.1 | Considered Model | 241 |
| 8.4.2 | Resonant Current | 241 |
| 8.4.3 | Circulating Current | 243 |
| 8.4.4 | Magnetizing Current | 244 |
| 8.4.5 | Choice of the Equivalent Circuit | 244 |
| 8.4.6 | Current Waveforms | 245 |
| 8.4.7 | ZVS Currents | 245 |
| 8.5 | Active Rectifier / Simulations | 247 |
| 8.5.1 | Phase Shift Operation | 249 |
| 8.5.2 | Robustness of the Modulation Scheme | 251 |
| 8.5.3 | Partial-Load Operation | 253 |

| | | |
|----------|--|------------|
| 8.6 | Measurements | 254 |
| 8.6.1 | Modulation Scheme | 254 |
| 8.6.2 | Efficiency Measurements | 256 |
| 8.7 | Summary | 258 |
| 9 | Conclusion and Outlook | 261 |
| 9.1 | MV/MF Transformer Technologies | 262 |
| 9.2 | DC-DC Demonstrator System | 264 |
| 9.3 | Outlook and Future Research Areas | 265 |
| | Appendices | 269 |
| A | Equivalent Circuit Comparison | 271 |
| A.1 | Transformer Equivalent Circuits | 271 |
| A.2 | Analytical Computations | 274 |
| A.3 | FEM Simulations | 275 |
| A.4 | Designs with High Coupling Factors | 275 |
| B | Approximations of Dielectric Losses | 279 |
| B.1 | Frequency-Independent Materials | 279 |
| B.2 | Upper Bound on the Dielectric Losses | 280 |
| B.3 | Frequency-Dependent Materials | 281 |
| B.4 | Kramers-Kronig Approximations | 282 |
| B.5 | Accuracies of the Approximations | 283 |
| | Bibliography | 285 |
| | Curriculum Vitae | 319 |

1

Introduction

IN 1831, the British scientist Michael Faraday discovered the law of induction and constructed an electrical generator, laying the theoretical foundation for an industrial use of electricity [1]. Only 50 years later, in 1880, the US-American Thomas Edison founded the “Edison Illuminating Company” with the ambition to develop DC distribution grids [2]. A few years later, in 1886, the US-American George Westinghouse founded the “Westinghouse Electric Company” with similar goals, however, using AC technology [2].

The competition between these two companies and between the two technologies (DC and AC) led to the “war of the currents” [2]. The main challenge was to obtain an electrical grid which would be scalable with respect to the grid size and the power level. The “war of the currents” was then settled by a technology, which emerged in Europe some years earlier: the electrical power transformer.

1.1 Power Transformer Development

A transformer consists of two (or more) windings which are magnetically coupled, usually by means of a magnetic core. The AC voltage applied to one winding creates a magnetic flux which induces voltages in the other windings, allowing for voltage transformation and galvanic isolation. The first prototype was built in 1831 by Faraday himself and is known as “Faraday’s ring coil” [1]. The first practical application of the transformer principle was proposed in 1876 by the Russian Pavel Yablochkov for supplying electric candles [3]. A few years later, in 1883, the French Lucien Gaulard, associated to the British John Dixon Gibbs, constructed a transformer as part of a 40 km transmission system operated at 2 kV and demonstrated the interest of power transformers [4].

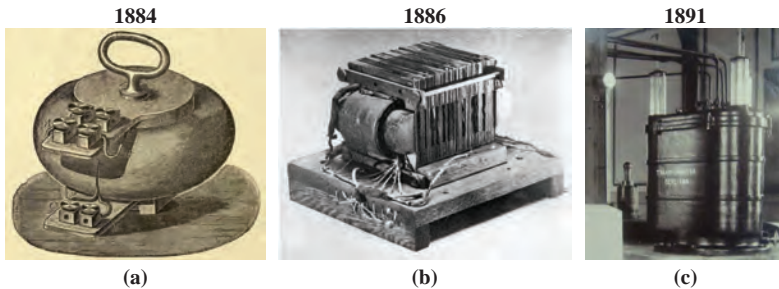


Fig. 1.1: (a) Single-phase transformer designed by Zipernowsky, Bláthy, and Déri in 1884. (b) Single-phase distribution transformer designed by Stanley in 1886. (c) Three-phase distribution transformer realized by “Maschinenfabrik Oerlikon” in 1891. Images in the public domain.

However, this design, which featured an open magnetic circuit, was not able to provide a stable and/or load-independent voltage. This problem was solved in 1884 by the Hungarians Károly Zipernowsky, Ottó Bláthy, and Miksa Déri, who proposed the first modern transformer (cf. Fig. 1.1(a)), using a closed magnetic circuit, core-type or shell-type arrangements, and a laminated core [5].

The development of the transformer gave a decisive advantage to the AC technology. The possibility to step-up the voltage allowed for an efficient and stable energy transfer over long distances and the galvanic isolation gave the opportunity to easily interconnect grids. This was quickly recognized by George Westinghouse, who assigned to the US-American William Stanley the task to transform the European prototypes into commercial products(cf. Fig. 1.1(b)) [6]. This was achieved in 1886 with the realization of the first modern AC distribution grid in Great Barrington [6]. From this point on, the AC technology started to supplant the DC technology. In 1890, the Polish-Russian Mikhail Dolivo-Dobrovolsky patented the three-phase transformer [7]. One year later, in 1891, the Swiss company “Maschinenfabrik Oerlikon” and the German company “AEG” built the first three-phase AC transmission system (180 kW, 175 km, 40 Hz, and 25 kV) featuring transformers (cf. Fig. 1.1(c)) [8]. The “war of the currents” was considered as definitely settled in favor of the AC technology in 1893, when “General Electric” built the Niagara Falls power plant, which featured an unprecedented power rating (3.7 MW and 25 Hz) [9].

However, the “war of the currents” continued as a battle concerning the frequency, which will turn out to be one of the central elements of this

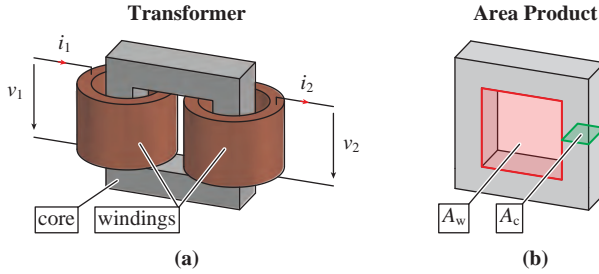


Fig. 1.2: (a) Considered single-phase transformer featuring a core-type configuration. (b) Definition of the area product of the core. For illustrative purposes only, the two windings are placed around two different limbs (such winding arrangement is, due to the increased HF winding losses, unusual for MF transformers).

thesis. By the end of the nineteenth century, many different frequencies were coexisting (from 25 Hz to 133 Hz) [10]. With the increasing power rating of generators, the frequency standardization became a necessity for allowing the interconnection of the different grids. The frequencies below 40 Hz were problematic due to flicker of the lamps and the massive size of the power transformers. The frequencies above 60 Hz were difficult to handle for the generators, the motors, and the transmission lines [10]. At the beginning of the twentieth century, two standard grid frequencies were emerging: 50 Hz in Europe and 60 Hz in North America [10, 11]. However, the standardization of the frequency was a slow and incomplete process. The last 25 Hz generators of the aforementioned Niagara Falls power plant were only disconnected in 2006 [12]. There are, however, some niche applications, such as traction power networks, which are still running with DC, 16.7 Hz, or 25 Hz [13].

Around 1890, power transformers (at 50 Hz or 60 Hz) were already reaching efficiencies above 97% [14]. From this point on, only slow incremental innovations were achieved for grid-connected power transformers [6]. Of course, the power ratings, voltage levels, and efficiencies have been slightly improved with better designs and materials, but modern power transformers remain extremely similar to the designs shown in Fig. 1.1 [6, 15].

1.2 Power Transformer Limitations

For understanding the fundamental characteristics and limitations of power transformers, a simple model is sufficient. Fig. 1.2(a) depicts a single-phase

transformer consisting of two windings and a magnetic core. However, the derived equations also apply to three-phase transformers. The induced voltages on the windings can be expressed as

$$v_1 = N_1 \frac{\partial \phi_1}{\partial t}, \quad (1.1)$$

$$v_2 = N_2 \frac{\partial \phi_2}{\partial t}, \quad (1.2)$$

where v_1/v_2 are the terminal voltages, N_1/N_2 the numbers of turns, and ϕ_1/ϕ_2 the magnetic fluxes. An ideal transformer features the following characteristics: no losses, no stored energy, and perfect magnetic coupling between the windings (all the turns of both windings are assumed to be linked with the same flux):

$$\phi = \phi_1 = \phi_2, \quad (1.3)$$

$$v_1 i_1 = v_2 i_2, \quad (1.4)$$

where i_1/i_2 are the terminal currents. The combination of these hypotheses with the equations for the induced voltages lead to the two fundamental transformer equations:

$$\frac{v_1}{v_2} = \frac{N_1}{N_2}, \quad (1.5)$$

$$\frac{i_1}{i_2} = \frac{N_2}{N_1}. \quad (1.6)$$

The following properties can be extracted for an ideal transformer: fixed (load-independent) voltage and current transfer ratio, no losses, no stored energy, and galvanic isolation between the windings. The shape and, therefore, the frequency of the voltages is identical between the primary and the secondary-side. This holds true as long as the transformer core does not saturate.

However, for extracting the fundamental limitations of power transformers, additional parameters are required. For deriving the considered model, sinusoidal currents and voltages are accepted. The current density (J_{RMS}) and the winding losses (P_{w}) can be expressed as [16–18]

$$J_{\text{RMS}} = \frac{2N_1 I_{1,\text{RMS}}}{k_{\text{w}} A_{\text{w}}} = \frac{2N_2 I_{2,\text{RMS}}}{k_{\text{w}} A_{\text{w}}}, \quad (1.7)$$

$$P_{\text{w}} = (V_{\text{w}} k_{\text{w}}) \frac{J_{\text{RMS}}^2}{\sigma}, \quad (1.8)$$

where V_w is the winding volume, A_w the winding window area (cf. Fig. 1.2(b)), k_w the winding filling factor, and σ the conductivity of the winding conductors. The skin and proximity effect losses in the windings are neglected. The flux density (B_{pk}) and the core losses (P_c) can be expressed as [17–19]

$$B_{pk} = \frac{\sqrt{2}V_{1,RMS}}{2\pi f N_1 A_c} = \frac{\sqrt{2}V_{2,RMS}}{2\pi f N_2 A_c}, \quad (1.9)$$

$$P_c = V_c k_c f^{\alpha_c} B_{pk}^{\beta_c}, \quad (1.10)$$

where V_c is the core volume and A_c is the core cross section (cf. Fig. 1.2(b)). The core losses are described by the three empirical Steinmetz parameters (k_c , α_c , and β_c).

From these equations, it can be seen that the choice of the number of turns is a trade-off between the obtained current density and flux density and, hence, between the winding and the core losses. However, the number of turns can be eliminated, which results in the area product [17, 20]:

$$A_c A_w = \frac{\sqrt{2}}{\pi k_w B_{pk} J_{RMS}} \frac{S}{f}, \quad (1.11)$$

where S is the transformer apparent power. The filling factor (k_w) is limited by geometrical and insulation constraints, the current density (J_{RMS}) by the heat extraction capabilities of the cooling system, and the flux density (B_{pk}) by the saturation flux density of the core material. Hence, these parameters are fixed for a given core material, insulation material, and cooling concept. Therefore, the volume (V_t) and mass (m_t) of a transformer are scaling as follows:

$$V_t \sim \left(\frac{S}{f}\right)^{\frac{3}{4}}, \quad (1.12)$$

$$m_t \sim \left(\frac{S}{f}\right)^{\frac{3}{4}}. \quad (1.13)$$

This implies that the volume and mass of a transformer scale approximately linearly with the power rating. It also results that, for a fixed power rating, the operating frequency is the only free parameter which can be used to significantly improve the transformer design. However, the scaling laws based on the area product should be considered carefully since the efficiency is not kept constant and the HF losses are neglected.

The impact of the operating frequency is illustrated in Fig. 1.3, where the performances of a 25 kW transformer are considered. It can be immediately

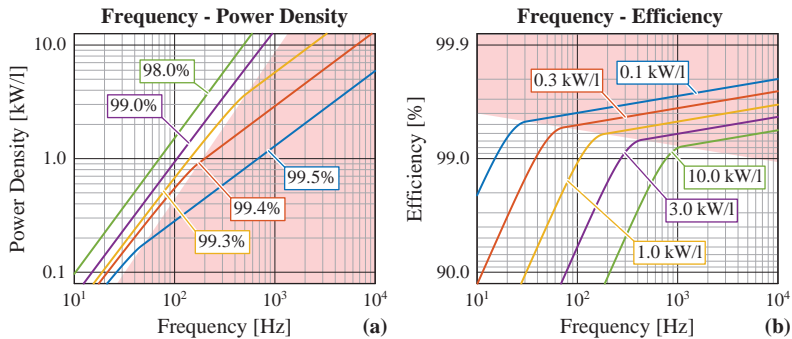


Fig. 1.3: (a) Scaling of a transformer for a fixed efficiency and variable frequencies. (b) Scaling of a transformer for a fixed power density and variable frequencies. The shaded red region represents the domain where the designs are operated below the saturation flux density of the core. A 25 kW transformer with copper windings and an amorphous core (“Metglas 2605SA1”) is considered [21]. The skin and proximity winding losses are neglected. The thermal limit of the transformer is also neglected.

recognized that designs with increased operating frequencies achieve better efficiencies and power densities. However, above a certain frequency, the flux density in the core should be reduced (below the saturation flux density) in order to limit the core losses. This flux density reduction mitigates the advantages of increased operating frequencies, without suppressing it, as long as the HF winding losses remain at low values [18, 22–25].

The advantages of operating a transformer at increased frequencies were already highlighted in 1893 [26]. However, as already mentioned, the selection of the grid frequency was strongly influenced by the performance of the generators, motors, and transmission lines [10]. Therefore, the standardized grid frequencies (mostly 50 Hz and 60 Hz) are sub-optimal for the power transformers. From the presented model, the following limitations and drawbacks of grid-connected power transformers can be extracted:

- ▶ Transformers operated at LF (mostly 50 Hz and 60 Hz) are intrinsically bulky and/or feature a limited efficiency [27]. This holds especially true for LF traction grids (16.7 Hz or 25 Hz) [13].
- ▶ Transformers are not able to interconnect grids, loads, or generators operating at different frequencies. Moreover, transformers are by definition unable to generate DC voltages [27, 28].

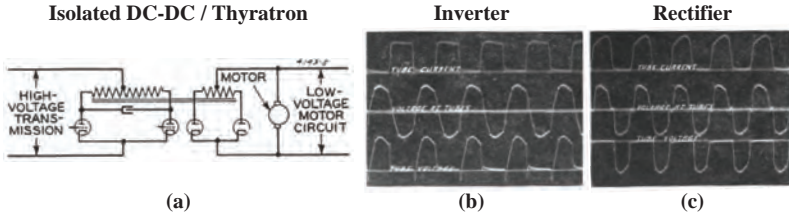


Fig. 1.4: (a) Isolated DC-DC converter based on Thyatron mercury-arc valves, proposed in 1928 [35]. (b) Waveforms of the inverter bridge. (c) Waveforms of the rectifier bridge. This figure is taken (and adapted) from [33].

- Transformers are passive devices, which are not able to provide voltage control, power flow control, or reactive power compensation. [27, 28].

1.3 Power Electronics Development

Already by the end of the nineteenth century, the need for interconnecting grids operating at different frequencies and supplying DC loads started appearing [10]. First, such frequency converters and rectifiers were realized with the back-to-back connection of electrical machines [29–31]. However, such installations were bulky, expensive, and featured a limited efficiency.

In 1902, the invention of the mercury-arc valves, allowed to switch voltages and currents and, therefore, to actively shape electrical waveforms [32]. The possibilities offered by this technology led to the development of the a branch of electrical engineering: power electronics [33]. The utilization of mercury-arc valves first allowed the development of AC-DC rectifiers (around 1910), DC-AC inverters (around 1920), and variable-frequency drives (around 1920) [32, 34].

Finally, the isolated DC-DC converter, which is the subject of this thesis, emerged in 1928, using Thyatron mercury-arc valves [35]. However, different patents, filled in 1899, 1913, and 1916, already used the same principle with mechanical commutators [36–38]. The isolated DC-DC converter with Thyatron mercury-arc valves is described in Fig. 1.4 [33, 35]. An inverter bridge chops the input DC voltage into a rectangular AC voltage which is exciting the primary-side of a transformer. The rectangular AC voltage also appears at the secondary-side of the transformer and is transformed back into a DC voltage by the rectifier bridge. This operating principle is still used nowadays by isolated DC-DC converters. However, the switching performances

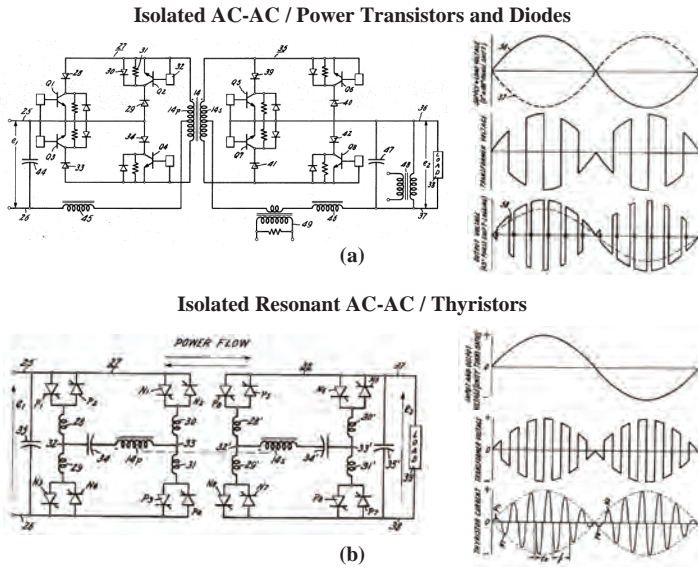


Fig. 1.5: (a) Isolated AC-AC converter based on power transistors (with series diodes for achieving neagtive voltage blocking capabilities), proposed in 1968 [39]. (b) Isolated resonant AC-AC converter based on thyristors, proposed in 1968 [40]. The key waveforms are illustrated for AC-AC operation, however, both topologies can also be used as DC-DC converters. This figure is taken (and adapted) from [39, 40].

of the mercury-arc valves were limited and the advantageous properties of transformers at increased frequencies could not be exploited (cf. Fig. 1.3).

The transistor was invented in 1947 and opened new possibilities for realizing efficient electrical switches. Soon after, in 1958, the first thyristor was commercialized and was followed, in 1962, by the GTO thyristor, offering a viable alternative to mercury-arc valves [32]. In 1968, two circuit topologies were proposed in order to build AC-AC and DC-DC isolated converters featuring transformers operated at MF [39, 40]. For the first time, the advantageous properties of MF transformers could be exploited, leading to compact and efficient systems (cf. Fig. 1.3). Moreover, compared to a grid-connected transformer, the proposed circuit offers additional voltage and current control capabilities. The first circuit, which is shown in Fig. 1.5(a), is based on power transistors (with series diodes) [39]. Again, the LF AC or DC voltages are chopped into rectangular pulses, transmitted through the MF transformer,

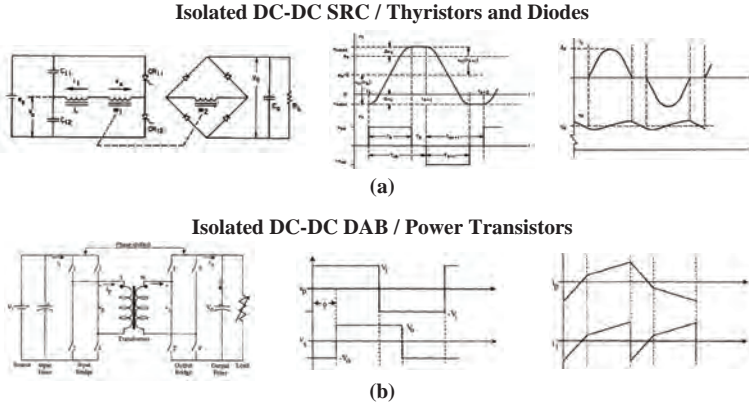


Fig. 1.6: (a) Isolated DC-DC SRC based on thyristors, proposed in 1968 [40]. (b) Isolated DC-DC DAB based on power transistors, proposed in 1988 [43]. The key waveforms are illustrated for DC-DC operation. This figure is taken (and adapted) from [42, 44].

and, finally, rectified. The second circuit, which is depicted in Fig. 1.5(b), features an additional resonant tank, which allows the usage of thyristors in place of turn-off power transistors [40]. This last topology is actually the early version of the popular DC-DC SRC, which is shown in Fig. 1.6(a) [41, 42].

The apparition of power MOSFETS, in 1976, and IGBTs, in 1984, allowed to push further the switching frequency of isolated DC-DC converters [32]. New topologies, were also introduced for taking advantages of the switching behavior of these new devices, such as the DC-DC DAB, in 1988 [43–45]. The DC-DC DAB, which is shown in Fig. 1.6(b), operates a MF transformer between two bridges (voltage sources) operated with different duty cycles and phases, similarly to a patent filled in 1913 [37].

Over the years, the emergence of new applications for isolated converters such as wind turbines and photovoltaic panels has contributed to the development of high power isolated DC-DC converter, where the SRC and DAB topologies (or their numerous variants) are widely used [28, 46–48]. The introduction of SiC MOSFETs, with reduced conduction and switching losses (in 2011), promises further improvements of such converters [49]. Therefore, many new applications, which require MV grid-connected power electronic converters using MV/MF transformers, are considered in literature.

1.4 MV/MF Transformer Applications

It should be noted that the definition of MV and MF significantly depends on the considered power level and application (e.g., power system, traction, automotive, and radio-frequency). In this thesis, the following definition is accepted for MV: [1, 35] kV. For electronic converters, MF can be defined with the power/frequency product, which is usually in the following range: [0.05, 2.0] MHzkW.

High power MV/MF transformers are usually operated between two DC (or more rarely AC) buses with the help of an inverter and a rectifier. In the literature, such systems are sometimes called Solid-State Transformers (SSTs), Smart Transformers, DC Transformers, or Power Electronic Transformers [28, 50]. The applications of such high power MV/MF transformers can be decomposed into several categories:

- ▶ *Distribution transformers* - MV/LV AC grid distribution transformers can be replaced by SSTs using MV/MF transformers [28, 50, 51]. For such applications, increasing the efficiency is not possible, given that LF distributions transformers are already extremely efficient (above 99.0 %) [52, 53]. The gain of volume and mass is also a minor advantage for such transformers. The main benefits of SSTs are the advanced control capabilities (e.g., voltage, power, and harmonics compensation), which are essential for realizing future smart-grids [50, 51, 53–55]. In addition to the AC terminals, DC terminals can be added for integrating battery storage, connecting small renewable energy plants, or connecting DC microgrids [48, 53, 54, 56].
- ▶ *Renewable energies* - Most of the emerging renewable energy sources are DC sources (e.g., full converters wind turbines with subsequent rectifier stage and photovoltaic systems), which are, nowadays, connected to the MV or HV AC grid with inverters and LF step-up transformers [28, 46–48]. The inverter and the LF step-up transformer can be replaced by a single SST using MV/MF transformers, which allows for increased efficiencies, reduced volume, and reduced weight [50, 53, 55]. Moreover, SSTs can also be used to directly interface large renewable energy plants with MVDC or HVDC collecting grids instead of AC grids [46–48].
- ▶ *DC loads* - Next to the traditional DC loads (e.g., aluminum production plants and variable-frequency drives) many new applications feature large LV DC loads, such as datacenters, electrical vehicle fast chargers, and power-to-gas systems [28, 57–59]. Instead of the series connection

of a LF step-down transformer and a rectifier, a SST can be used to directly connect the LV DC load to the MV AC grid, which allows for increased efficiencies, reduced volume, and reduced weight [50, 53, 55].

- ▶ *Traction applications* - Locomotives or trains with distributed traction, which are connected to a MV AC traction grid, use step-down LF transformers combined with rectifiers in order to supply the DC-buses used by the motor inverters [27, 28, 60–64]. Such transformers are bulky, heavy, and feature limited efficiencies, especially for 16.7 Hz or 25 Hz traction grids. In such volume constrained environments, SSTs offer decisive competitive advantages [61, 62, 64]. Moreover, SSTs can be used as static converters for supplying the AC (16.7 Hz or 25 Hz) or DC traction grids from the utility AC grid (50 Hz or 60 Hz) [28].
- ▶ *Marine applications* - Large military or civilian ships often feature diesel-electric propulsion and, therefore, a frequency-independent (generator speed) supply of large electric loads (motors and auxiliary systems), from on-board MVDC distribution grids, is envisioned [65–67]. MVDC transmission is also proposed for supplying docked ships, oil/gas terminals, and off-shore oil/gas stations [28, 68, 69].
- ▶ *Aircraft applications* - Reducing the weight and volume of the electrical system is extremely important for aircraft, explaining why such systems are nowadays utilizing a 400 Hz on-board grid in order to reduce the size of the transformers [70, 71]. However, with future more-electric or all-electric aircraft, the LV 400 Hz system will not be able to achieve the required power density and efficiency, for which MVDC buses are needed [71–74]. Therefore, DC-DC SSTs are envisioned for supplying the systems requiring large voltage conversion ratios and/or galvanic isolation [28, 72, 73, 75].

1.5 MV DC-DC Converters

Different circuit topologies can be used for the aforementioned applications and are listed in [27, 28, 50, 76, 77]. Almost all the considered circuit topologies require high power isolated DC-DC converters using MV/MF transformers. These converters can provide several functionalities: voltage scaling, voltage control, power flow control, and galvanic isolation [27, 28, 78]. For systems connected to a MV grid, galvanic isolation is required for safety reasons, for isolating faults (especially with DC grids), and due to different earthing

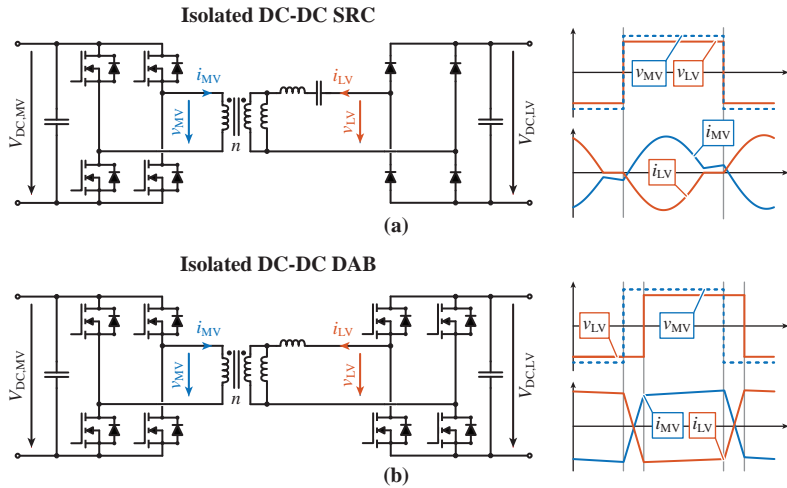


Fig. 1.7: (a) Isolated DC-DC SRC operated in half-cycle discontinuous conduction mode (switching frequency below the resonance frequency). (b) Isolated DC-DC DAB DC-DC operated with phase shift modulation.

policies of the MV and LV grids [79, 80]. The most common topologies for high power isolated DC-DC converters are the SRC and the DAB, which are shown in Fig. 1.7 [27, 42, 44, 56, 61, 78, 81–84].

The DC-DC SRC consists of a transformer and a resonant capacitor placed between an active inverter bridge and a passive rectifier bridge [42, 81]. If bidirectional power flow is required, both bridges should be realized with active switches [25, 27, 61, 85]. High power DC-DC SRCs are usually operated below the resonance frequency (half-cycle discontinuous current mode) with an active inverter bridge (50 % duty cycle) and a passive rectifier bridge (diode rectifier or synchronous rectifier), as shown in Fig. 1.7(a) [42, 86, 87]. This operating mode of the DC-DC SRC is sometimes referred to as DCX since it provides a constant voltage transfer ratio without requiring any closed-loop control [61, 82, 84, 86, 88–90]. With this modulation scheme, ZCS, ZVS, and quasi-sinusoidal currents are achieved. However, the voltage and the power flow cannot be actively controlled in DCX operating mode. Nevertheless, the control of the voltage and power flow is possible with frequency and/or duty cycle modulation, which is unusual in high power DC-DC SRCs [81, 85–87].

The DC-DC DAB consists of a transformer placed between two active (converter) bridges [44, 78]. Therefore, the DC-DC DAB intrinsically allows

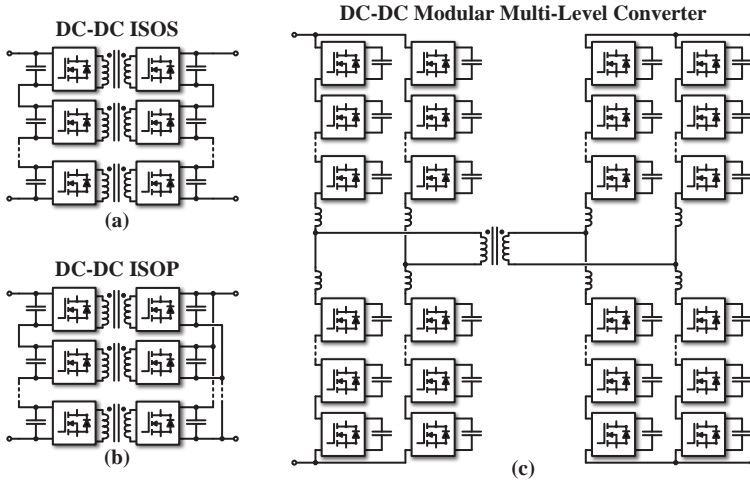


Fig. 1.8: (a) Modular multi-cell isolated DC-DC converter with an ISOS structure. (b) Modular multi-cell isolated DC-DC converter with an ISOP structure. (c) MMLC featuring modular inverter and rectifier bridges and a single MF transformer.

for bidirectional power flow. For DC-DC DABs, the simplest modulation is the phase shift modulation, where both bridges (50 % duty cycle) are operated with a phase shift, as shown in Fig. 1.7(b) [44, 56, 78]. With this modulation scheme, ZVS and quasi-rectangular currents are achieved. Many other modulation schemes exist in order to achieve ZVS, ZCS, or buck-boost operation [44, 78, 91]. However, the DC-DC DAB requires a closed-loop control for stabilizing the voltage and the power flow [78, 91].

Several possibilities exist for realizing the inverter and rectifier bridges of SRCs and DABs: full-bridges, half-bridges with split DC-buses, NPC bridges, or flying capacitor bridges [27, 92–95]. Many extensions of these converters can be found, featuring three-phase transformers, multiple ports, snubbers, alternative resonant circuits, etc. [44, 96–99].

However, the blocking voltages of commercially available power semiconductors are limited (6.5 kV for IGBTs and 10.0 kV for GTOs), i.e. not adapted to the voltage levels of MV/HV grids [32]. Moreover, these devices feature poor switching performance. This limitation can be avoided by using multi-level bridges, such as diode-clamped (NPC) or capacitor-clamped (flying capacitor) arrangements [92–95]. However, for large voltages, a modular structure is often required [27, 61, 76, 100].

Figs. 1.8(a)-(b) shows fully modular multi-cell structures based on the series and/or parallel connection of isolated DC-DC converters [50, 101–105]. This structure reduces the power and voltage ratings of the MF transformers composing the structure. Moreover, the voltage transfer ratio of the converter can be partially or totally realized with a series and parallel connection of the cells (and not with the MF transformers). Fig. 1.8(c) depicts an alternative structure based on the MMLC, which features modular inverter and rectifier bridges and a single MF transformer [60, 106, 107].

However, such modular structures feature a high number of switches, transformers, capacitors, measurements, etc. [103, 104]. The apparition of MV SiC MOSFETs (blocking voltages up to 15 kV), which are still in the prototype stage, allows a reduction of the complexity of MV isolated DC-DC converters [108–110]. Converters up to 10 kV (or even more with multi-level bridges) can be realized with a single-cell design [51, 83, 95, 99]. Moreover, compared to IGBTs, these SiC MOSFETs feature extremely reduced switching losses, which allow the operation of MV converters at unprecedented frequencies (up to 200 kHz) [111, 112]. However, such frequencies and voltages create new challenges for the design of MV/MF transformers, which start to become the bottleneck of isolated DC-DC converters [18, 25, 113].

1.6 MV/MF Transformer Technologies

The design of MV/MF high power transformers is a complex process which requires many trade-offs [17, 114, 115]. Many a priori incompatible objectives, such as power density, efficiency, large operating frequency, and large voltages should be combined. Over the years, many studies have been conducted regarding the optimization and design of such systems. The main challenges and approaches can be summarized as follows:

- ▶ *Geometry* - Different geometries can be used to realize MF transformers [16, 17]. The main variants are depicted in Fig. 1.9. The solutions shown in Figs. 1.9(a)-(c) are the typical choices for high power MF transformers [17, 25, 27, 61, 64, 116]. Planar MF transformers (cf. Fig. 1.9(d)), which often feature PCB windings, are limited to lower power ranges [117–119]. Finally, coaxial MF transformers (cf. Figs. 1.9(e)-(f)) represent an interesting alternative, which, however, has been found difficult to implement in practice [63, 120–122].
- ▶ *Equivalent circuit* - Three degrees of freedom exist for a MF transformer equivalent circuit: the voltage transfer ratio, the leakage inductance,

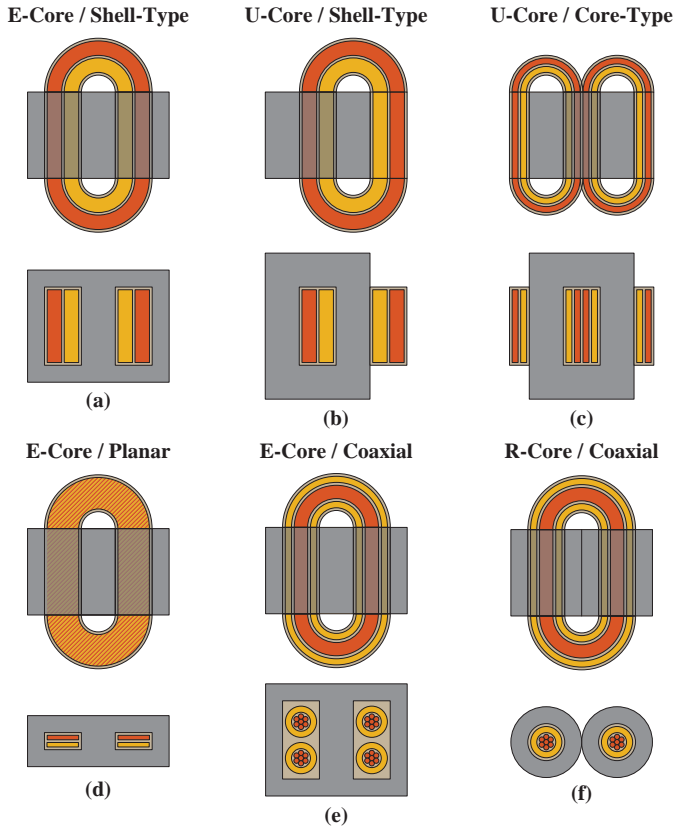


Fig. 1.9: Typical MF transformer types. (a) Shell-type transformer with E-core. (b) Shell-type transformer with U-core (C-core). (c) Core-type transformer with U-core (C-core). (d) Planar transformer with E-core. (e) Coaxial transformer with E-core. (f) Coaxial transformer with R-core (toroidal core).

and the magnetizing inductance [19, 123–126]. The voltage transfer ratio is, obviously, the most critical parameter for a DC-DC converter. However, the leakage inductance is actively used by converter topologies (e.g., DAB and SRC) and the magnetizing inductance is often required for achieving soft-switching (ZVS or ZCS) [44, 78, 84, 86]. Therefore, all the magnetic parameters of a MF transformer must be carefully controlled.

- ▶ *Core losses* - The core material should be selected with respect to the selected operating frequency and the desired performance (efficiency and power density). For designs running with limited frequencies (up to 2 kHz), silicon-steel laminated cores with high saturation flux densities are typically used [17, 114]. For higher frequencies, tape-wound cores (amorphous or nanocrystalline) can be selected (up to 40 kHz) [17, 18, 114, 127]. For even higher frequencies, ferrite materials with reduced saturation flux densities are the only option [17, 18, 114]. The core losses (i.e. hysteresis and eddy current losses) are usually computed with semi-empirical methods (e.g., GSE, iGSE), which are calibrated with measurements (frequency, flux density, waveform shape, and temperature dependences) [17, 19, 24, 128].
- ▶ *Winding losses* - For designs running with limited frequencies (up to 2 kHz), solid-wires or Roebel bars are used [15, 18]. For higher frequencies, the skin and proximity effect losses are quickly increasing. Therefore, special geometries such as foil conductors or litz wires are selected in order to mitigate HF losses [16, 18, 129, 130]. Many analytical and numerical methods have been published for calculating the magnetic field in the windings and the associated losses of such HF conductors for arbitrary periodic waveforms [18, 19, 19, 129, 131–135].
- ▶ *Thermal management* - The thermal design of a MF transformer is critical, even for a highly efficient design. Due to the achieved high power density, the loss density is also increased [18]. Moreover, the temperature distribution inside a MF transformer has a direct impact on the losses [19, 91, 136]. The heat transfer inside a MF transformer can be achieved with thermal conduction, air ducts, heat-pipes, water-pipes, or oil [25, 61, 63, 64, 137]. The heat extraction to the ambient air is realized with natural convection, forced convection, heat sinks, or heat exchangers (water or oil) [17, 17, 115]. Many analytical and numerical methods have been published for calculating the temperature distribution of a MF transformer [17, 91, 114, 115, 138, 139].

- ▶ *Insulation design* - Electrical insulation is required inside the windings, between the windings, and between the windings and the core [15, 17]. The insulation is typically realized with dry-type materials and/or oil [15, 61, 63, 140–142]. For a MV/MF transformer, the volume occupied by the insulation can be significant, and, therefore, reduces the achieved power density [137, 143]. Moreover, the thermal resistance of the insulation is also limiting the thermal performance [25, 137, 139, 142]. The fact that the insulation is subject to MV/MF PWM voltages is also increasing the risk of thermal breakdowns and partial discharge induced breakdowns [144–150]. Finally, the capacitive reactive power oscillating in the insulation and the associated dielectric losses can be significant for MV/MF transformers [151–154].

- ▶ *Parasitics* - The parasitic capacitances (and inductances) of a MF transformer lead to resonances, and, potentially, to oscillations [155–158]. Such oscillations can disturb the modulation scheme of the converter, create additional losses, overvoltages, and EMI issues [156, 159–161]. The CM capacitance of the transformer creates, at HF, a short-circuit through the galvanic isolation, which can also be problematic [79, 80, 143]. Moreover, the electric and magnetic fields, originating from a MF transformer, can also cause disturbances in the control and measurement circuits located nearby [143, 158, 162].

- ▶ *Optimization process* - The aforementioned aspects and corresponding models can be combined in order to obtain an optimization procedure for MF transformers [19, 22, 114, 115]. Different criteria can be considered, such as efficiency, power density, manufacturability, and cost, resulting in a multi-objective optimization problem [91, 163]. Different methods have been proposed (e.g., brute-force, gradient optimization, and genetic algorithm) for solving such problems, where the results are often presented with Pareto fronts [91, 114, 115, 138, 164–166]. It should be noted that the optimization of the MF transformer cannot be decoupled from the optimization of the complete DC-DC converter. This is mainly due to the switching frequency, which is a shared parameter between the MF transformer and the converter bridges. Therefore, a sub-optimal MF transformer can lead to an optimal DC-DC converter [18, 91, 163].

1.7 Aims and Contributions

As outlined above, the design of MF transformers is a complex process involving many different fields of physics and engineering. This thesis focuses on MV/MF transformers and, more specifically, on the possibilities and challenges linked to the new MV SiC MOSFETs [108–110]. The goal of this thesis is to provide the tools for designing highly efficient MV/MF transformers and to demonstrate the feasibility of a 99.0 % efficient MV isolated DC-DC converter featuring a power density above 2.5 kW/l.

1.7.1 Scientific Contributions

Despite the numerous publications in the area of MF transformer design, large discrepancies between the models and the measurements are still common, especially for highly efficient MF transformers (above 99.5 %) [25, 27, 167–169]. Moreover, the impact of the large MV/MF voltages on the electrical insulation, which has been identified as critical, is often neglected [147–149, 152, 156, 170, 171]. More specifically, the following points, which have been identified as critical and insufficiently studied, are treated in this thesis:

- ▶ *Optimization and scaling laws* - Explicit analytical equations for the design of optimal MF transformers have been successfully given in [16, 18, 23, 172]. Scaling laws (scaling of the figures of merit of transformers with respect to a reference design) have been proposed for different volumes, efficiencies, and frequencies in [18, 20, 24, 173]. The complexity of the mapping between the design space and the performance space has been observed in [91, 113, 172]. However, all three aspects (optimal design, scaling laws, and performance space mapping) have never been brought together in order to highlight the fundamental characteristics and limitations of MF transformers. Therefore, the design equations of MF transformers and the corresponding optima are reviewed. Scaling laws are found for different power ratings, power densities, efficiencies, and temperature rises. With these scaling laws, the performance limits of MF transformers can be extracted. Moreover, the mapping between the design space and the performance space of MF transformers is analyzed with analytical and numerical models. Finally, the limitations of the analytical optimizations are emphasized.
- ▶ *Equivalent circuit uncertainties* - As already mentioned, three degrees of freedom exist for a MF transformer equivalent circuit: the voltage transfer ratio, the leakage inductance, and the magnetizing in-

ductance [19, 123, 124]. All these three parameters should be carefully controlled for the operation of a MF transformer inside a DC-DC converter [44, 86, 174–176]. In the literature, many methods have been proposed for computing the equivalent circuit of MF transformers [16, 17, 19, 124, 130, 177–180]. However, only few comparisons between the methods can be found [131, 181], where the impact of tolerances and uncertainties is ignored. Therefore, different methods are compared with respect to modeling complexity, computational cost, and achieved accuracy. Moreover, a statistical analysis framework is presented to analyze the impact of the model uncertainties and parameter tolerances. This statistical analysis highlights the limits of detailed models based on numerical field simulations. The presented results are verified with measurements.

- ▶ *Losses of non-ideal litz wires* - Litz wire windings are the most common choice for MF transformers since they allow for low losses and great flexibility in the design [25, 64, 82, 114, 182]. Many computation methods have been proposed for extracting the losses in such windings [19, 133, 134, 183–185]. However, it is found that the measured losses are often larger than the values computed with the aforementioned methods [25, 27, 82, 186]. This is due to the numerous hypothesis required for the analytical methods (perfect packing, perfect twisting, negligible pitch length, and homogeneous external magnetic field), which are, in practice, not respected. Different 3D simulation methods, based on integral equations (e.g., PEEC), differential equations (e.g., FEM simulations) [183, 187, 188], or both [189] have been proposed for simulating litz wires with non-idealities. However, 3D methods are complex to implement and demand for a very high computational cost, which restricts such simulations to litz wires with a reduced number of strands [183, 188]. Therefore, a new numerical field simulation tool, based on a 2.5D PEEC model (mixed 2D and 3D modeling), is developed for simulating the impact of twisting imperfections and pitch length on the current sharing and the losses of litz wires. The critical impact of the twisting scheme is highlighted and experimentally demonstrated. Simple analytical approximations are also given for selecting high performance twisting schemes.
- ▶ *Electrical shielding with PWM voltages* - MV/MF transformers operated inside DC-DC converters are subject to large PWM voltages (CM and DM) with fast switching transitions, especially with the new MV SiC

MOSFETs [108, 111, 112, 156]. Additionally, DC CM voltages and/or LF AC CM voltages can also be applied to MV/MF transformers. This leads to challenging situations with respect to CM currents, parasitic resonances, insulation design, and EMI [25, 156, 158–160, 162, 171, 190]. For all these effects, it appears that the magnetic and electric fields are of key importance for MV/MF transformers [105, 191]. Therefore, the field patterns (inside the insulation, at the surface of the insulation, and in the surrounding air) of MV/MF transformers are analyzed with numerical field simulations. The impact of the electric and magnetic fields on the eddy current losses, insulation design, capacitively coupled voltages, and CM currents is discussed. A resistive shield, which drastically reduces the electric field without creating additional losses, is proposed and experimentally verified with a prototype.

- ▶ *Dielectric losses with PWM voltages* - The critical impact of PWM voltages on the insulation has already been identified, particularly for drive systems [146–149, 152, 170]. The examination of the dielectric losses is of particular interest since it allows for a quantification of the insulation stress with MF voltages [151, 192]. More specifically, the dielectric losses (or changes thereof), which are related to the lifetime and the reliability of insulation systems, can be used for insulation design or monitoring [144, 145, 147, 150, 192, 193]. Moreover, for MV converters operated with fast PWM voltages, the dielectric losses can represent a significant share of the losses and could lead to a thermal breakdown [151, 152]. This is particularly critical with the new MV SiC MOSFETs [108, 111, 112]. However, the exact impact of the harmonics contained in PWM voltages (compared to sinusoidal voltages) on the dielectric losses, has not yet been studied in detail. Therefore, a thorough analysis of the dielectric loss mechanisms occurring in polymeric insulation materials under PWM voltages is carried out. Scalable analytical expressions are proposed for the losses produced by PWM voltages, taking into account the frequency and temperature dependences of the material parameters. The validity of the proposed approach is confirmed with measurements conducted with material samples and with a complete MV/MF transformer. Finally, design guidelines are extracted for the selection of dry-type insulation materials for MV/MF applications.
- ▶ *ZVS modulation of SRC-DCXs* - High power DC-DC SRCs are usually operated at or below the resonance frequency in the half-cycle discontinuous current mode. The primary-side bridge is actively operated (50 %

duty cycle) and the secondary-side bridge operates as a passive rectifier bridge (diode rectifier or synchronous rectifier) [42, 86, 87]. This operating mode is usually called DCX and provides a load-independent voltage transfer ratio without requiring any closed-loop control [61, 82, 84, 89, 90]. However, it has been found that passive rectification is problematic for converter bridges with large semiconductor output capacitances (e.g., oscillations, current distortion, and load-dependent voltage transfer ratio). This is especially true for systems using MV SiC MOSFETs, which feature significant output capacitances [111, 112]. A phase shift modulation scheme (MCS-ZVS), which allows for an active sharing of the transformer magnetizing current between the bridges, is proposed and experimentally verified. The presented modulation scheme features robust open-loop operation, load-independent voltage transfer ratio, load-independent ZVS for both bridges, and quasi-sinusoidal currents.

1.7.2 DC-DC Demonstrator System

The targetted SST demonstrator system should highlight the potential of the new MV SiC MOSFETs and should show that the advantages of such semiconductors can be fully exploited by MV/MF transformers [108–110]. For the demonstrator, the power supply chain of datacenters is considered [194, 195]. Fig. 1.11(a) shows the classical power supply chain with a LF transformer and a LV AC distribution architecture. Fig. 1.11(b) depicts a state-of-the-art power supply chain with a LF transformer and a LV DC distribution architecture featuring reduced complexity and increased efficiency. In order to further reduce the number of stages of the supply chain, the LF transformer and the LV rectifier can be replaced by a SST, which is directly interfacing the MV AC grid to a LV DC bus, as shown in Fig. 1.11(c) [59, 196]. This enables the realization of a highly efficient and highly compact datacenter power supply chain [28, 59, 196–198]. In order to reduce the conduction losses in the power distribution cables (or reducing the copper cross-sections) and increase the redundancy, a MV AC distribution architecture with distributed SSTs is also envisioned, cf. Fig. 1.11(d) [28, 196]. This last architecture has been chosen for the SST demonstrator.

The SST should interface a MV AC grid (3.8 kV phase-to-neutral RMS voltage and 6.6 kV phase-to-phase RMS voltage) to a LV DC bus (400 V) [59, 194, 195]. In the chosen architecture (cf. Fig. 1.11(d)), each server rack is supplied from an individual single-phase SST featuring a rated power of 25 kW. For the complete datacenter, many single-phase SSTs would be connected in

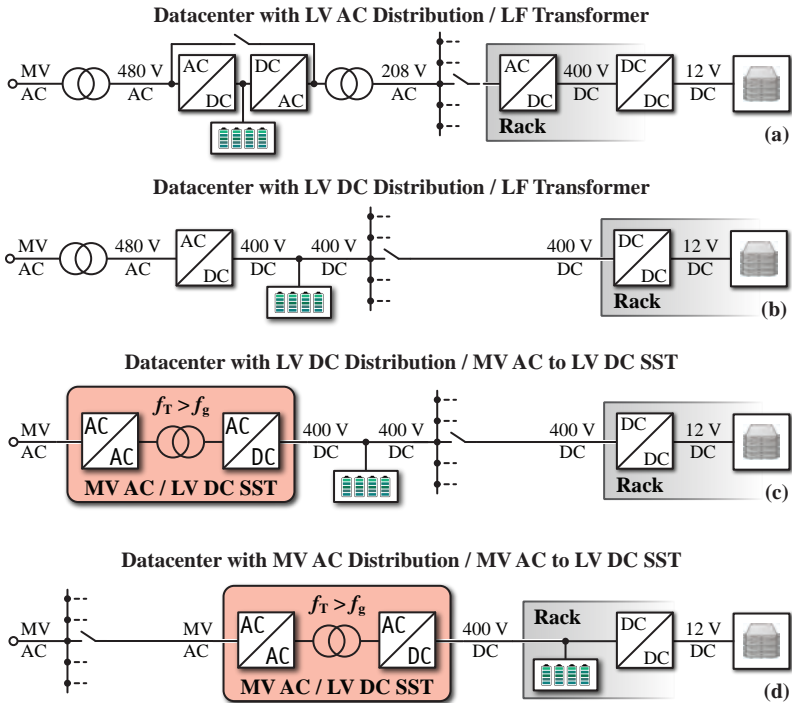


Fig. 1.10: (a) Traditional data power supply chain with LV AC distribution. (b) LF transformer based power supply chain with LV DC distribution. (c) SST based power supply chain with LV DC distribution. (d) SST based power supply of individual racks with MV AC distribution.

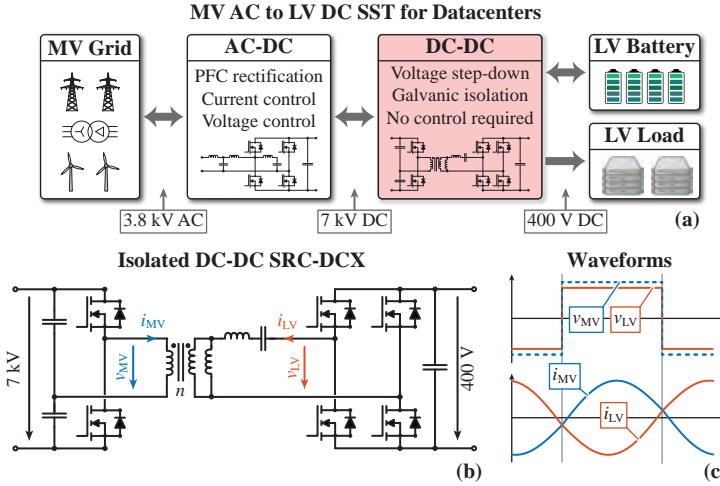


Fig. 1.11: (a) Considered SST consisting of an AC-DC converter and an isolated DC-DC converter. The DC-DC converter, which is considered in this thesis, is highlighted. The structure features a rated power of 25 kW. (b) DC-DC SRC operated at the resonance frequency, i.e. acting as bidirectional DCX. (c) Schematic view of the current and voltage waveforms.

order to ensure a symmetric loading of the MV AC three-phase grid. This power rating and single-phase distributed architecture has also been chosen for the industrial system presented in [196]. Additionally, the SST should provide galvanic isolation since it is not possible, for safety reasons, to connect the earth of the MV AC grid with the LV DC bus. The complete converter structure is bidirectional in order to allow for the batteries (uninterruptible power supply) to offer energy storage for the grid (smart-grid service) [54, 199].

The usage of 10 kV SiC MOSFETs allows for the realization of the aforementioned SST with a single-cell structure [108, 109]. Fig. 1.11(a) shows the selected SST structure, comprising an AC-DC converter and an isolated DC-DC converter which are connected via a common MV DC bus:

- *AC-DC converter* - The AC-DC converter interfaces a single-phase MV AC grid (3.8 kV, phase-to-neutral RMS voltage) to a MV DC bus (7 kV) [197]. Additionally, this converter controls the DC bus voltages and the power flow. The design and construction of the AC-DC converter is not part of this thesis and is described in [197, 200, 201].

- ▶ *DC-DC converter* - The DC-DC stage provides the voltage step-down between the MV DC bus (7 kV) and the LV DC bus (400 V), which is used to connect the loads (server) and the batteries (uninterruptible power supply) [196, 198]. Additionally, the galvanic isolation should be provided by this converter. However, voltage control and power flow control are not required since these functionalities are already provided by the AC-DC converter. The design and construction of the semiconductor bridges of the DC-DC converter are not part of this thesis and can be found in [111, 112, 198, 200, 201]. In this thesis, the design, construction, and measurements of the MV/MF transformer are considered. Moreover, the operation of the MV/MF transformer inside the SRC-DCX (modulation scheme) is examined.

The DC-DC converter should meet the following specifications: 99.0 % efficiency at rated power and a volume below 10 l (power density above 2.5 kW/l). For achieving this goal, the MF transformer should feature, at least, the following performance: 99.6 % efficiency at rated power and a power density above 5 kW/l. Such extreme efficiencies are required for SSTs in order to offer a competitive solution against a LF transformer coupled with a LV rectifier, given that modern dry-type LF transformers (without the LV rectifier) are typically achieving full-load efficiencies of [98.899.2] % [52, 53, 55].

Due to the aforementioned requirements, the DC-DC SRC topology, which is shown in Fig. 1.11(b), has been selected. Both converter bridges (LV side and MV side) are realized with SiC MOSFETs. Fig. 1.11(c) depicts the obtained current and voltage waveforms, which are similar to the classical half-cycle discontinuous conduction mode operation (cf. Fig. 1.7(a)), except that the discontinuous conduction interval is not present [82, 86, 88]. The converter is operated at the resonance frequency, which is set to 48 kHz. Due to the high switching frequency (for a MV converter), complete ZVS should be achieved for all semiconductors for all load conditions [111, 112, 202]. For achieving ZVS, the magnetizing inductance of the transformer is used. With this modulation, the DC-DC SRC acts as DCX, providing a constant voltage transfer ratio without requiring any closed-loop control [61, 82, 84, 86, 88–90]. The SRC-DCX topology also features other advantages compared to the DAB: sinusoidal currents, no requirement for a specific value of the leakage inductance, and load-independent ZVS with reduced switched currents (quasi-ZCS).

In order to reduce the number of switches and for reducing the voltage transfer ratio of the transformer, the combination of a half-bridge on the MV side and a full-bridge on the LV side is used. The chosen single-cell structure is extremely simple since it only consists of one MV/MF transformer, two MV

Tab. 1.1: Comparison of Single-Cell DC-DC SSTs

| System | ETHZ 25 kW | NCSU 20 kW | NCSU 10 kW |
|----------------------|---------------|-----------------------|--------------------|
| Date | 2018 | 2018 [99] | 2017 [83] |
| Circuit topology | SRC-DCX | CFSRC | SRC/DAB |
| Power rating | 25 kW | 20 kW ^a | 10 kW ^b |
| Bus voltages | 7 kV to 400 V | 10 kV to 340 V | 6 kV to 400 V |
| Switching frequency | 48 kHz | 37 kHz | 40 kHz |
| Semiconductors | SiC MOSFETs | SiC MOSFETs | SiC MOSFETs |
| Cooling | Air | Air | Air |
| Power density | 3.8 kW/l | 1.5 kW/l ^c | n/a ^d |
| Peak efficiency | 99.0 % | 98.0 % | 98.1 % |
| Full-load efficiency | 99.0 % | 97.3 % | 97.4 % |

^a Maximum achieved power is 17 kW (85 % load).

^b Maximum achieved power is 13 kW (130 % load).

^c Power density is estimated from the converter photography.

^d Power density is below 2.5 kW/l (upper bound derived from the given dimensions).

SiC MOSFETs, and four LV SiC MOSFETs. In comparison, the multi-cell SST presented in [196], which features the same power rating and the same target application, features five cells, ten MF transformers, and sixty LV MOSFETs.

1.7.3 Performance Benchmark

In the literature, it can be seen that most isolated high power DC-DC systems feature efficiencies ranging from 97.0 % to 98.5 % [64, 82, 83, 99, 196, 196, 203–205]. Different theoretical computations have demonstrated the feasibility of 99.0 % efficient systems [98, 206–209]. Several LV (below 1 kV) prototypes reach efficiencies ranging from 98.5 % to 98.8 % [163, 206, 209–212]. The highest measured efficiency is found for a high power (100 kW) and LV (850 V) converter based on SiC MOSFETs (99.2 %, measured without auxiliary and cooling losses, no indication of the power density) [213].

Nevertheless, the comparison of the realized prototype with the state-of-the-art is difficult since the published converters feature different power ratings, voltage ratings, semiconductor technologies, cooling methods, etc.

Tab. 1.2: Comparison of Single-Cell and Multi-Cell DC-DC SSTs

| System | ETHZ 25 kW | CPES 75 kW | Fuji 25 kW |
|----------------------|---------------|----------------------------|-----------------------------|
| Date | 2018 | 2018 [82] | 2017 [196] |
| Circuit topology | SRC-DCX | ISOP | ISOP |
| Power rating | 25 kW | 75 kW ^a | 25 kW ^b |
| Bus voltages | 7 kV to 400 V | 4 kV to 400 V ^a | 3.8 kV to 54 V ^b |
| Switching frequency | 48 kHz | 500 kHz | 70 kHz |
| Semiconductors | SiC MOSFETs | SiC/GaN FETs | Si MOSFETs |
| Cooling | Air | Air | Air |
| Power density | 3.8 kW/l | 2.9 kW/l | 3.5 kW/l ^c |
| Peak efficiency | 99.0 % | 98.0 % | 98.2 % |
| Full-load efficiency | 99.0 % | 97.9 % | 97.5 % |

^a ISOP / $5 \times 15 \text{ kW} = 75 \text{ kW} / 5 \times 800 \text{ V} = 4.0 \text{ kV}$ / only one cell was built.

^b ISOP / $5 \times 5 \text{ kW} = 25 \text{ kW} / 5 \times 760 \text{ V} = 3.8 \text{ kV}$ / all cells were built.

^c Power density is estimated from the converter photography.

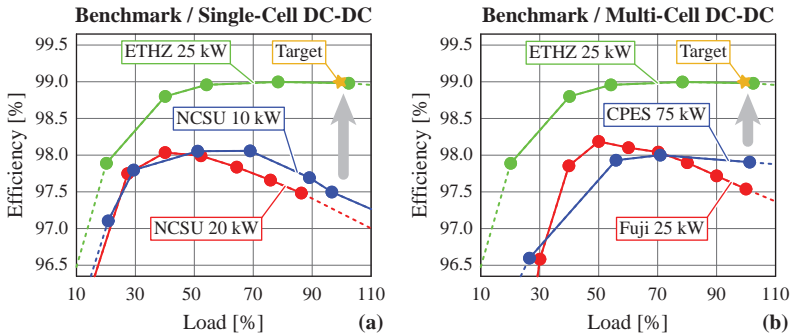


Fig. 1.12: (a) Measured efficiency curves for the realized prototype and two different single-cell converters taken from literature [83, 99]. (b) Measured efficiency curves for the realized prototype and two different multi-cell converters taken from literature [82, 196]. The realized prototype is labeled as (“ETHZ 25 kW”). The dashed lines represent extrapolated data.

For a better benchmark, only systems featuring similar ratings are compared. First, two single-cell DC-DC SSTs based on MV SiC MOSFETs are selected: a 20 kW system from the North Carolina State University (“NCSU 20 kW”) published in [99] and a 10 kW system from the North Carolina State University (“NCSU 10 kW”) published in [83]. In a second step, it is also interesting to compare the realized prototype with multi-cell systems, using LV switches (cf. Fig. 1.8(b)). The following multi-cell converters are considered: a 75 kW system from the Center for Power Electronics Systems at Virginia Tech (“CPES 75 kW”) published in [82] and a 25 kW datacenter power supply from Fuji Electric (“Fuji 25 kW”) published in [196]. The system designed in this thesis is labeled as (“ETHZ 25 kW”).

The key parameters of the different systems are summarized in Tab. 1.1 and Tab. 1.2. The measured efficiency curves are shown in Fig. 1.12. It can be seen that the achieved efficiency with the system of this thesis (99.0 % at full-load) is significantly beyond the state-of-the-art. Moreover, the designed system features an extremely flat efficiency curve between 50 % and 100 % load. The reduced losses of the converter translate into a small cooling system, which implies that the realized system is more compact (3.8 kW/l, 62 W/in³, 2.9 kW/kg, and 1.3 kW/lb) than the benchmarked systems, despite the higher achieved efficiency. Furthermore, in terms of power density, the realized prototype is only marginally bulkier than water-cooled systems, which typically feature power densities of [4, 6] kW/l [25, 27, 205].

As expected, the modular structures feature higher switching frequencies due to the usage of LV semiconductors [103, 104]. Still, the realized single-cell prototype shows a slightly higher power density with twice lower losses. Nevertheless, the modular topologies could advantageously feature redundancy if the basic structure is accordingly extended (e.g., bypass switch, short-circuit breakers, and additional cells). For single-cell systems, such redundancy would require the parallel connection of individual SSTs. Finally, it should be noted that the system from Fuji Electric (“Fuji 25 kW”) achieves very good performance without using wide-bandgap semiconductors, which would not be possible with a single-cell structure.

1.8 List of Publications

Key insights presented in this thesis have already been published or will be published in international scientific journals, conference proceedings, or presented at workshops. The publications created as part of this thesis, or also in the scope of other related projects, are listed below.

1.8.1 Journal Papers

- ▶ T. Guillod and J. W. Kolar, “Medium-Frequency Transformer Scaling Laws: Derivation, Verification, and Critical Analysis,” *Springer Electrical Engineering*, 2019, under review. DOI: not available.
- ▶ T. Guillod, R. Färber, F. Krismer, C. M. Franck, and J. W. Kolar, “Dielectric Losses in Dry-Type Insulation of Medium-Voltage Power Electronic Converters,” *IEEE Journal of Emerging and Selected Topics in Power Electronics*, 2019, early access. DOI: [10.1109/JESTPE.2019.2914997](https://doi.org/10.1109/JESTPE.2019.2914997).
- ▶ T. Guillod, D. Rothmund, and J. W. Kolar, “Active Magnetizing Current Splitting ZVS Modulation of a 7kV/400 V DC Transformer,” *IEEE Transactions on Power Electronics*, 2019, early access. DOI: [10.1109/TPEL.2019.2918622](https://doi.org/10.1109/TPEL.2019.2918622).
- ▶ T. Guillod, F. Krismer, and J. W. Kolar, “Magnetic Equivalent Circuit of MF Transformers: Modeling and Parameter Uncertainties,” *Springer Electrical Engineering*, vol. 100, no. 4, pp. 2261-2275, December 2018. DOI: [10.1007/s00202-018-0701-0](https://doi.org/10.1007/s00202-018-0701-0).
- ▶ T. Guillod, F. Krismer, and J. W. Kolar, “Protection of MV Converters in the Grid: The Case of MV/LV Solid-State Transformers,” *IEEE Journal of Emerging and Selected Topics in Power Electronics*, vol. 5, no. 1, pp. 393-408, March 2017. DOI: [10.1109/JESTPE.2016.2617620](https://doi.org/10.1109/JESTPE.2016.2617620).

1.8.2 Conference Papers

- ▶ T. Guillod, J. Huber, F. Krismer, and J. W. Kolar, “Litz Wire Losses: Effects of Twisting Imperfections,” in *Proc. of the IEEE Workshop on Control and Modeling for Power Electronics (COMPEL)*, Stanford, USA, July 2017. DOI: [10.1109/COMPEL.2017.8013327](https://doi.org/10.1109/COMPEL.2017.8013327).
- ▶ T. Guillod, F. Krismer, and J. W. Kolar, “Electrical Shielding of MV/MF Transformers Subjected to High dv/dt PWM Voltages,” in *Proc. of the IEEE Applied Power Electronics Conference and Exposition (APEC)*, Tampa, USA, March 2017. DOI: [10.1109/APEC.2017.7931050](https://doi.org/10.1109/APEC.2017.7931050).
- ▶ T. Guillod, R. Färber, F. Krismer, C. M. Franck, and J. W. Kolar, “Computation and Analysis of Dielectric Losses in MV Power Electronic Converter Insulation,” in *Proc. of the Energy Conversion Congress and Exposition (ECCE USA)*, Milwaukee, USA, September 2016. DOI: [10.1109/ECCE.2016.7854952](https://doi.org/10.1109/ECCE.2016.7854952).

- ▶ T. Guillod, F. Krismer, R. Färber, C. M. Franck, and J. W. Kolar, “Protection of MV/LV Solid-State Transformers in the Distribution Grid,” in *Proc. of the Annual Conference of the IEEE Industrial Electronics Society (IECON)*, Yokohama, Japan, November 2015, *Best Presentation Recognition*. DOI: [10.1109/IECON.2015.7392648](https://doi.org/10.1109/IECON.2015.7392648).
- ▶ T. Guillod, J. Huber, G. Ortiz, A. De, C. M. Franck, and J. W. Kolar, “Characterization of the Voltage and Electric Field Stresses in Multi-Cell Solid-State Transformers,” in *Proc. of the Energy Conversion Congress and Exposition (ECCE USA)*, Pittsburgh, USA, September 2014, *Best Overall Oral Presentation, Best Overall Student Paper*. DOI: [10.1109/ECCE.2014.6954048](https://doi.org/10.1109/ECCE.2014.6954048).

1.8.3 Workshops and Seminars

- ▶ T. Guillod, D. Rothmund, and J. W. Kolar, “10 kV SiC MOSFETs for Solid-State Transformers: Opportunities and Challenges,” presented at the *X-Power Electronics Conference*, Songshan Lake, China, May 2019. DOI: not available.
- ▶ T. Guillod and J. W. Kolar, “Dielectric Losses in the Insulation of Dry-Type Medium-Frequency Transformers,” presented at the *ECPE Solid-State Transformer Workshop*, Lausanne, Switzerland, February 2019. DOI: not available.
- ▶ T. Guillod, F. Krismer, and J. W. Kolar, “Dielectric Losses: MV/MF Converter Insulation,” presented at the *SCCER FURIES Technical Workshop*, Fribourg, Switzerland, September 2017. DOI: not available.
- ▶ T. Guillod and J. W. Kolar, “Medium-Frequency Transformers for Smart Grid Applications: Challenges and Opportunities,” presented at the *SCCER-FURIES Annual Conference*, Lausanne, Switzerland, December 2016. DOI: not available.
- ▶ T. Guillod, R. Färber, C. M. Franck, and J. W. Kolar, “Effects of Mixed-Frequency Voltage Stress on Dry-Type Insulation Systems,” presented at the *SCCER-FURIES Annual Conference*, Lausanne, Switzerland, November 2015. DOI: not available.

1.8.4 Further Scientific Contributions

- ▶ R. Färber, T. Guillod, F. Krismer, J. W. Kolar, and C. M. Franck, “Endurance of Polymeric Insulation under Mixed-Frequency Medium-Voltage Stress,” *IEEE Transactions on Dielectrics and Electrical Insulation*, 2019, under review. DOI: not available.
- ▶ P. Czyz, P. Papamanolis, F. Krismer, T. Guillod, and J. W. Kolar, “New 40 kV/300 kVA Quasi-2-Level Operated 5-Level Flying Capacitor SiC “Super-Switch” IPM,” in *Proc. of the Energy Conversion Congress and Exposition (ECCE Asia)*, Busan, Korea, May 2019. DOI: not available.
- ▶ D. Rothmund, T. Guillod, D. Bortis, and J. W. Kolar, “Design and Experimental Analysis of a 10 kV SiC MOSFET Based 50 kHz Soft-Switching Single-Phase 3.8 kV AC/400 V DC Solid-State Transformer,” presented at the *IEEE Energy Conversion Congress and Exposition (ECCE USA), Special Session*, Portland, USA, September 2018. DOI: not available.
- ▶ D. Rothmund, T. Guillod, D. Bortis, and J. W. Kolar, “99% Efficient 10 kV SiC-Based 7 kV/400 V DC-Transformer for Future Data Centers,” *IEEE Journal of Emerging and Selected Topics in Power Electronics*, vol. 7, no. 2, pp. 753-767, June 2019. DOI: [10.1109/JESTPE.2018.2886139](https://doi.org/10.1109/JESTPE.2018.2886139).
- ▶ D. Rothmund, T. Guillod, D. Bortis, and J. W. Kolar, “99.1% Efficient 10 kV SiC-Based Medium Voltage ZVS Bidirectional Single-Phase PFC AC/DC Stage,” *IEEE Journal of Emerging and Selected Topics in Power Electronics*, vol. 7, no. 2, pp. 779-797, June 2019. DOI: [10.1109/JESTPE.2018.2886140](https://doi.org/10.1109/JESTPE.2018.2886140).
- ▶ P. Czyz, T. Guillod, F. Krismer, and J. W. Kolar, “Exploration of the Design and Performance Space of a High Frequency 166 kW/10 kV SiC Solid-State Air-Core Transformer,” in *Proc. of the Energy Conversion Congress and Exposition (ECCE Asia)*, Niigata, Japan, May 2018, *Best Paper Award*. DOI: [10.23919/IPEC.2018.8507746](https://doi.org/10.23919/IPEC.2018.8507746).
- ▶ R. Bosshard, T. Guillod, and J. W. Kolar, “Electromagnetic Field Patterns and Energy Flux of Efficiency Optimal Inductive Power Transfer Systems,” *Springer Electrical Engineering*, vol. 99, no. 3, pp. 969-977, September 2017. DOI: [10.1007/s00202-016-0461-7](https://doi.org/10.1007/s00202-016-0461-7).
- ▶ D. Rothmund, G. Ortiz, T. Guillod, and J. W. Kolar, “10 kV SiC-Based Isolated DC-DC Converter for Medium-Voltage-Connected SSTs,” in

Proc. of the IEEE Applied Power Electronics Conference and Exposition (APEC), Charlotte, USA, March 2015. DOI: [10.1109/APEC.2015.7104485](https://doi.org/10.1109/APEC.2015.7104485).

1.9 Thesis Outline

According to the goals and contributions mentioned above, the content of the thesis is divided into seven main chapters and conclusions. All the chapters can be read independently since the interdependencies have been reduced to the strict minimum.

- ▶ **Chapter 2** first defines the fundamental design equations of MF transformers. With this model, analytical expressions are derived for optimal MF transformers. Scaling laws are proposed for optimal transformers and the mapping between the design and performance space is analyzed. A 20 kW MF transformer operated with 600 V sinusoidal voltages is considered. This chapter is based on [22].
- ▶ **Chapter 3** presents and compares different models for computing the equivalent circuit of MF transformers. A statistical analysis is performed for assessing the impact of the model uncertainties and parameter tolerances. The presented methods are experimentally verified on a 20 kW MF transformer operated at 100 kHz inside a 400 V to 400 V SRC-DCX. This chapter is adapted from [125].
- ▶ **Chapter 4** proposes a numerical field simulation method for computing the current sharing and the losses of litz wires with imperfect twisting patterns. A simple analytical model of litz wire with imperfect twisting is also proposed. A 65 kW MF transformer operated at 7.5 kHz inside a SST is considered for the experimental verification. The chapter is based on [135].
- ▶ **Chapter 5** presents the optimization, design, construction, and measurement of the MV/MF transformer used inside the aforementioned 25 kW DC-DC converter demonstrator (cf. Fig. 1.11).
- ▶ **Chapter 6** analyzes the electric field patterns of MV/MF transformers subject to PWM voltages with fast switching transitions. The electrical insulation challenges and parasitic disturbances associated with the electric field are analyzed and shielding methods are compared. The 25 kW MF transformer utilized in the aforementioned DC-DC converter demonstrator (cf. Fig. 1.11) is considered. This chapter is based on [143].

- ▶ **Chapter 7** investigates the dielectric losses of dry-type insulation material subject to PWM voltages with fast switching transitions. The modeling of dielectric losses in time and frequency domain is analyzed and analytical approximations are proposed for the dielectric losses under PWM voltages. The 25 kW MF transformer utilized in the aforementioned DC-DC converter demonstrator (cf. Fig. 1.11) is considered for the experimental verification. This chapter is adapted from [153,154].
- ▶ **Chapter 8** presents the modulation scheme of the aforementioned 25 kW SRC-DCX demonstrator (cf. Fig. 1.11). The advantages of the proposed ZVS phase shift modulation scheme (MCS-ZVS), compared to a classical modulation scheme using a passive rectifier, are highlighted. Finally, measurements on the realized DC-DC converter are shown. This chapter is based on [88,198].
- ▶ **Chapter 9** concludes the thesis and briefly summarizes the main contributions and key findings. In addition, an outlook on possible future research is provided.

2

MF Transformer Scaling Laws

Chapter Abstract

MF transformers are one of the fundamental building blocks of modern power electronic converters. The usage of increased frequencies leads to improved figures of merit (efficiency, volume, and mass) but also to design challenges and constraints. This chapter reviews the analytical modeling of MF transformers. More particularly, the mapping between the design space and the performance space is analyzed. It is found that wide regions of the design space are mapped to a narrow region in the performance space (flat optimum, design space diversity). Scaling laws are derived for optimal MF transformers operated at different power ratings and power densities, which provide a comprehensive and general insight on the achievable performances. In a next step, the results obtained with the analytical model are compared to numerical simulations. It is concluded that the derived scaling laws capture qualitatively and quantitatively the behavior of MF transformers, but should be used with caution for accurate design processes.

2.1 Introduction

LF power transformers are widely used for voltage transformation and galvanic isolation in electrical systems [15, 52, 55]. The performance of such LF transformers (efficiency, volume, and mass) is subject to fundamental physical limitations due to the saturation flux density of the core material, the (thermally) limited current density in the windings, and the cooling capabilities [15, 214].

MF transformers, where the operating frequency is used as an additional degree of freedom, can mitigate (with a reduced volt-second product applied

to the magnetic core) the impact of the aforementioned limitations [16, 17, 25, 64, 82, 143]. Fig. 2.1 illustrates the Pareto fronts of 50 Hz LF transformers and MF transformers for a 20 kW system. It can be seen that increasing the operating frequency allows for significant improvements in terms of power density and efficiency.

However, the usage of MF introduces new challenges: additional core losses (e.g., eddy currents in the core and magnetic relaxation), HF losses in the windings (e.g., skin and proximity effects), and parasitic resonances [16, 17]. Moreover, MF transformers require power electronic converters, which are inverting and rectifying the voltages and currents at the desired operating frequency [25, 42, 64, 82, 163]. With Si IGBTs (or Si MOSFETs), the operating frequency of MF transformers is mainly limited by the switching losses of the inverter and rectifier stages. However, with newly available fast-switching SiC MOSFETs (or GaN HEMTs) power transistors, the complete design space of MF transformers can be used [82, 113, 143]. This implies that a detailed knowledge of the design procedure of MF transformers is required for realizing efficient, compact, and inexpensive MF transformers utilizing the full potential of modern semiconductors.

Multiple degrees of freedom are available for the design of MF transformers: frequency, winding type, winding geometry, core shape, core material, and cooling concept (cf. Section 1.6) [16, 17, 114]. These aspects are typically combined in order to obtain a full model, which allows for the optimization of MF transformers. Such models can be classified into three categories:

- ▶ *Full-analytical models* - The model is based on analytical equations and features a closed-form analytical solution [16–18, 20, 23, 25]. The approach is simple and features a clear physical interpretation. Nevertheless, the accuracy of full-analytical models is limited.
- ▶ *Semi-numerical models* - The model is based on analytical equations, but does not feature an explicit solution. The optimal design is obtained with numerical optimization (e.g., brute-force, gradient optimization, and genetic algorithm) [115, 138, 163–166]. Such numerical optimizations are accurate and reasonably fast. However, it is difficult to identify the mechanisms leading to the optimal design. Furthermore, the obtained results are specific to the given specifications and cannot be easily generalized.
- ▶ *Numerical models* - The MF transformer parameters are extracted from numerical field simulations (e.g., FEM simulations) [82, 153, 154]. However, such models are time-consuming (modeling complexity and com-

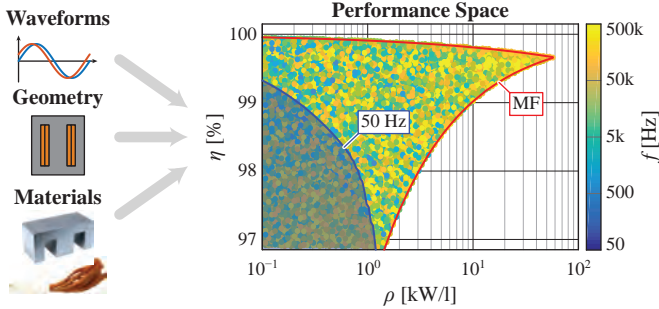


Fig. 2.1: Comparison between the Pareto fronts of 50 Hz LF transformers and MF transformers for a 20 kW and 600 V (RMS) system. The LF transformers are constructed with solid copper wires and with grain oriented electrical steel cores (“ThyssenKrupp Powercore H 100-27”, 2.0 T saturation flux) [215]. The considered designs are constructed with litz wires (100 μ m stranding) and ferrite cores (“TDK N97”, 300 mT saturation flux) [216].

putational cost) and only provide limited advantages compared to the semi-numerical approach [125]. Therefore, such models are usually not used for optimization processes.

Explicit analytical equations for the design of optimal MF transformers have been successfully given in [16, 18, 23, 172]. Analytical scaling laws (scaling of the figures of merit of transformers with respect to a reference design) have been proposed for different power densities, efficiencies, and frequencies in [18, 20, 24, 173]. The complexity of the mapping between the design space and the performance space can be seen in Fig. 2.1 (mapping of the operating frequency to the performance space) and has also been observed in [91, 113, 172]. However, to the knowledge of the author, all three aspects (optimal design, scaling laws, and performance space mapping) have not been brought together up to now, but would highlight the fundamental characteristics and limitations of MF transformers.

Therefore, this chapter examines the optimization and the scaling of MF transformers in detail and is organized as follows. Section 2.2 presents the chosen full-analytical MF transformer model. Section 2.3 shows which point in the design space is mapped to the optimal design and which regions are mapped to quasi-optimal designs (design space diversity). Moreover, scaling laws are derived for the optimal designs for different power densities, power ratings, temperature rises, and efficiencies. Section 2.4 applies the presented

methods to a 20 kW and 20 kW/1 MF transformer. Section 2.5 successfully compares the results obtained with the full-analytical model with a more elaborate semi-numerical model. Finally, Section 2.6 highlights the limits of the full-analytical models and the corresponding scaling laws.

2.2 Full-Analytical Modeling

In this section, a full-analytical model of MF transformers is presented. The core losses, the winding losses, and the thermal limit are considered with simplified analytical models. Tab. 2.1 summarizes the variables used for describing the geometry and the operating conditions of the MF transformer. Tab. 2.2 describes the variables used for computing the losses and the temperature of the MF transformer.

2.2.1 Geometry and Operating Conditions

The MF transformer depicted in Fig. 2.2 is considered and features the most common design choices: E-core (without air gap) with a shell-type arrangement and litz wire windings (without interleaving). The boxed volume (V_{box}) together with the geometrical aspect ratios (x_{cw} , x_{c} , and x_{w}) defines uniquely the geometry of the MF transformer (cf. Fig. 2.2). For simplifying the design equations, a turns ratio of 1 : 1 is first selected. The volumetric (ρ) and gravimetric (γ) power densities are used as figures of merit for the geometry of the MF transformer:

$$\rho = P/V_{\text{box}}, \quad (2.1)$$

$$\gamma = P/m_{\text{tot}}. \quad (2.2)$$

The MF transformer is assumed to operate with sinusoidal currents and voltages. The apparent power of the transformer (S) can then be expressed with the help of the power factor and the active rated power:

$$S = P/\cos(\phi) = I_{\text{RMS}}V_{\text{RMS}}. \quad (2.3)$$

The aforementioned design choices have been selected since they represent the most typical operation condition of MF transformers [25,64,82,115,164]. Nevertheless, the presented method can be adapted to other MF transformer designs and operating conditions, without fundamentally changing the obtained results:

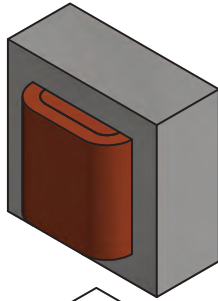
Tab. 2.1: Variable List: Geometry / Operation

| Name | Description |
|--------------|------------------------------------|
| A_c | Core cross section |
| t_c | Core limb width |
| z_c | Core depth |
| V_c | Core volume |
| A_w | Winding window cross section |
| d_w | Winding window width |
| h_w | Winding window height |
| V_w | Winding volume |
| x_{cw} | Ratio between A_c and A_w |
| x_c | Ratio between z_c and $2t_c$ |
| x_w | Ratio between h_w and d_w |
| A_t | Exposed area for cooling |
| V_{tot} | MF transformer boxed volume |
| m_{tot} | MF transformer mass |
| n | Number of turns (both windings) |
| ρ | Volumetric power density |
| γ | Gravimetric power density |
| P | MF transformer active rated power |
| S | MF transformer apparent power |
| $\cos(\phi)$ | MF transformer power factor |
| f | MF transformer operating frequency |
| I_{RMS} | MF transformer RMS current |
| V_{RMS} | MF transformer RMS voltage |

Tab. 2.2: Variable List: Losses / Thermal

| Name | Description |
|----------------------------|--|
| B_{pk} | Core peak flux density |
| $k_c / \alpha_c / \beta_c$ | Core Steinmetz parameters (empirical) |
| $f_{c,max}$ | Max. frequency for the core |
| B_{sat} | Core saturation flux density |
| p_c | Core loss density |
| P_c | Core losses |
| μ_0 | Vacuum permeability |
| k_w | Winding filling factor |
| J_{RMS} | Winding RMS current density |
| d_s | Winding strand diameter |
| σ | Winding copper conductivity |
| a_w | Proximity effect factor |
| δ | Skin depth |
| p_w | Winding loss density |
| P_w | Winding losses |
| $J_{RMS,max}$ | Max. winding RMS current density |
| h_t | Surface convection coefficient |
| $k_t / v_t / \kappa_t$ | Convection parameters (empirical) |
| ΔT | Temperature rise (with respect to ambient) |
| ΔT_{max} | Max temperature rise |
| r_{cw} | Ratio between P_c and P_w |
| r_w | AC/DC winding resistance ratio |
| P_l | Total losses (core and windings) |
| η | MF transformer efficiency |

MF Transformer Geometry



$$A_c = 2 t_c z_c = \text{Core cross section}$$

$$A_w = d_w h_w = \text{Winding cross section}$$

$$A_t = \text{Exposed area for cooling}$$

$$V_c = \text{Core volume}$$

$$V_w = \text{Winding volume}$$

$$V_{\text{tot}} = \text{MF transformer boxed volume}$$

$$m_{\text{tot}} = \text{MF transformer mass}$$

$$x_{cw} = A_c / A_w, \quad x_c = z_c / 2 t_c, \quad x_w = h_w / d_w$$

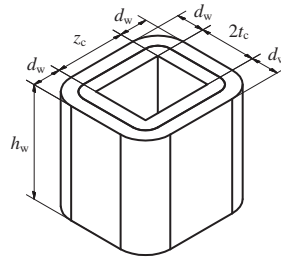
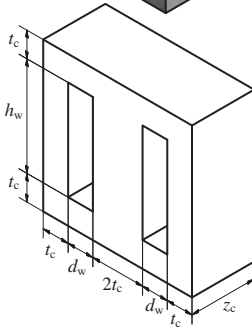


Fig. 2.2: Considered MF transformer geometry with E-core, shell-type arrangement, and without winding interleaving. The ratios x_{cw} , x_c , and x_w define the geometrical aspect ratios of the MF transformer.

- ▶ *Transformer type* - Transformers with multiple windings (e.g., three-phase transformers) can be considered with small adaptations of the design equations [15, 18].
- ▶ *Core shape* - Other core shapes (e.g., ETD, RM, and U) can be used without any problem by adapting the relations shown in Fig. 2.2.
- ▶ *Winding type* - Windings composed of solid wires or foils can also be used with minor adaptations of the formulas used for the computations of the losses [17, 25]. Interleaving of the winding can also be considered [16, 17].
- ▶ *Turns ratio* - The turns ratio of the MF transformer can be adapted to change the voltage transformation ratio with a small impact on the design variables [18, 25].
- ▶ *Excitation* - Arbitrary (instead of sinusoidal) current and voltage waveforms can be considered with the models presented in [19, 128, 129].

2.2.2 Core and Winding Losses

The core losses of the MF transformer are computed with the GSE, where the lamination factor (if applicable) is included in the Steinmetz parameters [17, 128]. Then, the flux density (B_{pk}), the loss density (p_c), and the core losses (P_c) can be expressed:

$$B_{pk} = \frac{\sqrt{2}V_{RMS}}{2\pi n f A_c}, \quad (2.4)$$

$$p_c = k_c f^{\alpha_c} B_{pk}^{\beta_c}, \quad (2.5)$$

$$P_c = V_c p_c, \quad (2.6)$$

This model neglects the frequency and temperature dependences of the Steinmetz parameters [19, 136]. In addition, the following limitations (saturation flux and maximal operating frequency of the core material) apply to the aforementioned model:

$$n > \frac{\sqrt{2}V_{RMS}}{2\pi f B_{sat} A_c} \Leftrightarrow B_{pk} < B_{sat}, \quad (2.7)$$

$$f < f_{c,max}. \quad (2.8)$$

The winding losses of litz wire windings (shell-type arrangement) are computed with the asymptotic approximation of the proximity effect losses (without interleaving) [18, 23, 25, 129]. Then, the current density (J_{RMS}), the proximity effect factor (a_{w}), the skin depth (δ), the loss density (p_{w}), and the winding losses (P_{w}) can be expressed as

$$J_{\text{RMS}} = \frac{2nI_{\text{RMS}}}{k_{\text{w}}A_{\text{w}}}, \quad (2.9)$$

$$a_{\text{w}} = \frac{1}{24} (\pi\mu_0\sigma k_{\text{w}}d_{\text{w}}d_{\text{s}})^2, \quad (2.10)$$

$$\delta = \frac{1}{\sqrt{\pi\sigma\mu_0 f}}, \quad (2.11)$$

$$p_{\text{w}} = (1 + a_{\text{w}}f^2) \frac{J_{\text{RMS}}^2}{\sigma}, \quad (2.12)$$

$$P_{\text{w}} = (V_{\text{w}}k_{\text{w}})p_{\text{w}}. \quad (2.13)$$

This model neglects the temperature dependence of the winding losses, the exact placement of the wires, and the additional losses occurring when the skin depth reaches the strand diameter [125, 135]. The filling factor considers the packing of the strands (litz wire), the packing of the turns, and the insulation distances. The following limitations (maximal current density and skin depth) apply to the aforementioned model:

$$n < \frac{k_{\text{w}}A_{\text{w}}J_{\text{RMS,max}}}{I_{\text{RMS}}} \Leftrightarrow J_{\text{RMS}} < J_{\text{RMS,max}}, \quad (2.14)$$

$$f < \frac{1}{\pi\sigma\mu_0 d_{\text{s}}^2} \Leftrightarrow d_{\text{s}} < \delta. \quad (2.15)$$

From the core and winding losses, different figures of merit can be extracted. The ratio between the core and winding losses (r_{cw}), the ratio between the AC and DC winding resistances (r_{w}), the total MF transformer losses (P_1), and the efficiency (η) can be expressed as

$$r_{\text{cw}} = P_{\text{c}}/P_{\text{w}}, \quad (2.16)$$

$$r_{\text{w}} = 1 + a_{\text{w}}f^2, \quad (2.17)$$

$$P_1 = P_{\text{w}} + P_{\text{c}}, \quad (2.18)$$

$$\eta = 1 - P_1/P. \quad (2.19)$$

2.2.3 Thermal Modeling

A thermal model is required for ensuring that the MF transformer is not operated beyond the thermal limit. However, complex thermal models [19, 25, 115, 138, 139] are not adapted for deriving scaling laws. A model based on the convection coefficient and the exposed area of the MF transformer [20, 23] has been selected. The convection coefficient (h_t) is obtained with a fit (temperature and exposed area dependences) of the empirical formulas provided in [17]:

$$h_t = k_t \Delta T^{\nu_t} A_t^{\kappa_t}. \quad (2.20)$$

This model can be used to describe natural and/or forced convection processes. Heat conduction and radiation processes are neglected. Then, the temperature rise (ΔT) and the corresponding thermal limit can be expressed as

$$\Delta T = \frac{P_1}{h_t A_t} = \left(\frac{P_1}{k_t A_t^{1+\kappa_t}} \right)^{\frac{1}{1+\nu_t}}, \quad (2.21)$$

$$\Delta T < \Delta T_{\max}. \quad (2.22)$$

2.3 Optimization and Scaling Laws

In this section, the presented full-analytical model (cf. Section 2.2) is used to derive conditions for optimal designs. Furthermore, the properties of the optimal designs are analyzed for different frequencies, power densities, and power ratings.

2.3.1 Area Product

The area product (product of the core and winding window cross sections) is a common method for designing LF transformers [17, 20]. The area product and the corresponding impact on the transformer power rating can be expressed as

$$A_c A_w = \frac{\sqrt{2} V_{\text{RMS}}}{2\pi f n B_{\text{pk}}} \frac{2n I_{\text{RMS}}}{k_w J_{\text{RMS}}} = \frac{\sqrt{2}}{\pi k_w B_{\text{pk}} J_{\text{RMS}}} \frac{S}{f}. \quad (2.23)$$

For LF transformers, the core losses are low and the peak flux density (B_{pk}) can be set to the saturation flux density level (B_{sat}) and the current density (J_{RMS}) to the maximum value ($J_{\text{RMS,max}}$). Then, the area product represents a valuable

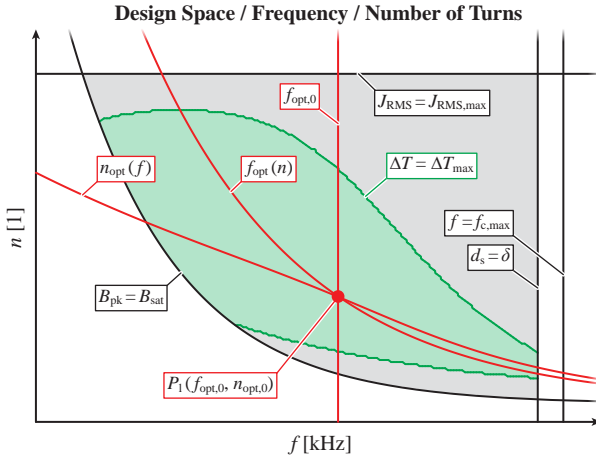


Fig. 2.3: Transformer design space for different frequencies and numbers of turns, assuming a constant area product and/or core size. The design space limits (black and gray), the thermal limit (green), and the optimal designs (red) are shown.

design equation for obtaining a first approximation of a LF transformer size and performance. The area product also indicates that the operation at an increased frequency will lead to more compact designs (cf. Section 1.2).

However, for MF transformers, the optimal flux and current densities can be significantly lower than the maximum values [23–25]. This is due to the increased core losses (parameter α_c) and the proximity effect losses in the windings (parameter a_w). This implies that the area product cannot be directly used for designing MF transformers. Nevertheless, the area product still represents an upper bound for MF transformers, which can be useful as a starting point during the design process.

2.3.2 Optimal MF Design

With the aforementioned models (cf. Section 2.2), it is possible to derive a closed-form solution for optimal MF transformers [18, 25]. However, several assumptions are required for obtaining a simple solution:

- The power rating, power factor, and voltage level (P , $\cos(\phi)$, and V_{RMS}) are fixed. Therefore, it is accepted that the reactive power is not strongly dependent on the leakage and magnetizing inductances of the different

designs. This is the case for MF transformers with high magnetic coupling factors.

- ▶ The geometry is fixed (V_{box} , x_{cw} , x_{c} , and x_{w}). This corresponds to a specific magnetic core size.
- ▶ The core material (B_{sat} , k_{c} , α_{c} , and β_{c}) and the winding stranding ($J_{\text{RMS,max}}$, k_{w} , σ , and d_{s}) are selected, i.e. not variable.
- ▶ The number of turns (n) is accepted to be a continuous (non-discrete) variable. The winding filling factor is independent of the number of turns and the exact packing pattern of the turns is not considered.

With these assumptions, the only remaining degrees of freedom are the operating frequency (f) and the number of turns (n). This design space is constrained by the saturation flux density (cf. (2.7)), the current density (cf. (2.14)), and the maximum frequency (cf. (2.8) and (2.15)). Fig. 2.3 shows the resulting design space. With the presented models, the MF transformer losses can be expressed as

$$P_{\text{c}}(f, n) = C_{\text{c}} f^{\alpha_{\text{c}} - \beta_{\text{c}}} n^{-\beta_{\text{c}}}, \quad (2.24)$$

$$P_{\text{w}}(f, n) = C_{\text{w}} (1 + a_{\text{w}} f^2) n^2, \quad (2.25)$$

$$P_1(f, n) = P_{\text{c}}(f, n) + P_{\text{w}}(f, n), \quad (2.26)$$

where the following constants are defined:

$$C_{\text{c}} = (k_{\text{c}} V_{\text{c}}) \left(\frac{\sqrt{2} V_{\text{RMS}}}{2\pi A_{\text{c}}} \right)^{\beta_{\text{c}}}, \quad (2.27)$$

$$C_{\text{w}} = \frac{V_{\text{w}} I_{\text{RMS}}^2}{\sigma k_{\text{w}} A_{\text{w}}^2}. \quad (2.28)$$

Now, the optimal number of turns for a given frequency (n_{opt}) and the optimal frequency (f_{opt}) for a given number of turns can be calculated (cf. Fig. 2.3). The following expressions can be derived with partial derivatives:

$$\frac{\partial P_1(f, n)}{\partial n} = 0 \Rightarrow n_{\text{opt}}(f) = \left(\frac{C_{\text{c}} \beta_{\text{c}} f^{\alpha_{\text{c}} - \beta_{\text{c}}}}{2C_{\text{w}} (1 + a_{\text{w}} f^2)} \right)^{\frac{1}{2 + \beta_{\text{c}}}}, \quad (2.29)$$

$$\frac{\partial P_1(f, n)}{\partial f} = 0 \Rightarrow f_{\text{opt}}(n) = \left(\frac{2C_{\text{w}} a_{\text{w}} n^{2 + \beta_{\text{c}}}}{C_{\text{c}} (\beta_{\text{c}} - \alpha_{\text{c}})} \right)^{\frac{1}{\alpha_{\text{c}} - \beta_{\text{c}} - 2}}. \quad (2.30)$$

It should be noted that the optimal frequency (f_{opt}) only exists if $\beta_c > \alpha_c$, which is almost always respected for core materials operated with typical frequencies. For $\beta_c = \alpha_c$, the optimal frequency would be zero, and all the designs would be operated at the saturation limit [24]. The optimal number of turns (n_{opt}) can be very low or very high, which can lead to practical problems for the construction of the windings. However, the number of turns can be adapted by changing the core geometrical aspect ratios, i.e. the ratio between the core (A_c) and winding (A_w) areas (cf. Fig. 2.2).

The intersection between n_{opt} and f_{opt} represents the global optimum (gradient of the loss function is zero) and can be expressed as (cf. Fig. 2.3)

$$f_{\text{opt},0} = \sqrt{\frac{\beta_c - \alpha_c}{\alpha_c a_w}}, \quad n_{\text{opt},0} = n_{\text{opt}}(f_{\text{opt},0}). \quad (2.31)$$

This implies that beyond $f_{\text{opt},0}$, the increase of the proximity effect losses in the windings exceeds the reduction of the core losses. The designs with the optimal number of turns feature the following property between the core and winding losses (at any frequency as long as the saturation flux, maximum current density, and maximum frequency are not reached) [18, 23, 25]:

$$n = n_{\text{opt}}(f) \Rightarrow r_{\text{cw}} = \frac{2}{\beta_c}. \quad (2.32)$$

The global optimum, additionally, features a specific ratio between the AC and DC winding resistances [18, 23, 25]:

$$(f = f_{\text{opt},0}) \wedge (n = n_{\text{opt},0}) \Rightarrow \left(r_w = \frac{\beta_c}{\alpha_c} \right) \wedge \left(r_{\text{cw}} = \frac{2}{\beta_c} \right). \quad (2.33)$$

The global optimum can be situated outside the design space, especially for designs with large power densities. Then, the feasible optimum will be located at the boundary of the design space, typically at the core saturation limit. Furthermore, the thermal limit is also restricting the valid designs around the global optimum (cf. Fig. 2.3). However, MF transformers are typically operated below the saturation, frequency, and current density limits [25, 64, 82, 163] and, therefore, the derived optimum can be used. Hence, the nature of this global optimum is analyzed in more details in the next subsection.

2.3.3 Frequency Diversity

In the design space shown in Fig. 2.3, all the designs with an optimal number of turns (n_{opt} , as long as the saturation flux is not reached) are considered for

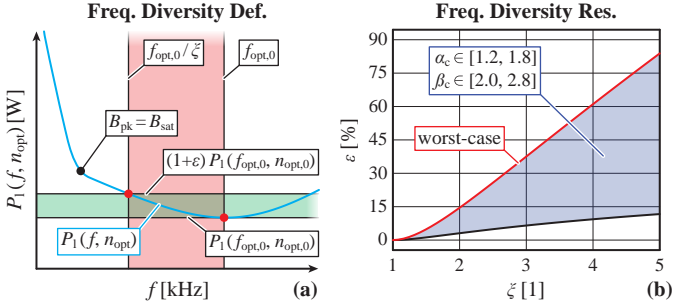


Fig. 2.4: (a) Definition of the frequency diversity (cf. (2.34)) with reference to global optimum (cf. (2.33)). For the different frequencies ($f_{\text{opt}} \neq f_{\text{opt},0}$), the respective optimal number of turns ($n_{\text{opt}} \neq n_{\text{opt},0}$) is considered, as long the saturation flux is not reached ($B_{\text{pk}} < B_{\text{sat}}$). (b) Obtained frequency diversity (cf. (2.35)) considering a typical range of Steinmetz parameters.

different frequencies. This restriction is accepted since there are no reasons to build a MF transformer with a non-optimal number of turns. By contrast, it can be desirable to select an operating frequency below $f_{\text{opt},0}$ (e.g., switching losses of the semiconductors and EMI issues). The impact of the selection of a sub-optimal operating frequency can be described with the following equation:

$$\epsilon = \max \left\{ \frac{P_1(f, n_{\text{opt}})}{P_1(f_{\text{opt},0}, n_{\text{opt},0})} - 1 \right\}, \quad \text{with } \frac{f_{\text{opt},0}}{f} < \xi, \quad (2.34)$$

where ξ represents the allowed relative deviation compared to the optimal frequency ($f_{\text{opt},0}$) and ϵ the corresponding relative impact on the losses, as illustrated in Fig. 2.4(a).

The resulting characteristic of the losses curve is rather flat with respect to frequency ($f < f_{\text{opt},0}$) as long as the saturation flux is not reached (n_{opt} is located inside the design space). As soon as n_{opt} crosses the saturation limit, the number of turns should be selected with respect to the saturation limit (and not anymore with n_{opt}). This leads to a rapid increase of the winding losses and the optimal ratios between the core and winding losses (cf. (2.32)) cannot be anymore achieved. Therefore, at the saturation limit, the total losses are rapidly increasing.

The aforementioned equation can be solved analytically if all the designs are located inside the design space limitations (n_{opt} is not limited by the

saturation flux), which is the case for typical MF transformer designs. This leads to

$$\epsilon = \left(\frac{1}{\xi^2} \right)^{\frac{\alpha_c}{2+\beta_c}} \left(\frac{\beta_c - \alpha_c (1 - \xi^2)}{\beta_c} \right)^{\frac{\beta_c}{2+\beta_c}} - 1, \quad (2.35)$$

where it should be noted that the solution of the equation is only dependent on α_c , β_c , and ξ . Therefore, the solution can be evaluated numerically for a range of Steinmetz parameters covering typical core materials [17, 21, 216–221].

Fig. 2.4(b) shows the obtained results. It can be observed that frequencies significantly below $f_{\text{opt},0}$ can be selected with a minor impact on the efficiency. For example, with half of the optimal frequency ($\xi = 2$), the losses are, at most, only 15 % higher than the global optimum. It can be concluded that the MF transformer loss curve is always flat around $f_{\text{opt},0}$. This implies that the optimum ($f_{\text{opt},0}$) should be considered carefully for converter designs. A small amount of frequency-dependent losses in the converter (e.g., switching losses of the semiconductors) can significantly shift down the optimal operating frequency of the complete converter with respect to the MF transformer optimum. Due to the flat optimum, model uncertainties and parameter tolerances can also significantly shift the value of the optimal operating frequency (cf. Chapter 3) [125].

Nevertheless, if the selected operating frequency is significantly below $f_{\text{opt},0}$, this indicates that a less expensive core material and litz wire could be selected with a minor impact on the achieved performance. Moreover, the optimal frequency ($f_{\text{opt},0}$) is interesting for examining the fundamental design limitations of power converters. This holds particularly true with modern SiC and GaN transistors, where the magnetic components often limit the achievable efficiency and power density [113]. Therefore, scaling laws are derived for the optimal MF transformer ($f_{\text{opt},0}$ and $n_{\text{opt},0}$) in the next subsection.

2.3.4 Scaling Laws

The scaling of MF transformers is considered for different power ratings (P) and power densities (ρ) [20, 173]. Different hypotheses are made in order to obtain simple and general scaling laws:

- The power factor and voltage levels ($\cos(\phi)$, and V_{RMS}) are fixed. The power rating is scaled with the current. However, the impedance of the MF transformer (ratio between V_{RMS} and I_{RMS}) has only a minor impact on the derived scaling laws.

- ▶ The volume (or power density) of the MF transformer is scaled with fixed geometrical aspect ratios (x_{cw} , x_c , and x_w).
- ▶ The core material (B_{sat} , k_c , α_c , and β_c) and the winding stranding ($J_{\text{RMS,max}}$, k_w , σ , and d_s) are fixed.
- ▶ The number of turns (n) is accepted to be a continuous (non-discrete) variable. The winding filling factor is independent of the number of turns, the power rating, and the power density.
- ▶ The global optimum is considered for all the designs ($f_{\text{opt},0}$ and $n_{\text{opt},0}$). It is accepted that the global optimum is located inside (and not at the boundary) of the design space (cf. Fig. 2.3), which is the case for typical MF transformer designs.

With the aforementioned hypotheses, it is possible to derive analytical scaling laws for the power density (ρ) and the power rating (P):

$$\frac{\text{FOM}}{\text{FOM}_{\text{ref}}} = \left(\frac{\rho}{\rho_{\text{ref}}} \right)^\lambda \left| \begin{array}{l} (f = f_{\text{opt},0}) \wedge (n = n_{\text{opt},0}), \end{array} \right. \quad (2.36)$$

$$\frac{\text{FOM}}{\text{FOM}_{\text{ref}}} = \left(\frac{P}{P_{\text{ref}}} \right)^\lambda \left| \begin{array}{l} (f = f_{\text{opt},0}) \wedge (n = n_{\text{opt},0}), \end{array} \right. \quad (2.37)$$

where ρ_{ref} and P_{ref} represents the reference design and λ the scaling exponent. Each figure of merit, FOM, can be scaled with respect to the reference value, FOM_{ref} . The following figures of merit are considered: the power rating (P), the volumetric power density (ρ), the gravimetric power density (γ), the temperature rise (ΔT), the loss fraction ($1 - \eta$), the frequency ($f_{\text{opt},0}$), the number of turns ($n_{\text{opt},0}$), the peak flux density (B_{pk}), the current density (J_{RMS}), the AC/DC winding resistance ratio (r_w), and the ratio between the core and winding losses (r_{cw}). It should be noted that simple exponential scaling laws only exist due to the special properties of the global optimum (cf. (2.33)).

There are several ways of scaling a MF transformer for different power ratings and power densities. However, in order to give meaningful results, certain parameters (i.e. figures of merit) should be kept constant, as shown in Fig. 2.5(a) [20]:

- ▶ $P = \text{const.}$ - The power rating of the MF transformer is constant and the power density is scaled (cf. (2.36)).
- ▶ $\rho = \text{const.}$ - The power density of the MF transformer is constant and the power rating is scaled (cf. (2.37)).

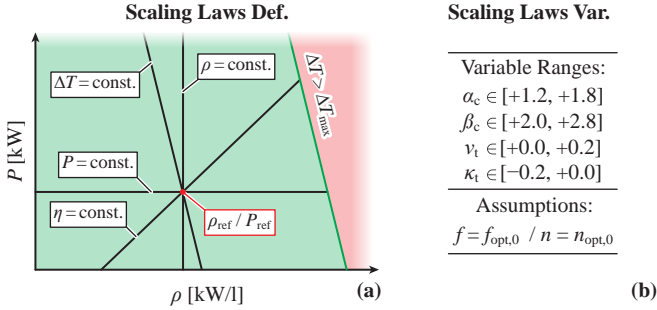


Fig. 2.5: (a) Scaling of MF transformers for different power ratings (P) and power densities (ρ) with characteristics for constant power rating, constant power density, constant temperature rise, and constant efficiency. For the scaling, the global optimum (cf. (2.33)) is considered with a given set of (constant) parameters for the core material (α_c and β_c) and the heat transfer mechanism (ν_t and κ_t). (b) Considered parameter ranges and assumptions for Tab. 2.3, Tab. 2.4, Tab. 2.5, and Tab. 2.6.

- ▶ $\eta = \text{const.}$ - The power rating of the MF transformer is scaled with a constant efficiency (cf. (2.37)).
- ▶ $\Delta T = \text{const.}$ - The power rating of the MF transformer is scaled with a constant temperature rise (cf. (2.37)).

Exact analytical solutions exist for the scaling coefficients (λ). The solutions only depend on the empirical parameters α_c , β_c , ν_t , and κ_t . For extracting general statements, the scaling coefficients are extracted for all the parameter combinations occurring for typical core materials and convective heat transfer mechanisms, cf. Fig. 2.5(b) [17, 21, 216–221]. The power rating of the MF transformer is scaled with a constant voltage. However, it should be noted that all the parameters, except the number of turns ($n_{\text{opt},0}$), are independent of the impedance of the MF transformer (ratio between V_{RMS} and I_{RMS}).

Tab. 2.3 shows the scaling coefficients for a constant power rating ($P = \text{const.}$). For increasing power densities, the frequency, and temperature rise are increasing, until the thermal limit is reached. The loss fraction is slowly increasing with the power density, indicating that the Pareto front is flat with respect to the power density.

Tab. 2.4 depicts the scaling coefficients for a constant power density ($\rho = \text{const.}$). For increasing power ratings, the temperature rise is increasing while the frequency is decreasing. The loss fraction is also slowly decreasing with

Tab. 2.3: Scaling Coeff. / $P = \text{const.}$ / $\rho = \text{var.}$

| FOM | Coeff. (λ) | Range (λ) |
|--------------------|---|---------------------|
| P | 0 | [+0.00, +0.00] |
| ρ | 1 | [+1.00, +1.00] |
| γ | 1 | [+1.00, +1.00] |
| ΔT | $\frac{2\alpha_c + 5\beta_c + 4\kappa_t + 2\beta_c\kappa_t - 2}{3(\beta_c + 2)(\nu_t + 1)}$ | [+0.61, +1.08] |
| $1 - \eta$ | $\frac{2\alpha_c + 3\beta_c - 6}{3\beta_c + 6}$ | [+0.20, +0.42] |
| $f_{\text{opt},0}$ | $\frac{1}{3}$ | [+0.33, +0.33] |
| $n_{\text{opt},0}$ | $\frac{\alpha_c + \beta_c - 4}{3\beta_c + 6}$ | [-0.07, +0.04] |
| B_{pk} | $\frac{6 - \alpha_c}{3\beta_c + 6}$ | [+0.29, +0.40] |
| J_{RMS} | $\frac{\alpha_c + 3\beta_c}{3\beta_c + 6}$ | [+0.60, +0.71] |
| r_w | 0 | [+0.00, +0.00] |
| r_{cw} | 0 | [+0.00, +0.00] |

Tab. 2.4: Scaling Coeff. / $\rho = \text{const.}$ / $P = \text{var.}$

| FOM | Coeff. (λ) | Range (λ) |
|--------------------|--|---------------------|
| ρ | 0 | [+0.00, +0.00] |
| P | 1 | [+1.00, +1.00] |
| γ | 0 | [+0.00, +0.00] |
| ΔT | $\frac{\beta_c - 2\alpha_c - 4\kappa_t - 2\beta_c\kappa_t + 2}{3(\beta_c + 2)(\nu_t + 1)}$ | [+0.03, +0.30] |
| $1 - \eta$ | $\frac{-2\alpha_c}{3\beta_c + 6}$ | [-0.30, -0.17] |
| $f_{\text{opt},0}$ | $\frac{-1}{3}$ | [-0.33, -0.33] |
| $n_{\text{opt},0}$ | $\frac{-\alpha_c - \beta_c - 2}{3\beta_c + 6}$ | [-0.48, -0.42] |
| B_{pk} | $\frac{\alpha_c}{3\beta_c + 6}$ | [+0.08, +0.15] |
| J_{RMS} | $\frac{-\alpha_c}{3\beta_c + 6}$ | [-0.15, -0.08] |
| r_w | 0 | [+0.00, +0.00] |
| r_{cw} | 0 | [+0.00, +0.00] |

Tab. 2.5: Scaling Coeff. / $\eta = \text{const.}$ / $P = \text{var.}$

| FOM | Coeff. (λ) | Range (λ) |
|--------------------|--|---------------------|
| $1 - \eta$ | 0 | [+0.00, +0.00] |
| P | 1 | [+1.00, +1.00] |
| ρ | $\frac{2\alpha_c}{2\alpha_c+3\beta_c-6}$ | [+0.50, +1.00] |
| γ | $\frac{2\alpha_c}{2\alpha_c+3\beta_c-6}$ | [+0.50, +1.00] |
| ΔT | $\frac{2\alpha_c+\beta_c+4\kappa_1-2\beta_c\kappa_1-2}{(\nu_1+1)(2\alpha_c+3\beta_c-6)}$ | [+0.56, +1.00] |
| $f_{\text{opt},0}$ | $\frac{2-\beta_c}{2\alpha_c+3\beta_c-6}$ | [-0.17, -0.00] |
| $n_{\text{opt},0}$ | $\frac{2-\beta_c-\alpha_c}{2\alpha_c+3\beta_c-6}$ | [-0.50, -0.42] |
| B_{pk} | $\frac{\alpha_c}{2\alpha_c+3\beta_c-6}$ | [+0.25, +0.50] |
| J_{RMS} | $\frac{\alpha_c}{2\alpha_c+3\beta_c-6}$ | [+0.25, +0.50] |
| r_w | 0 | [+0.00, +0.00] |
| r_{cw} | 0 | [+0.00, +0.00] |

the power rating, implying that high power MF transformers are intrinsically more efficient but difficult to cool down.

Tab. 2.5 shows the scaling coefficients for a constant efficiency ($\eta = \text{const.}$). For increasing power ratings, the power density is increasing while the frequency is decreasing. The temperature rise is also increasing, which implies that high power designs are hitting the thermal limit. This is due to the reduction of the ratio between the surface area (A_h) and the volume (V_{tot}) for large MF transformers.

Tab. 2.6 shows the scaling coefficients for a constant temperature rise ($\Delta T = \text{const.}$). For increasing power ratings, the power density and the frequency are decreasing. The loss fraction is decreasing, implying that high power MF transformers should be efficient for staying thermally feasible. The same trend can also be observed for LF transformers [15, 214].

General trends can be identified independently of the chosen core material and convective cooling mechanisms (cf. Fig. 2.5(b)). The following conclusions are drawn from the scaling laws. Compact designs are running with higher frequencies, temperature rises, flux densities, and current densities but feature limited efficiencies. High power designs feature lower frequencies and higher efficiencies but limited cooling capabilities.

Tab. 2.6: Scaling Coeff. / $\Delta T = \text{const.}$ / $P = \text{var.}$

| FOM | Coeff. (λ) | Range (λ) |
|--------------------|--|---------------------|
| ΔT | 0 | [+0.00, +0.00] |
| P | 1 | [+1.00, +1.00] |
| ρ | $\frac{2\alpha_c - \beta_c + 4\kappa_1 + 2\beta_c \kappa_1 - 2}{2\alpha_c + 5\beta_c + 4\kappa_1 + 2\beta_c \kappa_1 - 2}$ | [-0.36, -0.03] |
| γ | $\frac{2\alpha_c - \beta_c + 4\kappa_1 + 2\beta_c \kappa_1 - 2}{2\alpha_c + 5\beta_c + 4\kappa_1 + 2\beta_c \kappa_1 - 2}$ | [-0.36, -0.03] |
| $1 - \eta$ | $\frac{2\beta_c \kappa_1 - \beta_c - 4\kappa_1 - 2\alpha_c + 2}{2\alpha_c + 5\beta_c + 4\kappa_1 + 2\beta_c \kappa_1 - 2}$ | [-0.36, -0.22] |
| $f_{\text{opt},0}$ | $\frac{-2\beta_c}{2\alpha_c + 5\beta_c + 4\kappa_1 + 2\beta_c \kappa_1 - 2}$ | [-0.45, -0.34] |
| $n_{\text{opt},0}$ | $\frac{2 - 2\beta_c - 4\kappa_1 - 2\alpha_c}{2\alpha_c + 5\beta_c + 4\kappa_1 + 2\beta_c \kappa_1 - 2}$ | [-0.48, -0.41] |
| B_{pk} | $\frac{2\alpha_c + 4\kappa_1 - 2}{2\alpha_c + 5\beta_c + 4\kappa_1 + 2\beta_c \kappa_1 - 2}$ | [-0.05, +0.14] |
| J_{RMS} | $\frac{\beta_c(2\kappa_1 - 1)}{2\alpha_c + 5\beta_c + 4\kappa_1 + 2\beta_c \kappa_1 - 2}$ | [-0.32, -0.17] |
| r_w | 0 | [+0.00, +0.00] |
| r_{cw} | 0 | [+0.00, +0.00] |

Scaling laws can also be derived for a fixed frequency (different from $f_{\text{opt},0}$) and for designs at the saturation limit. However, for obtaining simple scaling coefficients (cf. (2.36) and (2.37)), additional assumptions on r_w and/or r_{cw} are necessary [173]. Furthermore, it is difficult to draw general conclusions from scaling laws with sub-optimal designs. Therefore, only the scaling of optimal designs ($f_{\text{opt},0}$ and $n_{\text{opt},0}$) is considered in the following.

2.4 Analytical Results

In this section, the aforementioned optimum, frequency diversity, and scaling laws are applied to a specific MF transformer design. The reference design features the following ratings: $P = 20 \text{ kW}$, $\rho = 20 \text{ kW/l}$, and $V_{\text{RMS}} = 600 \text{ V}$. It should be noted that these ratings differ from the MV/MF transformer used for SST demonstrator presented in Subsection 1.7.2. The choice of a LV/MF transformer has been made for this analysis for obtaining the intrinsic limitations of MF transformers, without including electrical insulation constraints, which are extremely specific to MV/MF transformers.

Tab. 2.7: MF Transformer Parameters (cf. Fig. 2.2)

| Parameter | Value |
|-----------|---|
| General | $\cos(\phi) = 0.85 / V_{\text{RMS}} = 600 \text{ V}$ $x_{\text{cw}} = 1.5 / x_{\text{c}} = 1.5 / x_{\text{w}} = 5.0$ |
| Core | “TDK N97” $k_{\text{c}} = 1.35 / \alpha_{\text{c}} = 1.44 / \beta_{\text{c}} = 2.46$ $f_{\text{c,max}} = 700 \text{ kHz} / B_{\text{sat}} = 300 \text{ mT}$ |
| Winding | Litz Wire $k_{\text{w}} = 25 \% / d_{\text{s}} = 100 \mu\text{m} / \sigma = 46 \text{ MS}$ $J_{\text{RMS,max}} = 8.0 \text{ A/mm}^2$ |
| Thermal | $k_{\text{t}} = 12.0 / v_{\text{t}} = +0.09 / \kappa_{\text{t}} = -0.11$ $\Delta T_{\text{max}} = 100 \text{ }^\circ\text{C}$ |

2.4.1 Considered Parameters

An E-core based MF transformer with shell-type arrangement is considered (cf. Fig. 2.2). The key parameters are summarized in Tab. 2.7. A “TDK N97” ferrite core is selected where the Steinmetz parameters are extracted with a least square fit of the losses ($T = 70 \text{ }^\circ\text{C}$, $B_{\text{pk}} \in [25, 150] \text{ mT}$, and $f \in [50, 200] \text{ kHz}$) [216]. The winding is composed of litz wires with $100 \mu\text{m}$ strands. The filling factor of 25 % considers the filling factor of the litz wire itself, the filling factor of the turns, and the insulation distances to the core. The convection coefficient parameters are fitted for the chosen geometry with an air speed of 3 m/s with the formula presented in [17].

2.4.2 Optimal Design

Fig. 2.6 depicts the obtained design space (cf. Fig. 2.3) for $P = 20 \text{ kW}$ and $\rho = 20 \text{ kW/l}$. The core losses are diminishing with increasing number of turns and/or frequencies (volt-second product), as shown in Fig. 2.7. On the contrary, the winding losses are increasing with increasing number of turns (current density) and/or frequencies (proximity effect), as shown Fig. 2.8. Therefore, an optimum exists and has the following characteristics: $f_{\text{opt},0} = 86 \text{ kHz}$, $n_{\text{opt},0} = 10.5$, $B_{\text{pk}} = 84 \text{ mT}$, $J_{\text{RMS}} = 2.9 \text{ A/mm}^2$, $r_{\text{w}} = 1.71$, $r_{\text{cw}} = 0.81$, $\gamma = 6.4 \text{ kW/kg}$,

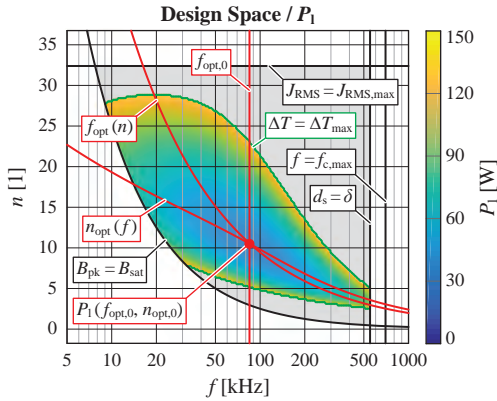


Fig. 2.6: Total losses of a 20 kW and 20 kW/1 MF transformer (cf. Tab. 2.7) for different frequencies and numbers of turns. The design space limits (black and gray), the thermal limit (green), and the optimal designs (red) are highlighted.

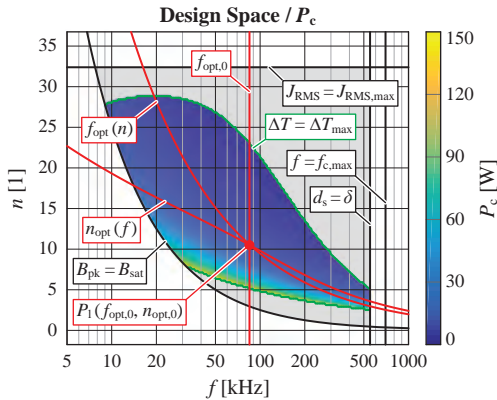


Fig. 2.7: Core losses of a 20 kW and 20 kW/1 MF transformer (cf. Tab. 2.7) for different frequencies and numbers of turns. The design space limits (black and gray), the thermal limit (green), and the optimal designs (red) are highlighted.

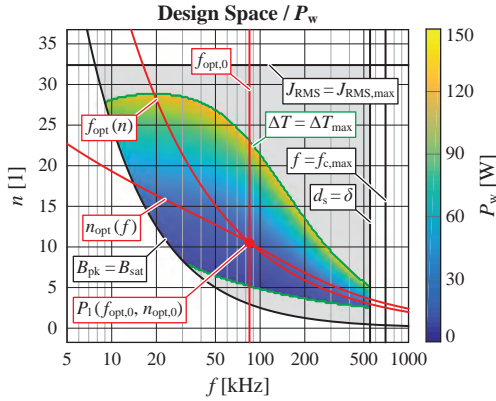


Fig. 2.8: Winding losses of a 20 kW and 20 kW/1 MF transformer (cf. Tab. 2.7) for different frequencies and numbers of turns. The design space limits (black and gray), the thermal limit (green), and the optimal designs (red) are highlighted.

$\Delta T = 41^\circ\text{C}$, and $\eta = 99.76\%$. It can be seen that the optimal design is located far away from the design space limits (saturation flux, maximum current density, maximum frequency, and thermal limit).

2.4.3 Frequency Diversity

Fig. 2.9(a) shows the design space for $P = 20\text{ kW}$ and different power densities and frequencies. The optimal number of turns (n_{opt} , as long the saturation flux is not reached) is considered for all the designs. It can be seen that all the optimal designs ($f_{\text{opt},0}$) are not restricted by the saturation flux, maximum current density, or maximum frequency. This means that the optimum derived in Subsection 2.3.2 can be used. The efficiency is rapidly dropping for designs operated at the saturation flux (cf. Fig. 2.4).

The frequency diversity presented in Subsection 2.3.3 can be observed in Fig. 2.9(b) where the Pareto fronts are shown for $f < f_{\text{opt},0}$. As expected (cf. Fig. 2.4(b)), frequencies well below $f_{\text{opt},0}$ can be chosen with a minor impact on the efficiency: $\epsilon = 11\%$ for $\xi = 2$ and $\epsilon = 26\%$ for $\xi = 3$ (cf. (2.35)).

2.4.4 Scaling Laws

Fig. 2.10 depicts the scaling of the aforementioned MF transformer for different power ratings and power densities (cf. Subsection 2.3.4). All the designs are

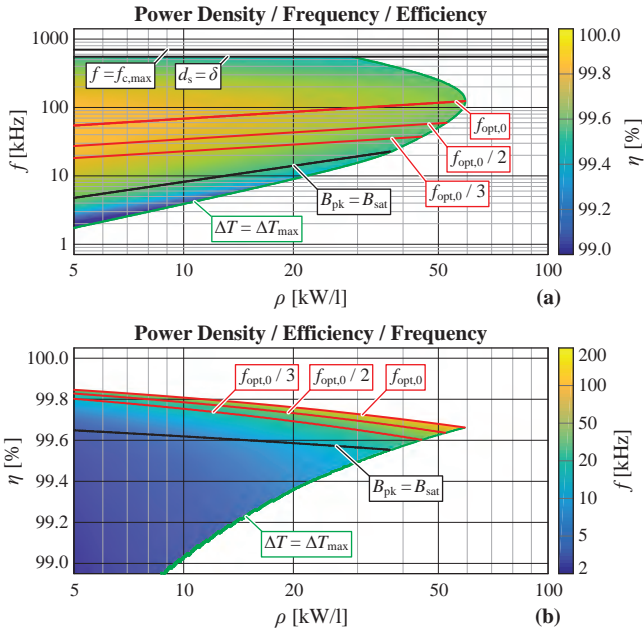


Fig. 2.9: (a) Design space for different frequencies and power densities. (b) Pareto front for $f < f_{opt,0}$. The design space limits (black), the thermal limit (green), and the optimal designs (red) are shown. The optimal number of turns (n_{opt} , as long the saturation flux is not reached) is considered for all the designs. The power rating is fixed to 20 kW.

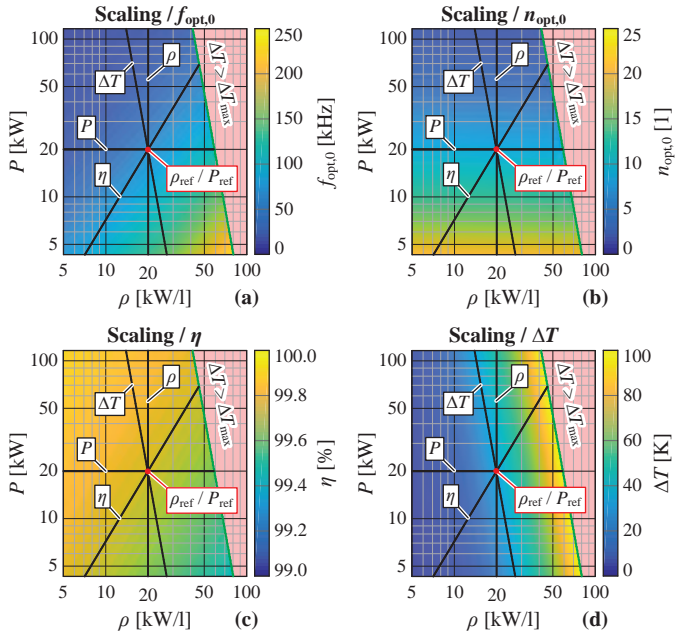


Fig. 2.10: Scaling of MF transformers for different power ratings (P) and power densities (ρ). Scaling of (a) the frequency, (b) the number of turns, (c) the efficiency, and (d) the temperature rise. All the designs are operated with the optimal frequency and the optimal number of turns ($f_{\text{opt},0}$ and $n_{\text{opt},0}$).

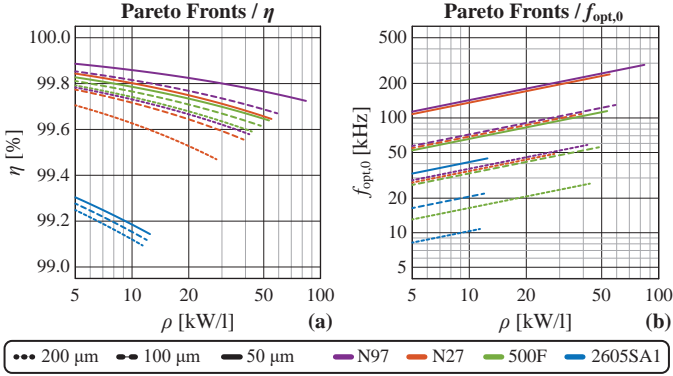


Fig. 2.11: (a) Pareto fronts and (b) operating frequencies for different core materials and winding strandings. All the designs are operated with the optimal frequency and the optimal number of turns ($f_{opt,0}$ and $n_{opt,0}$). The power rating is fixed to 20 kW.

operated with the optimal frequency and the optimal number of turns ($f_{opt,0}$ and $n_{opt,0}$). The scaling trajectories are shown for constant power rating, constant power density, constant temperature rise, and constant efficiency around the following reference design: $P_{ref} = 20$ kW and $\rho_{ref} = 20$ kW/l.

The general conclusions drawn in Subsection 2.3.4 are verified: the compact designs are operated at higher frequencies, but have reduced efficiencies. High power designs are featuring higher efficiencies and reduced frequencies but also limited cooling capabilities.

2.4.5 Core Material and Winding Stranding

The Pareto front obtained with the defined parameters (cf. Fig. 2.9(b)) can be pushed by changing the core material and the stranding of the windings (all the other parameters remains unchanged, cf. Tab. 2.7). The following core materials are considered: a low performance ferrite (“TDK N27”), a high performance ferrite (“TDK N97”), a nanocrystalline material (“VAC VITROPERM 500F”), and an amorphous material (“Metglas 2605SA1”) [21, 216–218]. The strand diameter is chosen between 50 μ m, 100 μ m, and 200 μ m. All the designs are operated with the optimal frequency and the optimal number of turns ($f_{opt,0}$ and $n_{opt,0}$).

Fig. 2.11 shows the obtained Pareto fronts with the corresponding optimal operating frequencies for $P = 20$ kW. It should be noted that all the designs

(until the thermal limit) are not limited by the saturation flux, maximum current density, and maximum frequency. Logically, the designs with fine strands are operated at higher frequencies (cf. (2.31)). The designs with the ferrite materials feature comparable operating frequencies ($\beta_c - \alpha_c$ difference is similar, cf. (2.31)). However, the designs based on the N97 ferrite material are more efficient compared to the designs using the N27 ferrite. The designs with an amorphous core feature low operating frequencies but also low efficiencies. The MF transformers with a nanocrystalline core feature high efficiencies with reduced operating frequencies ($\beta_c - \alpha_c$ difference is small) and, therefore, represent an interesting alternative.

It can be concluded that the choice of the core material and the winding stranding are interconnected. Designs with large $\beta_c - \alpha_c$ differences and reduced d_s are operated at higher frequencies (cf. (2.31)) and feature a reduced $B_{pk}J_{RMS}$ product (cf. (2.23)). However, high optimal operating frequencies do not directly imply high efficiencies. This last statement is highlighted by comparing the N27 ferrite and the nanocrystalline materials in Fig. 2.11.

2.5 Numerical Verification

The full-analytical model presented in Section 2.2 and the optimum derived in Section 2.3 are subject to several simplifications. In this section, the results obtained with the full-analytical model (cf. Section 2.4) are verified with a more elaborate semi-numerical model.

2.5.1 Semi-Numerical Model

A semi-numerical model of MF transformers, which is based on the analysis presented in [19,25,115,138], is considered. The following effects and limitations are taken into account:

- ▶ *Geometry* - An discrete (integer) number of turns is considered with the exact packing pattern of the turns. The insulation distances (between the turns and to the core) are taken into account.
- ▶ *Core losses* - The flux density, frequency, and temperature dependences of the core losses are considered with a loss map [19, 128].
- ▶ *Winding losses* - The winding losses are computed with the exact packing pattern of the turns and the temperature dependence is taken into account [19, 138].

- ▶ *Thermal model* - A complex thermal model is used where the heat conduction, natural convection, forced convection, and radiation mechanisms are considered. The cross-coupling between the losses and the temperature distribution is taken into account [17, 91, 115, 138].
- ▶ *Insulation design* - The stress in the insulation (electric field and dielectric losses) is computed [153, 154]. Designs with too large electric field values are excluded.
- ▶ *Equivalent circuit* - The effect of the magnetizing and leakage inductances on the applied waveforms is also taken into account [125].
- ▶ *Parasitic resonances* - The effect of the open-circuit and short-circuit resonances on the MF transformer operation is investigated. [17, 156]. Designs with critically low resonance frequencies are excluded.

This semi-numerical model is based on analytical equations, but does not feature an analytical solution. Most important, the computation cost for a single design is reasonable: less than 5k FLOPs [222]. Nevertheless, such a model leads to a multi-variable, multi-constrained, mixed-integer, and non-linear optimization problem. Therefore, the optimization problem should be solved with a numerical solver. In the following, the computations methods listed below are compared:

- ▶ *Full-analytical* - The presented full-analytical model (cf. Section 2.2) is considered. The derived analytical optimum and scaling laws (cf. Section 2.3) are used.
- ▶ *Semi-numerical / fixed ratios* - The semi-numerical method is used with fixed geometrical aspect ratios (x_{cw} , x_c , and x_w).
- ▶ *Semi-numerical / free ratios* - The semi-numerical method is used and the geometrical aspect ratios of the MF transformer (x_{cw} , x_c , and x_w) are also optimized.

2.5.2 Scaling Laws

The specifications considered in Subsection 2.4.1 (cf. Tab. 2.7) are selected and the methods defined in Subsection 2.5.1 are compared. The reference design for the scaling is featuring the following ratings: $P_{\text{ref}} = 20 \text{ kW}$ and $\rho_{\text{ref}} = 20 \text{ kW/l}$. The scaling laws with constant power density ($\rho = \text{const.}$) and

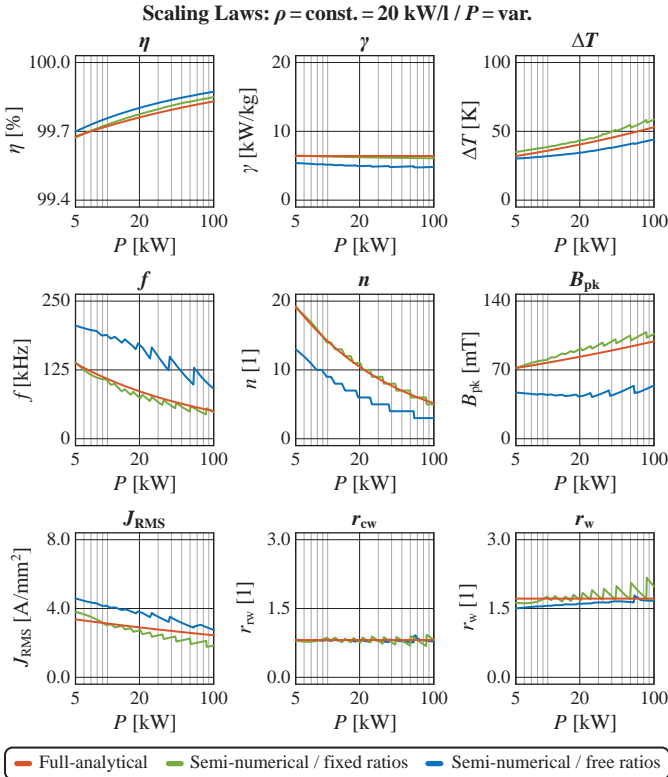


Fig. 2.12: Scaling for $\rho = \text{const.} = 20 \text{ kW/l}$. The presented scaling laws are compared to semi-numerical models with fixed and free geometrical aspect ratios.

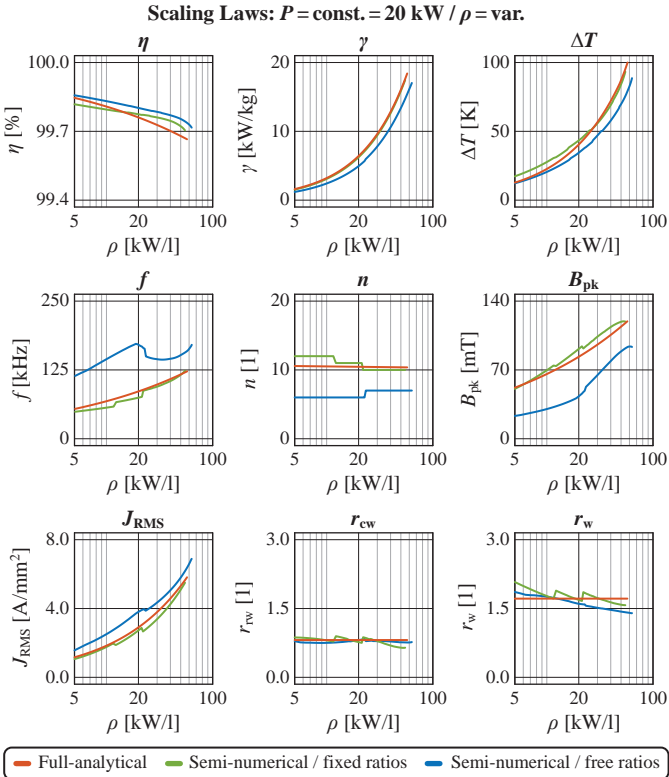


Fig. 2.13: Scaling for $P = \text{const.} = 20 \text{ kW}$. The presented full-analytical model is compared to semi-numerical models with fixed and free geometrical aspect ratios.

constant power ($P = \text{const.}$) are considered since they cover a representative part of the designs shown in Fig. 2.10.

For the full-analytical model, the derived optimum is used ($f_{\text{opt},0}$ and $n_{\text{opt},0}$). For the two semi-numerical models, the optimum design (with respect to the efficiency) is selected with a mixed-integer multi-constrained genetic algorithm [165,223]. The results are shown in Fig. 2.12 and Fig. 2.13 for constant power density ($\rho = \text{const.}$) and constant power ($P = \text{const.}$), respectively.

It can be seen immediately that the consideration of discrete (integer) numbers of turns leads to discontinuous curves for the optimal designs. The derived scaling laws are valid as they correctly predict (qualitatively and quantitatively) the trends for all the considered parameters for fixed geometrical aspect ratios.

With free geometrical aspect ratios, the optimal designs feature narrow winding windows and, therefore, reduced proximity effect losses (cf. (2.10)) and higher switching frequencies (cf. (2.31)). The increased switching frequencies also explain the reduced numbers of turns and the low flux densities. However, the thickness of the winding window cannot be reduced beyond a certain limit, due to practical constraints (packing of the turns) and due to the incompressible insulation distances (e.g., coil former thickness). Nevertheless, the optimization of the geometrical aspect ratios only provides limited advantages for the achieved efficiencies and power densities. This confirms the aspect ratios can be kept constant for the analysis of the fundamental characteristics of MF transformers with an analytical model (i.e. scaling laws).

High efficiencies (up to 99.85 %) and power densities (up to 63 kW/l) are achieved for the selected parameters. However, it should be noted that the presented designs are based on ideal characteristics: every core shape and every litz wire (number of strands and shape) is considered as available. The thermal model assumes a uniform cooling from all the sides (40 °C ambient). Moreover, the volume and the losses of the cooling system (e.g., fans) are not taken into account. Finally, only the MF transformer is optimized without considering external factors (e.g., switching losses of the power semiconductors). Therefore, the performances shown in Fig. 2.12 and Fig. 2.13 are unlikely to be achieved for a constructed prototype and represent the theoretical limit. Nevertheless, such practical design restrictions could be easily integrated into the aforementioned computation methods.

The optimal designs obtained with the three considered models feature similar efficiencies but different parameters, especially for the semi-numerical model with free geometrical aspect ratios. More particularly, large deviations can be observed for the operating frequency, the number of turns, and,

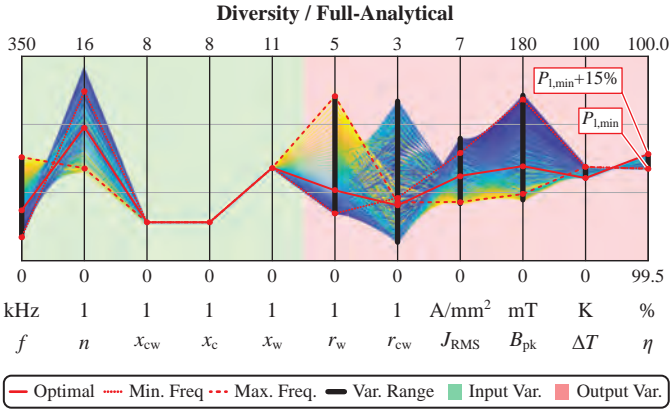


Fig. 2.14: Parallel coordinate plots (1200 designs) obtained with the full-analytical model for $P = \text{const.} = 20 \text{ kW}$ and $\rho = 20 \text{ kW/l}$. All the designs, which feature less than 15 % more losses than the optimal design are shown. The designs with the optimal, minimum, and maximum frequencies are highlighted in red.

therefore, the flux density. The discrepancies between the models and the underlying design space diversity are analyzed in more details in the next subsection.

2.5.3 Design Space Diversity

The parameter ranges defined in Subsection 2.4.1 (cf. Tab. 2.7) are selected with the following ratings: $P = 20 \text{ kW}$ and $\rho = 20 \text{ kW/l}$. The complete design space is swept for the three methods defined in Subsection 2.5.1. A brute-force algorithm is used in order to explore the complete design space including eventual local minima. For each method, all the designs, which feature less than 15 % more losses than the optimal design are kept. Fig. 2.14 shows the results obtained with the full-analytical model, Fig. 2.15 shows the results obtained with the semi-numerical model with fixed geometrical aspect ratios, and, finally, Fig. 2.16 depicts the results obtained with the semi-numerical model with free geometrical aspect ratios. The results are displayed with parallel coordinate plots, where the designs with the optimal, minimum, and maximum frequencies are highlighted [224].

The full-analytical model delivers results similar to the semi-numerical model for fixed geometrical aspect ratios. A significant frequency diversity

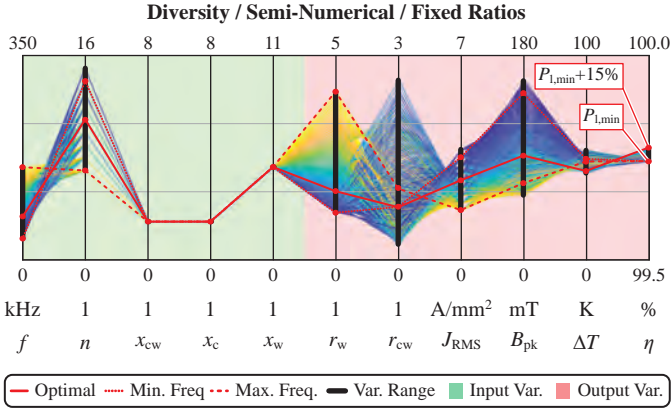


Fig. 2.15: Parallel coordinate plots (500 designs) obtained with semi-numerical models (fixed geometrical aspect ratios) for $P = \text{const.} = 20 \text{ kW}$ and $\rho = 20 \text{ kW/l}$. All the designs, which feature less than 15% more losses than the optimal design are shown. The designs with the optimal, minimum, and maximum frequencies are highlighted in red.

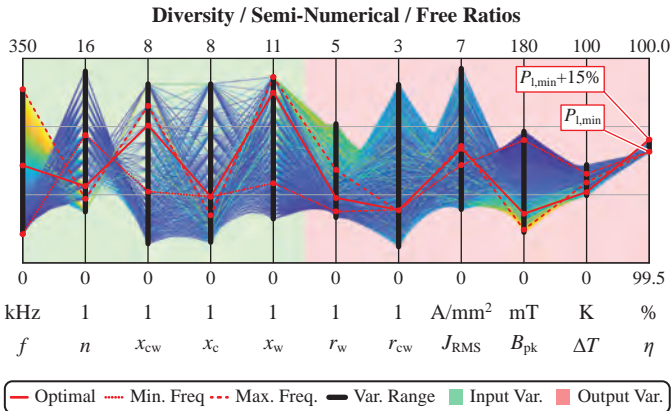


Fig. 2.16: Parallel coordinate plots (300000 designs) obtained with semi-numerical models (free geometrical aspect ratios) for $P = \text{const.} = 20 \text{ kW}$ and $\rho = 20 \text{ kW/l}$. All the designs, which feature less than 15% more losses than the optimal design are shown. The designs with the optimal, minimum, and maximum frequencies are highlighted in red.

Tab. 2.8: Design Space Diversity / 20 kW / 20 kW/l

| Var. | Unit | D1 | D2 | D3 | D4 | D5 |
|------------|-------------------|-------|-------|-------|-------|-------|
| f | kHz | 167 | 49 | 297 | 159 | 161 |
| n | 1 | 6 | 10 | 5 | 8 | 5 |
| x_{cw} | 1 | 5.38 | 2.79 | 7.00 | 4.72 | 4.14 |
| x_c | 1 | 2.59 | 3.06 | 2.19 | 3.06 | 2.59 |
| x_w | 1 | 9.19 | 4.67 | 10.00 | 9.19 | 10.00 |
| r_w | 1 | 1.59 | 1.23 | 2.12 | 1.59 | 1.62 |
| r_{cw} | 1 | 0.77 | 0.77 | 0.61 | 0.24 | 2.60 |
| J_{RMS} | A/mm ² | 3.9 | 3.3 | 4.4 | 4.6 | 2.7 |
| \hat{B} | mT | 43 | 106 | 27 | 35 | 59 |
| ΔT | K | 35 | 43 | 39 | 41 | 37 |
| η | % | 99.80 | 99.77 | 99.77 | 99.77 | 99.77 |

can be observed (cf. Subsection 2.3.3). The designs with high operating frequencies feature low numbers of turns, low flux densities, and low current densities. The design space diversity is even greater if the geometrical aspect ratios are additionally optimized. For this last case, the variables vary in the following ranges: $f \in [49, 297]$ kHz, $r_w \in [1.11, 3.40]$, $r_{cw} \in [0.24, 2.60]$, $J_{RMS} \in [1.8, 6.7]$ A/mm², $B_{pk} \in [27, 116]$ mT. Some designs, computed with the semi-numerical model, are highlighted in Tab. 2.8. The following designs are selected: minimum losses (“D1”), minimum frequency (“D2”), maximum frequency (“D3”), minimum ratio between core and winding losses (“D4”), and maximum ratio between core and winding losses (“D5”).

It can be seen that extremely different designs feature similar performances. This diversity would be even greater with additional degrees of freedom (e.g., core material and winding stranding). The design space diversity can be used to select a quasi-optimal design with additional design restrictions (e.g., available core shapes, available litz wires, and switching losses of the power semiconductors). The systematic exploration of the design space is also useful for drawing general conclusions on the advantages and limitations of the different models.

2.6 Critical Analysis

With the aforementioned results, different conclusions can be made on the full-analytical modeling (cf. Section 2.2), the corresponding optimum, and the scaling laws (cf. Section 2.3):

- ▶ The full-analytical model is able to correctly capture qualitatively and quantitatively the design process of MF transformers. However, many effects are neglected. This implies that some designs can be invalid (e.g., due to parasitics and thermal limits), difficult to construct (e.g., turn packing), and/or feature reduced efficiencies (e.g., due to simplified loss models and neglected temperature dependences of the losses).
- ▶ For a given core geometry, the optimal design can be analytically extracted. Since the optimum is always flat with respect to frequency, the optimal operating frequency of the converter (considering switching losses of the power semiconductors) can be significantly lower than the optimal frequency of the MF transformer.
- ▶ The analytical optimum of the MF transformers should be considered with caution. Extremely different designs (e.g., concerning frequency, flux density, and ratio between core and winding losses) can lead to similar performances (design space diversity). This implies that the designs located around the global minimum (analytical optimum) and around local minima cannot be neglected during the design process. Nevertheless, the analytical optimum is useful to quantitatively understand the fundamental limitations of MF transformers.
- ▶ An optimal design can be scaled for different power ratings and power densities. These scaling laws correctly predict the trends and limitations of MF transformer designs. However, due to the required assumptions (e.g., fixed core material, fixed winding stranding, and fixed geometrical aspect ratios), these scaling laws are limited to theoretical analysis and cannot be used directly for the design process of MF transformers.

It appears that the limitations of the full-analytical model are problematic for obtaining an accurate model of MF transformers, which is required for virtual prototyping and design automation. Therefore, semi-numerical models should be used and the following guidelines can be extracted (cf. Section 2.5):

- ▶ A multi-variable, multi-constrained, mixed-integer, and non-linear optimization problem should be solved. Due to the design space diversity,

many local minima exist. Moreover, the different local minima are flat, implying that designs located near a minimum can be almost as good as the minimum itself. Therefore, a robust optimization algorithm (e.g., particle swarm and genetic) should be selected [165, 223]. For designs with many discrete variables, a brute-force search algorithm may be the only practicable solution.

- ▶ For a practical MF transformer design, many additional restrictions apply (e.g., available core shapes, available litz wires, and switching losses of semiconductors). The aforementioned design space diversity mitigates the impact of such design restrictions on the achievable performances.
- ▶ The full-analytical model can be used as a filter to reduce the design space (e.g., geometry, core material, and litz wire) before applying the more complex semi-numerical model.
- ▶ Models based on numerical field simulations (e.g., FEM simulations) are extremely time-consuming (modeling complexity, and computational cost) and, therefore, are not adapted for optimizations [143, 153, 154]. However, field simulations are useful for checking and fine-tuning the designs extracted during the optimization process.

2.7 Summary

This chapter investigates the optimization and scaling of MF transformers. A simple full-analytical model is presented for the core losses (using the Steinmetz parameters), winding losses (including the HF losses), and temperature rise (convection process). With this model, the design space of MF transformers is analyzed and the optimum is derived (frequency and number of turns). An increased operating frequency allows for more efficient and more compact designs. However, beyond a certain frequency, the performance cannot be further improved due to the increased core and HF winding losses. The properties of the optimum are analyzed and it is found that the optimum is always flat: the optimal operating frequency can be divided by two with less than 15 % additional losses (the number of turns is adapted). At the optimum, the flux density is typically lower than the saturation flux density of the core.

Scaling laws are derived for optimal MF transformers operated at different power ratings (with constant power density, constant efficiency, or constant temperature rise) and power densities (with constant power rating). These

scaling laws allow the extraction of general statements about MF transformer performances. Compact designs are operated at higher frequencies, but have reduced efficiencies. High power designs are featuring higher efficiencies and reduced frequencies but also limited cooling capabilities.

A 20 kW and 20 kW/l MF transformer with a ferrite core and litz wire windings is considered for a numerical evaluation. The proposed full-analytical model, optimum, and scaling laws are applied. The obtained results are successfully verified with a more elaborate semi-numerical model. It is found that the full-analytical model correctly predicts the behavior of MF transformers. However, due to the multiple local minima of the mapping between the design space and the performance space (design space diversity), the analytical optimum cannot be used for the final design process of MF transformers. Global optimization should be performed with more advanced semi-numerical models.

3

MF Transformer Equivalent Circuit

Chapter Abstract

MF transformers are extensively used in power electronic converters. Accordingly, accurate models of such devices are required, especially for the magnetic equivalent circuit. Literature documents many different methods to calculate the magnetizing and leakage inductances of transformers, where, however, few comparisons exist between the methods. Furthermore, the impact of underlying hypotheses and parameter uncertainties is usually neglected. This chapter analyzes nine different models, ranging from simple analytical expressions to detailed numerical 3D simulations. The accuracy of the different methods is assessed by means of Monte-Carlo simulations and linearized statistical models. The experimental results, conducted with a MF transformer (400 V to 400 V, 100 kHz, 20 kW) employed in a converter for a 400 V DC distribution system, are in agreement with the simulations (below 14 % inaccuracy for all the considered methods). It is concluded that, considering typical tolerances, analytical models are accurate enough for most applications and that the tolerance analysis can be conducted with linearized models.

3.1 Introduction

Many power electronic converters feature MF transformers for voltage transformation, impedance matching, and galvanic isolation [25, 64, 82, 143]. Multiple degrees of freedom are available for the design of MF transformers, i.e. frequency, winding geometry, core shape, core material, and cooling concept (cf. Chapter 2) [22]. It appears that the extraction of the magnetic parameters of a MF transformer is particularly important for determining the currents, the voltages, the losses, and the parasitic resonances [16, 17, 19].

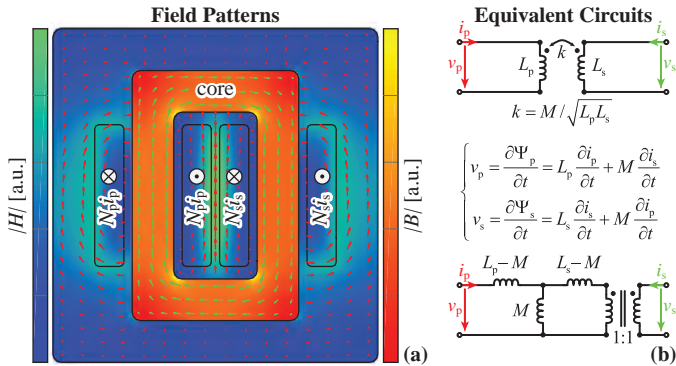


Fig. 3.1: (a) MF transformer field patterns during rated operating condition: magnetic flux density inside the core (magnetizing flux) and magnetic field in the winding window (leakage flux). For illustrative purposes only, the two windings are placed around two different limbs. However, such winding arrangement is, due to the increased HF losses, unusual for MF transformers. (b) Inductance matrix with the corresponding (lossless) linear equivalent circuits.

The magnetic equivalent circuit describes, with lumped quantities, the magnetic fluxes occurring in the transformer. Fig. 3.1(a) illustrates the different magnetic fluxes, which are defining the flux linkages of a transformer. The resulting inductance matrix, cf. Fig. 3.1(b), can be expressed with equivalent circuits, which are analyzed in detail in Appendix A.1. Typically, the following magnetic parameters are used to characterize a transformer [17, 123]:

- ▶ *Voltage transfer ratio* - The voltage transfer ratio is the ratio between the primary and secondary voltages of a transformer. For a transformer with a high magnetic coupling factor, the voltage transfer ratio is almost equal to the turns ratio and load-independent (near the nominal load).
- ▶ *Transformer magnetization* - A magnetizing current is required for generating the flux inside the core of the transformer (cf. Fig. 3.1(a)). The magnetizing current is related to the open-circuit inductances (self-inductances) of the transformer, which are measured from the primary and secondary-sides. The open-circuit inductances are important for determining the core losses and the saturation current [177]. The magnetizing current can also be used for the converter operation, typically for achieving ZVS [78, 86, 143, 202].

- *Transformer leakage* - The leakage flux is the magnetic flux which does not contribute to the magnetic coupling between the windings (cf. Fig. 3.1(a)). For a transformer with a high magnetic coupling factor, the leakage flux is related to the short-circuit inductances, which are measured from the primary and secondary-sides. The short-circuit inductances are important for determining the winding losses and the short-circuit impedance of the transformer [19]. Moreover, the leakage inductance can be used equivalent to a series inductor for the power converter operation [42, 44, 78, 86].

Therefore, the extraction of an accurate equivalent circuit is critical for the design and optimization of transformers. Inaccurate values can lead to increased losses [25, 175] or to improper converter operation [176]. The magnetic parameters of the transformer can also be used for diagnosis (production and aging) [174]. This indicates that the selection of the most suitable (concerning accuracy, modeling complexity, and computational cost) computation method for determining the equivalent circuit is a challenging and important task.

Literature identifies different methods for the computation of the equivalent circuit inductances: approximations of the air gap fringing field [17, 124, 177, 225], core reluctance computation [17, 19], analytical computation of the leakage field [17, 19, 126, 178–180], semi-analytical computation of the leakage field [16, 19], and numerical simulations of the magnetic field distribution [19, 130, 178]. A detailed review of the existing methods can be found in [126, 131, 136]. Nevertheless, deviations between the measured values and the expected values can arise from model inaccuracies, geometric tolerances, material parameter tolerances, and measurement uncertainties. However, only few comparisons between the methods can be found [131, 181], where the impact of tolerances and uncertainties is ignored.

This chapter analyzes the impact of tolerances on the magnetic equivalent circuit of MF transformers for different computation methods. Section 3.2 defines the parameters of the considered MF transformer (400 V to 400 V, 100 kHz, 20 kW). Section 3.3 discusses four different models for computing the magnetic parameters: standard analytical methods [16, 17], analytical methods with semi-empirical correction factors (e.g., Rogowski and McLyman factors) [17, 177, 180], and more elaborate semi-analytical methods (e.g., Schwarz-Christoffel mapping and mirroring method) [16, 19, 124, 226, 227]. Section 3.4 presents five numerical FEM models (2D and 3D models) with different levels of detail. Afterwards, Section 3.5 summarizes two approaches (Monte-Carlo simulations and linearized statistical models) for assessing the impact of tolerances on the equivalent circuit. Finally, Section 3.6 presents

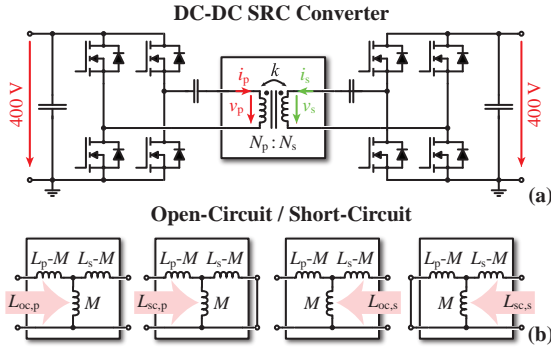


Fig. 3.2: (a) Considered SRC-DCX (400 V to 400 V, 100 kHz, 20 kW). (b) MF transformer equivalent circuit with the definitions of the open-circuit and short-circuit inductances.

simulation and measurement results for the considered MF transformer and concludes that simple analytical methods are very accurate and that linearized tolerance analyses are valid.

3.2 Considered Transformer

Fig. 3.2(a) depicts the considered SRC-DCX (400 V to 400 V, 100 kHz, 20 kW). This converter, which does not provide any voltage scaling, provides galvanic isolation for a section of a 400 V DC distribution grid (e.g., datacenters and DC microgrids) [56,194,195]. The SRC-DCX is operated at the resonance frequency with 50 % duty cycle and acts as DCX, i.e. advantageously provides voltage transformation nearly independent of the load conditions [42, 61, 82, 84, 89, 90]. It should be noted that these ratings differ from the MV DC-DC converter used for the SST demonstrator presented in Subsection 1.7.2. A LV system has been chosen for this analysis since the computation of the equivalent circuit is similar for LV and MV transformers. Moreover, LV transformers, which are more compact, are more sensitive to geometric tolerances.

Fig. 3.2(b) shows the considered MF transformer equivalent circuit and the corresponding short-circuit and open-circuit inductances. The leakage inductance of the MF transformer is part of the converter resonant tank [42,44] and the magnetizing inductance is used for achieving ZVS [163,202]. Fig. 3.3(a) shows the voltage and current waveforms applied to the MF transformer (cf. Chapter 8). Since the leakage and magnetizing inductances of the MF

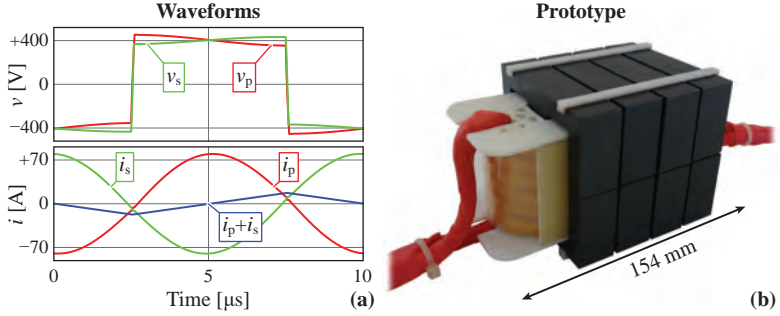


Fig. 3.3: (a) Voltage and current waveforms for operation of the SRC-DCX (cf. Fig. 3.2(a)) at the resonance frequency, ensuring a nearly load-independent voltage transfer ratio. (b) Constructed MF transformer prototype (cf. Tab. 3.1).

Tab. 3.1: MF Transformer Parameters

| Parameter | Value |
|-----------------|--|
| Power | $P = 20.0 \text{ kW} / S = 22.8 \text{ kVA}$ |
| Excitation | 400 V (DC-buses) / 57 A (RMS) / 100 kHz |
| Windings | 6 : 6 shell-type / 2500 \times 100 μm litz wire |
| Insulation | Mylar / 1kV (RMS, CM) / 1kV (RMS, DM) |
| Core | 4 \times E80/38/20 / ferrite / “TDK N87” material |
| Air gaps | 2 \times 0.7 mm (geometry) / 1.4 mm (magnetic) |
| Terminations | 2 \times 220 mm (parallel wires) |
| Volume / weight | 80 mm \times 82 mm \times 154 mm / 1.01 / 2.4 kg |
| Performance | 99.65 % @ 20 kW / 99.60 % @ 10 kW |

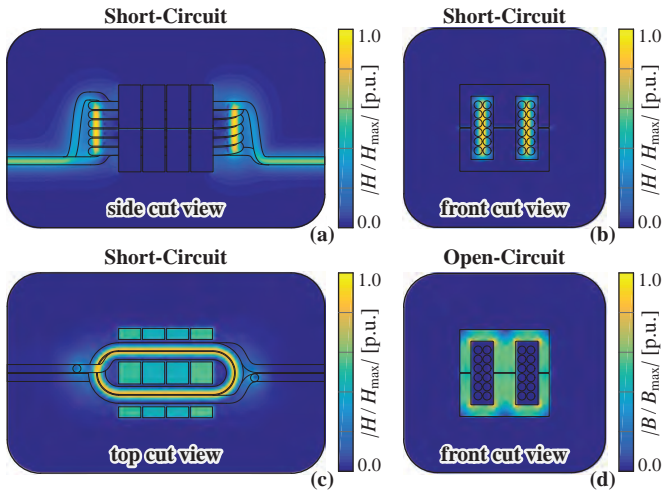


Fig. 3.4: (a) Side view, (b) front view, and (c) top view (through the air gap) of the magnetic field during short-circuit operation. (d) Front view of the magnetic flux density during open-circuit operation. All cut planes are intersecting at the MF transformer center point.

transformer are actively used for the converter operation, any mismatch between the measured and simulated values will lead to non-optimal operating conditions and/or will require an adaptation of the modulation scheme (e.g., dead times and switching frequency) [175, 176].

Fig. 3.3(b) depicts the constructed prototype and the key parameters are listed in Tab. 3.1. A large magnetizing current is required for achieving complete soft switching [163, 202]. Accordingly, two air gaps are introduced into the magnetic circuit, which, due to the associated fringing field, complicates the computation of the equivalent circuit. The air gaps also help the flux balancing between the paralleled core sets. Otherwise, this MF transformer features the most common design choices: E-shaped ferrite core, shell-type arrangement, and litz wires [25, 64, 82, 143]. However, the presented methods can also be adapted to designs employing nanocrystalline cores, core-type transformer, coaxial transformer, solid wires, foil conductors, etc.

Fig. 3.4 shows the magnetic field and magnetic flux density during short-circuit and open-circuit operations [228]. For short-circuit operation, the energy is mostly stored in the winding window and in the cable terminations. For open-circuit operation, the energy is stored in the air gaps and inside

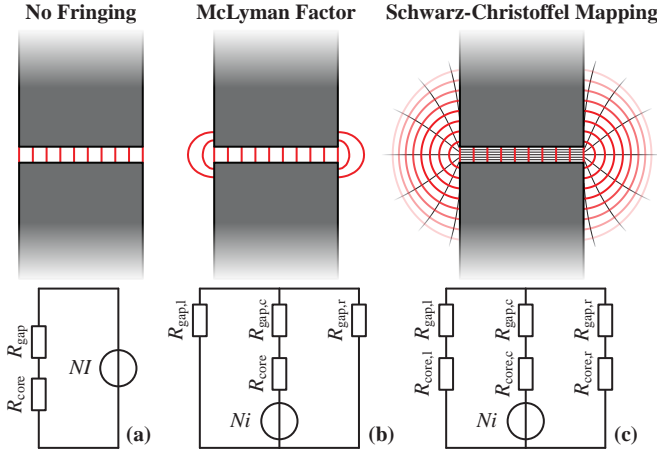


Fig. 3.5: Reluctance circuits (shown for E-shaped gapped core). (a) Single-element core model without fringing field model [17], (b) single-element core model with a semi-empirical fringing field model (McLyman factor) [177], and (c) detailed core model with a detailed fringing field model (Schwarz-Christoffel mapping) [19, 124]. The red lines indicate the distribution of the magnetic flux density (streamlines).

the core. This indicates that the considered MF transformer features a high magnetic coupling factor. In accordance, different methods can be used to extract the magnetic parameters of the transformer.

3.3 Analytical Methods

The extraction of the equivalent circuit parameters depicted in Fig. 3.1(b) is described in this section for different analytical and semi-analytical methods. Additional information about the extraction of the equivalent circuit from analytical computations is given in Appendix A.2 and Appendix A.4.

3.3.1 Open-Circuit

First, the inductance is computed for the following operation condition: $i_p = 0 \vee i_s = 0$, i.e. one of the two windings is open-circuited. This computation is similar to the computation of inductors, which implies that the presented methods can also be applied to inductors. Most of the analytical methods are based on reluctance circuits:

- ▶ The core is modeled with a single reluctance and the fringing field of the air gaps is neglected (single equivalent reluctance), cf. Fig. 3.5(a) [17].
- ▶ The core is modeled with a single reluctance and the McLyman factor (simple semi-empirical model) is used for describing the fringing field of the air gaps, cf. Fig. 3.5(b) [177].
- ▶ The core is described with a detailed reluctance model (limbs, yokes, and corners) and a 3D model of the fringing field is used (based on Schwarz-Christoffel mapping), cf. Fig. 3.5(c) [19, 124]. However, the interactions between the different air gaps and the placement of the wires are not considered.

The main hypothesis of these reluctance models is that a perfect magnetic coupling between the turns composing a winding (same flux through all the turns) is given (cf. Fig. 3.4(d)). This implies that these computation methods are limited to transformers with high magnetic coupling factors. If required, the nonlinearities of the core material (flux density and/or frequency dependences) can be considered for the reluctance computations, especially for designs with small air gaps [177].

3.3.2 Short-Circuit

In a second step, the inductance is computed for the following excitation: $+N_p i_p = -N_s i_s$. With this operating condition, most of the energy is stored in the winding window (cf. Fig. 3.4(b)) and the following computation methods can be used:

- ▶ A 1D approximation of the leakage field is computed using Ampère's circuital law, cf. Fig. 3.6(a) [16, 17]. This model is inaccurate for windings with low filling factors, for large distances between the windings and/or the core, and for modeling the leakage near the winding heads [16, 175].
- ▶ The 2D effects occurring near the winding tips, cf. Fig. 3.6(b) can be approximated with the Rogowski factor, which is a correction factor for the height of the windings [126, 180].
- ▶ The 2D field distribution can be computed with the mirroring method (method of images) where the effect of the magnetic core is replaced by current images, cf. Fig. 3.6(c) [16, 132, 229]. The equivalent inductance can be extracted from the energy stored in the field [132], or, more conveniently, directly from the inductance matrix between the

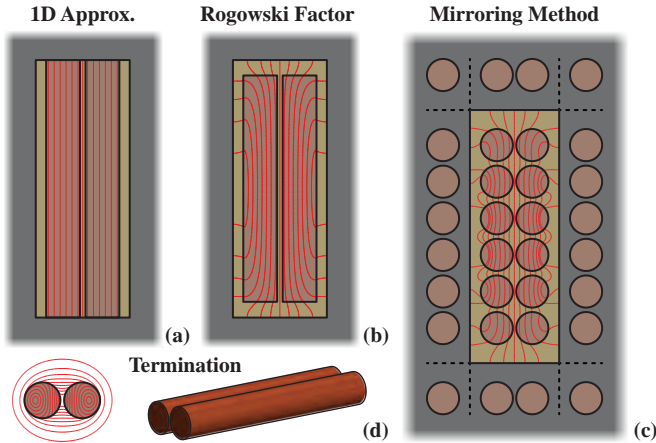


Fig. 3.6: Leakage magnetic field distribution (shown for a 6 : 6 shell-type E-core transformer). (a) 1D approximation (Ampère’s circuital law) [16, 17], (b) 2D approximation of the field near the winding tips (Rogowski factor) [126, 180], (c) 2D computation (mirroring method) [16, 229], and (d) cable termination field (Biot-Savart law). The red lines indicate the distribution of the magnetic field (streamlines).

wires [226, 227]. The boundary conditions near the winding heads and the finite core permeability can be considered [16]. However, this method is only accurate if the leakage field can be approximated in 2D (cf. Figs. 3.4(b)-(c)).

- For a transformer with a reduced leakage inductance, the energy stored inside the cable terminations cannot be neglected [230]. For calculating the corresponding inductance, the inductance of two parallel wires (Biot-Savart law) can be used, cf. Fig. 3.6(d) [231]. Nevertheless, the field distribution near the cable terminations is intrinsically a 3D problem, which cannot be perfectly modeled analytically (cf. Fig. 3.4(a)).

If required, the aforementioned methods can be extended to other transformer geometries (e.g., core-type transformer, planar transformer, three-phase windings, and interleaved windings) [17, 179]. The frequency dependence of the short-circuit inductances can be considered, especially for designs with solid wires [114, 178].

3.3.3 Circuit Extraction

The equivalent circuit can be extracted from the obtained values ($i_p = 0 \vee i_s = 0$ and $+N_p i_p = -N_s i_s$) such that the energy stored in the equivalent circuit matches with the computed cases. This procedure is explained in detail in Appendix A.2. It should be noted that the analytical methods are inaccurate for transformers with low coupling factors ($k < 0.95$), where the aforementioned hypothesis (e.g., reluctance circuit and energy distribution) are not valid anymore (cf. Appendix A.4).

3.4 FEM Simulations

In this section, different FEM simulations models, with different levels of detail, are described (cf. Fig. 3.1(b)). Additional information about the procedure used for extracting the equivalent circuit parameters from the FEM simulations is given in Appendix A.3.

3.4.1 Circuit Extraction

The equivalent circuit of a transformer can also be obtained from numerical simulations, where FEM is typically selected [64, 82, 143, 228, 232]. The exact geometry, the nonlinearities of the core material, and the frequency dependences of the current distribution (e.g., skin and proximity effects) can be represented. For extracting the equivalent circuit, which features three degrees of freedom, different simulations are required. In this work, the extraction of the equivalent circuit is done with the following numerically stable procedure. The energy inside the system is extracted for the following cases: $i_p \neq 0 \wedge i_s = 0$ (energy in the primary self-inductance, L_p), $i_p = 0 \wedge i_s \neq 0$ (energy in the secondary self-inductance, L_s), and $+N_p i_p = -N_s i_s$ (approximately, for high magnetic coupling factors, the energy in the leakage magnetic field). Then, the equivalent circuit is determined such that the stored energy matches with the simulations (cf. Appendix A.3). This method is also applicable to transformers with low magnetic coupling factors.

3.4.2 2D Modeling

Fig. 3.7(a) depicts a 2D FEM model with a simplified winding structure and Fig. 3.7(b) considers the actual placement of the wires (turn packing). For both cases, a planar and an axisymmetric model are used for modeling the core window and the winding heads, respectively (E-shaped core, shell-type

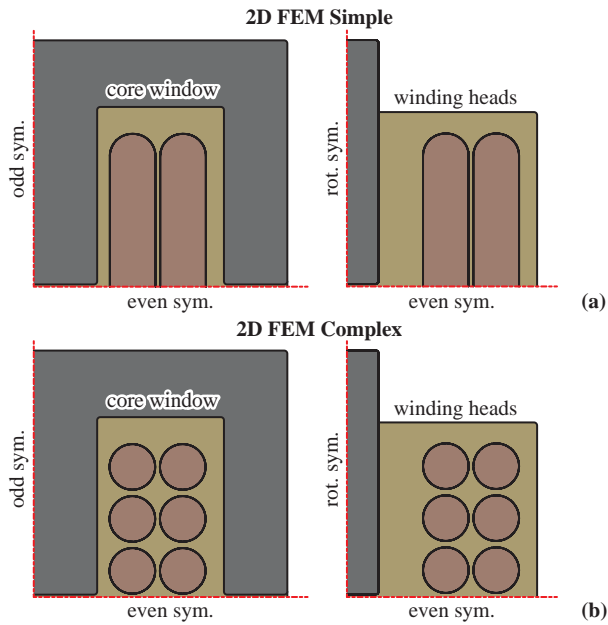


Fig. 3.7: (a) 2D FEM model with a simplified winding geometry and (b) with a detailed winding geometry. For both cases, a different model is used for the core window and the winding heads. The symmetry axes are also indicated.

arrangement). Different symmetry axes are used for reducing the size of the simulated models.

3.4.3 3D Modeling

Fig. 3.8(a) shows a simple 3D model with simplified core and winding structures (single bodies). Fig. 3.8(b) considers the exact shape of the cores (core sets) and the different wires (turn packing). These two models neglect the pitch of the windings and the cable terminations, such that different symmetry planes exist. Finally, Fig. 3.8(c) represents a full 3D model of the transformer and the cable terminations, which does not feature any symmetry plane. This last model represents, as accurately as possible, the geometry of the realized prototype.

3.5 Statistical Analysis

The aforementioned computation methods for the short-circuit ($L_{sc,p}$ and $L_{sc,s}$) and open-circuit ($L_{oc,p}$ and $L_{oc,s}$) inductances (cf. Section 3.3 and Section 3.4) are subject to uncertainties of the used geometric and material parameters. Therefore, the question arises if accurate calculations are actually necessary and/or advantageous compared to the simple models. However, the measurement of the uncertainties requires the construction of many identical transformers and, therefore, cannot be sensibly conducted during the design of a transformer. Accordingly, in the following, the tolerance analysis is conducted with computation models.

3.5.1 Considered Parameters

The different uncertain parameters are named x_i , the tolerances $\pm\delta_i$, and the nominal values $x_{i,0}$. These parameters represent the uncertainties linked with the geometric tolerances and the material parameter tolerances. For the statistical analysis, the following expressions are considered:

$$L = F_L(x_1, x_2, \dots), \quad (3.1)$$

$$L_0 = F_L(x_{1,0}, x_{2,0}, \dots), \quad (3.2)$$

where L is the computed inductance, L_0 the nominal value, and F_L the function describing the inductance computation method (cf. Section 3.3 and Section 3.4). Tab. 3.2 and Tab. 3.3 summarize the variables used to describe the uncertain input parameters and the obtained inductances, respectively.

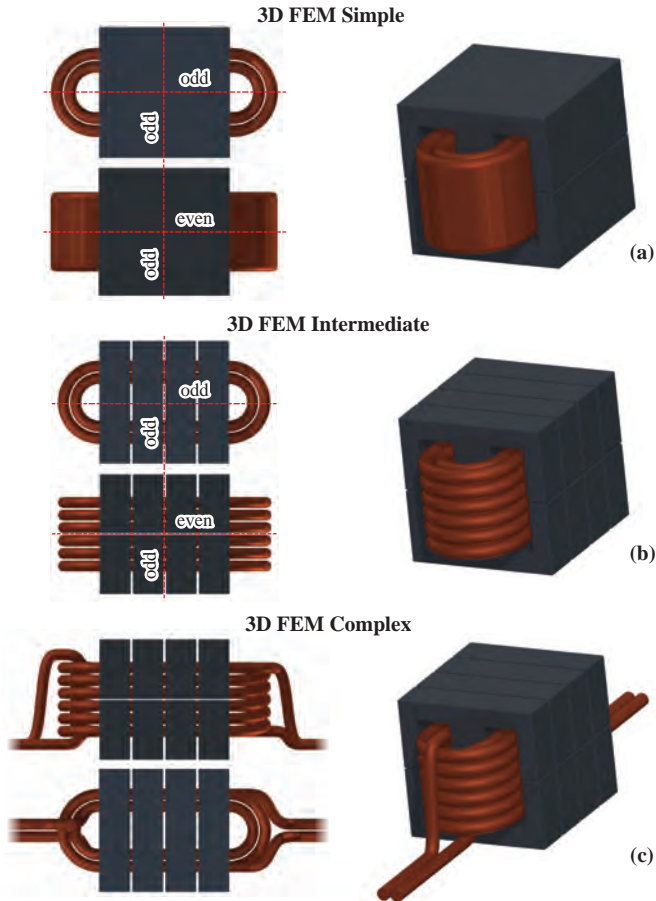


Fig. 3.8: (a) 3D FEM model with a simplified winding and core geometry, (b) with a more detailed winding and core geometry, and (c) with the actual transformer geometry (with the cable terminations). The considered symmetry planes are also indicated.

Tab. 3.2: Uncertain Parameters / Input Variables

| Variable | Description |
|---|---|
| Uncertain parameter (input variable) | |
| n_x | Number of uncertain parameters |
| x_i | Uncertain value of the parameter |
| $x_{i,0}$ | Nominal value of the parameter |
| $\pm\delta_i$ | Tolerance around $x_{i,0}$ |
| Worst-case analysis | |
| $f_{i,wc}$ | Probability density function (uniform distribution) |
| $MC_{i,wc}$ | Monte-Carlo samples |
| Normal distribution analysis | |
| $f_{i,nd}$ | Probability density function (normal distribution) |
| $\sigma_{i,nd}$ | Standard deviation of $f_{i,nd}$ |
| $p_{i,nd}$ | Confidence interval for $\sigma_{i,nd}$ |
| $MC_{i,nd}$ | Monte-Carlo samples |

In the following, a simple exemplary function F_L is considered for explaining the tolerance stacking analysis. Afterwards, in Section 3.6, the defined analysis framework is used for analyzing the tolerances for the open-circuit and short-circuit inductances of the considered transformer (cf. Section 3.2), using the aforementioned computation methods (cf. Section 3.3 and Section 3.4).

3.5.2 Worst-Case Analysis

For a worst-case analysis, the variables x_i are assumed to be uniformly distributed in the tolerance intervals and independent of each other. The probability density distribution function, $f_{i,wc}$, can be set to

$$f_{i,wc}(x_i) = f_{\text{uniform}}(x_i, x_{i,0} - \delta_i, x_{i,0} + \delta_i), \quad (3.3)$$

where f_{uniform} describes the probability density distribution function of the continuous uniform distribution. With the help of F_L (cf. (3.1)), the probability distribution of L can be computed and the extrema can be extracted, cf. Fig. 3.9(a).

For the magnetic equivalent circuit, many variables are present, F_L is nonlinear, and F_L , for some computation methods (e.g., FEM simulations),

Tab. 3.3: Uncertain Parameters / Output Variables

| Variable | Description |
|--|---|
| Computed inductance (output variable) | |
| L | Uncertain value of the inductance |
| L_0 | Nominal value of the inductance |
| F_L | Function describing the computation method |
| C_L | Computational cost of F_L |
| Worst-case analysis | |
| $\pm\delta_{L,wc}$ | Tolerance around L_0 (linearized analysis) |
| $MC_{L,wc}$ | Monte-Carlo samples |
| $\{L\}_{lin,wc}$ | Tolerance interval (linearized analysis) |
| $\{L\}_{MC,wc}$ | Tolerance interval (Monte-Carlo simulations) |
| Normal distribution analysis | |
| $f_{L,nd}$ | Probability density function (linearized analysis) |
| $\sigma_{L,nd}$ | Standard deviation of $f_{L,nd}$ (linearized analysis) |
| $p_{L,nd}$ | Confidence interval for $\sigma_{L,nd}$ (linearized analysis) |
| $\pm\delta_{L,nd}$ | Tolerance around L_0 (linearized analysis) |
| $MC_{i,nd}$ | Monte-Carlo samples |
| $\{L\}_{lin,nd}$ | Tolerance interval (linearized analysis) |
| $\{L\}_{MC,nd}$ | Tolerance interval (Monte-Carlo simulations) |

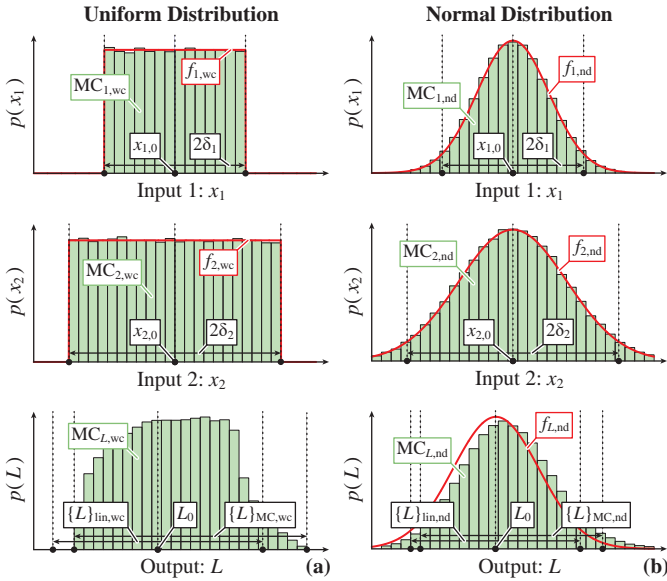


Fig. 3.9: (a) Worst-case analysis with uniform distributions. (b) Statistical analysis with normal distributions. Monte-Carlo simulations and linearized computations are compared. The following exemplary parameters are used: $n_x = 2$, $x_1 \pm \delta_1 = 0 \pm 1.0$, $x_2 \pm \delta_2 = 0 \pm 1.5$, $F_L = x_1 + ((x_2/2) - 0.2)^2$. The confidence intervals ($p_{i,nd}$ and $p_{L,nd}$) are set to 95%. The number of Monte-Carlo samples is 10^4 .

cannot be expressed analytically. For these reasons, the probability density distribution function is obtained by means of Monte-Carlo simulations [233]. In the course of the Monte-Carlo simulations, a large number of random parameter combinations is generated with respect to the input probability distributions (cf. (3.3)) and the corresponding inductance values are computed. Then, it is straightforward to extract the interval, $\{L\}_{\text{MC,wc}}$, where the inductance value is fluctuating.

However, Monte-Carlo simulations require the computation of many designs (hundreds or thousands). Alternatively, the function F_L can be linearized near the nominal values of the different parameters, which leads to [234]

$$\delta_{L,\text{wc}} = \sum_{i=1}^n \left| \frac{\partial F_L}{\partial x_i} \Big|_{x_{i,0}} \delta_i \right| \quad (3.4)$$

$$\{L\}_{\text{lin,wc}} = [L_0 - \delta_{L,\text{wc}}, L_0 + \delta_{L,\text{wc}}], \quad (3.5)$$

where $\delta_{L,\text{wc}}$ is the obtained tolerance and $\{L\}_{\text{lin,wc}}$ the corresponding interval. Beside the reduced computational cost, the linearization allows the analysis of the sensitivity of the inductance value with respect to the different parameters. If the linearization is valid, the ranges $\{L\}_{\text{MC,wc}}$ and $\{L\}_{\text{lin,wc}}$ should match together. In Fig. 3.9(a), some differences can be observed due to the strong nonlinearities of the considered exemplary function F_L .

3.5.3 Normal Distribution Analysis

The aforementioned worst-case analysis is often too conservative. For this reason, normal (Gaussian) distributions are often used for tolerance stacking analysis [234]. The probability density distribution function, $f_{i,\text{nd}}$, and the standard deviation, $\sigma_{i,\text{nd}}$, can be set to

$$f_{i,\text{nd}}(x_i) = f_{\text{normal}}(x_i, x_{i,0}, \sigma_{i,\text{nd}}), \quad (3.6)$$

$$\sigma_{i,\text{nd}} = \frac{\delta_i}{\sqrt{2} \text{erf}^{-1}(p_{i,\text{nd}})}, \quad (3.7)$$

where f_{normal} is the probability density distribution function of the normal distribution and erf^{-1} the inverse Gauss error function [235]. The confidence intervals, $p_{i,\text{nd}}$, are describing the percentage of the data lying within the accepted tolerances $\pm\delta_i$. With these definitions, the probability distribution of L can be computed, cf. Fig. 3.9(b).

Again, the probability density distribution function can be obtained by means of Monte-Carlo simulations, where the nonlinearities of F_L are considered [233]. The interval, where $p_{L,\text{nd}}$ percent of the values are located

(confidence interval), is depicted as $\{L\}_{MC,nd}$. Alternatively, a linearization of F_L can be conducted. A linear combination of normal distributions results in a normal distribution. The property is used and leads to

$$f_{L,nd}(L) = f_{\text{normal}}(L, L_0, \sigma_{L,nd}), \quad (3.8)$$

$$\sigma_{L,nd} = \sqrt{\sum_{i=1}^n \left(\left. \frac{\partial F_L}{\partial x_i} \right|_{x_{i,0}} \sigma_{i,nd} \right)^2}, \quad (3.9)$$

where $f_{L,nd}(L)$ is the probability density distribution function and $\sigma_{L,nd}$ the standard deviation. With the confidence interval, $p_{L,nd}$, the tolerance of the inductance value can be expressed as

$$\delta_{L,nd} = \sigma_{L,nd} \sqrt{2} \text{erf}^{-1}(p_{L,nd}), \quad (3.10)$$

$$\{L\}_{lin,nd} = [L_0 - \delta_{L,nd}, L_0 + \delta_{L,nd}], \quad (3.11)$$

where $\delta_{L,nd}$ is the obtained tolerance and $\{L\}_{lin,nd}$ the corresponding interval. In Fig. 3.9(b), the mismatch between the probability density distribution function obtained with Monte-Carlo simulations and $f_{L,nd}(L)$ results from the nonlinearities of the chosen exemplary function F_L .

3.6 Results

The MF transformer depicted in Section 3.2 is considered. First, the magnetic parameters of the MF transformer are measured. In a second step, the aforementioned computation methods (cf. Section 3.3 and Section 3.4) and tolerance stacking analyses (cf. Section 3.5) are applied. Finally, the measurement and computation results are compared.

3.6.1 Measurements

The open-circuit ($L_{oc,p}$ and $L_{oc,s}$) and short-circuit ($L_{sc,p}$ and $L_{sc,s}$) inductances (cf. Fig. 3.2(b)) are extracted from small-signal impedance measurements [238]. Figs. 3.10(a)-(b) depict the measured impedances, where the resonance frequencies of the MF transformer can be seen. Figs. 3.10(c)-(d) show the extracted nominal inductances with the corresponding measurement uncertainties. The inductances are extracted with a resistive-inductive series equivalent circuit.

These measurements are obtained with an “Agilent 4924A” precision impedance analyzer [236]. The uncertainties are composed of the measurement device tolerances and an absolute error. The absolute error, which is

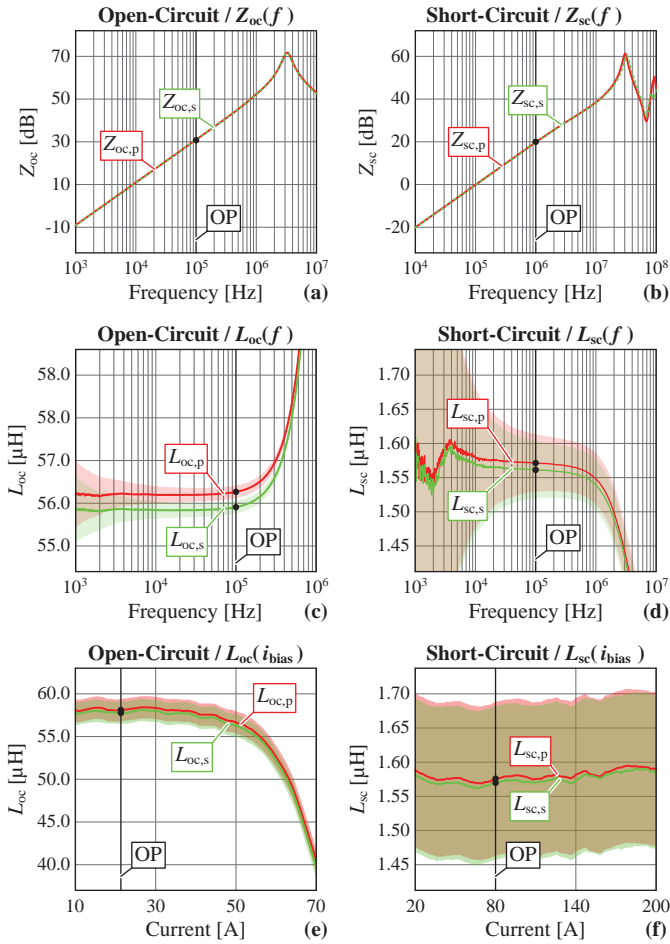


Fig. 3.10: (a) Measured open-circuit and (b) short-circuit impedances for the prototype shown in Fig. 3.3(b) [236]. (c) Open-circuit and (d) short-circuit inductances for different frequencies [236]. (e) Open-circuit and (f) short-circuit small-signal differential inductances for different bias currents [237]. The primary and secondary windings are the outer and inner windings (with respect to the central limb), respectively. The measurement uncertainties (shaded area) and the operating points (“OP”, cf. Fig. 3.3(a)) are indicated.

estimated from measurements, is set to 20 nH for short-circuit measurements (interconnection inductances) and to 100 nH for open-circuit measurements (interconnection inductances and slight variation of the length of the air gaps in case the core halves are pressed together). These measurements have been successfully reproduced (less than 1% deviation) with an “Omicron Bode 100” network analyzer [239, 240].

Figs. 3.10(c)-(d) indicate that the frequency dependence of the inductances is negligible due to the used ferrite cores and litz wires [17, 178]. The slight increase of the open-circuit inductances near 1 MHz is due to the capacitive currents (resonance frequency of 3.2 MHz) [143]. The slight decrease of the short-circuit inductances near 10 MHz is explained by HF effects (induced currents in the windings and permeability change of the core) [135, 178]. However, near the operating frequency (100 kHz), the impact of these HF effects is negligible (constant open-circuit and short-circuit inductances below 1 MHz). Due to the high magnetic coupling factor of the MF transformer ($k = 0.986$), the inductances measured from the primary and secondary-sides are very similar ($N_p = N_s$).

However, the MF transformer is not operated with small-signal excitations. For this reason, the MF transformer has also been measured with an “ed-k DPG10/1000A” power choke tester [237]. This device applies a current ramp to the MF transformer and measures the induced voltage. This enables the extraction of the small-signal differential inductance ($L = \partial\Psi/\partial i$) for different bias currents, cf. Figs. 3.10(e)-(f). The uncertainties are composed of the measurement device tolerances and an absolute error. The absolute error is set to 50 nH and 120 nH, respectively, for short-circuit (interconnection inductances) and open-circuit measurements (interconnection inductances and variation of the length of the air gaps). Figs. 3.10(e)-(f) shows that the open-circuit inductances are also linear below 40 A (magnetizing current), which means that the MF transformer is operated well below the saturation (cf. Fig. 3.3(a)). As expected, the short-circuit inductances are independent of the current.

For these reasons, the small-signal inductances ($i_{\text{bias}} = 0$ A) at the switching frequency ($f = 100$ kHz) are extracted for the comparison with the computations. Moreover, only the averages of the primary ($L_{\text{oc,p}}$ and $L_{\text{sc,p}}$) and secondary-side inductances ($L_{\text{oc,p}}$ and $L_{\text{sc,p}}$) are further considered (called L_{oc} and L_{sc} , cf. Fig. 3.2(b)). The obtained nominal values (L_{meas}) and measurement uncertainties ($\{L\}_{\text{meas}}$) are used for comparing the measurement results with the values obtained with the different computation methods.

Tab. 3.4: Computation Methods

| Name | Model | C_L | n_x |
|-----------------------|--------------------------------|------------|-------|
| Analytic simple | Figs. 3.5(a) / 3.6(a) | 50 FLOPs | 12 |
| Analytic intermediate | Figs. 3.5(b) / 3.6(b) | 150 FLOPs | 14 |
| Analytic complex | Figs. 3.5(c) / 3.6(c) | 200 kFLOPs | 16 |
| Analytic termination | Figs. 3.5(c) / 3.6(c) / 3.6(d) | 200 kFLOPs | 20 |
| 2D FEM simple | Figs. 3.7(a) / 3.6(d) | 8 kDOFs | 19 |
| 2D FEM complex | Figs. 3.7(b) / 3.6(d) | 12 kDOFs | 20 |
| 3D FEM simple | Figs. 3.8(a) / 3.6(d) | 0.9 MDOFs | 17 |
| 3D FEM intermediate | Figs. 3.8(b) / 3.6(d) | 1.4 MDOFs | 17 |
| 3D FEM complex | Fig. 3.8(c) | 7.2 MDOFs | 16 |

3.6.2 Computations

The computation methods described in Section 3.3 and Section 3.4 are combined, as shown in Tab. 3.4, for extracting the equivalent circuit of the MF transformer. For the analytical models, the computational cost, C_L , is measured in FLOPs [222]. For FEM models, the computational cost, C_L , is expressed with the number of DOFs [228, 232], given that three operating points are solved for extracting the equivalent circuit (cf. Section 3.4).

For the statistical analysis, the methods described in Section 3.5 are used. The confidence intervals for the parameters ($p_{i,\text{nd}}$) and for the inductances ($p_{L,\text{nd}}$) are set to 95%. The number of uncertain parameters, n_x , is indicated in Tab. 3.4. Concerning the classification of the uncertain parameters, the following remarks are important:

- ▶ The geometric and material tolerances are mostly extracted from the datasheets (e.g., core, coil former, and litz wire). The uncertainties linked to the construction of the MF transformer (e.g., air gaps and insulation distances) are estimated. The main tolerances are the air gaps length ($0.7 \text{ mm} \pm 0.05 \text{ mm}$), the distance between the two windings ($0.75 \text{ mm} \pm 0.3 \text{ mm}$), the wire diameter ($7.2 \text{ mm} \pm 0.2 \text{ mm}$), the core permeability (2200 ± 500), and the core cross section ($1600 \text{ mm}^2 \pm 40 \text{ mm}^2$).
- ▶ Some geometric parameter uncertainties are also linked to the geometric approximations included in the modeling. The fact that a 3D geometry is modeled in 1D/2D (e.g., winding heads and cable terminations)

introduces additional uncertainties since some geometric parameters in the 1D/2D models do not exist in the 3D models.

- ▶ The simplifications used in the different computation methods (e.g., 1D/2D modeling, no fringing field model, and no cable terminations model) are intrinsic inaccuracies of the methods and, therefore, are not considered as uncertainties.

The computational cost of the FEM models is too high for Monte-Carlo simulations. On the other hand, the simple analytical models (“Analytic simple”, “Analytic intermediate”, and “Analytic complex”) neglect many parameters (e.g., placement of the wires and cable terminations). Therefore, the full statistical analysis is performed with the model “Analytic termination”, where 2×10^3 Monte-Carlo samples are considered.

Fig. 3.11 shows the obtained tolerances for the inductances, which are significant. It appears that the linearized statistical analysis is valid (compared to Monte-Carlo simulations). The linearized analysis allows the extraction of the sensitivities concerning the different parameters (cf. (3.4)), which is shown in Fig. 3.12. The main uncertainties are originating from the air gaps length, the size of the core, the permeability of the core, the insulation distances, and the simplification of the 3D geometry (depicted as “model approx.”).

Therefore, the linearized statistical analysis is applied to all the computation methods described in Tab. 3.4. This greatly reduces the computational cost since only $2n_x + 1$ equivalent circuit computations are required. The obtained values (L_0 , $\{L\}_{\text{lin,wc}}$, and $\{L\}_{\text{lin,nd}}$) are used for comparing the computations and the measurements.

3.6.3 Comparison: Measurements and Computations

Fig. 3.13 and Fig. 3.14 show the comparison between measurements and computations (cf. Tab. 3.4) for the open-circuit and short-circuit inductances, respectively. The most accurate measurements, i.e. the values obtained with the Agilent 4294A precision impedance analyzer (cf. Figs. 3.10(c)-(d)), are selected as reference values for the extraction of the relative errors. The deviations between the nominal values and the reference value are smaller than 14 % for all the methods.

For the open-circuit inductance, the method “Analytic simple” underestimates the inductance, which is due to the neglected fringing field of the air gaps. For all the other methods, the tolerances ($\{L\}_{\text{lin,wc}}$ and $\{L\}_{\text{lin,nd}}$) match with the measurement uncertainties. The methods based on Schwarz-

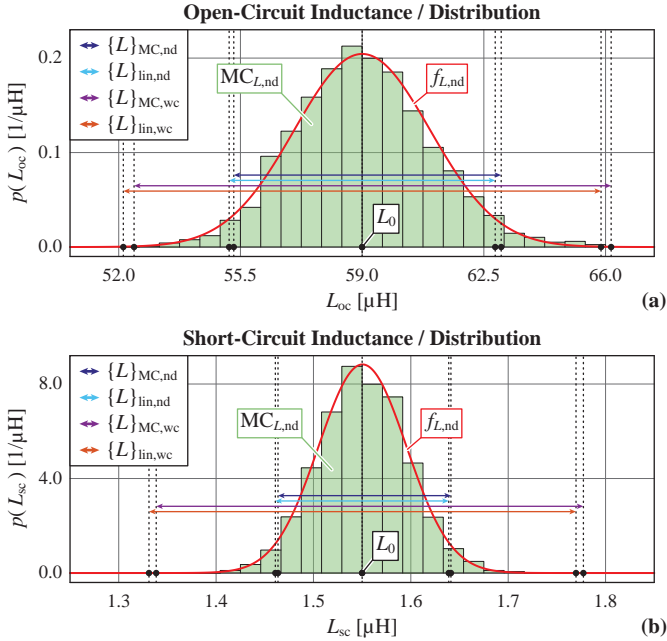


Fig. 3.11: (a) Tolerance analysis for the open-circuit and (b) short-circuit inductances. Worst-case and normal distribution analyses are performed by means of Monte-Carlo simulations and linearization (cf. Section 3.5). The model “Analytic termination” is considered with 2×10^3 Monte-Carlo samples (cf. Tab. 3.4). The confidence intervals ($p_{i,nd}$ and $p_{L,nd}$) are set to 95 %.

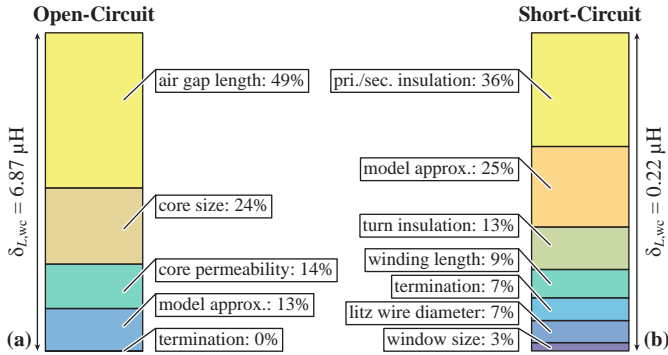


Fig. 3.12: (a) Sensitivity analysis for the open-circuit and (b) short-circuit inductances. The model “Analytic termination” is considered (cf. Tab. 3.4) and a linearized worst-case analysis is applied (cf. (3.4)).

Christoffel mapping (“Analytic complex” and “Analytic termination”) are in good agreement with the “3D FEM complex” method (1% error).

For the short-circuit inductance, the methods which neglect the cable terminations (“Analytic simple”, “Analytic intermediate”, and “Analytic complex”) underestimate the inductance. For all the other methods, the tolerances ($\{L\}_{\text{lin,wc}}$ and $\{L\}_{\text{lin,nd}}$) match with the measurement uncertainties. The method “Analytic termination” is also in good agreement with the “3D FEM complex” method (5% error).

Therefore, it can be concluded that the complex computation methods (2D and 3D FEM models) only feature limited advantages over the analytical methods. The main advantage of the 3D FEM methods is a slight reduction of the tolerances since the tolerances linked with the model approximations vanish (“model approx.”, cf. Fig. 3.12). The method “Analytic termination” represents an interesting trade-off between modeling complexity, computational cost, and accuracy.

It also appears that the measurement uncertainties are smaller than the computation tolerances. Furthermore, the deviation between the nominal value of the computation methods is smaller than the tolerances. This implies that the extraction of MF transformer equivalent circuit parameters can only be marginally improved with new computation and measurement methods. Only a reduction of the uncertainties on the geometry and material parameters will lead to better matching between measurements and computations.

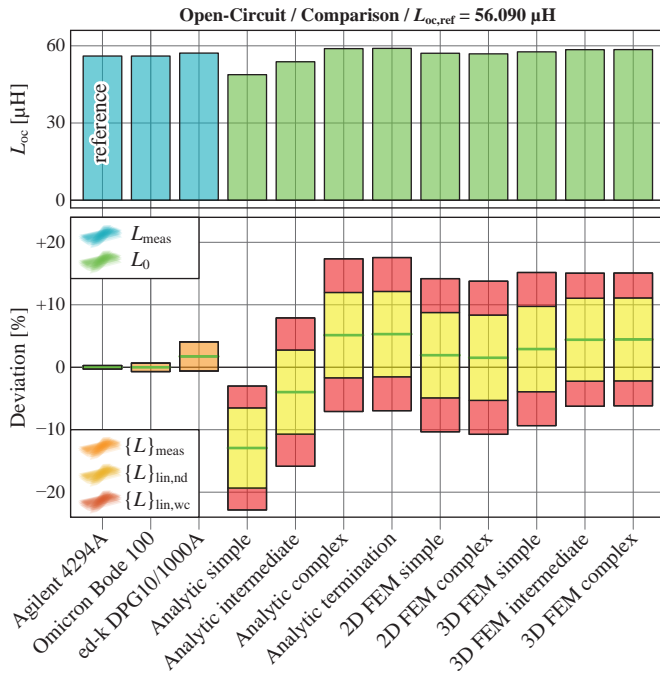


Fig. 3.13: Comparison between measurements (cf. Subsection 3.6.1) and computations (cf. Subsection 3.6.2) for the open-circuit inductance (L_{oc}). The reference value is the measurement obtained with an Agilent 4294A precision impedance analyzer [236].

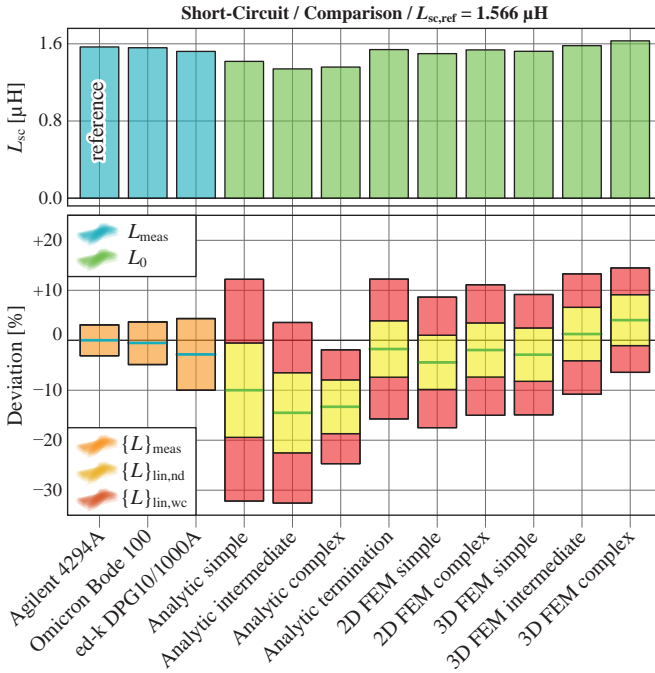


Fig. 3.14: Comparison between measurements (cf. Subsection 3.6.1) and computations (cf. Subsection 3.6.2) for the short-circuit inductance (L_{sc}). The reference value is the measurement obtained with an Agilent 4294A precision impedance analyzer [236].

3.7 Summary

This chapter first investigates various computation methods for extracting the magnetic equivalent circuit of MF transformers, which is a critical parameter for the modeling and optimization of power electronic converters. Analytical models are presented for the magnetizing (reluctance circuit, Rogowski factor, and Schwarz-Christoffel mapping) and leakage (1D Ampère's circuital law, Rogowski factor, 2D mirroring method, and cable termination model) inductances. The advantages and limitations of the analytical methods are discussed and compared to numerical simulations (2D and 3D FEM).

In a next step, the uncertainties linked to model inaccuracies, geometric tolerances, and material tolerances are analyzed in detail with a statistical analysis applied to the computation models. Computationally intensive Monte-Carlo simulations and simple linearized statistical models, which allow the analysis of the sensitivities for the different parameters, are considered.

The presented methods are finally applied for calculating the short-circuit and open-circuit inductances of a MF transformer prototype (400 V to 400 V, 100 kHz, 20 kW). It is concluded that a linearized statistical analysis is sufficient, which greatly simplifies the tolerance analysis. The deviations between the measurements and the different computation methods (below 14 %) can be explained with the computed tolerances. For the open-circuit and short-circuit inductances, the measurement uncertainties (between $\pm 0.3\%$ and $\pm 2.7\%$) are smaller than the computation tolerances (between $\pm 5\%$ and $\pm 22\%$).

The comparison between the different computation methods shows that the combination of a reluctance circuit, Schwarz-Christoffel mapping, mirroring method, and a cable termination model is a good trade-off between computational cost and obtained accuracy. Moreover, only marginal improvements are achieved with complex numerical field simulation methods. Finally, it is concluded that the consideration of the uncertainties is required for improving the modeling of MF transformers. Moreover, the obtained uncertainties are also useful for production diagnosis and for selecting the right margin of safety during the design process.

4

Litz Wire Losses

Chapter Abstract

HF litz wires are extensively used for the windings of MF magnetic components in order to reduce the impact of eddy current losses that originate from skin and proximity effects. Literature documents different methods to calculate eddy current losses in HF litz wires, however, most of the computation methods rely on a perfect twisting of the strands, which is often not present in practice. This chapter analyzes the implications of imperfect twisting on the current distribution among the different strands of HF litz wires and the corresponding losses by means of a fast 2.5D PEEC method. The effects of different types of twisting imperfections are examined. It is found that imperfect twisting can lead to increased losses (more than 100 %). However, perfect twisting of the strands, which is difficult to achieve, is often not required, i.e. suboptimal twisting is sufficient. Analytical expressions are also given for distinguishing between critical and uncritical imperfections. The experimental results, conducted with a MV/MF transformer prototype (7.5 kHz, 65 kW), reveal a reduction of the error on the predicted losses from 52 % (ideal HF litz wire model) to 8 % (proposed model) and, thus, confirm the accuracy improvement achieved with the proposed approach.

4.1 Introduction

The computation of winding losses represents an essential part of the modeling process of inductors and transformers. Power electronic converters are usually operating at MF and, therefore, the impacts of eddy current losses cannot be neglected anymore. Usually, eddy current losses are split up into losses due to skin and proximity effects: the skin effect describes the eddy currents due to the magnetic field created by the current in the conductor itself and the proximity effect characterizes eddy currents that originate from an external

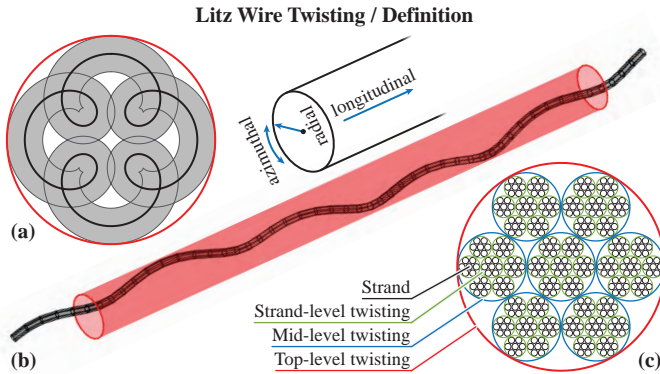


Fig. 4.1: (a) Projection and (b) 3D view of the twisting scheme (azimuthal and radial) of a single strand. The depicted path depends on the structure of the bundle, the pitch lengths of the bundles, and the used twisting scheme. (c) Packing structure of a HF litz wire with bundles and sub-bundles.

magnetic field. In order to obtain efficient MF inductors and transformers, the impacts of losses due to skin and proximity effects need to be mitigated. This is usually achieved with foil conductors or HF stranded conductors (e.g., Roebel bars or HF litz wires). In this regard, HF litz wires are very popular since they allow for low losses and great flexibility in the design of the magnetic component in a wide frequency range [25, 64, 82, 143, 182].

HF litz wires are composed of multiple insulated strands, as shown in Fig. 4.1. Each single strand is subject to skin and proximity effects and thus, the single strand diameter is selected with regard to acceptable losses [133]. The strands are twisted together in both radial and azimuthal directions:

- ▶ *Radial* - The permutation in radial direction prevents eddy currents in case of an azimuthal magnetic field. An azimuthal field is created by the currents that are present in the considered HF litz wire itself.
- ▶ *Azimuthal* - The permutation in azimuthal direction suppress the oriented area spanned between the strands with respect to a homogeneous external field. The cancellation of the magnetic flux between the strands, prevents the formation of circulating eddy currents.
- ▶ *Pitch* - In addition to the number of strands and the diameter of a single strand, the pitch (or length of lay), which is the spatial period length

of the twisting (in longitudinal direction), denotes a third important parameter of a HF litz wire.

For HF litz wires with a high number of strands, simultaneous azimuthal and radial twisting is difficult to achieve. Such HF litz wires are often constructed in a recursive manner, i.e. the total HF litz wire is composed of twisted bundles of HF litz wires and each bundle itself can again be composed of twisted bundles or single strands. In this work, the first twisting level (twisting of the strands) and the last level (forming the complete HF litz wire) are called strand-level and top-level twisting, respectively. Additional twisting levels between the top-level and the strand-level are denoted as mid-levels, cf. Fig. 4.1(c).

With high numbers of strands and complex twisting schemes, the accurate computation of losses in such stranded conductors is a challenging task. Over the years, different calculation methods have been proposed for the calculation of the losses, which rely on analytical and/or numerical calculations [19, 133, 134, 183–185]. However, it is found that the measured losses are often larger than the values computed with the aforementioned methods [25, 82, 186]. Different effects can explain such deviations:

- ▶ The (external) magnetic field is inaccurately computed [189, 241]. Moreover, certain computational methods presuppose the external magnetic field to be homogeneous across the cross section of the HF litz wire [19].
- ▶ The terminations of the HF litz wire are generating losses. Moreover, terminations can add an impedance mismatch between the strands which leads to undesired circulating currents [25, 186, 241, 242].
- ▶ Due to twisting, the length of the strands is greater than the length of the HF litz wire [243]. For typical HF litz wire, however, this effect is often negligible (less than 10 %).
- ▶ The packing (hexagonal, square, etc.) of the strands is not homogeneous and/or not perfectly modeled [134, 184]. The exact packing in a HF litz wire, which is often not clearly defined, has only a limited impact on the losses (less than 10 %).
- ▶ A non-integer number of pitches is used, leading to circulating currents inside the HF litz wire [183, 244]. Alternatively, local variations (along distances that are similar to the pitch length) of the external magnetic field also create additional losses [186]. Such local variations are typically produced by the fringing fields of air gaps.

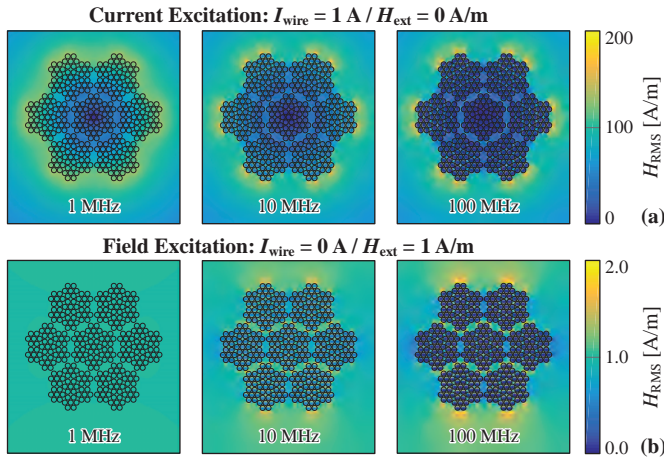


Fig. 4.2: (a) LF and HF magnetic field patterns for current and (b) external field excitation. A $343 \times 100 \mu\text{m}$ HF litz wire is considered (2.5 mm outer diameter).

- An imperfect twisting scheme is used, leading to an inhomogeneous current distribution in the strands. This includes improper azimuthal and/or radial twisting (at the top-level, strand-level, or mid-level), poor choices of the ratios of the pitch lengths between twisting levels, etc.

The last two effects can lead to significant additional losses and commonly occur in practice. In particular, commercially available HF litz wires are frequently found to be subject to imperfect twisting [25, 27, 186, 245]. Therefore, this chapter analyzes the impact of the twisting scheme on the losses, which, to the knowledge of the author, has not been studied in detail in the literature. Section 4.2 summarizes loss computation methods for perfectly twisted HF litz wires. Section 4.3 analyzes the implications of twisting imperfections on the losses. Finally, Section 4.4, compares calculated results to experimental results, using a MF transformer that employs HF litz wires with imperfect twisting.

4.2 Perfect Twisting

A perfectly twisted (radial and azimuthal directions) HF litz wire with an infinitesimally small pitch length is considered (ideal HF litz wire). The HF litz wire conducts the current I_{wire} and is subject to a homogeneous external

magnetic field, H_{ext} . Fig. 4.2 depicts the magnetic field determined with FEM simulations for a $343 \times 100 \mu\text{m}$ HF litz wire at different frequencies [228]. At 1 MHz, the eddy currents generate losses but have a limited impact on the magnetic field distribution. For $f \gg 1$ MHz the skin depth is less than the strand diameter of a single strand and the eddy currents alter the magnetic field distribution, leading to a shielding effect inside the strands. The corresponding losses, P , are expressed as [18,19]

$$P(f) = R_{\text{DC}} \left(K_I(f) I_{\text{wire}}^2 + K_H(f) H_{\text{ext}}^2 \right), \quad (4.1)$$

where K_I and K_H are frequency-dependent parameters and R_{DC} denotes the DC resistance. The RMS values of the current and the external magnetic field are considered. The losses can be split up into four categories:

- ▶ *DC losses* - These losses are included in R_{DC} and represent the conduction losses which are not linked to eddy currents.
- ▶ *Skin effect* - These losses are included in K_I and represent the eddy current losses in a strand that originate from the field created by the current in the same strand.
- ▶ *Internal proximity effect* - These losses are included in K_I and represent the eddy current losses in a strand that originate from the field created by the currents in the other strands.
- ▶ *External proximity effect* - These losses are included in K_H and represent the eddy current losses in a strand by reason of an externally applied homogeneous magnetic field.

In (4.1), the factors K_I and K_H represent the current and external field dependent losses, respectively. It should be noted that a different definition of (4.1), separating the skin effect and the proximity effects (internal and external) is also common in literature [18, 19, 25, 133, 185].

The parameters R_{DC} , K_I , and K_H are figures of merit for the HF litz wire itself. In a magnetic component (e.g., inductor and transformer), the relevant part of the external magnetic field, H_{ext} , depends on the conductor current, I_{wire} , and the geometrical properties of the component (e.g., selected core, air gap length, and number of turns). This allows the definition of the equivalent AC resistance, which is a figure of merit for the complete winding of a defined magnetic component and not only for the HF litz wire. With (4.1), the equivalent AC resistance can be calculated according to

$$P = R_{\text{AC}}(f) I_{\text{wire}}^2, \quad \text{with } H_{\text{ext}} \sim I_{\text{wire}}. \quad (4.2)$$

Different methods exist for the computation of the losses, which are based on different assumptions, HF accuracies, and computational costs. The most common methods are listed below:

- ▶ *Asymptotic approximation* (“*Asymp.*”) - The losses by reason of skin effect are neglected (the skin depth is assumed to be larger than the diameter of the strands) and the losses due to proximity effects (internal and external) are modeled with a LF asymptotic approximation. The packing pattern is only modeled with the filling factor [25, 133, 185].
- ▶ *Bessel functions* (“*Bessel fct.*”) - The losses due to skin and proximity effects are modeled with Bessel functions. HF effects are considered for every strand but the shielding effect of the eddy currents on the magnetic field (cf. Fig. 4.2) is not completely modeled. The packing pattern is only modeled with the filling factor [19, 25, 78].
- ▶ *Biot-Savart discrete modeling* (“*Biot-Savart*”) - The losses by reason of skin and proximity effects are modeled with the aforementioned Bessel functions. The exact packing pattern is modeled and the magnetic field is computed with a Biot-Savart summation (frequency-independent field pattern) [182].
- ▶ *FEM homogenization* (“*FEM hom.*”) - The packing pattern of the HF litz wire is assumed to be periodic. A unit cell of the pattern is solved with FEM simulations and virtual material parameters (conductivity and permeability) are extracted for the packing pattern [228, 232]. Subsequently, the virtual conductor parameters are used to compute the losses. All HF effects are modeled. The limitations of this approach are the presupposed periodicity of the packing pattern and inaccuracies at the boundary of the HF litz wire [134, 184].
- ▶ *FEM discrete modeling* (“*FEM disc.*”) - All strands are modeled with FEM [228, 232]. The obtained solution contains all HF effects and considers the exact packing pattern [228, 241, 242]. The perfect twisting of the HF litz wire is taken into account by imposing an equal current sharing between the strands. Alternatively, the PEEC method can be used [241, 242, 246].

Fig. 4.3 depicts a comparison between the methods for a $343 \times 100 \mu\text{m}$ HF litz wire (cf. Fig. 4.2). The corner frequency $f_{c,\text{HF}}$ characterizes the maximum frequency up to which the LF asymptote of the proximity effect losses is

considered to be valid and can be expressed as

$$\delta(f) = \frac{1}{\sqrt{\pi\sigma\mu_0 f}}, \quad (4.3)$$

$$f_{c,\text{HF}}(d_s) \approx \frac{32^{\frac{2}{3}}}{\pi\sigma\mu_0 d_s^2}, \quad (4.4)$$

$$\delta(f_{c,\text{HF}}) \approx \frac{d_s}{32^{\frac{1}{3}}}, \quad (4.5)$$

where δ is the skin depth, σ the conductivity, and d_s the diameter of the strands. For $f < f_{c,\text{HF}}$, it can be concluded that the simplest method, the asymptotic approximation, features sufficient accuracy for most applications. For $f > f_{c,\text{HF}}$, the solutions based on Bessel functions or, if higher accuracy is required, FEM-based methods need to be considered (cf. Fig. 4.2). Most commonly, however, $f > f_{c,\text{HF}}$ is avoided in order to avoid excessive HF losses and a HF litz wire with a smaller single strand diameter is considered [25, 247]. Therefore, in this work, $f < f_{c,\text{HF}}$ is presupposed. Furthermore, the comparative evaluation given in Fig. 4.3 reveals that an exact model of the packing pattern is not required.

For $f < f_{c,\text{HF}}$ the results obtained with all considered computational methods are matching. This indicates that potential deviations between computed and measured losses originate from phenomena that violate the assumption of a perfectly twisted HF litz wire with an infinitesimally small pitch length.

4.3 Twisting Imperfections

This section investigates the implications of different twisting schemes (e.g., radial, azimuthal, and combined) and numbers of pitches (integer or non-integer) on the expected AC losses of HF litz wires. In such HF litz wires, the assumption of an equal current distribution among the strands is, in general, incorrect and the aforementioned methods are not applicable.

4.3.1 Computation Method

In the literature, an analytical method for the simulation of imperfect HF litz wires has been proposed [244], especially with regard to the impact of the pitches. However, this method, which does not compute the current sharing between the strands, cannot be used for simulating complex twisting

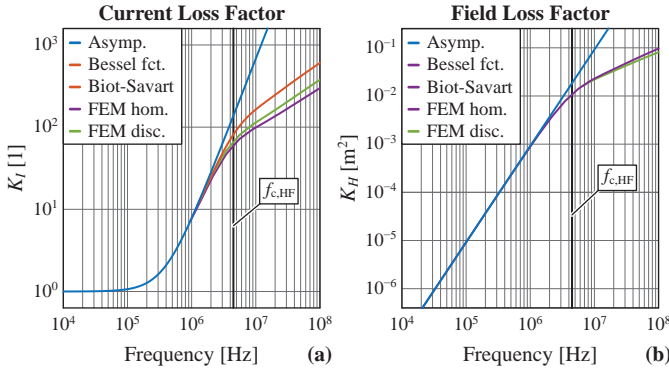


Fig. 4.3: (a) Loss factor K_I and (b) K_H computed with different methods (asymptotic approximation, Bessel functions, Biot-Savart summation, FEM homogenization, and FEM discrete modeling). A $343 \times 100 \mu m$ HF litz wire is considered (2.5 mm outer diameter).

schemes. Further references propose 3D simulation methods, based on integral equations (e.g., PEEC), differential equations (e.g., FEM) [183, 187, 188], or both [189, 241]. However, 3D methods are complex to implement and demand for very high computational cost, which limits the number of strands to less than a hundred [183, 188]. For larger HF litz wires, massively parallel computing is required [187]. Furthermore, the 3D methods require a complete parametric representation of all strands, which is difficult to obtain for HF litz wires with a high number of strands (e.g., consideration of deformations of the bundles or glitches in the twisting pattern) [118, 185].

The proposed numerical method offers a trade-off between modeling accuracy, modeling effort, and computational cost. The method is based on the 2.5D PEEC method, where a custom-built solver is used [246, 248, 249]. Fig. 4.4 presents the main steps of the method, which are described as follows:

- ▶ First, the geometry (packing and twisting) of the HF litz wire is generated and the HF litz wire is sliced into different sections (about ten per pitch). For taking the twisting scheme into account, permutation matrices are generated for each sliced section of the HF litz wire.
- ▶ In a second step, the inductance and resistance matrices are calculated using a 2D PEEC model. An analytical solution exists for the self and mutual inductances of infinite wires. If the operating frequency is selected such that no significant skin effect occurs inside the strands

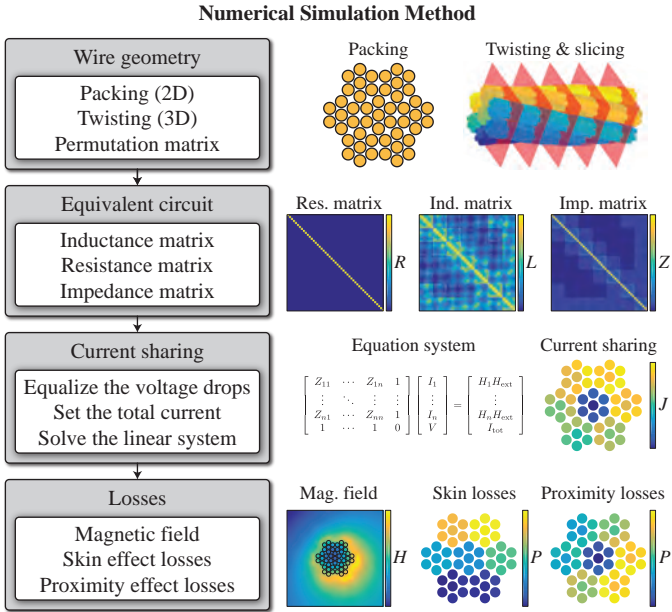


Fig. 4.4: Workflow for the computation of losses in HF litz wires with arbitrary twisting schemes and numbers of pitches. The analysis is based on a 2.5D PEEC method.

($f < f_{c, \text{HF}}$), each strand can be modeled by a single conductor. Otherwise, a meshing of the strands is required. With the inductance and resistance matrices, the impedance matrix can be easily computed.

- ▶ Afterwards, with the impedance matrix and the aforementioned permutation matrices are combined in order to find the impedance matrix of the twisted HF litz wire. Then, the current sharing problem is solved by equalizing the voltage drops between the strands [118]. The solution of this linear equation system gives the current flowing in each strand.
- ▶ Finally, with the obtained currents, the magnetic field distribution can be computed (Biot-Savart). With the magnetic field and the currents, the losses (due to skin and proximity effects) of each strand are extracted.

It should be noted that the energy, and, therefore, the inductance, of an infinitely long straight wire is infinite. This is explained by the fact that a current should always flow in a closed loop, making the hypothesis of an infinitely long straight wire unphysical. However, this does not represent a problem for the presented method since only the differences between the inductances of the different strands are considered and not the absolute values. Alternatively, the current sharing problem could be solved for the circulating currents (and not for the total current). This variable transformation would remove the unphysical coefficients (the sum of the circulating currents is zero) and would lead to the same results.

Compared to a full 3D method, the 2.5D PEEC method neglects the current flows in azimuthal and radial directions, which are, however, much smaller than the longitudinal currents [118]. This implies that the method is not able to simulate configurations with a large external field applied in longitudinal direction, which are, anyway, uncommon for magnetic components. The main advantage of the 2.5D PEEC method is the reduced computational cost (and memory requirement), which enables the simulation of a HF litz wire with thousands of strands in less than a minutes on a personal computer. Moreover, the method does not require a complete 3D full parametric representation of the HF litz wire and, hence, substantially reduces the modeling complexity. Finally, the fact that the PEEC method is based on an equivalent circuit allows the combination of the HF litz wire model with external models, such as terminations, busbars, or magnetic cores [25, 241, 242, 246, 250]. Furthermore, the method is also applicable to higher frequencies ($f > f_{c, \text{HF}}$), even if this case is not considered in this work.

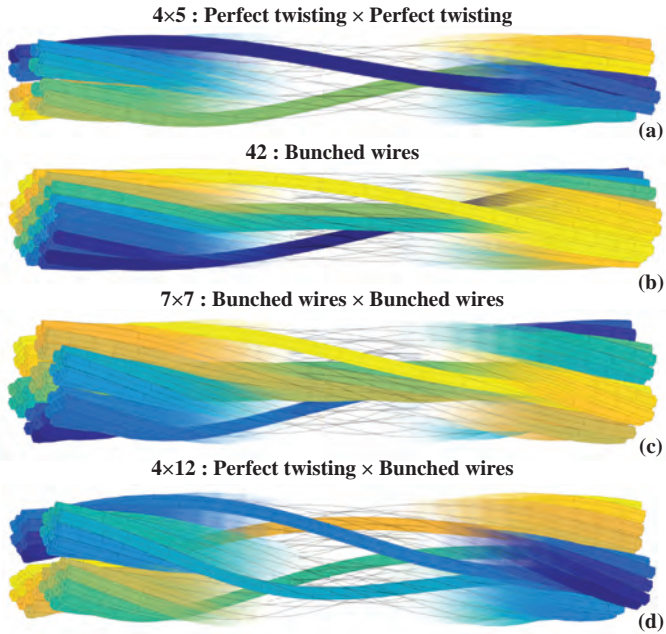


Fig. 4.5: (a) Perfect twisting, (b) bunched wires, (c) bundle in the center, and (d) hybrid twisting (perfect and bunched). Each title line specifies the corresponding number of bundles and the number of strands per bundle.

4.3.2 Considered Twisting Imperfections

Many different twisting schemes exist for HF litz wires [133, 188, 241, 242], featuring different bundle structures, radial and/or azimuthal permutations, etc. However, most litz wires are constructed with the following twisting schemes:

- ▶ *Perfect twisting* (“PT”) - The strands are perfectly twisted (radial and azimuthal direction). This ideal construction is difficult to realize with a large number of strands (more than six).
- ▶ *Bunched wires* (“BW”) - The strands are only twisted in azimuthal direction. The strands located in the center of the wire, stay in the center and are not twisted. This represents the easiest and cheapest twisting scheme and is commonly found in commercially available HF litz wires [25, 133, 186, 245].

Tab. 4.1: Twisting Schemes ($343 \times 100 \mu\text{m}$)

| Name | Twisting scheme | Number of wires |
|----------------|----------------------------|-----------------------|
| “343/PT/PT/PT” | PT \times PT \times PT | $7 \times 7 \times 7$ |
| “343/PT/PT/BW” | PT \times PT \times BW | $7 \times 7 \times 7$ |
| “343/PT/BW/BW” | PT \times BW \times BW | $7 \times 7 \times 7$ |
| “343/BW/BW/BW” | BW \times BW \times BW | $7 \times 7 \times 7$ |
| “343/PT/BW” | PT \times BW | 7×49 |
| “343/BW” | BW | 343 |

- *Braiding* - The braiding of the strands is, theoretically, possible. However, the high complexity of such a twisting scheme makes it economically unattractive and uncommon for HF litz wires used for power electronic components [251]. Therefore, this twisting scheme is not further considered.

The two aforementioned twisting schemes (“PT” and “BW”) feature correct twisting in azimuthal direction since imperfect azimuthal twisting is uncommon for HF litz wires. Fig. 4.5 illustrates different combinations of the aforementioned twisting schemes (many levels of twisting). Fig. 4.5(a) depicts a perfectly twisted HF litz wire. Fig. 4.5(b) shows a HF litz wire composed of bunched strands, which is clearly imperfect due to the lack of radial twisting. Fig. 4.5(c) shows an imperfect twisting scheme which features an untwisted bundle in the center of the wire [25]. Fig. 4.5(d) depicts a hybrid twisting scheme, which is also commonly found: the “BW” twisting scheme is used at the strand-level and all other levels (e.g., the top-level) employ perfect twisting (“PT”) [133, 186].

All simulations consider the HF litz wire introduced in Section 4.2 ($343 \times 100 \mu\text{m}$) and six different combinations of the aforementioned twisting schemes (“PT”, “BW”, cf. Fig. 4.5) are listed in Tab. 4.1. The pitch length of the top-level twisting is 30 mm. The ratio of the pitches between two successive twisting levels is set to 2.0 (given that the strand-level twisting pitch is the shortest).

4.3.3 Simulation: Twisting Schemes

The six twisting schemes listed in Tab. 4.1 are considered with an integer number of pitches. Fig. 4.6 illustrates the current sharing for the case of a

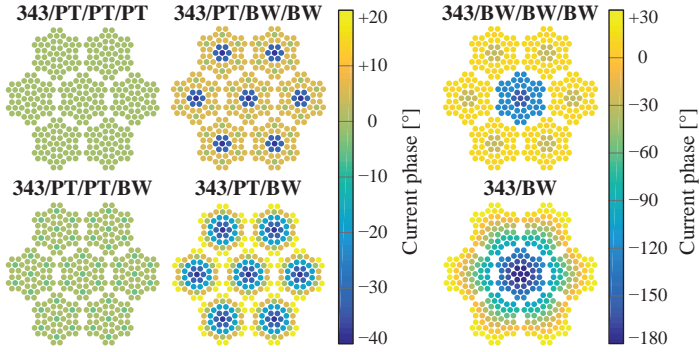


Fig. 4.6: Phase differences of the strand currents (with respect to the phase of the total current, I_{wire}) at 100 kHz for different twisting schemes ($I_{\text{wire}} = 1 \text{ A}$, $H_{\text{ext}} = 0 \text{ A/m}$). A $343 \times 100 \mu\text{m}$ HF litz wire is considered (2.5 mm outer diameter).

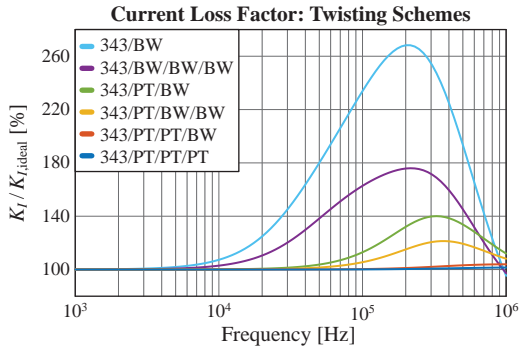


Fig. 4.7: Factor K_I (cf. (4.1)) for different twisting imperfections (cf. Tab. 4.1), compared to a perfectly twisted HF litz wire (cf. Fig. 4.3). A $343 \times 100 \mu\text{m}$ HF litz wire is considered (2.5 mm outer diameter).

current excitation (no external field excitation). The current in the bundles which are not perfectly radially twisted is phase shifted with respect to the total current. This implies that more current is flowing in the other bundles. This leads to increased losses according to Fig. 4.7 for K_I (cf. (4.1)). The effect of the twisting on the DC resistance is small (less than 5 %) and is, therefore, neglected.

As expected, the increase of the losses is particularly pronounced (more than 100 %) for twisting imperfections at the top-level (“343/BW” and “343/BW/BW/BW”). For imperfect twisting at the mid-level (“343/PT/BW” and “343/PT/BW/BW”), the increase is already much smaller (less than 40 %). A twisting imperfection at the strand-level (“343/PT/PT/BW”) has a negligible impact on the losses, showing that a perfect twisting is actually not required. Finally, the ideal twisting scheme (“343/PT/PT/PT”) matches perfectly with the methods presented in Section 4.2. At higher frequencies ($f \approx 1$ MHz, cf. Fig. 4.7), the effects of twisting imperfections disappear and imperfectly twisted HF litz wires feature even lower losses, due to the better current distribution with respect to the HF proximity effect losses [19, 133, 186, 247]. However, litz wires are typically not operated in this region. The impact of the twisting schemes on the external field factor K_H (cf. (4.1)) is negligible since the considered HF litz wires are correctly twisted in azimuthal direction and an integer number of pitches is chosen.

4.3.4 Simulation: Number of Pitches

The losses are further affected by the number of pitches (number of twisting periods) of the HF litz wire. For the sake of simplicity and brevity, only the twisting scheme “343/BW” is considered. However, the results are similar for the remaining five schemes since the impacts of the pitch lengths of the sub-bundles (e.g., mid-level and strand-level) are less critical [244]. Moreover, the radial twisting scheme is not critical for the case of an external magnetic field excitation, which is considered for this test.

If a non-integer number of pitches is used, the impedance asymmetry between the strands is leading to circulating currents, as shown in Fig. 4.8(a) for 5.5 pitches and an external magnetic field excitation (without current excitation in the HF litz wire). Fig. 4.8(b) illustrates the impact of the number of pitches on the external field factor K_H (cf. (4.1)). The impact on K_I is much smaller and, therefore, not considered.

The loss increase is particularly pronounced (more than 100 %) for short HF litz wires which is critical for windings with reduced number of turns.

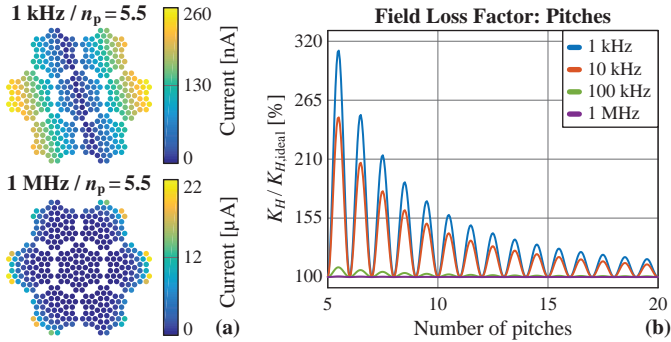


Fig. 4.8: (a) Amplitude of the strand currents for the twisting scheme “343/BW” with 5.5 pitches ($H_{\text{ext}} = 1 \text{ A/m}$, $I_{\text{wire}} = 0 \text{ A}$). (b) Factor K_H (cf. (4.1)) for the twisting scheme “343/BW” and for different numbers of pitches compared to a perfectly twisted HF litz wire (cf. Fig. 4.3). A $343 \times 100 \mu\text{m}$ HF litz wire is considered (2.5 mm outer diameter).

As expected, the impacts of non-integer numbers of pitches is significantly reduced for increased lengths of the HF litz wire. At higher frequencies, the spatial distributions of the circulating currents change (cf. Fig. 4.8(a)), which leads to a mitigation of the losses due to circulating currents between the strands [19]. By contrast, as shown in Fig. 4.3, the factor K_H of an ideal HF litz wire (circulating current inside the strands) increases rapidly over frequency. This implies that the effects of a non-integer number of pitches become negligible at higher frequencies.

The same effect appears for a winding with an integer number of pitches placed in a non-homogeneous external magnetic field (variable in the longitudinal direction). Such local variations, which are typically produced by the fringing fields of air gaps, also lead to circulating currents, as shown in Fig. 4.8(a). The proposed 2.5D PEEC solver is also able, if required, to deal with inhomogeneous external magnetic fields, where different external field patterns are applied to the different slices (cf. Subsection 4.3.1).

4.3.5 Analytical Approximations

Even though the 2.5D PEEC simulations are fast, analytical formulas are still required for a rapid assessment of the impacts of twisting imperfections on the losses. For computing the increase of the losses due a non-integer number of pitches or a non-homogeneous external field, the analytical formulas presented in [244] can be used. For the evaluation of different twisting schemes

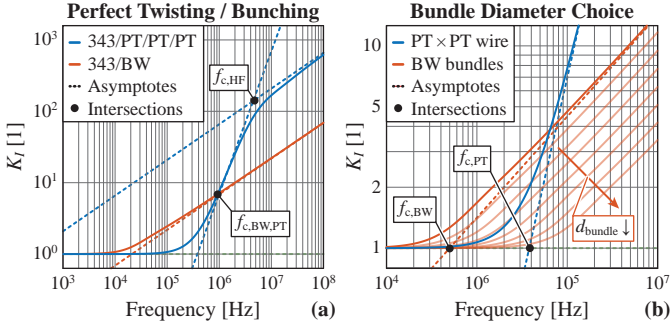


Fig. 4.9: (a) Loss factors, K_I , for the twisting schemes “343/PT/PT/PT” and “343/BW”. (b) Loss factors, K_I , for the bunched bundles (diameter d_{bundle}) and the perfectly twisted HF litz wire (diameter d_{outer}). Different diameters are considered for d_{bundle} (from 0.3 mm to 1.6 mm). For both plots, the corresponding asymptotes (dashed lines) and intersections are also shown. A $343 \times 100 \mu\text{m}$ HF litz wire is considered ($d_{\text{outer}} = 2.5 \text{ mm}$).

(cf. Fig. 4.5), the following approach is proposed. The different equations are derived from the different asymptotes shown in [18].

First, the twisting schemes “343/PT/PT/PT” and “343/BW”, which represent the extreme cases (cf. Fig. 4.6), are considered. Fig. 4.9(a) depicts the corresponding loss factors, K_I , and presents the different asymptotes. With these asymptotes, an expression for the frequency, $f_{c,\text{BW,PT}}$, where the two curves intersect, can be derived as

$$f_{c,\text{BW,PT}}(d_{\text{outer}}, d_s) \approx \frac{1024^{\frac{1}{3}}}{\pi \sigma \mu_0 F d_{\text{outer}}^{\frac{2}{3}} d_s^{\frac{4}{3}}}, \quad (4.6)$$

where σ is the conductivity and d_s the diameter of the strands, d_{outer} the external HF litz wire diameter, and F the filling factor. It can be seen that a bunching of the all strands would be preferable for $f > f_{c,\text{BW,PT}}$, due to the superior HF properties, as explained in [133, 247]. However, HF litz wires are usually operated at $f < f_{c,\text{BW,PT}}$ such that twisting in radial direction is also required [25, 133, 247].

Radial twisting is difficult to achieve for large numbers of strands and a construction based on bundles with reduced numbers of single strands is preferred, instead. In case of HF litz wires with very high numbers of single strands, many levels of bundles are required, which makes the process of

twisting difficult and expensive. According to the results depicted in Fig. 4.7, however, certain twisting imperfections can be acceptable. Therefore, an expression is required in order to assess the impacts of given imperfections on the expected losses.

Since imperfections in the top-most level are most critical and should be avoided (for $f < f_{c,BW,PT}$), a HF litz wire with the twisting scheme “PT × BW” is selected and compared to a perfectly twisted HF litz wire (“PT × PT”). The diameter of each bundle is d_{bundle} and the outer diameter of the HF litz wire is d_{outer} . Fig. 4.9(b) shows the loss factors, K_I , calculated for the single bunched bundles and the loss factor of the (complete) perfectly twisted HF litz wire. The corner frequencies for the perfectly twisted HF litz wire and the bundles, $f_{c,PT}$ and $f_{c,BW}$, can be expressed as

$$f_{c,PT}(d_{\text{outer}}, d_s) \approx \frac{\sqrt{128}}{\pi \sigma \mu_0 F d_{\text{outer}} d_s}, \quad (4.7)$$

$$f_{c,BW}(d_{\text{bundle}}) \approx \frac{16}{\pi \sigma \mu_0 F d_{\text{bundle}}^2}. \quad (4.8)$$

In order to avoid that the eddy current losses in the bunched bundles lead to a considerable increase of the overall losses, the corner frequency of the bundles needs to be greater than the operating frequency or greater than the corner frequency of the perfectly twisted HF litz wire. However, at the corner frequency, the losses are already larger than the DC losses. Therefore, the corner frequency of the bundles should be approximately two times larger than the operating frequency. With this, the following condition for the diameter of each bundle is derived:

$$d_{\text{bundle}}(f_{c,BW} \approx 2f) < \max \left\{ \frac{4}{\sqrt{\pi \sigma \mu_0 F f_{c,BW}}}, 2^{\frac{1}{4}} \sqrt{d_{\text{outer}} d_s} \right\}, \quad (4.9)$$

where $f_{c,BW}$ is the selected corner frequency and f the operating frequency. It can be noticed that, beyond a given frequency (when $f_{c,BW} = f_{c,PT}$), the diameter of the bundles does not need to be further reduced since the internal proximity effect losses of the perfectly twisted HF litz wire are larger than the losses arising from the twisting imperfections (cf. Fig. 4.9(b)). This matching of corner frequencies between the bundles and the ideal HF litz wire leads to

$$d_{\text{bundle}} = 2^{\frac{1}{4}} \sqrt{d_{\text{outer}} d_s}, \quad \text{with } f_{c,BW} = f_{c,PT}. \quad (4.10)$$

This implies that a perfect twisting scheme is actually not required. A non-ideal HF litz wire respecting this last condition will feature (nearly) the same

losses as an ideally twisted HF litz wire. These results can also be generalized to HF litz wires with arbitrary numbers of twisting levels. The diameters of the largest bundles resulting from an imperfect twisting scheme (e.g., “BW”) should not exceed the value computed with (4.9) or (4.10).

The aforementioned analytical equations have been successfully verified with the presented 2.5D PEEC method. The analytical equations can be used for providing design guidelines for the construction of nearly ideal HF litz wires. A HF litz wire with a given outer diameter (d_{outer}) and strand diameter (d_s) is considered and the following design procedure (for $f < f_{c,\text{BW,PT}}$) is proposed:

- ▶ The diameter of the bundles (d_{bundle} , cf. (4.9) or (4.10)) is computed for the strand-level twisting. This strand-level bundle is composed of bunched strands. Using bundles with a smaller diameter only marginally reduces the losses but significantly increases the complexity of the twisting scheme and, potentially, reduces the filling factor.
- ▶ From the obtained diameters (d_{bundle}) and the specified outer diameter (d_{outer}), the number of bundles is extracted, considering the achievable filling factor between the bundles.
- ▶ If the number of bundles is too large (typically more than six) for a “PT \times BW” twisting scheme additional mid-level twisting steps should be added (e.g., “PT \times PT \times BW”).

Now, it is possible to consider the aforementioned effects (e.g., non ideal twisting and number of pitches) and apply the corresponding models (2.5D PEEC and analytical equations) to a real component (e.g., transformer, choke, and inductors) featuring non-ideal HF litz wires.

4.4 Measurements of Twisting Imperfections

A MV/MF transformer (7.5 kHz, 65 kW) is considered, cf. Fig. 4.10. This transformer is used in a DC-DC converter composing a multi-cell “MEGALink” SST [50, 53, 105]. It should be noted that these ratings differ from the MV/MF transformer used for the SST demonstrator presented in Subsection 1.7.2. This choice has been dictated by the necessity of analyzing a MF transformer using non-ideal litz wires.

The considered MV/MF transformer features a shell-type arrangement with a nanocrystalline core (E-core). Tab. 4.2 summarizes the relevant parameters of the windings and the employed HF litz wires. All measurements are

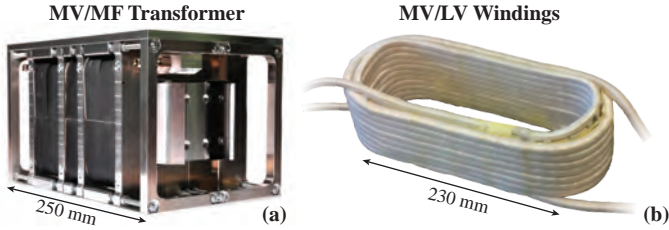


Fig. 4.10: (a) Considered MV/MF transformer (7.5 kHz, 65 kW). (b) MV/LV windings without the magnetic core. More information about this prototype can be found in [50, 53, 105].

Tab. 4.2: MV/MF Transformer (7.5 kHz, 65 kW)

| Name | MV winding | LV winding |
|-------------------|----------------------------|-------------------------------|
| Voltage | ± 1.1 kV | ± 0.8 kV |
| RMS current | 70 A | 95 A |
| Winding size | 6.0×72 mm | 8.1×70 mm |
| Litz wire profile | Rectangular | Rectangular |
| Litz wire size | 6.0×6.0 mm | 8.1×8.1 mm |
| Number of strands | 700×200 μ m | 1000×200 μ m |
| Twisting Scheme | BW \times PT \times BW | BW \times BW \times BW |
| Number of wires | $7 \times 5 \times 20$ | $7 \times [10, 11] \times 14$ |

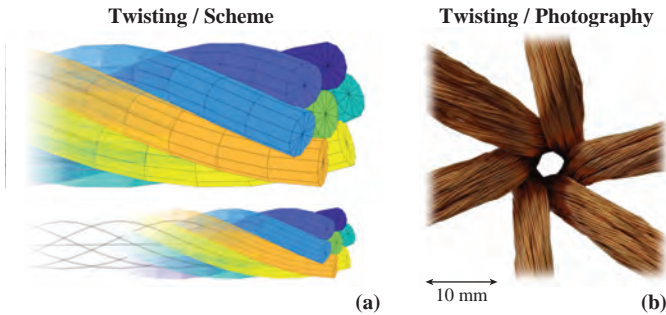


Fig. 4.11: (a) Twisting scheme of the top-level bundles (“BW”, cf. Fig. 4.5) of the MV winding where seven bundles are present. (b) Photography of the HF litz wire structure for the MV winding where the untwisted bundle in the center has been removed.

conducted with the magnetic (nanocrystalline) core being installed in order to obtain a realistic distribution of the magnetic field. The simulations employ the method presented in Fig. 4.4 and the external magnetic field is calculated with FEM simulations [228]. The number of pitches is very large (more than 70 for each winding), hence, an integer number of pitches has been assumed in the simulations.

In a first step, the current distribution among the bundles of the MV winding has been measured at different frequencies, with a short-circuit being applied to the LV winding. Fig. 4.11(a) shows the structure of the HF litz wire of the MV winding, for which an untwisted bundle is present in the center (“BW” at the top-level twisting, cf. Fig. 4.5(c)). This center bundle has been removed in Fig. 4.11(b) to highlight the twisting scheme of the HF litz wire. This HF litz wire does not respect the aforementioned requirements (cf. (4.9) and (4.10)). Therefore, an unequal current distribution (cf. Fig. 4.6) among the bundles is expected .

Fig. 4.12 shows the measured current in the center bundle and the total current (in the seven bundles) at different frequencies. Fig. 4.13 depicts the ratio of the currents in the center bundle to the total current (in the seven bundles), with respect to amplitude and phase. As expected, the phase of the current in the center bundle is slowly drifting from 0° to -180° , cf. Fig. 4.6. Therefore, it appears that measuring the amplitude of the current in the center bundle is insufficient since almost only the phase is affected by the imperfect twisting. A very good agreement between simulations (2.5D PEEC method)

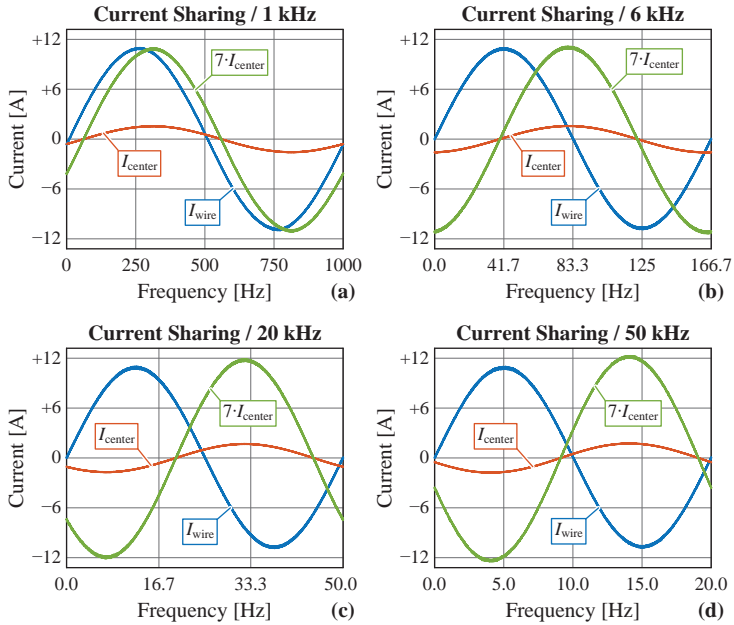


Fig. 4.12: Measured currents at (a) 1 kHz, (b) 6 kHz, (c) 20 kHz, and (d) 50 kHz in the MV winding. The current in the center bundle (I_{center}) and the total current (I_{wire}) are shown.

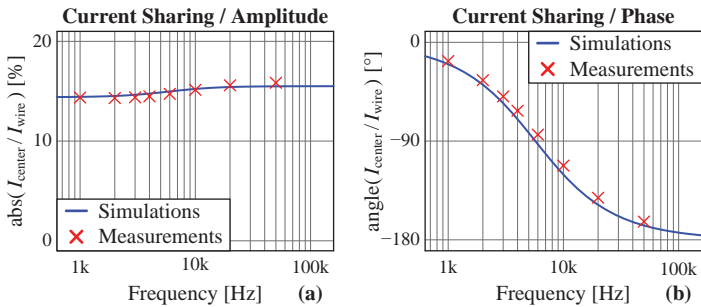


Fig. 4.13: (a) Amplitude and (b) phase of the current in the center bundle (I_{center}) compared to the total current (I_{wire}) in the MV winding. The simulations (2.5D PEEC method) and the measurements are compared.

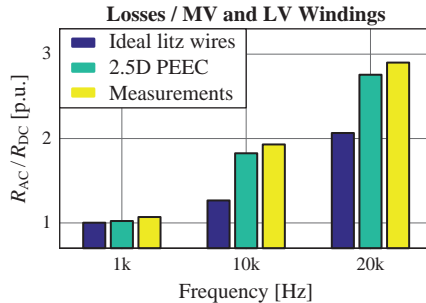


Fig. 4.14: Winding resistance ratio R_{AC}/R_{DC} (cf. (4.2), for both windings). Also shown are the simulated losses for hypothetical perfectly twisted HF litz wires and for the actually present imperfect twisting (2.5D PEEC method).

and measurements is achieved. Furthermore, it is found that the presence of the magnetic core has only a minor impact on the current distribution in the HF litz wire (in both, simulations and measurements).

In a second step, the winding losses have been measured with a “Yokogawa WT3000” power analyzer (LV winding short-circuited) [252]. In the course of this measurement, the ratio R_{AC}/R_{DC} is determined (cf. (4.2)). Due to the current distribution during short-circuit operation, this ratio quantifies the HF losses of both windings (cf. Chapter 3) [125]. Fig. 4.14 presents a comparative evaluation of the results for the simulations and the measurements conducted with the non-ideal HF litz wires and, in addition, includes the simulation results for hypothetical perfectly twisted HF litz wires. At 10 kHz (near the operating frequency), the resistance ratio for hypothetical perfectly twisted HF litz wires is 1.27, the simulated ratio for the non-ideal HF litz wires is 1.79, and the measurement returns 1.93. Hence, the mismatch between expected losses with perfectly twisted HF litz wires and the measurements (52 %) implies that the hypothesis of perfectly twisted HF litz wires is not valid. The deviation between the 2.5D PEEC simulations and the measurements is only 8 %, implying that the proposed approach features a high accuracy.

4.5 Summary

This chapter investigates the implications of imperfections in HF litz wires (e.g., number of pitches and twisting scheme) on the losses and particularly focuses on imperfect twisting which is commonly observed in commercially

available HF litz wires. A fast 2.5D PEEC solver, which is able to simulate HF litz wires with thousands of strands, has been implemented to simulate the current distribution among the strands and to determine the losses.

According to the results obtained from the analysis of different types of imperfect twisting schemes, it is found that imperfect twisting, in particular of the top-level bundles, can lead to a significant increase of the losses due to eddy currents (up to 100 % increase). It is also found that imperfections may be tolerated at sub-bundle-levels. In this context, simple analytical expressions are derived and the results are summarized in design guidelines for the construction of suitable HF litz wires. Furthermore, an increase of the losses is to be expected for windings with low numbers of pitches and/or non-homogeneous external magnetic fields.

The presented method is finally applied to a MV/MF transformer prototype (7.5 kHz, 65 kW), which employs imperfectly twisted HF litz wires, for experimental verification. Both, the measured current distribution among the bundles and the losses, are in good agreement with the simulations. The imperfections of the HF litz wires lead to an increase of the winding losses by 52 %.

5

MV/MF Transformer Prototype

Chapter Abstract

This chapter analyzes the design, construction, and measurements of the MV/MF transformer (± 3.5 kV to ± 400 V, 48 kHz, 25 kW) used in the DC-DC converter of the considered SST demonstrator. First, the transformer parameters are optimized. An optimal design is selected and the transformer construction process is explained in detail (e.g. insulation vacuum potting). Afterwards, the equivalent circuit and the losses of the transformer are measured. Finally, the efficiency is extracted for the operation of the transformer inside the considered DC-DC converter. The realized MV/MF transformer prototype features a power density of 7.4 kW/l (121 kW/in³, 4.0 kW/kg, and 1.8 kW/lb) and achieves a full-load measured efficiency of 99.65 %.

5.1 Introduction

As mentioned in Chapter 2, the design of MF transformers involves many parameters and trade-offs, which are best analyzed using multi-objective optimization [16–18, 22, 23, 115]. However, it is not straightforward to construct a high performance MF transformer from optimization results. Several problems can appear, such as limited availability of components (e.g., litz wire and core), model inaccuracies, manufacturability, manufacturing tolerances (e.g., litz wire, coil former, and core), fault handling capabilities (e.g., short-circuit and saturation), impact of the CM capacitances, and impact of resonance frequencies in the range of the switching frequency [25, 82, 156, 159, 160]. Moreover, the measurement of a highly efficient MF transformer is also a challenging task due to the ratios between the losses, the transferred power,

Tab. 5.1: Specifications of the MV/MF Transformer

| Parameter | Value |
|---------------------|--------------------------------------|
| Topology | SRC-DCX |
| Power | 25.0 kW |
| Voltage | ± 3.5 kV (DM) / ± 400 V (DM) |
| Magnetizing current | 3.5 A (minimum value) / MV side |
| Magnetic coupling | 95 % (minimum value) |
| Cooling | Forced-air cooling / 40 °C ambient |
| Insulation | Dry-type / 15 kV (CM voltage) |
| Efficiency | 99.6 % (minimum value) |
| Power density | 5 kW/l (minimum value) |

and the reactive power. Therefore, this chapter first presents the optimization of a highly efficient MF transformer operated with MV and, afterwards, the practical challenges appearing during the CAD design, construction, and measurement of a prototype.

The SRC-DCX of the single-cell SST demonstrator presented in Subsection 1.7.2 is considered. The MV/MF transformer (± 3.5 kV to ± 400 V, 48 kHz, 25 kW) of the SRC-DCX is designed according to the specifications shown in Tab. 5.1. The limitations for the magnetizing current and the magnetic coupling are necessary for the ZVS modulation scheme of the SRC-DCX (cf. Chapter 8) [88]. The requirements on the efficiency (99.6 %) and the power density (5 kW/l) for the MV/MF transformer originate from the performance target of the complete DC-DC: 99.0 % and 2.5 kW/l (cf. Subsection 1.7.2). It has to be noted that the transformer is subject to particularly high electrical CM and DM voltages, such that the insulation materials, insulation geometry, and electric field stress must be examined carefully, as well as the impact of the insulation on the thermal performance.

This chapter is organized as follows. In Section 5.2 the design space of the transformer is first evaluated. Subsequently, an optimal design is selected. The construction of the prototype is examined in Section 5.3 and the properties (e.g., short-circuit, saturation, resonance, insulation testing, thermal response) of the realized transformer are measured in Section 5.4. Finally, Section 5.5 presents the measured and simulated losses.

5.2 Optimization

This section defines and justifies the different assumptions made during the design process of the transformer. Afterwards, the transformer is optimized with analytical equations and the impact of the MV insulation on the achievable performance is highlighted. Finally, the selected design is presented.

5.2.1 Design Space Restrictions

The number of degrees of freedom of the transformer design (e.g., geometry, core, winding, and insulation) is extremely large and, therefore, would lead to an optimization problem with problematic modeling and computational costs. Therefore, the design space of the MV/MF transformer is restricted and, in the following, only the design combinations which can, potentially, lead to an optimal design are considered for the Pareto optimization.

From the different possible geometries (cf. Fig. 1.9), the following choices are made. Planar windings are not considered since they are not adapted for realizing a high power MV/MF transformer [117,119]. Coaxial transformers are also excluded since it is difficult to achieve a large voltage transfer ratio [63, 120–122]. The integration of a low magnetizing inductance (e.g., air gap) is also problematic for coaxial transformers. Core-type transformers would also be an option but are difficult to design for large voltage transfer ratios and MV insulation. The fact that both windings are divided between the limbs is increasing the number of required cable terminations and the complexity of the insulation. Therefore, designs featuring an E-core or a U-core with a shell-type arrangement (cf. Fig. 1.9), which represent the typical choice for MV/MF transformers, are considered for the Pareto optimization, [25, 64, 114, 115, 137, 172, 205].

For the winding geometry, foil conductors and litz wires are the common choices for MF transformers. Foil conductors are not considered for the following reasons [18,19]. Typically, foil windings are interleaved for reducing the proximity effect losses, which is not possible in the case at hand due to the MV insulation requirements [167,168]. Moreover, the presence of an air gap, which is necessary to obtain the desired magnetizing current, massively increase the losses of foil conductors [250]. Therefore, litz wires are considered since they offer low HF losses and a great design flexibility [16, 18, 129]. Due to the insulation requirements, it has been found that an interleaving of the windings is not advantageous.

For the selection of the core material, three different options are typically used: amorphous, nanocrystalline, and ferrite. Amorphous materials are

Tab. 5.2: Optimization Parameters of the MV/MF Transformer

| Parameter | Value |
|----------------------|--|
| Frequency | [20, 70] kHz |
| Core type | E-core / U-core |
| Core material | Ferrite / “BLINZINGER BFM8” [256] |
| Core geometry | [0.25, 6.0], cross section aspect ratio |
| Flux density | [50, 250] mT |
| Winding type | Shell-type / litz wire |
| Current density | [0.5, 10.0] A/mm ² |
| Litz wire strands | 71 μ m / 100 μ m / 200 μ m |
| Number of layer | [1, 2], LV winding / [2, 4], MV winding |
| Number of turns | [3, 15], LV side / [25, 130], MV winding |
| Insulation thickness | 4 mm, around the MV winding |

not further considered since the hysteresis and eddy current losses are too important for reaching the fixed target efficiency [21, 22, 91]. Nanocrystalline materials are typically used for frequencies below 20 kHz [61–63, 116]. For higher frequencies, the eddy current losses are rapidly increasing [25, 27, 253]. Moreover, the presence of air gaps is also critical with nanocrystalline cores [127, 254]. Finally, the presence of large capacitively coupled voltages in the core, can create short-circuits between the nanocrystalline layers [255]. For all these reasons, ferrite cores, which do not feature the aforementioned problems, are selected for the design process.

The thermal management of the transformer is based on heat conduction and forced air cooling [91, 139]. With the fixed target efficiency, water cooling is not required. Dry-type materials are selected for the electrical insulation. The power level of the transformer is not sufficient to justify the overhead linked to oil insulation (e.g., oil tank, expansion tank, and dehydration breather) [15, 61].

5.2.2 Optimization Results

The following analytical models are used for the optimization of the transformer. The magnetic field in the winding window and the leakage inductance are computed with the mirroring method [16, 19, 229]. With the obtained field, the winding losses (with the skin and proximity effects) are analytically

computed [18, 19]. The magnetizing inductance and the flux inside the core are obtained with a reluctance circuit, which considers the air gap fringing field [19, 124]. The core losses are computed with the iGSE using a loss map (frequency, flux density, and temperature dependences) [91, 128]. The dielectric losses are estimated with the formulas proposed in Chapter 7 [153, 154]. Finally, a lumped thermal model is used, where the coupling between the temperature distribution and the losses is considered [17, 91, 115, 138]. A model of the SRC-DCX operated at the resonance frequency is used for computing the currents and voltages applied to the transformer, cf. Chapter 8 [88].

Tab. 5.2 lists the parameters used for the optimization of the MV/MF transformer. The switching frequency is limited by the ZVS switching losses of the semiconductors, such that frequencies above 70 kHz are not expected to be advantageous [111, 112]. The ferrite material “BLINZINGER BFM8” is considered [256]. This material, which is equivalent to the well-known “TDK N87”, has been selected due to the availability of cores with large cross-sections and winding windows. Ferrite materials with higher performances exist, but are usually expensive and, therefore, not available for large core shapes [216, 219, 221]. The optimization is conducted with the core shapes and the litz wire diameters considered as free parameters (not restricted by the commercially available sizes). In order to capture the local minima of the design space (cf. Chapter 2), a brute force algorithm is used [22].

Fig. 5.1(a) shows the obtained volume/efficiency Pareto front of the considered MV/MF transformer. As expected (cf. Chapter 2), there is a trend towards higher efficiencies and power densities for increased operating frequencies [22]. However, above 50 kHz, the efficiency can only be marginally improved, which is due to fact that the optimum is always flat with respect to the operating frequency (cf. Chapter 2) [22]. Fig. 5.1(b) depicts the same Pareto front, where the electrical insulation requirements are ignored (e.g., insulation distances and dielectric losses). These designs are naturally invalid but are presented to highlight the critical impact of the insulation on the achievable performance. It can be concluded that the performance of MV/MF transformers cannot be directly compared to those of LV/MF transformers. More precisely, the electrical insulation impacts the performance in several ways:

- The insulation volume decreases the winding filling factor. This has a direct impact on the achievable power density. Moreover, the insulation material limits the heat extraction capabilities of the windings (cf. Chapter 2) [22].

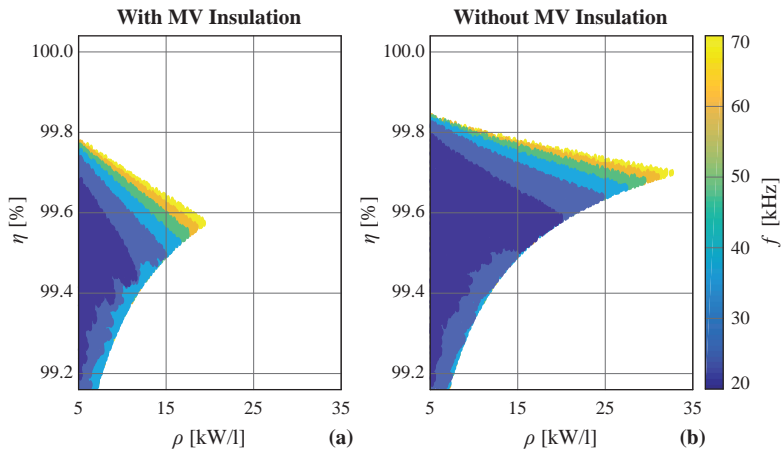


Fig. 5.1: (a) Boxed volume/efficiency Pareto optimization of the MV/MF transformer for different operating frequencies (3.5 million designs). (b) Volume/efficiency Pareto optimization of the MV/MF transformer for different operating frequencies, where the electrical insulation requirements are ignored (4.9 million designs). The optimization does not include the volume of the fan and the cable terminations. The losses of the fan are, however, included.

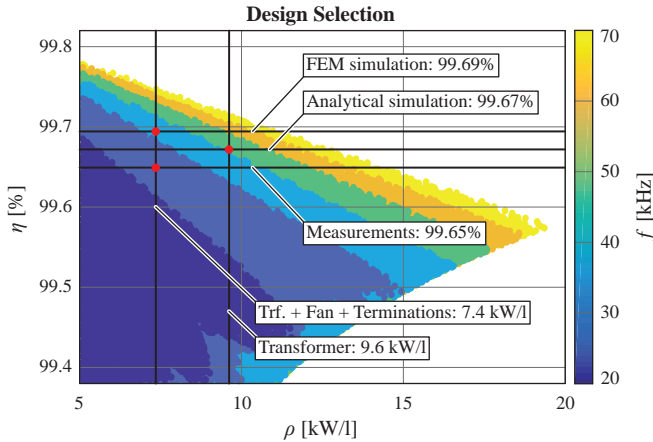


Fig. 5.2: Boxed volume/efficiency Pareto optimization of the MV/MF transformer for different operating frequencies. The selected design is highlighted, where the simulated (analytical models and FEM simulations) and the measured values are shown. The boxed volume of the selected design is indicated with and without the volume of fan and the cable terminations. The optimization does not include the volume of the fan and the cable terminations. The losses of the fan are, however, included.

- ▶ The reduced filling factor of the winding (or the increased winding window area) has also a critical impact of the core volume required for achieving a given core cross-section. Therefore, the core losses, which are proportional to the core volume, are increased (cf. Chapter 2) [22].
- ▶ The dielectric losses, originating from the insulation, are also decreasing the efficiency of the MV/MF transformer (cf. Chapter 7) [153, 154]. Moreover, the dielectric losses in the insulation can lead to thermal runaways.

5.2.3 Design Selection

Fig. 5.2 depicts the Pareto front (cf. Fig. 5.1(a)) for the relevant power density and efficiency ranges. From the optimization results, it can be identified that frequencies above 50 kHz are suboptimal since a small reduction of the transformer losses would be compensated by an increase of the semiconductor switching losses [111, 111, 198]. Therefore, a switching frequency of 48 kHz

is selected. Moreover, this frequency (48 kHz instead of 50 kHz) is advantageous for respecting EMI standards, which can apply to the LV side of the converter [257, 258].

It should be noted that the obtained design space is restricted by the available core shapes and litz wire diameters, which are not considered during the Pareto optimization. Considering these limitations, the following design has been selected:

- ▶ *Core* - The magnetic core is composed of three “U93/60/30” ferrite core sets stacked together [256]. For obtaining an optimal filling factor, the limbs of a standard “U93/76/30” core are cut in order to obtain the desired “U93/60/30” core [256]. It should be noted that, theoretically, designs based on E-cores feature slightly higher power densities. Nevertheless, a design based on U-cores has been selected due to the improved cooling capability of U-core transformers (larger exposed area of the winding package). Moreover, the winding window of typical E-cores is too narrow for accommodating the MV insulation.
- ▶ *Windings* - A turns ratio of 52 : 6 is selected. The LV and MV windings are realized with a $2500 \times 100 \mu\text{m}$ litz wire and a $630 \times 71 \mu\text{m}$ litz wire, respectively. The LV winding is arranged on one layer and the MV winding on three layers.

The aforementioned analytical method is applied to the selected design and an efficiency of 99.67 % is obtained with a power density of 9.6 kW/l (cf. Fig. 5.2). The peak flux density in the core is 125 mT, the RMS current density is 3.7 A/mm² for the LV winding and 3.3 A/mm² for the MV winding. The ratio between the core and the winding losses is close to one, which is slightly higher than the theoretical optimum (cf. Chapter 2) [22]. This trade-off is made in order to obtain reduced winding losses at the cost of slightly increased core losses. The reason behind this choice is the increased thermal resistance of the windings (due to the MV insulation) compared to the low thermal resistance of the ferrite core.

At a power density of 9.6 kW/l and an operating frequency of 50 kHz, the maximum power density achievable in the optimization is 99.70 % and the selected design achieves 99.67 %. This implies that the availability of core shapes and litz wire diameters is only marginally impacting the achieved performance (0.03 %). This can be explained by the design space diversity of MF transformers (cf. Chapter 2), which offers many possibilities to accommodate the available parameters and components [22].

Tab. 5.3: Parameters of the MV/MF Transformer

| Parameter | Value |
|----------------------|---|
| Frequency | 48.0 kHz |
| Windings | 52 : 6 turns / litz wire / shell-type |
| MV wire | 630 × 71 μm / three layers / two chambers |
| LV wire | 2500 × 100 μm / single layer |
| Core type | Ferrite BFM8 / 3 × U93/60/30 / 2500 mm ² |
| Air gaps | 2 × 1.1 mm |
| Insulation type | Dry-type / vacuum potting |
| Insulation material | Silicone / “Dow Corning TC4605 HLV” |
| Insulation thickness | 4.0 mm (around the MV winding) |
| Insulation rating | 15 kV (CM voltage) |
| Boxed volume | 2.6 l (transformer) |
| Boxed volume | 3.4 l (transformer, fan, and terminations) |
| Mass | 6.2 kg (transformer, fan, and terminations) |

5.3 Design and Construction

The section describes the design the transformer from the selected specifications (e.g., concerning geometry, coil formers, and terminations). Afterwards, the construction process of the transformer is described with a special focus on the insulation design. The vacuum potting process of the windings is also described in detail.

5.3.1 Transformer Design

Fig. 5.3 shows the transformer CAD design and Tab. 5.3 depicts the corresponding design parameters. As explained above, the design is based on a U-core configuration with shell-type arrangement. The key considerations, leading to such a design, are listed as follows:

- ▶ The three U-cores (“U93/60/30”) are stacked together [256]. A distance (1 mm) is kept between the stacked cores for taking the geometrical tolerances of the cores into considerations. Moreover, this distance decouples the resonance modes of the ferrite cores (dimensional resonance), which can be critical for large ferrite cores [259, 260].

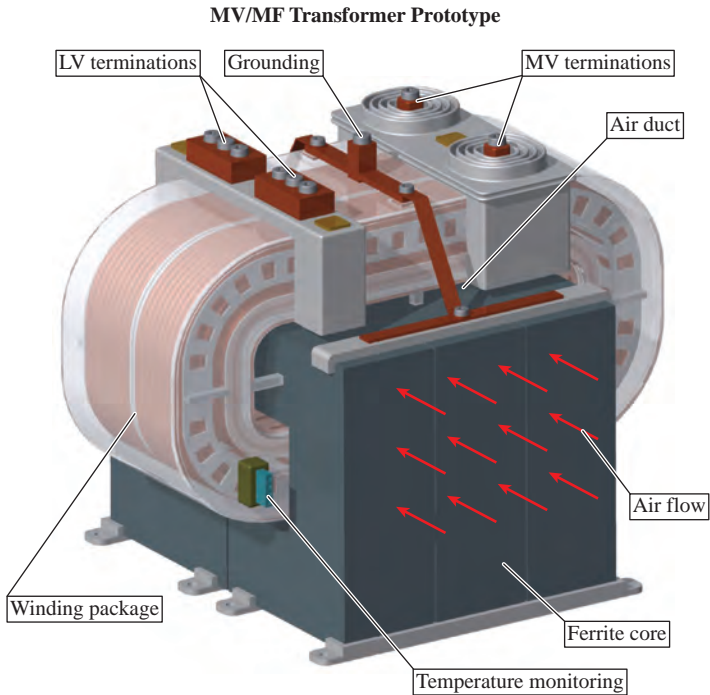


Fig. 5.3: CAD rendering of the MV/MF transformer. For the rendering, a transparent winding package is considered, even if the used material is, in reality, not transparent. The fan providing forced air cooling is not shown in this picture.

- ▶ In order to obtain enough current for ZVS, the magnetizing inductance of the transformer should be reduced. For this reason, an air gap (2×1.1 mm) is introduced between the core halves (for both limbs). The air gap also ensures an equal flux sharing between the core sets [25, 27].
- ▶ The ferrite cores (all core sets) are grounded with respect to the LV side of the DC-DC converter. This is required to prevent large voltages to appear on the core, which would cause insulation issues for the LV winding. Such voltages can originate from AC capacitive coupling or from DC leakage currents. Contacting ferrite cores is a difficult task and it has been found that using a silver-based epoxy glue (“MG Chemicals 8331”) produces the best results [261].
- ▶ The complete winding package is encapsulated in a plastic cover. Air channels (4 mm) are placed between the core window and the winding package. These air channels are used for the cooling of the winding, where a single 120 mm fan is used (“NMB 11925SA-12Q”) for creating the air flow [262]. Moreover, these air channels are limiting the thermal and capacitive couplings between the winding package and the core.

Due to the electrical insulation constraints, the realization of the winding package is especially critical. Fig. 5.4 shows the assembly of the winding package and Fig. 5.5 depicts the winding package geometry and the winding scheme in detail. The insulation concept is described as follows:

- ▶ The LV winding is placed near the core limb (cf. Fig. 5.4) for several reasons: this winding arrangement improves the cooling of the MV winding, which is critical [63, 139]. Furthermore, the capacitance between the MV winding and the core is reduced, and the realization of the MV cable terminations is facilitated.
- ▶ The LV winding is placed directly on a 3D printed polycarbonate coil former (cf. Fig. 5.5) [263]. The litz wire is directly composed of the bare strands (no wrapping) [264]. The original wrapping of the litz wire (Mylar) has been removed in order to allow for the potting material (silicone) to flow inside the litz wire for improving the thermal conductivity. Afterwards, Mylar foils are placed between the turns for guaranteeing the DM insulation. No additional MV insulation (except the coil former) is required between the LV winding and the core since the core is grounded with respect to the LV side.

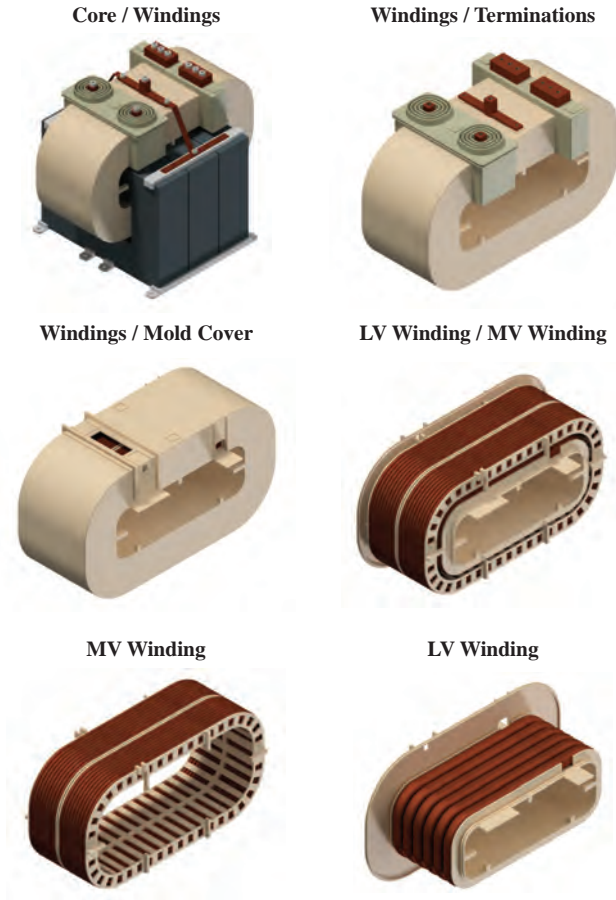


Fig. 5.4: Step-by-step assembly of the MV/MF transformer, where the magnetic core, the winding terminations, the grounding bars, the coil formers, the windings, and the potting mold are shown.

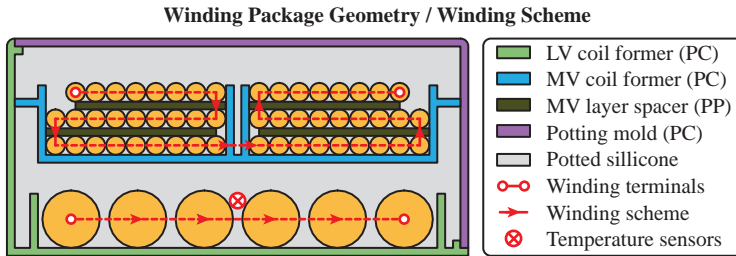


Fig. 5.5: Cut view of the transformer windings. The different coil formers and insulation materials are shown. Moreover, the winding scheme is highlighted. Different insulation materials are used: polycarbonate (“PC”), polypropylene (“PP”), and silicone.

- ▶ Two NTC temperature sensors “Vishay NTCS0805E3104FXT” are placed inside the windings [265]. These sensors are placed between the LV winding and the MV winding inside the core window, where the highest temperatures are expected. The NTC sensors are positioned right next to the LV winding, such that the LV litz wires are shielding the sensors from the electric field coming from the MV winding (cf. Fig. 5.5).
- ▶ The MV winding is wound on a 3D printed polycarbonate coil former (cf. Fig. 5.5) [263]. The considered litz wire features a nylon wrapping, which together with the insulating capabilities of the strands, guarantees the insulation between the turns [266]. Such a wrapping (nylon thread) allows the potting material (silicone) to flow inside the litz wire in order to improve the thermal performance and prevent cavities inside the winding. The MV winding is divided in two chambers and three layers (cf. Fig. 5.5). Such a winding scheme reduces the voltage stress between the layers and the winding capacitance [155]. Windings with more than two chambers are suboptimal due to the space required by the walls placed between the chambers. Moreover, a construction with two chambers and three layers features two key practical advantages. First, the winding process is started between the chambers and no crossing of the wires between the layers is required. Secondly, the fact that both winding terminals are located outside the transformer facilitates the realization of the MV cable terminations (no crossing required). Polypropylene spacers are placed between the layers for the

DM insulation, where the material has been chosen for its low losses and high breakdown strength [267].

- ▶ The two coil formers with the corresponding windings are assembled concentrically where the insulation distances are guaranteed by spacers, without producing critical creepage paths. Finally, a mold cover (3D printed polycarbonate) is placed over both windings in order to close the winding package. The assembly of the two coil formers is shown in Fig. 5.4.
- ▶ All the terminations (MV winding, LV winding, and ground) are placed at the top of the transformer, near the winding head. The litz wires are soldered with copper screw contacts, which feature low losses, as analyzed in [27, 186, 242]. The MV cable terminations respect the required creepage and clearance distances. The LV cable terminations are built for allowing the direct connection of coplanar busbars. Polycarbonate covers are placed on top of the cable terminations (cf. Fig. 5.4) [263].
- ▶ Finally, the complete winding package (coil former, winding, and terminations) is potted with a vacuum process. The silicone elastomer “Dow Corning TC4605 HLV” has been chosen for its reduced losses and high thermal conductivity (cf. Chapter 7) [154, 268]. The different parts, and more particularly the MV coil former, are designed such that the potting material can easily flow everywhere.

In the course of the design, the maximum operating temperature of the different components should be examined. The magnetic core should be kept under 120 °C for limiting the losses [256]. The maximum operating temperatures of the different elements composing the winding package are extracted from the datasheets: 155 °C for the litz wires [264, 266], 200 °C for the silicone [268], 138 °C for the polycarbonate coil formers [263], and 121 °C for the polypropylene spacers [267]. Therefore, the maximum operating temperature of the transformer is 120 °C.

It should be noted that the volume of cable terminations and the fan, which were not considered in the optimization process, increases the boxed volume from 2.6 l to 3.4 l and, therefore, reduces the power density from 9.6 kW/l to 7.4 kW/l (cf. Fig. 5.2). The total mass of the transformer is 6.2 kg, which leads to a gravimetric power density of 4.0 kW/kg. However, the mass of the transformer was not considered as an objective during the optimization process.

Tab. 5.4: Creepage and Clearance of the MV/MF Transformer

| Type | Value |
|-----------|--|
| Clearance | Prototype values |
| | 40.0 mm (between MV terminals) 37.0 mm (between MV terminals and ground) |
| Clearance | IEC 60950-1 (primary circuit) [269] |
| | 17.5 mm for 7.0 kV (peak) / 4.9 kV (RMS) |
| | 37.0 mm for 14.0 kV (peak) / 9.9 kV (RMS) |
| Creepage | Prototype values |
| | 120.0 mm (between MV terminals) 87.0 mm (between MV terminals and ground) |
| | IEC 60950-1 (pollution degree 2, material group II) [269] |
| Creepage | 36 mm for 7.1 kV (peak) / 5.0 kV (RMS) |
| | 56 mm for 11.3 kV (peak) / 8.0 kV (RMS) |
| | 90 mm for 17.7 kV (peak) / 12.5 kV (RMS) |

5.3.2 Insulation Capabilities

The MV insulation capabilities of the transformer should also be examined. Creepage and clearance distances in the air are only present between the terminals since the complete winding package is encapsulated in silicone. The norm IEC 60950-1 determines the applicable values, where it should be noted that PWM voltages are not directly considered in the norm [269]. Tab. 5.4 shows the creepage and clearance distances of the prototype and compares the obtained value to the norm. It appears that the selected distances are sufficient for a peak voltage of 14 kV, which is significantly above the maximum operating voltage of 7 kV (cf. Subsection 1.7.2).

The DM voltage level, inside the insulation, is limited by the insulation between two layers of the MV winding. The total DM voltage is 3.5 kV and the maximum voltage between two layers is 1.2 kV (two chambers and three layers are used). The insulation thickness between the layers is 0.8 mm and, therefore, the electric field is approximately 1.5 kV/mm. This value is much lower than the breakdown electric field of the polypropylene spacers (40 kV/mm) and the silicone potting material (24 kV/mm) [267, 268]. The voltage between two turns is 66 V and, therefore, well below the breakdown voltage of the litz wire insulation [266].

The CM insulation capabilities are an important aspect of the transformer. The CM voltages applied to the insulation can have multiple origins: the selected converter topology (e.g., split DC-bus half-bridge configuration), the nodes used for the grounding of the power electronic bridges (e.g., DC-bus midpoint, DC-bus negative rail, AC-DC front-end), and/or the grounding schemes of the different grids (e.g., solid-earthing, resistive earthing, or unearthed operation). The CM voltages applied to the considered SST demonstrator are analyzed in detail in Chapter 6 and Chapter 7 [143, 154]. The thickness of the CM insulation, placed around the MV winding, is 4 mm. However, due to prototyping constraints, the polycarbonate coil formers are realized with 3D printing and, therefore, cannot be considered as a reliable insulation material [263]. Hence, only the 3 mm of silicone insulation (given that the coil former thicknesses is 1 mm) are considered for the evaluation of the insulation stress. With the desired CM insulation capability, which has been fixed to 15 kV, an electric field of 5 kV/mm is obtained. This value is much lower than the limit of the silicone potting material (24 kV/mm) [268].

The comparison between the breakdown electric field and the applied electric field should be considered with care. The electric field in the insulation is not homogeneous and local hot spots can exist. Furthermore, the breakdown voltage can be lowered by several factors such as aging, partial discharges, thermal stress, and dielectric losses [146, 148, 149, 151, 192, 193, 270]. Finally, a critical impact of the MV/MF PWM voltages with fast transitions has been identified in [146–149, 152, 170]. Therefore, the electric field in the insulation should be well below the breakdown electric field. Chapter 6 and Chapter 7 analyze the electric field distribution and the dielectric losses in the insulation in more detail [143, 154].

Moreover, the transformer should be able, eventually, to deal with surge overvoltages during abnormal situations [79, 80, 142, 271]. For the considered AC grid voltage (cf. Subsection 1.7.2), with a phase-to-neutral RMS voltage of 3.8 kV (6.6 kV phase-to-phase RMS voltage), a lightning surge level of 60 kV (IEC 1.2/50 μ s surge) and an applied voltage test of 20 kV (RMS value for 60 s), as specified in [272]. Nevertheless, this standard is meant for LF transformers and is not directly applicable to SSTs [79, 80]. A new standard, which was not yet published during the design process of the considered transformer, exists for MV power converters but is only applicable to complete converter systems and not specifically to MF transformers [273]. For these reasons, the surge rating of the transformer is not further examined.

5.3.3 Construction and Vacuum Potting

Fig. 5.6 depicts the assembly process of the winding package and Fig. 5.7 shows the realized prototype. The realization and the vacuum pressure potting of the winding package are critical for obtaining a reliable electrical insulation and are described in the following. During the complete construction process of the winding package, the presence of dust should be avoided since it can compromise the quality of the insulation. Moreover, the materials, adhesives, and solvents used during the construction process should be carefully checked together with the silicone rubber (“Dow Corning TC4605 HLV”) used for the potting [268]. Many chemicals, such as amines, amides, nitriles, and alcohols, can inhibit partially or totally the curing of the silicone [274]. More specifically, many cyanoacrylate-based instant adhesives and UV-curing adhesives have been identified as unsuitable for the realization of the winding package. The cyanoacrylate two-component instant adhesive “Loctite 3090” has been found to be compatible with the used silicone rubber [275].

After the assembly of the winding package, two pipes are glued to the extremities in order to create the inlet and outlet for the potting process. For the considered vacuum potting process, the winding package is placed into a vacuum vessel. Hence, a perfect sealing of the coil former is not required since the winding package itself is not used as a vacuum vessel. However, the sealing tightness of the winding package should be good enough for preventing any leakage of the liquid silicone before the curing. The sealing tightness of the coil former has been checked with the injection of pressurized air between the inlet and outlet.

Fig. 5.8 depicts, schematically, the silicone vacuum pressure potting process and Fig. 5.9 shows the utilized setup. This process guarantees a winding package, which is free of cavities or other imperfections, in order to prevent partial discharges and breakdowns. The vacuum pressure potting process can be described as follows:

- ▶ First, the two components composing the silicone are mixed [268]. The “Dow Corning TC4605 HLV” silicone contains a filler in order to increase the thermal conductivity [268]. Therefore, an electric mixer is required in order to obtain a homogeneous liquid silicone.
- ▶ The liquid silicone is placed in the right vacuum vessel and the winding package and the collecting tray are accommodated in the left vacuum vessel. The valves 2 and 5 are closed and the valves 1, 3, 4, and 6 are opened. With a vacuum pump, both vessels are evacuated down to a pressure of 30 mbar. Since there is no silicone in the collecting tray,

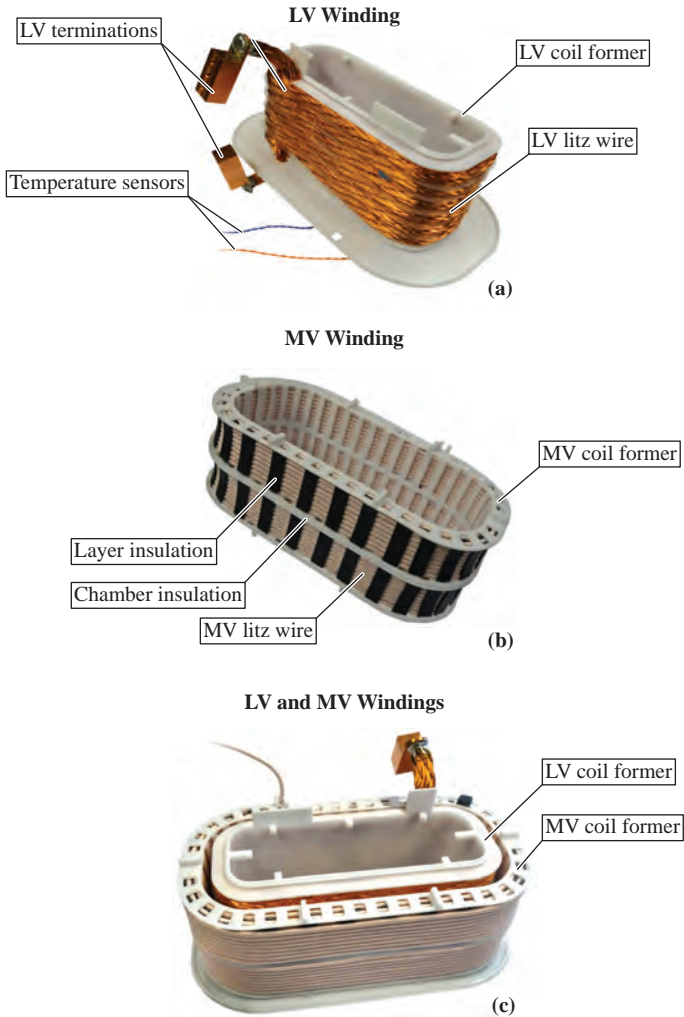


Fig. 5.6: Step-by-step assembly of the MV/MF transformer prototype: (a) LV winding, (b) MV winding, and (c) LV and MV windings.

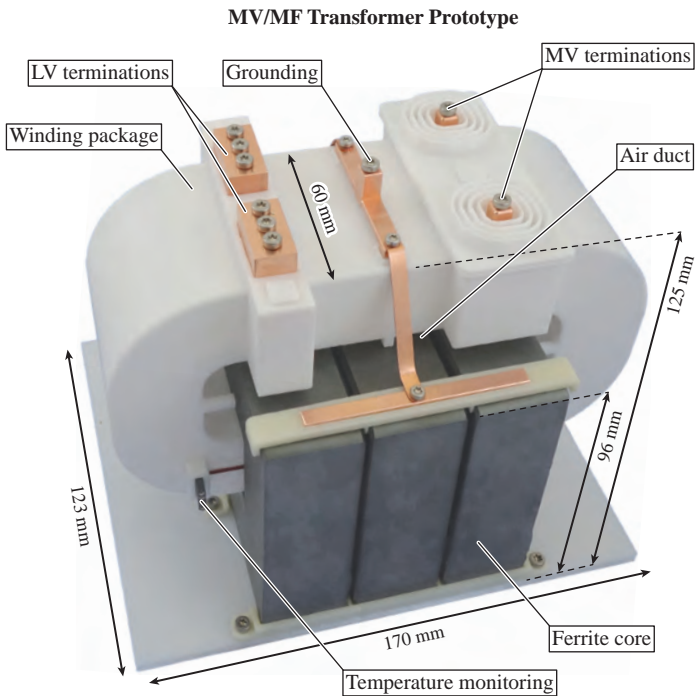


Fig. 5.7: Picture of the completed MV/MF transformer prototype. The dimensions of the transformer are given in the figure. The fan providing forced air cooling is not shown in this picture.

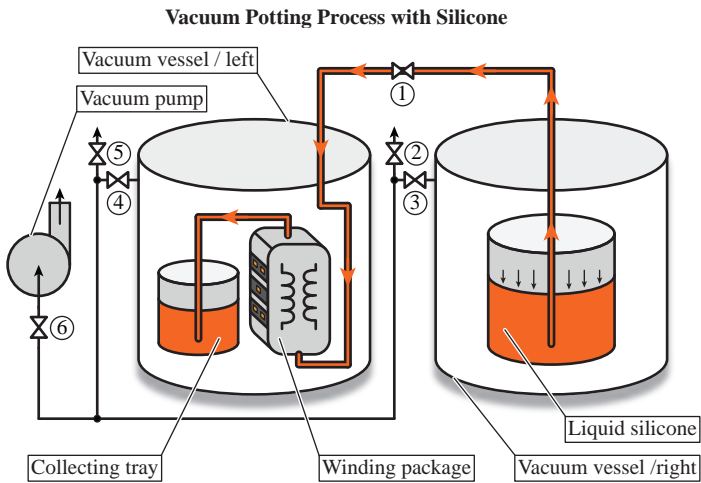


Fig. 5.8: Schematic drawing of the silicone vacuum pressure potting process. First, the air is evacuated to devolatilize the liquid silicone, for both vessels. Then, the pressure in the right vessel is slightly increased, pressing the silicone through the tubes into the sealed winding package. When the winding package is full, the silicone flows into a collecting tray. After the filling process, the pressure is increased to the atmospheric pressure again, in order to compress possible vacuum cavities. Finally, the silicone is cured in an oven.

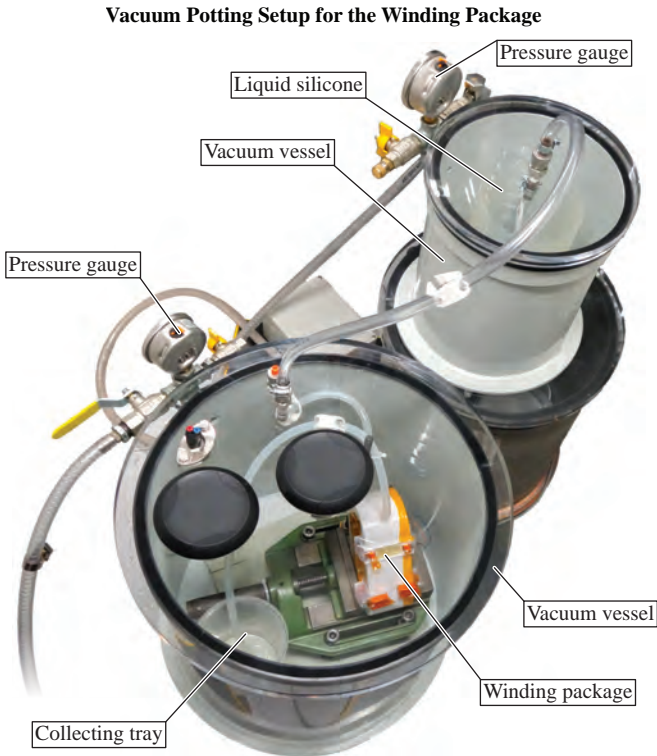


Fig. 5.9: Picture of the silicone vacuum pressure potting setup for the transformer winding package. The vessel containing the liquid silicone and the vessel containing the winding package and the collecting tray can be seen.

the pipes and the winding package are evacuated as well. It should be noted that a too high vacuum is not desirable since some compounds of the silicone would start to vaporize.

- ▶ After a certain time (ca. 10 minutes), when the liquid silicone is de-volatilized, valves 4 and 6 are closed. The pressure in the right vacuum vessel is then slightly increased by slowly and shortly opening the valve 2. The pressure difference between the two vessels presses the liquid silicone into the pipes. A pressure difference of ca. 300 mbar is required for this process.

- ▶ The liquid silicone starts to flow into the winding package. The inlet is placed at the bottom of the winding package and the outlet at the top, such that the potting process is done against the gravitational force. This guarantees that, when the silicone starts to flow out from the outlet, the winding package is completely filled.

- ▶ To remove possible cavities inside the winding package, the potting process continues until ca. 300 ml of liquid silicone are present in the collecting tray. At this point, the valve 1 is closed for preventing the silicone the flow further. Then the valves 2, 4, and 5 are opened and both vessels are pressurized again to atmospheric pressure, compressing possible vacuum cavities inside the winding package. This process should be done slowly in order to avoid any brutal (de)compression of the vacuum vessels.

- ▶ The vacuum vessels are opened, and the tubes entering and leaving the winding package are clamped to avoid any further flow of the silicone. During this process, the pipe ending into the collecting tray should remain immersed in order to prevent air to go into the winding package.

- ▶ Finally, the winding package is cured for several hours (at least 4 hours) at 120 °C in order to cure the silicone and to activate the adhesion of the silicone to the coil formers and litz wires. This is necessary to avoid voids between the insulation and the windings (delamination). The best results regarding adhesion are achieved when the temperature is applied immediately after the potting process

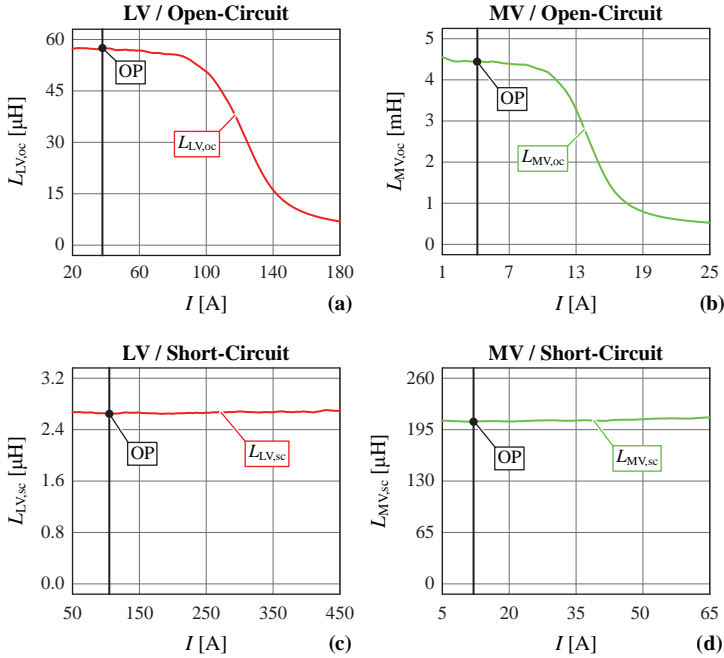


Fig. 5.10: Open-circuit and short-circuit small-signal differential inductances for different bias currents [237]. (a) LV winding open-circuit, (b) MV winding open-circuit, (c) LV winding short-circuit, and (d) MV winding short-circuit. The maximal peak currents, during nominal operation, are marked with a black dot (“OP”).

5.4 Experimental Testing

The section describes the experimental testing of the realized prototype. First, the short-circuit behavior, the saturation limit, and the impedances (inductances and capacitances) are examined. Afterwards, the impact of the resonances on the operation of the transformer is studied. Finally, the insulation testing and the thermal model are described. The different measurements are compared to FEM simulations.

5.4.1 Short-Circuit and Saturation

The short-circuit and open-circuit behaviors of the transformer have been measured with an “ed-k DPG10/1000A” power choke tester [237]. Fig. 5.10 depicts

Tab. 5.5: Large Signal Parameters of the MV/MF Transformer

| Parameter | Meas. | Sim. | Error |
|--------------------|---------------------|---------------------|-------|
| LV / open-circuit | 57.1 μH | 62.3 μH | 9.1 % |
| MV / open-circuit | 4.44 mH | 4.68 mH | 5.4 % |
| LV / short-circuit | 2.65 μH | 2.46 μH | 7.2 % |
| MV / short-circuit | 205.2 μH | 185.1 μH | 9.8 % |

the obtained small-signal differential inductances for different bias currents. As expected, the transformer is operated far away from the saturation limit. Moreover, the transformer is able to withstand short-circuit currents which are significantly larger than the nominal currents. The nominal currents are computed in Chapter 8 [88].

The inductance values are extracted from the measurements at the nominal peak current and compared to the results obtained from FEM simulations [228]. Tab. 5.5 shows the obtained results. For all measurements, the error between the simulations and the measurements is below 10 %. Moreover, it is concluded that the obtained magnetizing current (ca. 4 A) and magnetic coupling factor (ca. 97 %) match the specifications fixed in Tab. 5.1.

5.4.2 Impedance Measurements

The short-circuit and open-circuit impedances have been measured, from the LV and MV side, with an “Agilent 4924A” precision impedance analyzer [236]. Moreover, the CM impedances across the galvanic insulation are also critical parameters for a MV/MF transformer. Therefore, the following CM impedances have been measured:

- ▶ *Core to MV+LV* - The CM impedance is measured with respect to the ground. The first electrode is composed of the LV and MV windings, which are connected together, and the second electrode represents the magnetic core. This capacitance is shown for the sake of completeness but is not excited during the operation of the converter since the core is grounded together with the LV side of the converter.
- ▶ *MV to LV+Core* - The CM impedance is measured with respect to the MV winding. The first electrode is composed of the LV winding and the magnetic core, which are connected together, and the second electrode

Tab. 5.6: Small Signal Parameters of the MV/MF Transformer

| Parameter | Meas. | Sim. | Error |
|--------------------|---------------------|---------------------|--------|
| LV / open-circuit | 57.1 μH | 62.3 μH | 9.1 % |
| MV / open-circuit | 4.36 mH | 4.68 mH | 7.3 % |
| LV / short-circuit | 2.69 μH | 2.46 μH | 8.5 % |
| MV / short-circuit | 203.3 μH | 185.1 μH | 8.9 % |
| CM / Core to MV+LV | 54.9 pF | 62.3 pF | 13.5 % |
| CM / MV to LV+Core | 139.3 pF | 149.8 pF | 7.5 % |

represents the MV winding. This impedance characterizes the relevant CM path during a CM excitation of the MV winding.

Fig. 5.11 depicts the obtained results. The inductance and capacitance values are extracted from the measurements at the switching frequency (48 kHz) and compared to the results obtained from FEM simulations [228]. Tab. 5.6 shows the obtained results. For all measurements, the error between the simulations and the measurements is below 10 % for the inductances and below 15 % for the CM capacitances.

5.4.3 Resonances

In Fig. 5.11, different resonances can be observed above the switching frequency (48 kHz). These resonances can be excited by the harmonics contained in the PWM voltages applied to the transformer and, therefore, should be examined in detail [156, 159–161]. Resonances can also produce EMI issues, additional losses, and can lead to critical insulation stress (uneven voltage sharing between the turns) [155, 156, 276]. For analyzing the resonances, it should be noted that the transformer is operated inside a SRC-DCX (cf. Subsection 1.7.2). In such a converter, the transformer is placed between two power electronic bridges, which represent voltage sources.

For open-circuit operation (cf. Figs. 5.11(a)-(b)), the first resonance occurs at 340 kHz. However, this resonance features a high impedance (parallel resonance) and, therefore, no oscillations can occur when the circuit is fed by a voltage source. The first critical resonance (series resonance) occurs at 1.5 MHz, when the circuit is fed on the LV side. This case is shown in Fig. 5.12, where the LV winding is fed by an inverter (LV bridge of the SRC-DCX, cf. Subsection 1.7.2) with an open-circuited MV winding. Massive oscillations

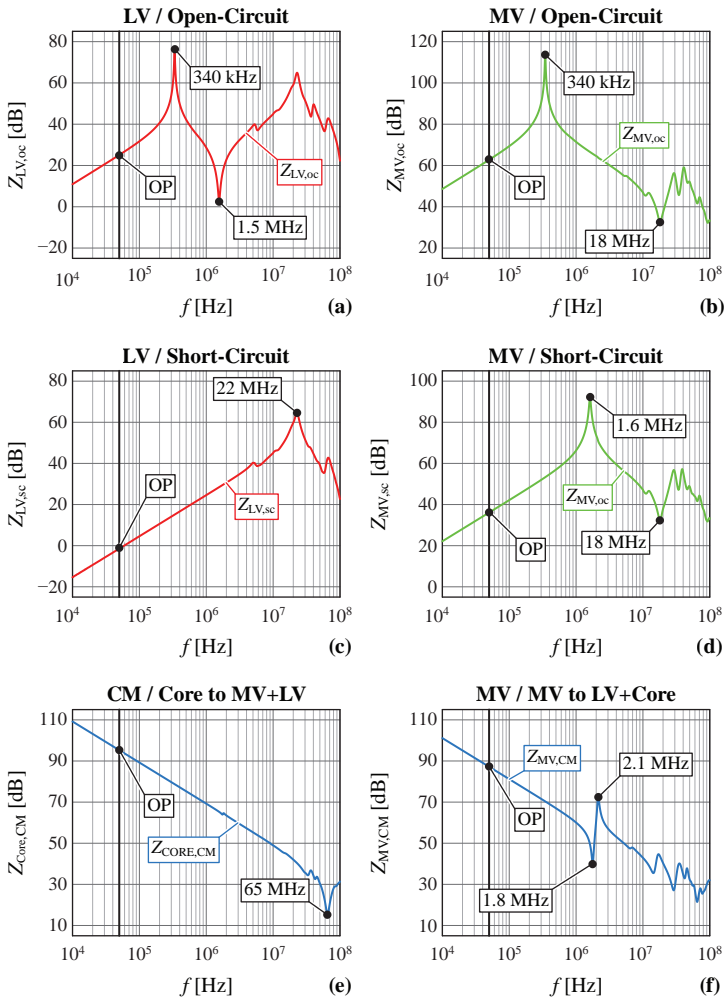


Fig. 5.11: Open-circuit, short-circuit, and CM impedance for different frequencies [236]. (a) LV winding open-circuit, (b) MV winding open-circuit, (c) LV winding short-circuit, (d) MV winding short-circuit, (e) CM capacitance with respect to the core, and (d) CM capacitance with respect to the MV winding. The switching frequency (48 kHz) is marked with a black dot (“OP”). The different resonance frequencies are also labeled.

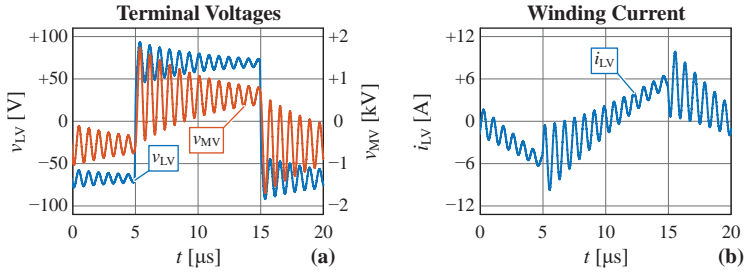


Fig. 5.12: (a) Measured voltages and (b) current during open-circuit operation. The LV side is fed by an inverter (50 kHz) with an open-circuited MV winding. The duration of the switching transitions is 130 ns. The oscillations, occurring after the switching transitions, feature a frequency of 1.4 MHz. Due to the linearity of the equivalent circuit, an arbitrary test voltage can be chosen.

are present at 1.4 MHz, which is close to the measured resonance frequency of 1.5 MHz. The deviation can be explained by the busbar inductance and the capacitance of the voltage probes. The oscillations are so large that the inverter voltage, which is connected to the LV winding, is also ringing. However, inside the SRC-DCX, the transformer is operated between two voltage sources. Therefore, the open-circuit resonances of the transformer are not excited inside the converter and are not critical.

For short-circuit operation (cf. Figs. 5.11(c)-(d)), the resonances occurring at 1.6 MHz and 22 MHz feature high impedances (parallel resonances) and, again, no oscillations can occur when the circuit is fed by a voltage source. The first critical resonance (series resonance) occurs at 18 MHz, when the circuit is fed on the MV side. The case is shown in Fig. 5.13, where the MV winding is fed by an inverter (LV bridge of the SRC-DCX, cf. Subsection 1.7.2) with a short-circuited LV winding. Even if the switching transition duration (150 ns) is much faster than the values obtained with the MV SiC MOSFETs, no oscillations are occurring [111, 112]. This implies that the short-circuit resonances, which are critical for the operation of the transformer inside the SRC-DCX, are not problematic for the realized prototype [156].

For the CM resonance (cf. Figs. 5.11(f)), the first critical frequency is located at 1.8 MHz. At this frequency, the CM impedance is extremely low, leading to a quasi-short-circuit across the galvanic insulation. Fig. 5.14 shows the measurement results where the CM capacitance between the MV and LV windings is excited by an inverter (MV bridge of the SRC-DCX, cf. Subsection 1.7.2). For this test, the magnetic core is connected with the LV winding,

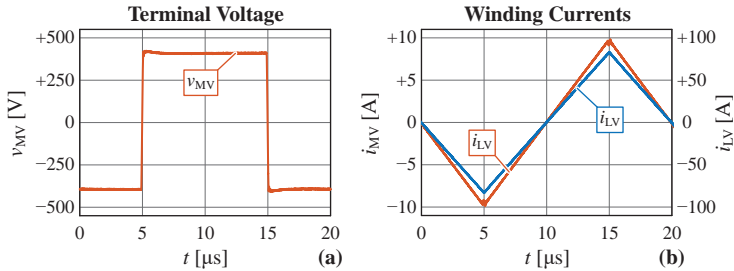


Fig. 5.13: (a) Measured voltage and (b) currents during short-circuit operation. The MV side is fed by an inverter (50 kHz) with a short-circuited LV winding. The duration of the switching transitions is 150 ns. Due to the linearity of the equivalent circuit, an arbitrary test voltage can be chosen.

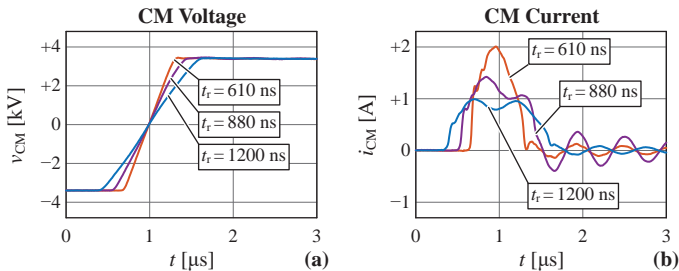


Fig. 5.14: (a) Measured voltage and (b) current during a CM transient applied between the MV and LV windings. The magnetic core is connected with the LV winding. Different switching transition durations are considered. The oscillations, occurring after the switching transition, feature a frequency of 1.8 MHz.

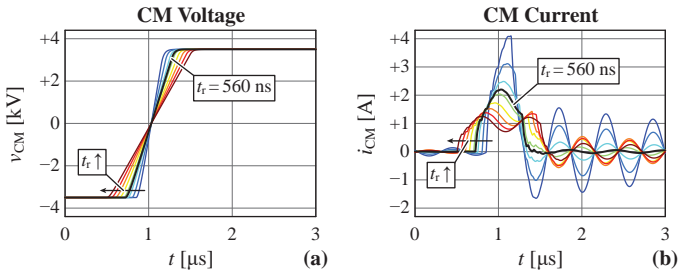


Fig. 5.15: (a) Simulated voltage and (b) current during a CM transient applied between the MV and LV windings. The magnetic core is connected with the LV winding. Different switching transition durations are considered between 300 ns and 1000 ns.

which also represents the operating condition occurring in the SRC-DCX. The switching speed of the MOSFETs is adjusted with the ZVS current, which is provided by a parallel inductor featuring an adjustable air gap. During the switching transition, the displacement current across the insulation is measured. After the end of the switching transition, oscillations at 1.8 MHz are visible. However, it should be noted that these oscillations are below 0.4 A, which is thirty times smaller than the peak load current flowing on the MV side.

In Fig. 5.14, it can be seen, as expected, that the amplitude of the current peak during the switching transition depends directly on the switching speed. However, the amplitude of the oscillations, occurring during and after the switching transitions, are not directly related to the switching speed. For example, the oscillations are larger for a switching transition duration of 880 ns compared to 610 ns or 1200 ns. This phenomenon is analyzed in Fig. 5.15 by simulations. Voltage transitions with different durations are applied and the currents are reconstructed, in frequency domain, using the curve measured in Fig. 5.11(f). It can be seen that the oscillations are minimum for a switching duration of 560 ns. With this switching duration, only one period of the oscillation is present ($1/1.8 \text{ MHz} \approx 560 \text{ ns}$). Therefore, at the end of the switching transition, the resonant current is zero and can be immediately interrupted.

It can be concluded that the transformer exhibits open-circuit oscillations, which, however, are not excited with the considered SRC-DCX. The short-circuit resonances are occurring at HF and, therefore, are not critical. Small CM resonances are occurring but can be suppressed by an appropriate choice

Tab. 5.7: Insulation Test Voltages of the MV/MF Transformer

| Type | Value |
|------|----------------------------------|
| CM | ± 15.0 kV DC |
| CM | ± 15 kV AC (peak) / 50 Hz |
| CM | ± 3.8 kV AC (peak) / 50 kHz |
| CM | ± 3.8 kV AC (peak) / 100 kHz |
| CM | ± 3.5 kV PWM / 50 kHz |
| DM | ± 3.8 kV AC (peak) / 50 kHz |
| DM | ± 3.8 kV AC (peak) / 100 kHz |
| DM | ± 3.5 kV PWM / 50 kHz |

of the switching transition duration. Finally, it should be noted that the capacitive currents flowing during a switching transition, even if they are not critical, are subtracted from the current available for ZVS. Nevertheless, it can be seen in Fig. 5.13 and Fig. 5.14 that the capacitive currents are small compared to the nominal currents.

5.4.4 Insulation Testing

First, the DC insulation resistance has been measured with a “Megger MIT₄₁₀” insulation tester [277]. A resistance of 25 G Ω has been measured between the MV winding and the LV winding (the magnetic core is connected with the LV winding). This represents a leakage current of 280 nA for an applied voltage of 7 kV. The measured resistance is significantly higher (more than a hundred times) than the minimum values specified in [278, 279] for electrical machines. However, the DC resistance of a new insulation system is only a poor indicator of the quality of the insulation [278]. Therefore, the DC leakage resistance only indicates that the insulation does not feature obvious flaws and that the potting process is properly done.

The CM insulation of the transformer is tested between the MV winding and the LV winding. During this test, the magnetic core is connected with the LV winding. The DM insulation of the MV winding has also been tested. The considered voltage levels, waveforms, and frequencies, which are equal or greater than the applied voltages during nominal operations, are summarized in Tab. 5.7. The transformer prototype has not been tested with higher voltages to avoid an eventual destruction of the unique prototype. However, such tests

have been performed on a test coil featuring the same insulation material (“Dow Corning TC4605 HLV”) and the same vacuum potting process [268]. This test coil features an insulation gap of 1.6 mm (silicone) and has been successfully tested for one hour with 20 kV DC [268]. This implies that the realized prototype, which features an insulation gap of 4 mm (3 mm of silicone and 1 mm of polycarbonate) should be able to withstand at least 30 kV of CM voltage [263, 268].

The measurement of partial discharges is a complex process and the interpretation of the partial discharge patterns requires empirical knowledge, which is not yet available for MV/MF transformers [280–282]. Furthermore, it has been shown, for electric drives, that the presence of MF PWM voltages has a critical impact on the partial discharges, such that the measurements cannot be conducted with standard setups [148, 149, 270, 282, 283]. Additionally, the coil formers of the prototype are realized with a 3D printer, due to fast prototyping constraints. In [284], it has been identified that such materials feature voids (pores), which are critical for partial discharges. Therefore, for partial discharge measurements, another prototype should be realized, where an industrial process (e.g., injection moulding) is used for realizing the coil former. For all these reasons, partial discharge tests have not been carried with the prototype. However, the peak electric field values simulated in Chapter 7 are below 23 kV/cm inside the insulation and below 19 kV/cm at the surface of the insulation, which is lower than the ionization electric field of air (ca. 25 kV/cm) [142, 154, 285, 286]. Therefore, partial discharges and surface discharges are not expected during rated operation [142, 287, 288]. Furthermore, the electric field at the surface of the insulation could be further reduced with the shielding concept presented in Chapter 6 [143].

5.4.5 Thermal Model

The thermal model of the transformer is based on FEM simulations [25, 139, 228]. Inside the transformer, only heat conduction processes are present (potted winding package). The heat extraction from the winding package and the core to the ambient is done with a forced convection process. The characteristic curve (pressure flow diagram) of the considered fan (“NMB 11925SA-12Q”) is also integrated into the model [262].

The thermal performance of the prototype has been measured in a calorimeter, which features a controlled ambient temperature (water heat exchanger). For the measurements, four NTC temperature sensors are placed as shown in Fig. 5.16. It has been identified that NTCs are less sensitive

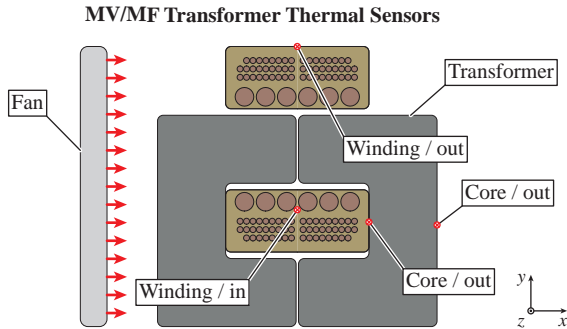


Fig. 5.16: Placement of the four NTC temperature sensors used to verify the thermal performance of the MV/MF transformer [265]. All four sensors are placed close to the middle of the transformer with respect to the z axis.

Tab. 5.8: Thermal Performance of the MV/MF Transformer

| Parameter | Meas. | Sim. |
|---|-------|-------|
| Short-circuit / 45 W winding losses / 50 °C amb. | | |
| Winding temperature / inside | 86 °C | 83 °C |
| Winding temperature / outside | 61 °C | 58 °C |
| Core temperature / inside | 66 °C | 63 °C |
| Core temperature / outside | 64 °C | 60 °C |
| Open-circuit / 41 W core losses / 40 °C amb. | | |
| Winding temperature / inside | 56 °C | 52 °C |
| Winding temperature / outside | 46 °C | 45 °C |
| Core temperature / inside | 65 °C | 60 °C |
| Core temperature / outside | 62 °C | 59 °C |

(compared to thermocouples) to electromagnetic disturbances originating from the PWM switching transitions. Due to the air channels placed between the winding package and the magnetic core, the thermal coupling between these two components is quite low. Therefore, the thermal model is verified with two different tests, which feature the following loss distributions:

- ▶ *Winding losses* - The transformer is operated in short-circuit (supplied from the MV side) and 45 W of winding losses are generated (in both windings). The ambient temperature is controlled to 50 °C and the fan of the transformer is running. The measured thermal time constant during this operating mode is ca. 19 min.
- ▶ *Core losses* - The transformer is operated in open-circuit (supplied from the LV side) and 41 W of core losses are generated. The small amount of winding losses, generated with the magnetizing current, are also considered. The ambient temperature is controlled to 40 °C and the fan of the transformer is running. The measured thermal time constant during this operating mode is ca. 18 min.

Tab. 5.8 shows the obtained temperature in steady-state. The maximum temperature deviation is 5 °C and the maximum relative error of the temperature elevation is 25 %. The considered winding and core losses match the expected losses during rated operation (83 W at 25 kW with an efficiency of 99.67 %). For estimating the temperature during rated operation, the temperature elevations shown in Tab. 5.8 are added (superposition principle), which represents a conservative approach. The obtained maximum temperature elevation is below 60 °C, which implies that the transformer is operated well below the thermal limit (120 °C). Moreover, the measured thermal time constant shows that the steady state is reached only after ca. 90 min. On the other hand, this indicates that the transformer could be massively overloaded for several minutes.

5.5 Losses Measurements

The section describes the measurements of the losses of the realized prototype (e.g., winding and core). Different measurement methods (electrical and calorimetric) are presented and compared to FEM simulations. Finally, the efficiency of transformer inside the SRC-DCX is considered.

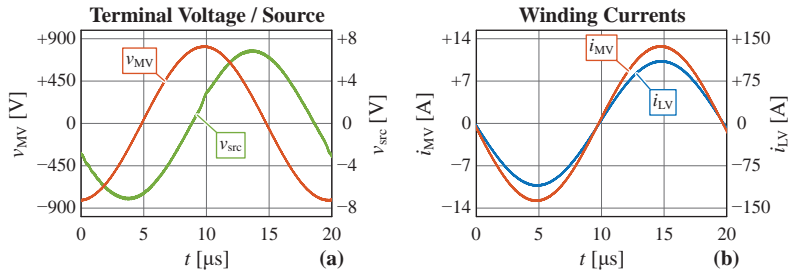


Fig. 5.17: (a) Measured MV side voltages and (b) winding currents during short-circuit operation at 50 kHz. The MV winding is fed with a short-circuited LV winding. The currents (i_{LV} and i_{MV}) are almost 90° phase shifted with respect to the voltage (v_{MV}). A series capacitor is used on the MV side to compensate the reactive power. Therefore, the voltage delivered by the source (v_{src}) is almost in phase with the currents and the losses can be easily measured.

5.5.1 Winding Losses

The winding losses are simulated with a hybrid method. The magnetic field in the winding window is extracted from FEM simulations [228]. Afterwards, the HF losses of the litz wires are computed with Bessel functions [19, 25, 78]. The considered litz wires respect the guidelines defined in Chapter 4, for the twisting scheme and the pitch length [135]. Therefore, perfectly twisted litz wires are assumed for the loss computations.

The winding losses of the prototype are measured during short-circuit operation. For limiting the current supplied by the source and the impact of parasitic busbar resistances, the transformer is supplied from the MV side and the LV winding is short-circuited. In the SRC-DCX (cf. Chapter 8), the currents applied to the transformer are quasi-sinusoidal [88]. Therefore, sinusoidal currents are considered for the measurements. The main challenge for the measurement of the winding resistance is the low power factor. The leakage inductance of the transformer is, due to the insulation distances, large. The expected power factor during short-circuit condition (at 48 kHz) is approximately equal to 0.008. Accordingly, small measurement errors can have a decisive impact on the achieved accuracy. Three different measurement methods are considered:

- *Impedance meas.* - The impedance is measured with an “Agilent 4924A” precision impedance analyzer [236]. For obtaining the resistance of the winding, the real part of the impedance is extracted. This measurement

is easy to obtain but features a limited accuracy due to the low power factor. Due to the linearity of the involved processes, the winding losses can be measured with reduced voltages and scaled afterwards.

- ▶ *Electrical meas.* - A series capacitor is placed in order to compensate the reactive power flowing in the leakage inductance. The system is fed by a linear amplifier, which is delivering the losses. Due to the reactive power compensation, the losses can be measured with high accuracy. However, the losses of the busbars and of the series capacitor are also measured. Therefore, low losses film capacitors are used for the reactive power compensation [289]. Fig. 5.17 depicts the measured waveforms.
- ▶ *Calorimetric meas.* - The complete transformer is placed in a calorimeter and the losses are measured in steady state [290]. A highly accurate calorimeter consisting of two isolated chambers with water cooling is used [291]. This method is the most accurate but also features the highest complexity and time requirement. For the different frequencies, the current amplitude is adapted in order to generate constant losses and, therefore, obtain similar temperature distributions.

Fig. 5.18 depicts the measured and simulated losses at different frequencies. A very good matching is observed between the measurements and the simulations. As expected, the calorimetric measurement method is the most accurate method. At the switching frequency (48 Hz), the error between the calorimetrically measured and the simulated losses is 6 % and the ratio between the AC and DC resistance is 1.23. Therefore, it can be concluded that the modeling of the winding losses of the transformer is correct and accurate.

5.5.2 Core Losses

The core losses are also simulated with a hybrid method. The magnetic flux in the core is extracted from FEM simulations [228]. Afterwards, the empirical iGSE equation is used for extracting the core losses [19, 128]. For the iGSE, the Steinmetz parameters of the core material are required (for sinusoidal excitation). The core losses have been measured for the considered material (“BLINZINGER BFM8”) with two “U93/60/30” core halves (without air gap) [256]. The core loss measurement method presented in [292, 293], which features a sensing winding for measuring the flux and a series capacitor for compensating the reactive power, is used. An error analysis shows that the uncertainty of this measurement method is $\pm 5\%$. Operating points with

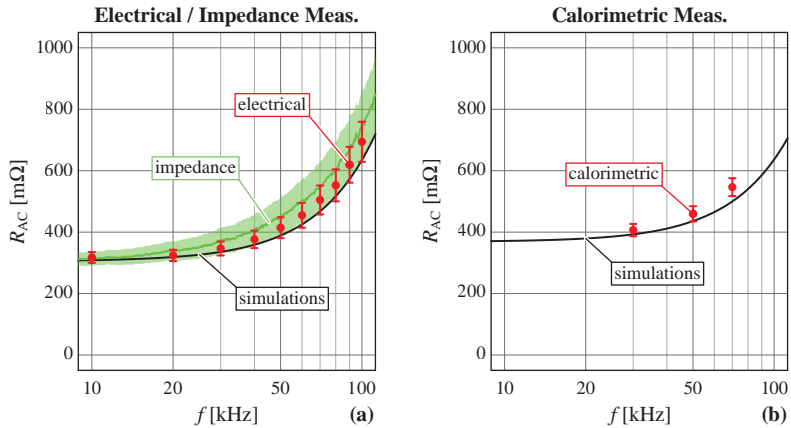


Fig. 5.18: (a) Winding losses measured with the impedance analyzer and with the electric method (25 °C winding temperature). (b) Winding losses measured with the calorimetric method (85 °C hot spot winding temperature, 50 °C ambient temperature). The measurement uncertainties and the simulated losses are indicated. The measured losses are scaled with respect to the current in order to obtain the AC resistance (related to the MV side) of the transformer. The difference between the two simulated curves is explained by the different winding temperatures.

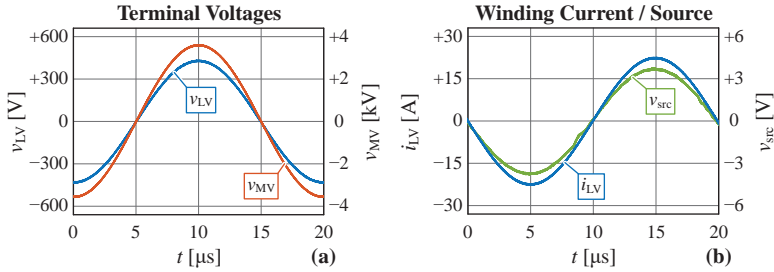


Fig. 5.19: (a) Measured terminal voltages and (b) winding currents during open-circuit operation at 50 kHz. The LV winding is fed with an open-circuited MV winding. The voltages (v_{LV} and v_{MV}) are almost 90° phase shifted with respect to the current (i_{LV}). A series capacitor is inserted on the LV side to compensate the reactive power. Therefore, the voltage delivered by the source (v_{src}) is almost in phase with the current and the losses can be easily measured.

different frequencies (between 30 kHz and 100 kHz), flux densities (between 80 mT and 180 mT), and temperatures (between 25°C and 95°C) have been measured. Afterwards, the Steinmetz parameters are extracted at the different operating points by interpolating between the 36 measured points [19, 91].

The winding losses of the prototype are measured during open-circuit operation of the transformer. For limiting the voltage supplied by the source, the transformer is supplied from the LV winding. The main challenge for the measurement of the core losses is, again, the low power factor. The magnetizing inductance of the transformer is, due to the presence of an air gap, relatively low. The expected power factor during nominal condition (48 kHz, 400 V, PWM voltages) is 0.006. Two different measurement methods are considered for measuring the core losses and the winding losses associated with the magnetizing current:

- *Electrical meas.* - A series capacitor is placed in order to compensate the reactive power flowing in the magnetizing inductance. The system is fed by a linear amplifier, which is delivering the losses. Due to the reactive power compensation, the losses can be measured with high accuracy. However, the losses of the busbars and of the series capacitor are also measured. Again, low losses film capacitors are used for the reactive power compensation [289]. Due to the resonance circuit, only sinusoidal voltages can be applied, which does not correspond to the PWM voltages used in the SRC-DCX (cf. Chapter 8) [88]. However,

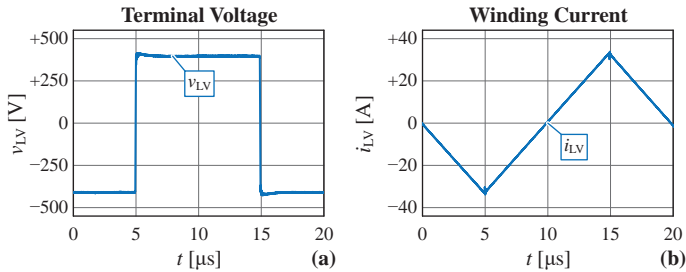


Fig. 5.20: (a) Measured terminal voltage and (b) winding current during open-circuit operation at 50 kHz. The LV winding is fed by an inverter. For avoiding parasitic resonances (cf. Fig. 5.12), the considered winding package features only the LV winding (no MV winding).

measurements with sinusoidal voltages are also interesting for validating the simulation models. Fig. 5.19 depicts the measured waveforms.

- *Calorimetric meas.* - The complete transformer is placed in a calorimeter and the losses are measured in steady state [290]. A highly accurate calorimeter consisting of two isolated chambers with water cooling is used [291]. This method is extremely accurate but also time-consuming. Due to the resonance frequency of the transformer (cf. Fig. 5.12), PWM voltages cannot be applied to the realized winding package. Therefore, another winding package, which only features the LV winding (same litz wire, same number of turns, and same geometry), has been realized for this measurement. The fact that the MV winding is not present does not change the losses, except for the proximity effect losses in the MV winding, which are below 500 mW for the considered operating conditions. Fig. 5.20 depicts the measured waveforms. It should be noted that, depending on the applied voltages and frequencies, the losses vary and, therefore, the core temperature is not constant.

Fig. 5.18 depicts the measured and simulated losses at different voltages and frequencies. The measured losses are slightly higher than the simulated losses, which could be explained by flux crowding near the air gaps or the corners, uneven flux sharing between the paralleled core sets, or modeling inaccuracies of the empirical iGSE method [19, 25, 128]. However, close to the nominal condition (50 kHz, 400 V, PWM voltages), the error between the calorimetrically measured and the simulated losses is only 11 %. Therefore, it is

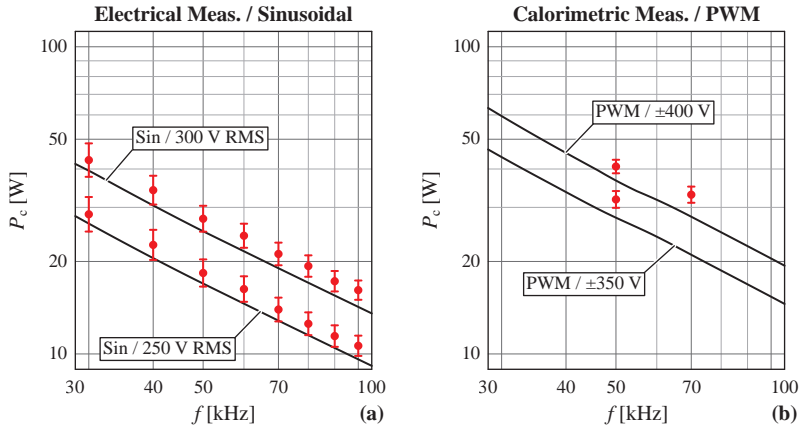


Fig. 5.21: (a) Core losses measured with the electric method (25 °C core temperature). (b) Core losses measured with the calorimetric method ([52, 65] °C surface hot spot core temperature, 40 °C ambient temperature). The measurement uncertainties and the simulated losses (black curves) are indicated. For the simulations, the temperature variations of the magnetic core and the conduction losses due to the magnetizing current are considered.

concluded that the model used for extracting the core losses of the transformer is valid.

5.5.3 Other Losses

The losses of the fan (“NMB 11925SA-12Q”) are measured electrically and are equal to 5.8 W, which is low for a 25 kW transformer [262]. This indicates that, if required, a more powerful fan could be easily mounted for improving the thermal performance or the rated power of the transformer. The realized prototype does not feature any metallic cooling elements (e.g., heat sink and/or heat extractor), which could produce eddy current losses [25, 167].

The dielectric losses inside the insulation are calculated and measured in detail in Chapter 7 [154]. It is found that the dielectric losses are 8.4 W, which is not negligible for a highly efficient transformer. The leakage current losses through the insulation are negligible. The losses due to the displacement currents flowing through the resistive ferrite core have been simulated and are also extremely small (below 2 W).

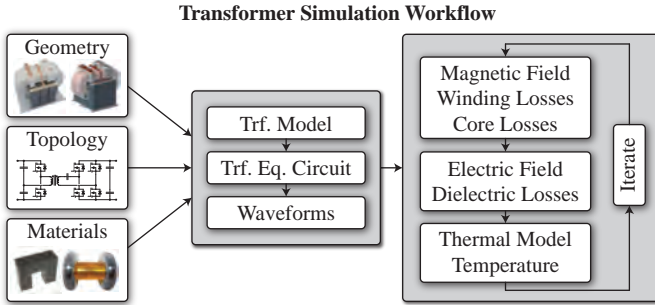


Fig. 5.22: Workflow for the simulation of the losses (core, winding, and insulation) of the MV/MF transformer. The electric field, magnetic field, and temperature distribution are obtained with FEM simulations.

5.5.4 Efficiency

For determining the efficiency, the total losses of the transformer inside the SRC-DCX (cf. Subsection 1.7.2) must be simulated. The aforementioned loss models and thermal models are combined as shown in Fig. 5.22. This workflow is based on FEM simulations and considers the cross coupling between the losses and the temperature distribution [91, 114, 115, 228]. The spatial dependence of the losses and the frequency and temperature dependences of the material parameters are considered (i.e. non-uniform loss distribution). For each point (mesh element), the losses are computed with the applied stress (magnetic flux, electric field, or current density) and temperature. The consideration of a non-uniform loss distribution is required for modeling an eventual thermal runaway, which would occur locally, at temperature hot spots. An iterative process is used in order to find the equilibrium temperature distribution with the corresponding local values of the material parameters. The waveforms applied to the transformer by the SRC-DCX are described in Chapter 8 [88]. Fig. 5.23 depicts the obtained results. An efficiency of 99.69 % is simulated at 25 kW. Moreover, it appears that the transformer can be operated at 35 kW (40 % overload) without experiencing a thermal runaway.

The measurement of the losses, by subtracting the input and output power, is extremely difficult for a MV/MF component featuring an efficiency above 99.0 %, which is clearly the case for the realized prototype. The power measurement error of high-end power analyzers is above $\pm 0.7\%$ at 50 kHz [252, 294]. Additionally, the error of MV/MF voltage dividers is

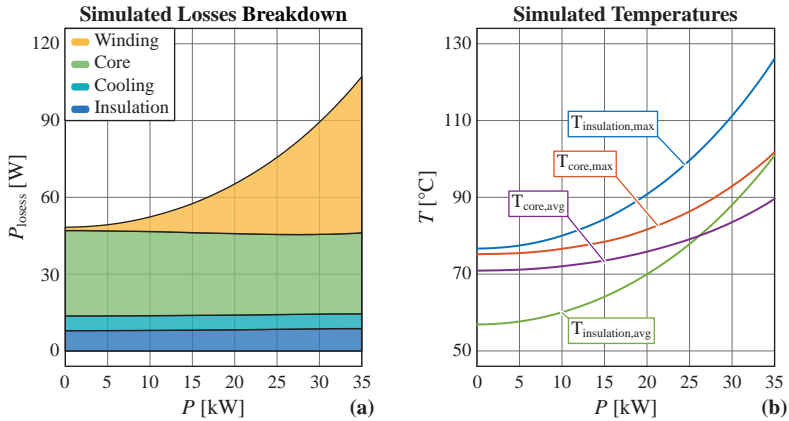


Fig. 5.23: (a) Simulated loss breakdown and (b) temperatures (averaged and hot spot) for the MV/MF transformer. The workflow shown in Fig. 5.22 is considered for the simulations with an ambient temperature of 40 °C.

above $\pm 0.3\%$ at 50 kHz [295]. Moreover, the applied PWM voltages contain significant harmonics up to 1 MHz. Hence, the combination of all the measurement uncertainties would lead to a measurement error above $\pm 1.5\%$, which indicates that it is impossible to extract the efficiency by subtracting the input and output power of the transformer. Calorimetric measurements of the complete transformer are possible but would require the construction of a custom measurement device. The calorimeter used for the core and winding losses cannot accommodate MV/MF bushings [291]. Furthermore, due to its extensive volume (2.4 m³), the calorimeter cannot be easily placed inside a Faraday cage [291]. Finally, the inductance of the supply cable (mostly on the LV side), would increase the series inductance (leakage inductance) and would perturb the operation of the SRC-DCX.

For all these reasons, another approach has been pursued. The measured winding, core, dielectric, and fan losses are combined for obtaining the total losses. The currents, voltages, and the switching transition durations measured inside the SRC-DCX are considered for assembling the different losses, cf. Chapter 8 [88]. The main limit of this approach is that the impact of the temperature on the losses is not exactly considered. The winding and the dielectric losses are increasing with the temperature while the core losses are reduced. However, the considered prototype features a low thermal coupling between the winding package and the magnetic core (due to the presence of

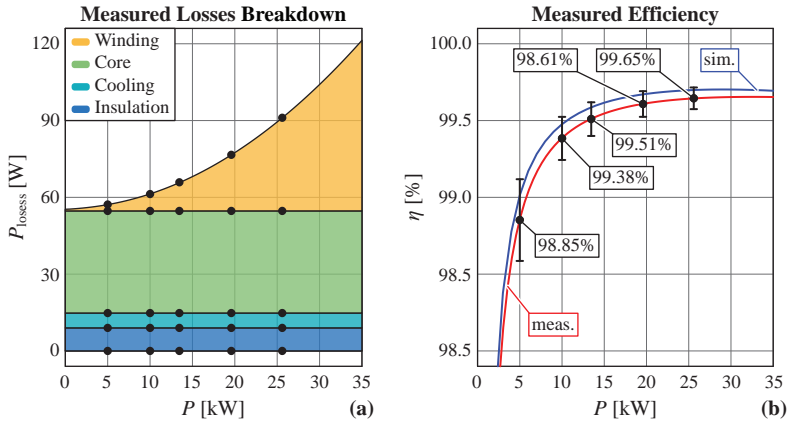


Fig. 5.24: (a) Measured loss breakdown between the different components for the MV/MF transformer. (a) Measured efficiency of the MV/MF transformer with the corresponding measurement tolerance. The simulated efficiency (cf. Fig. 5.23) is also shown. The black dots represent the measured operating points of the SRC-DCX, for which the different loss components are assembled.

air ducts). Nevertheless, the possible worst-case (low core temperature combined with a high winding package temperature) is considered for assembling the measured losses. The following conservative tolerances (cf. Section 5.5) are considered for the losses: $\pm 25\%$ for the core losses, $\pm 15\%$ for the winding losses, parse – numbers = false30 $\pm\%$ for the dielectric losses, and $\pm 5\%$ for the fan losses. The tolerance is particularly large for the core losses, due to the strong temperature dependence. The tolerance for the dielectric losses is also large since only the CM losses have been measured and the DM losses are simulated (cf. Chapter 7) [154].

Fig. 5.24 shows the measured loss breakdown and the corresponding efficiency. The transformer achieves a full-load efficiency of $99.65 \pm 0.07\%$ (measured at 25.6 kW). This implies that the estimated error on the measured losses is $\pm 20\%$. Moreover, it can be seen that the simulated efficiency and the measured efficiency are extremely similar for the complete load range. The absolute deviation between the simulated and measured efficiencies is, at full-load, 0.04%. The measured losses are 90.3 W and the simulated losses are 75.6 W, which corresponds to a deviation of 16%.

The different results are depicted in Fig. 5.2, where the analytically optimized design (99.67% and 9.6 kW/l), the numerically simulated prototype

(99.69 % and 7.4 kW/l), and the measured prototype (99.65 % and 7.4 kW/l) are shown. From this comparison, it is concluded that the chosen optimization and simulation approaches are valid and lead to a quasi-optimal prototype. The specified efficiency and power density (cf. Tab. 5.1), which are required for achieving the targets set for the complete SRC-DCX, have been reached.

5.6 Summary

This chapter studies the design, construction, and measurement of the MV/MF converter (± 3.5 kV to ± 400 V, 48 kHz, 25 kW) used in the considered SST demonstrator (cf. Subsection 1.7.2). First, the transformer is optimized with analytical models and the optimal design is extracted. Afterwards, the CAD design and construction of the prototype are detailed with a particular focus on the vacuum potting of the insulation.

The realized prototype is characterized with respect to the short-circuit behavior, the saturation limit, the impedances (inductances and capacitances), the resonances, the insulation testing, and the thermal model. Afterwards, the winding, core, and dielectric losses are measured. Calorimetric measurements, electrical measurements, and FEM simulations are successfully compared.

Finally, the total losses of the transformer inside the SRC-DCX are simulated and measured. The prototype features a power density of 7.4 kW/l (121 kW/in³, 4.0 kW/kg, and 1.8 kW/lb) and achieves a simulated full-load efficiency of 99.69 %, whereas the measured full-load efficiency is 99.65 %.

6

MV/MF Transformer Shielding

Chapter Abstract

The introduction of MV SiC MOSFETs devices enables the usage of higher power converter operating voltages, switching frequencies, and commutation speeds. This implies that MF and HF transients are applied to passive components, and particularly to inductors and transformers. Together with the operation at MV, this leads to challenging situations with respect to CM currents, parasitic resonances, insulation stresses, and EMI issues. The electric field is the key parameter for the aforementioned effects. Therefore, this chapter analyzes the electric field distribution (in the insulation, at the surface, and in the air) for the MV/MF transformer (± 3.5 kV to ± 400 V, 48 kHz, 25 kW) used in the DC-DC converter of the considered SST demonstrator. For reducing the electric field, a suitable shield is designed. It is found that the shield drastically reduces the electric field at the surface of the transformer and in the air without increasing the losses.

6.1 Introduction

The increased voltages (up to 15 kV), switching frequencies (up to 200 kHz), and commutation speeds (up to 100 kV/ μ s) applied to MV/MF transformers and inductors by MV SiC MOSFETs create new challenges [108–110]. As already mentioned in Chapter 2, an increased switching frequency has a direct impact on the core losses (eddy currents and hysteresis) and winding losses (skin and proximity effects) [19, 22, 25, 167, 168]. Additionally, the increased voltages and switching speeds lead to large CM currents [171], more intense excitations of parasitic resonances of the transformer [156, 159–161], and issues related to electrical insulation stress, such as dielectric losses or

partial discharges [63, 64, 141, 146–149]. For all these effects, it is necessary to study the magnetic and electric field patterns of MV/MF transformers in more detail [82, 105, 191].

Usually, the magnetic field is only calculated inside the transformer (analytically or numerically) for obtaining the equivalent circuit and the losses. However, the scattered magnetic field originating from the transformer is also an important parameter, which can produce losses in metallic elements placed near the transformer (e.g., heat sinks) and disturbances in electronic circuitry [25, 158, 162]. Additionally, the scattered electric field allows for displacement currents and/or capacitively coupled voltages due to the parasitic capacitances between the transformer and surrounding metallic elements, which can also cause disturbances in control and sensing circuitry [162, 190, 296] and electrical insulation issues for non-earthed parts (e.g., heat sinks, magnetic cores, and fans) [25]. The stray capacitances between the windings also provide HF conduction paths, which create and/or transmit conducted EMI across the galvanic isolation [156, 159, 160, 171].

The electric field inside the insulation is also a critical parameter for MV transformers and should be well-defined for a large frequency range (DC, MF, and HF). Exceedingly high electric field values (inside the insulation or at the surface) produce partial and/or surface discharges, which damage the insulation and lead to breakdowns and flashovers [142, 191, 193, 285, 288, 297]. This is particularly critical for MV/MF transformers operated with PWM voltages featuring fast switching transitions. Such voltages have been identified as harmful (compared to MV/LF sinusoidal voltages) for the insulation materials [144–149, 153, 154].

Therefore, this chapter analyzes the magnetic and electric field patterns with a special focus on MV/MF PWM voltages with fast switching transitions created by MV SiC MOSFETs. Section 6.2 presents the considered DC-DC converter structure and the MV/MF transformer. The electric and magnetic field patterns of the transformer are analyzed in Section 6.3. Finally, in Section 6.4, different shielding concepts, which reduce the electric field without increasing the losses, are presented.

6.2 MV/MF Transformer

The DC-DC converter of the SST demonstrator presented in Subsection 1.7.2 is considered. This 25 kW converter consists of the single-cell SRC-DCX operated at 48 kHz between a 7 kV DC bus and a 400 V DC bus. The design of the MV/MF transformer is described in Chapter 5. In [105, 153], the MV/MF

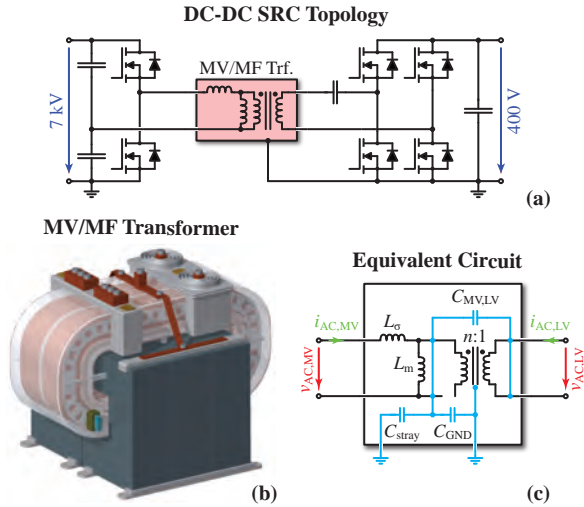


Fig. 6.1: (a) Considered SRC-DCX converter where the MV/MF transformer is highlighted. (b) 3D view of the realized prototype (cf. Chapter 5). (c) MV/MF transformer equivalent circuit with the relevant CM capacitances.

transformers of single-cell DC-DC converters have been identified as particularly critical with respect to the electric fields since a single transformer has to deal with the complete CM and DM voltages [64, 82, 105, 142]. Therefore, the considered system is particularly well-suited for an electric field analysis.

It should be noted that several small differences exist between the system simulated in this chapter and the constructed demonstrator prototype (cf. Chapter 5). In this chapter, the impact of the AC-DC stage on the MV/MF transformer (CM voltages) is not considered (cf. Subsection 1.7.2). The switching frequency of the DC-DC converter is set to 50 kHz, even if the demonstrator prototype is operated at 48 kHz. The number of turns for the MV winding is slightly different (54 in this chapter and 52 for the constructed demonstrator prototype). Moreover, the insulation thickness is slightly different (1 mm additional CM insulation thickness for the constructed demonstrator prototype). However, these differences have no significant impact on the presented results.

Figs. 6.1(a)-(b) shows the circuit topology of the DC-DC converter and the corresponding MV/MF transformer. The stray inductance of the transformer, together with the series capacitor located on the LV side, is used as

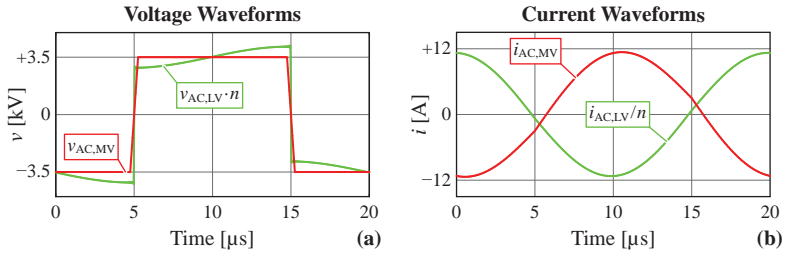


Fig. 6.2: (a) Simulated transformer voltages and (b) currents at the nominal power (25 kW). The power flow is oriented from the MV side to the LV side. The turns ratio of the transformer is $n = 54 : 6$ and the operating frequency 50 kHz.

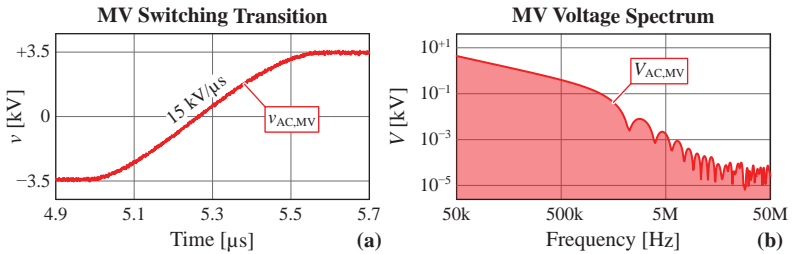


Fig. 6.3: (a) Measured ZVS transition for the MV side with (b) the RMS spectrum envelope. The switching transition is measured with a ZVS current of 4 A [111, 112]. This current corresponds to the value obtained with the magnetizing inductance of the transformer.

a resonant tank and the converter is operated at the resonance frequency (cf. Chapter 8) [88]. Fig. 6.2 depicts the corresponding currents and voltages applied to the transformer. ZVS is achieved with the magnetizing current of the transformer [82, 83, 86]. This implies that the switched current is small (quasi-ZCS) and nearly load-independent. Hence, the switching transition, shown in Fig. 6.3, features a limited speed [111, 112]. Compared to the DC-DC DABs presented in [153, 156, 160], this reduced switching speed limits the CM currents, the EMI emissions, and the excitation of the transformer resonances.

Different possibilities exist for the grounding of the converter: solid earthing, resistive earthing, or unearthed operation [79, 80]. Furthermore, different connecting nodes can be considered for the earthing: DC-bus mid-point, DC-bus negative rail, or nodes placed outside the DC-DC converter (e.g., AC-DC front-end). In this chapter, both DC-bus negative rails are earthed (solid earthing). The first terminal of the MV winding, which is connected to the DC-bus mid-point, has a constant potential of 3.5 kV. The second terminal of the MV winding, which is connected to the switch node, shows a steplike changing potential between 0 kV and 7 kV (PWM voltage). Therefore, the DM voltage applied to the MV winding is ± 3.5 kV. Additionally, a rectangular voltage, with an average value of 3.5 kV, is also applied to the MV winding [105]. Altogether, a CM DC voltage, a CM PWM voltage, and a DM PWM voltage are applied to the transformer insulation and the peak voltage is 7 kV.

The relevant CM capacitances of the transformer are shown in Fig. 6.1(c) where $C_{MV,LV}$ is the capacitance between the windings, C_{GND} the capacitance between the MV winding and the earth connection of the transformer (core), and C_{stray} the parasitic capacitance between the MV winding and earthed elements placed outside the transformer. A non-conductive frame is placed around the transformer (cf. Fig. 6.4). Additionally, a copper plane, which could represent the control PCB of the converter, is placed on the top of the transformer, near the transformer terminations (cf. Fig. 6.4). These two elements (frame and copper plane) are used to define quantitative figures of merit for the scattered field and the associated coupled disturbances originating from the transformer.

6.3 Magnetic and Electric Field Analysis

With these data, it is possible to compute the magnetic and electric fields by means of frequency-dependent FEM analysis using the waveforms shown in Fig. 6.2, i.e. including the harmonics [228]. In this section, the transformer is

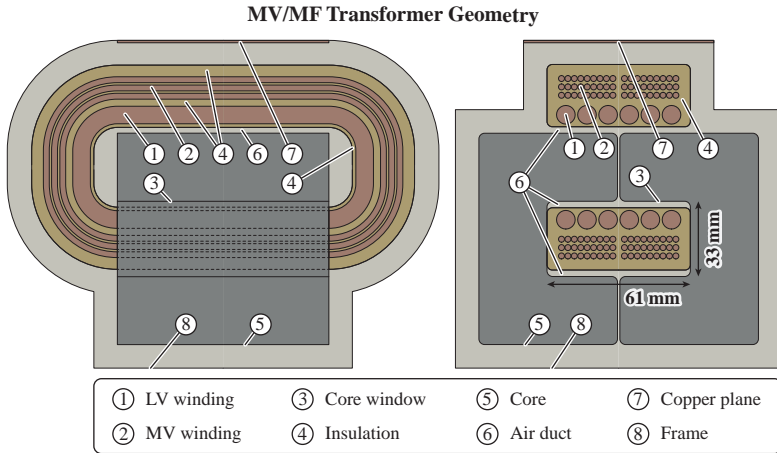


Fig. 6.4: Schematic cut side view and cut core window view of the transformer. The non-conductive frame is located 10 mm away from the transformer boundaries and is used for evaluating the scattered fields. At the top of the frame, a copper plane (90 × 80 mm, 75 μm) is placed. This plane, which represents the control PCB of the converter, is used to evaluate the coupled disturbances.

Tab. 6.1: Nomenclature (Voltages, Currents, and Fields)

| Variable | Description |
|------------------------------------|---|
| $\{V, I\}$ | RMS value |
| $\{v, i\}$ | Transient value |
| $\{V, I\}_{\text{peak}}$ | Peak transient value |
| $\{\underline{V}, \underline{I}\}$ | Complex RMS phasor |
| $\{E, B\}_{\text{RMS}}$ | RMS value (AC harmonics and DC component) |
| $\{E, B\}_{\text{AC,RMS}}$ | RMS value (AC harmonics) |
| $\{E, B\}_{\text{DC}}$ | DC component |
| $\{E, B\}_{\text{RMS,max}}$ | Local maximum of $\{E, B\}_{\text{RMS}}$ |
| $\{E, B\}_{\text{AC,RMS,max}}$ | Local maximum of $\{E, B\}_{\text{AC,RMS}}$ |
| $\{E, B\}_{\text{DC,max}}$ | Local maximum of $\{E, B\}_{\text{DC}}$ |
| $\{E, B\}_{\text{peak,max}}$ | Local maximum of the peak transient value |

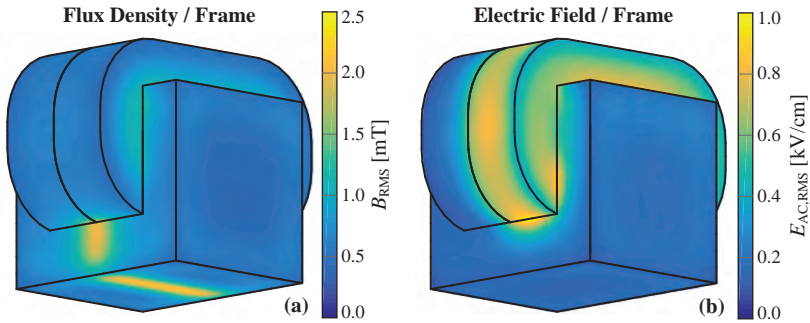


Fig. 6.5: (a) Magnetic flux density and (b) AC electric field evaluated at the surface of the (non-conductive) frame of the transformer, which is placed 10 mm away from the transformer boundaries.

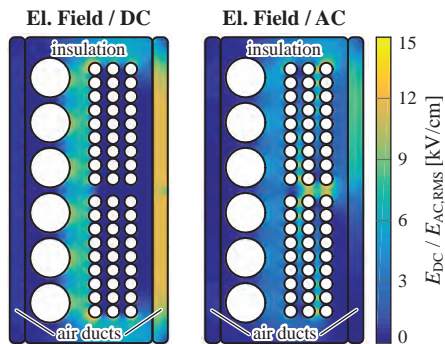


Fig. 6.6: DC and AC electric fields evaluated inside the core window (insulation and air ducts). Due to the permittivity mismatch between the potted insulation and the air, the electric field is pushed towards the air ducts.

considered without any shielding. Tab. 6.1 denotes the nomenclature used for the description of the voltages, currents, electric fields, and magnetic flux densities. Figs. 6.5 depicts the magnetic flux density and the AC electric field obtained at the surface of the non-conductive frame of the transformer (cf. Fig. 6.4). Fig. 6.6 shows the DC and AC electric fields inside the core window, where the highest electric field values are located (due to the equipotential surface defined by the earthed core). In reality, the electric field values are usually slightly larger than the simulated values due to imperfections of the potting process, surface roughness, unexpected triple points, etc. Furthermore, the values presented in Fig. 6.6 can be exceeded during abnormal operating situations (e.g., lightning surges) when a voltage drop is present between the LV and the MV earthing of the converter [79, 80].

Due to the large magnetizing current of the transformer, which forms a magnetic dipole, a magnetic stray field exists outside the transformer. As expected, the magnetic flux density is maximal ($B_{\text{peak,max}} = 3.1 \text{ mT}$) near the air gap, where the field is concentrated. This stray magnetic field can cause eddy current losses in surrounding conductive elements and EMI perturbations in electronic circuits [25, 27, 162]. In the considered copper plane (cf. Fig. 6.4), placed at the top of the transformer, the eddy current losses are 0.9 W. It has to be noted that the considered plane is magnetically thin. For a thicker plane, the losses can exceed 10 W. The stray magnetic field can be reduced if the air gap is only placed at the wound limb or with a magnetic shield placed between the transformer and the sensitive circuits [298].

However, the magnetic flux density is not a problem which is specific to MV transformers and has already been examined in [27, 158, 162, 205]. Therefore, the magnetic shielding is not further examined. In contrast, the electric field, which is directly related to the applied voltage, creates several issues:

- ▶ *DC field* - The DC electric field distribution is determined by the conductivity and not by the permittivity [193, 285]. The surface conductivity of the insulation is not clearly defined (e.g., influenced by pollution and moisture) and the conductivity of air depends on many environmental factors [278, 299]. Moreover, the conductivity of dry-type insulation materials is extremely low but massively temperature dependent and can exhibit non-linear effects (space charge migration) [287, 300]. Therefore, a simple model, based on constant electrical conductivities, is not accurate and the DC field distribution is ill-defined. This implies that the field pattern shown in Fig. 6.6(a) should be considered with caution. Since the bulk conductivity of the insulation is usually larger than the

conductivity of air, a large part of the DC electric field can be located in the air. This is particularly critical in the air ducts, due to the small distances and the reduced breakdown strength of air.

- ▶ *AC field* - If the frequency is higher than some mHz, the electric field distribution is determined by the permittivity [287, 301]. Still, due to the permittivity mismatch between the insulation material (silicone) and the air, a significant part of the AC electric field is located in the air. Again, this effect is particularly critical in the air ducts (cf. Fig. 6.6(b)).
- ▶ *Surface field* - The total electric field (DC and AC) in the air is maximal at the surface of the air ducts (cf. Fig. 6.6) and reaches a value of $E_{\text{peak,max}} = 21.2 \text{ kV/cm}$. This value, which is close to (but still below) the critical field in air (ca. 25 kV/cm , more for small air gaps) [285, 286], can lead to surface discharges (creeping with the tangential field component) [142, 288]. Such discharges damage the insulation, distort the potential distribution (space charge migration), and can lead to a flashover [297, 302, 303]. The triple points, i.e. locations with interfaces between the insulation, the core, and the air, are particularly sensitive [297, 304, 305]. Moreover, the MF and HF (due to the switching transients) harmonics applied to the insulation further reduce the lifetime of the transformer in the presence of discharges [148, 304, 305].
- ▶ *Near-field* - The AC electric field, evaluated at the surface of the non-conductive frame, is mainly located near the winding head and reaches a value of $E_{\text{AC,RMS,max}} = 1.0 \text{ kV/cm}$ (cf. Fig. 6.5(b)). If grounded conductors would be placed near the frame, the electric field would be even higher. Since this field contains HF components (cf. Fig. 6.3), this can create perturbations in electronic circuits or insulation issues in the cooling system of the transformer [25, 162].

Figs. 6.7 shows the capacitively coupled current and voltage in the considered copper plane placed near the transformer (cf. Fig. 6.4). If the plane is earthed, the displacement current ($I_{\text{plane,peak}} = 59.2 \text{ mA}$) can cause substantial perturbations, especially for sensors. For an unearthed plane, the capacitively coupled voltage ($V_{\text{plane,peak}} = 4.1 \text{ kV}$) is also problematic for the electrical insulation. Again, it should be noted that the DC field and, hence, the DC coupled voltage are ill-defined.

The simplest solution for reducing the surface electric field is to increase the thickness of the insulation. The capacitively coupled disturbances are reduced if the distances between the transformer and the sensitive circuits

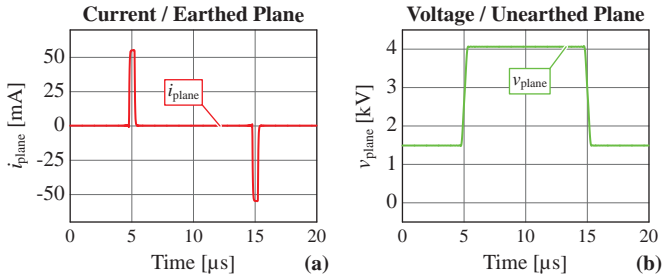


Fig. 6.7: (a) Capacitively coupled CM current in the earthed copper plane. (b) Capacitively coupled CM voltage in the unearthed copper plane. The plane is placed near the winding head (cf. Fig. 6.4).

are increased. However, these solutions reduce the achievable power density and cause thermal issues (cf. Chapter 5). For these reasons, another option, which is an electrical shielding of the transformer [105, 306], is examined in detail in the following.

6.4 Electrical Shielding

In this section, different shielding methods (i.e. geometric, capacitive, resistive, and refractive) are examined and compared for MV/MF transformers with PWM voltages. It is found that resistive shielding represents an interesting trade-off between the achieved bandwidth and the generated losses. Therefore, this solution is examined in detail.

6.4.1 Shielding Methods

Field control (grading) is well-established for LF MV and HV components (e.g., bushings and machine stators) [304, 307]. Different methods can be used to actively shape the electric field distribution and can be classified as follows [62, 285, 297]:

- ▶ *Geometric* - A conductive electrode with a large curvature radius is placed in order to shape the electric field with a defined equipotential surface.
- ▶ *Capacitive* - Many conductive electrodes are placed (often in a concentric configuration) in order to define many equipotential surfaces. The

voltage distribution between the electrodes is defined by the capacitance matrix.

- ▶ *Resistive* - A semi-resistive (semi-conducting) material is used in order to change the impedance of the insulation system and, therefore, the potential distribution. Often non-linear resistive materials are used, where the conductivity is increasing with the electric field.
- ▶ *Refractive* - A material with a high permittivity is placed at the surface of the insulation in order to shape the electric field (permittivity mismatch).

All these methods are applicable to the field grading of LF AC components. In [152, 308], it has been shown that LF field grading systems can produce dramatic failures in the presence of MF or DC electric fields. Therefore, for the shielding of MV/MF transformers, additional constraints appear as follows:

- ▶ *Compactness* - Due to the reduced dimension of the transformer (compared to standard LF components), complex field grading methods are difficult to implement (e.g., capacitive shielding).
- ▶ *Frequency* - The shield should be active at DC, MF, and HF. Accordingly, grading methods relying on the permittivity (e.g., capacitive shielding and refractive shielding) are not easily applicable to DC fields. Resistive gradings (particularly with non-linear materials) are difficult to design for a wide frequency range [304, 308].
- ▶ *Losses* - In [25], it has been shown that MF magnetic fields (cf. Fig. 6.5(a)) produce significant losses in metallic elements used for heat management of MF transformers. This is critical for the grading methods using metallic electrodes (e.g., geometric shielding and capacitive shielding) [306]. Furthermore, the displacement current flowing in a resistive material used for field grading can also produce losses at MF [152, 304].

6.4.2 Resistive Shielding

Taking all the aforementioned factors into account, it has been decided to place a resistive shield around both windings. Since the resistive layer is used to shield the electric field (and not for field grading), a linear material can be used. Different shielding configurations are considered and examined:

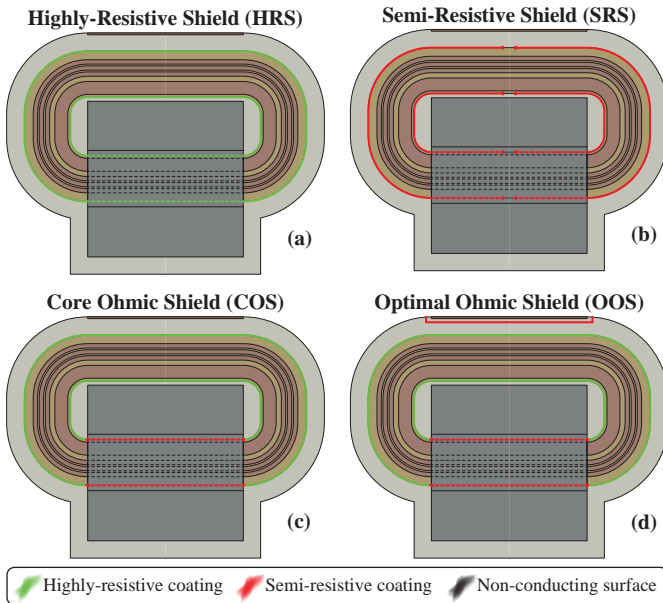


Fig. 6.8: Different resistive shielding methods for the transformer (cf. Fig. 6.4). (a) Highly-Resistive Shield (HRS), (b) Semi-Resistive Shield (SRS), (c) Core Ohmic Shield (COS), and (d) Optimal Ohmic Shield (OOS).

- ▶ *No Shielding* (“NS”) - The transformer is considered without any shielding as shown in Fig. 6.4. This corresponds to the simulations shown in Section 6.3.
- ▶ *Highly-Resistive Shield* (“HRS”) - The surface of the winding insulation (around both windings) is covered with a highly-resistive coating, as shown in Fig. 6.8(a).
- ▶ *Semi-Resistive Shield* (“SRS”) - The surface of the winding insulation (around both windings) is covered with a semi-resistive coating, as shown in Fig. 6.8(b). Two small gaps are inserted to prevent the formation of a closed current path for eddy currents (short-circuit winding).
- ▶ *Core Ohmic Shield* (“COS”) - The surface of the winding insulation (around both windings) near the core window, is covered with a semi-resistive coating. Moreover, a highly-resistive coating is used near the winding head, as shown in Fig. 6.8(c).
- ▶ *Optimal Ohmic Shield* (“OOS”) - Similar with respect to the COS. An additional semi-resistive shield is used near the copper plane (cf. Fig. 6.4), as shown in Fig. 6.8(d).

All the resistive shields are connected to the core (and, therefore, to the earth) and are easily obtained by a surface treatment of the insulation surface. It has to be noted that the shields should be terminated with a finite curvature radius in order to avoid an electric field hot spot (triple point) [62, 297]. Terminations of the shield are required at the following locations: cable terminations (bushings), shield gaps (SRS), and at the interfaces between a semi-resistive and a highly-resistive shield (COS and OOS).

6.4.3 Shield Functional Principle

The computation of the shielding effect and the losses of the inserted resistive elements is required for the evaluation of the proposed shielding methods. The shield is primarily defined by the surface conductivity of the coating [309]:

$$\sigma_{s,sh} = \sigma_{sh}d_{sh}, \quad (6.1)$$

where σ_{sh} is the bulk conductivity of the resistive material and d_{sh} the thickness of the coating. The shield is considered to be a linear material, i.e. the conductivity is independent of the applied electric field.

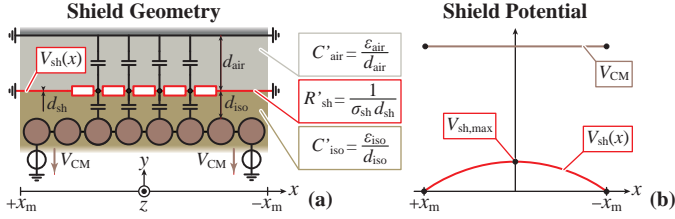


Fig. 6.9: (a) Electric equivalent circuit of an earthed resistive shield excited by a CM voltage source. (b) Voltage drop along the shield for the case $V_{sh,max} \ll V_{CM}$.

If the shield forms a short-circuit winding (i.e. HRS), the shield can be seen as a third winding with one turn. The load of this third winding is the resistance of the complete shield. In order to have low losses, the resistance of the shield should be very high compared to the load impedance of the transformer (equivalent impedance referred to a winding with one turn). Even if no short-circuit winding is present (i.e. HRS, COS, and OOS), the stray magnetic field of the transformer will still induce eddy current losses (cf. Fig. 6.5(a)) [25, 27, 205]. In order to limit the losses in the shield, the skin depth should be much larger than the thickness of the shield:

$$\delta_{sh} = \frac{1}{\sqrt{\pi \sigma_{sh} \mu_0 f}} \gg d_{sh}, \quad (6.2)$$

where f is the switching frequency. It has to be noted that this condition is required but not sufficient to have low losses. Even a magnetically thin layer can produce eddy current losses as calculated in [127] for a simple geometry. Since the shield of the transformer features a complex geometry and field distribution (tangential and orthogonal), numerical simulations are required for computing the eddy current losses.

Fig. 6.9 shows the electrical equivalent circuit of the shield inside the core window (cf. Fig. 6.4). In the y direction, the MV winding, the insulation, the shield, the air duct, and the core are placed contiguously. The shield is earthed at both ends (to the core) and the MV winding potential is changing (CM voltage). The equivalent circuit can be formulated with the following differential equations, which are similar to the telegrapher's equations:

$$\frac{\partial \underline{V}_{sh}(x)}{\partial x} = -R'_{sh} I_{sh}(x), \quad (6.3)$$

$$\frac{\partial I_{sh}(x)}{\partial x} = -j2\pi f (C'_{iso} (\underline{V}_{sh}(x) - V_{CM}) + C'_{air} \underline{V}_{sh}(x)), \quad (6.4)$$

where \underline{V}_{sh} is the voltage along the shield, I_{sh} the current along the shield, R'_{sh} the resistance of the shield, C'_{iso} the insulation capacitance, C'_{air} the air duct capacitance, \underline{V}_{CM} the applied winding voltage, and f the considered frequency. The different variables are scaled with respect to the depth of the shield in the out-of-plane direction (z direction). The earthing of the shield leads to the boundary conditions:

$$\underline{V}_{sh}(+x_m) = \underline{V}_{sh}(-x_m) = 0, \quad (6.5)$$

where $2x_m$ is the length of the shield. The solution of this boundary value problem is a large expression but a simple approximation exists (obtained with the perturbation theory) if the voltage drop along the shield is small [310]. This last condition ($V_{sh,max} \ll V_{CM}$) has to be respected for obtaining a shielding effect and leads to

$$\underline{V}_{sh}(x) \approx \underbrace{j2\pi f R'_{sh} C'_{iso} \frac{x_m^2}{2} V_{CM}}_{\underline{V}_{sh,max}} \left(1 - \left(\frac{x}{x_m} \right)^2 \right). \quad (6.6)$$

From this equation, it can be seen that, for a given configuration, the shielding is only efficient up to a maximum frequency. For obtaining a shielding at HF, a high surface conductivity is required. The losses per unit depth (z direction) of the shield can be expressed as

$$P' = \int_{-x_m}^{+x_m} R'_{sh} |I_{sh}(x)|^2 dx = \int_{-x_m}^{+x_m} \frac{1}{R'_{sh}} \left| \frac{\partial \underline{V}_{sh}(x)}{\partial x} \right|^2 dx. \quad (6.7)$$

This last equation shows that the losses converge to zero for very high surface conductivities. For very low surface conductivities, the losses are also converging towards zero (no current is flowing in the shield). The losses are maximal when the shield conductivity is not high enough for defining an equipotential surface but large enough for producing losses. Alternatively, the shield can be considered as a lumped circuit consisting of resistors and capacitors. The losses are low if the time constant is well below the switching frequency or well above the switching speed. Between these two cases, a non-negligible fraction of energy stored in the insulation capacitance is dissipated in the shield.

Finally, it can be seen (cf. (6.6)) that only the surface conductivity has an impact on the shielding effect. This offers a degree of freedom (bulk

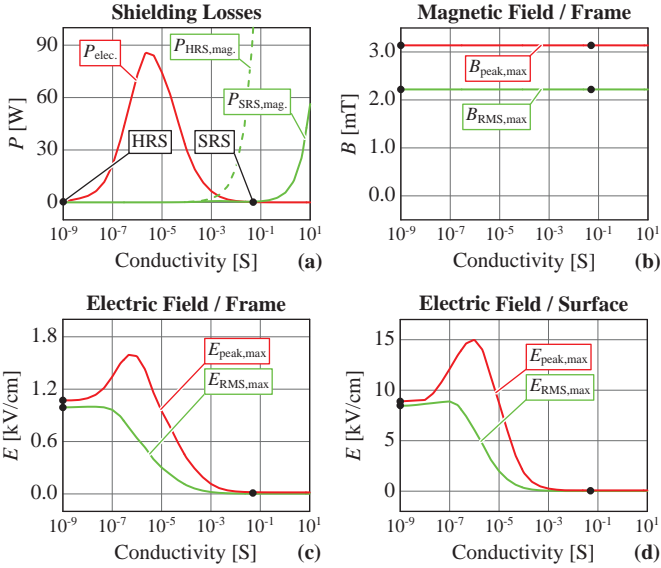


Fig. 6.10: (a) Electric ($P_{elec.}$) and magnetic losses ($P_{HRS,mag.}$ for HRS and $P_{SRS,mag.}$ for SRS) in the shield. (b) Maximum magnetic flux density and (c) electric field evaluated at the surface of the non-conductive frame of the transformer. (d) Maximum electric field at the surface of the insulation. Two optima are identified: one for the HRS and one for the SRS.

conductivity and thickness) for realizing the optimal surface conductivity such that low losses and an effective shielding are obtained. Nevertheless, the magnetic losses are not scaling directly with the thickness of the shield (cf. (6.1)), such that the magnetic simulations should be conducted with the correct coating thickness.

6.4.4 Optimal Shield Conductivity

It is concluded that the conductivity of the shield is a trade-off between the losses and the effectiveness of the shielding at HF. In order to find the optimal conductivity, 3D FEM simulations (cf. Fig. 6.5) are conducted [228]. Fig. 6.10(a) depicts the losses for the HRS and SRS concepts, which are the two critical configurations with respect to the losses, due to the proximity between the

shield and the windings. The simulations are conducted for a shield thickness of 250 μm . However, the results are very similar for 100 μm or 500 μm .

It is interesting to note that a large part of the eddy current losses in the shield is produced by the magnetizing current, which is much smaller than the load current (cf. Fig. 6.2). This is explained by the fact that the magnetizing current is mainly responsible for the stray field located outside the windings. This also implies that a shield placed between the MV and LV windings, where the stray field is maximal, would lead to high losses. As expected, an electric loss peak is present between very low and very high surface conductivities (cf. (6.7)). Therefore, the surface conductivities are selected for the different types of shields as follows:

- ▶ *HRS*: Due to the effective presence of a short-circuit winding, a very low conductivity of 10^{-9} S is selected (below the electric loss peak). The HRS can be obtained with a typical anti-static surface treatment of the windings (against electrostatic discharges).
- ▶ *SRS*: Due to the limited eddy current losses (no short-circuit winding), a higher conductivity (above the electric loss peak) can be selected. A surface conductivity of 0.05 S represents a good trade-off between the electric and magnetic losses and can be obtained with a carbon coating.

With the selected conductivities, the losses are less than 1.0 W for both shielding types. A closer look at Fig. 6.10(a) reveals that large tolerances are acceptable for the surface conductivity, which facilitates the coating process. Fig. 6.10(b) shows the magnetic flux density and indicates that the shield is magnetically thin compared to the skin depth (cf. (6.2)). Figs. 6.10(c)-(d) depict the electric field at the surface of the frame and at the surface of the insulation. For very low surface conductivity (i.e. HRS), the total (AC and DC) electric fields are equal to the AC fields shown Fig. 6.6. This implies that the HRS blocks the DC electric field while the MF and HF AC fields are unaffected. This corresponds to the shielding method presented in [105]. Depending on the chosen surface conductivity, the HRS can also block LF AC electric fields, originating from an AC-DC converter [105]. For the SRS, all the relevant frequency components are blocked (DC, LF, MF, and HF).

In Figs. 6.10(c)-(d), an increase of the electric field values can be observed around 10^{-6} S. This conductivity corresponds to the electrical loss peak shown in Figs. 6.10(a). With such a conductivity, the shield is able to partially shield the electric field at the switching frequency but not during the switching transitions (i.e. harmonics). This produces distortions of the electric field patterns and leads to increased field values.

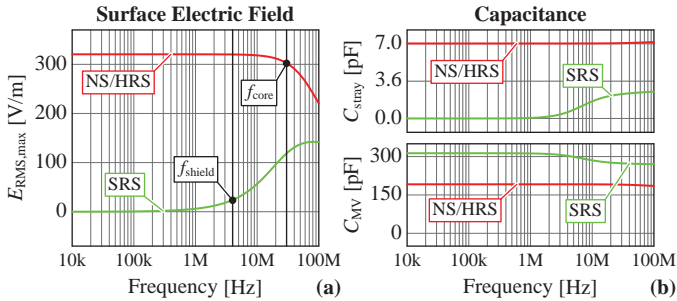


Fig. 6.11: (a) Maximum surface electric field in the air ducts for a normalized RMS CM excitation of the MV winding (1 V). Above f_{core} and f_{shield} , the core and the shield cannot be considered as equipotential surfaces anymore. (b) CM capacitances of the transformer. C_{stray} is the capacitance between the MV winding and the copper plane. C_{MV} is the total MV CM capacitance of the transformer which consists of $C_{\text{MV,LV}}$ and C_{GND} (cf. Fig. 6.1(c)).

6.4.5 Shielding Effects

The aforementioned results show that the SRC offers the best shielding effects and, therefore, this shielding method is further examined. Even if the SRS seems to provide a very effective shielding, some frequency dependence of the potential distribution is still expected (cf. (6.6)). Fig. 6.11(a) depicts the frequency dependence of the electric field at the surface of the air ducts, where the hot spot is located, for a normalized CM excitation of the MV winding. The SRS is only effective for frequencies below 10 MHz, which is compatible with the spectrum shown in Fig. 6.3. For higher frequencies, a large voltage drop appears along the shield, leading to non-negligible electric field values in the air ducts (cf. (6.6)). For the NS/HRS, the field is dropping near 100 MHz due to the limited conductivity of the ferrite core [155]. It has to be noted that, due to resonances of the transformer, at HF, the voltage distribution of the winding cannot be described with a single a CM/DM voltage (cf. Chapter 5) [156, 308]. However, the aforementioned CM excitation is still useful to assess the shielding effect without considering the transformer resonances.

Fig. 6.11(b) shows the CM capacitance between the MV winding and the earthed copper plane and the total MV CM capacitance, which consists of the CM capacitance towards the LV winding and the core (cf. Fig. 6.1(c)). For both curves, the effect of the limited shield conductivity also affects the capac-

itances at HF. The SRS drastically reduces the stray capacitance towards the copper plane, suppressing potential disturbance couplings (cf. Fig. 6.7). However, the SRS increases the total CM capacitance of the transformer by 60 %. This increased capacitance results from the field confinement provided by the shield (which is connected to the core), particularly near the winding head (cf. Fig. 6.5(b)). An increase of the CM capacitance is often problematic since it can create conducted EMI perturbations inside the converter and, potentially, reduce the resonance frequencies of the transformer. Such problems could be, partially, handled with CM chokes placed at the transformer's AC terminals or at the DC-buses, at the cost of an increased hardware complexity [171].

An alternative solution is to use the COS concept (cf. Fig. 6.8(c)) in order to mitigate the increase of the total MV CM capacitance. This concept uses a semi-resistive shield inside the core window in order to reduce the surface electric field (surface conductivity of 0.05 S, similar to SRS). This shield does not significantly increase the total MV CM capacitance since the core already defines the potential in this region. Near the winding head, where the surface electric field is lower, a highly-resistive anti-static shield is used for blocking the DC field (surface conductivity of 10^{-9} S, similar to HRS). With the COS, the total MV CM capacitance only increases by 10 %. However, this concept is not able to limit the parasitic capacitance towards the copper plane (cf. Fig. 6.7 and Fig. 6.11).

In order to limit the capacitively coupled disturbances, the OOS concept (cf. Fig. 6.8(d)), which features an additional semi-resistive shield near the copper plane, can be used (surface conductivity of 0.05 S, similar to SRS). Since this shield is placed near the frame and not near the transformer windings, the total MV CM capacitance is only marginally affected. Alternatively, the complete converter frame could be coated with a resistive coating for blocking the electric field without producing eddy current losses [62].

Tab. 6.2 summarizes the properties of the different shielding methods with respect to the magnetic flux density, electric field, capacitances, etc. The HRS blocks the DC field and, therefore, reduces the surface electric field. However, the AC field, which causes the capacitively coupled disturbances, remains unaffected. The SRS drastically limits the surface electric field and the capacitively coupled voltages or currents. Nevertheless, the coupling capacitance of the transformer is increased. The COS reduces the surface electric field without increasing the transformer coupling capacitance but does not prevent capacitively coupled disturbances. Finally, the OOS significantly decreases the surface electric field and the capacitively coupled disturbances without increasing the transformer coupling capacitance.

Tab. 6.2: Comparison of the Shielding Methods

| Type | NS ^a | HRS ^b | SRS ^c | COS ^d | OOS ^e |
|---|-----------------|------------------|------------------|------------------|------------------|
| Losses / shield / cf. Fig. 6.10(a) | | | | | |
| P [W] | 0.0 | 0.1 | 0.7 | 0.5 | 0.5 |
| Magnetic flux density / frame / cf. Fig. 6.5(a) and Fig. 6.10(b) | | | | | |
| $B_{\text{RMS,max}}$ [mT] | 2.2 | 2.2 | 2.2 | 2.2 | 2.2 |
| $B_{\text{peak,max}}$ [mT] | 3.1 | 3.1 | 3.1 | 3.1 | 3.1 |
| Electric field / frame / cf. Fig. 6.5(b) and Fig. 6.10(c) | | | | | |
| $E_{\text{DC,max}}$ [kV/cm] | 1.4 | < 0.1 | < 0.1 | < 0.1 | < 0.1 |
| $E_{\text{RMS,max}}$ [kV/cm] | 1.7 | 1.0 | < 0.1 | 0.9 | 0.9 |
| $E_{\text{peak,max}}$ [kV/cm] | 2.4 | 1.1 | < 0.1 | 1.0 | 1.0 |
| Electric field / surface / cf. Fig. 6.6 and Fig. 6.10(d) | | | | | |
| $E_{\text{DC,max}}$ [kV/cm] | 14.6 | < 0.1 | < 0.1 | < 0.1 | < 0.1 |
| $E_{\text{RMS,max}}$ [kV/cm] | 16.0 | 8.5 | < 0.1 | 4.2 | 4.2 |
| $E_{\text{peak,max}}$ [kV/cm] | 21.2 | 8.7 | < 0.1 | 4.3 | 4.3 |
| Coupling / copper plane / cf. Fig. 6.7 | | | | | |
| I_{plane} [mA] | 11.1 | 11.1 | < 0.1 | 10.9 | < 0.1 |
| $I_{\text{plane,peak}}$ [mA] | 59.5 | 59.5 | < 1.0 | 59.2 | < 1.0 |
| V_{plane} [kV] | 3.1 | 3.1 | < 0.1 | 3.0 | < 0.1 |
| $V_{\text{plane,peak}}$ [kV] | 4.1 | 4.1 | < 0.1 | 4.0 | < 0.1 |
| Capacitance / CM / cf. Fig. 6.11(b) | | | | | |
| C_{stray} [pF] | 7 | 7 | < 0.1 | 7 | < 0.1 |
| C_{MV} [pF] | 191 | 191 | 313 | 208 | 214 |

^a NS: No Shielding (0.0 S).^b HRS: Highly-Resistive Shield (10^{-9} S).^c SRS: Semi-Resistive Shield (0.05 S).^d COS: Core Ohmic Shield (10^{-9} S / 0.05 S).^e OOS: Optimal Ohmic Shield (10^{-9} S / 0.05 S).

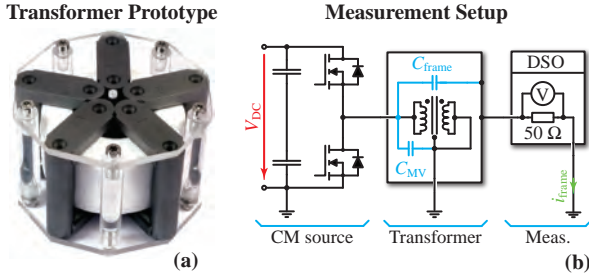


Fig. 6.12: (a) Considered transformer prototype (± 4 kV to ± 400 V, 50 kHz, 25 kW) [156]. (b) Measurement setup for the CM current in the metallic frame, which is placed 7 mm away from the transformer boundaries.

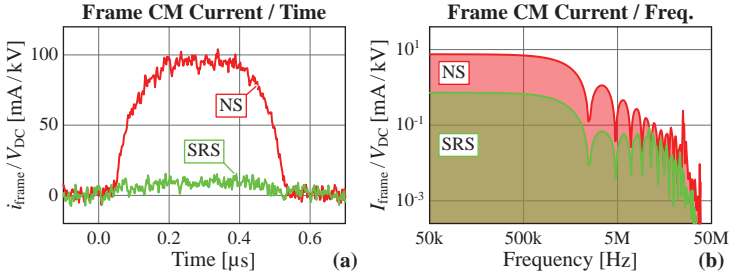


Fig. 6.13: (a) Measured displacement current through the frame and (b) RMS spectrum envelope of the measured current. The MV winding of the transformer is excited with a PWM voltage. The duration of the switching transitions is 450 ns.

6.4.6 Experimental Verification

The SRS is validated with the transformer presented in [156], cf. Fig. 6.12(a). This transformer features similar ratings (± 4 kV to ± 400 V, 50 kHz, 25 kW) as the transformer of the SRC-DCX demonstrator considered for the simulations (cf. Subsection 1.7.2 and Chapter 5). The prototype has first been measured without shielding (NS). In a second step, a carbon-based coating (“Kontakt Chemie GRAPHIT 33”, four coats) is added for obtaining a shield (SRS) with a measured surface conductivity of 220Ω [311]. The resistive coating is connected to the magnetic core. No additional losses are measured with the SRS, as long as the shield does not form a short-circuit winding.

The equivalent circuit of the transformer and the measurement setup are shown in Fig. 6.12(b) where a closed metallic frame (copper) is placed 7 mm

away from the transformer boundaries in order to quantify the scattered electric field. The energy stored in the near-field (between the transformer and the frame) is related to the capacitance towards the frame. First, the total CM capacitance of the transformer (C_{MV}) has been measured (capacitance of the MV winding against the LV winding and the core). As expected the SRS increases the total CM capacitance (from 151 pF to 228 pF). For assessing the shielding effect, the parasitic capacitance towards the frame (C_{frame}) is measured. With the shield, the parasitic capacitance is significantly reduced (from 38 pF to 4 pF), indicating that the electric field is confined in the insulation.

The displacement current has also been measured in time domain. The MV winding is excited with a rectangular CM voltage with 450 ns rise and fall times (cf. Fig. 6.3) and an amplitude of 200 V. The CM current in the frame is measured through a 50 Ω resistor (cf. Fig. 6.12(b)), given that the impedance of the frame capacitance is much larger than 50 Ω (for frequencies below 25 MHz). Fig. 6.13 shows the measured displacement current and the spectrum envelope, respectively. The peak value of the displacement current is reduced by a factor of ten. It can be concluded that the shield is effective in the frequency range where significant voltage harmonics exist.

6.5 Summary

The increased voltages, frequencies, and switching speeds achieved with modern SiC devices are generating critical voltage transients inside MV/MF transformers. In this chapter, the MV/MF transformer (± 3.5 kV to ± 400 V, 48 kHz, 25 kW) used in the DC-DC converter of the considered SST demonstrator (cf. Subsection 1.7.2) has been analyzed with respect to the shielding of the electric field. It is found that capacitively coupled voltages (peak value of 4.1 kV) and currents (peak value of 59.5 mA) could cause severe disturbances for circuitry placed near the transformer. Additionally, the electric field at the surface of the insulation (peak value of 21.2 kV/cm) is close to the critical field in air and could lead to surface discharges which damage the insulation.

The main challenge for the shielding of MV/MF transformers is to find a concept which is able to provide a shielding at DC, MF, and HF without adding significant eddy current losses. It is shown that a resistive shielding with an appropriate conductivity confines the electric field in the insulation without producing additional ohmic or eddy current losses. Furthermore, an optimal placement of the shield does not increase the coupling capacitance of the transformer to a significant extend. This shielding allows the usage of the transformer in EMI sensitive environments and provides a better electric

field distribution inside the electrical insulation. Furthermore, this shielding concept can be used for other devices, such as power modules, inductors, cooling systems, etc. However, the shield, which prevents capacitively coupled disturbances towards external circuitry, does not suppress the coupling capacitance of the transformer itself (between the windings and to the core). This means that conducted EMI is still present in the power section of the converter.

However, despite the promising simulation and experimental results, the proposed resistive shield has not been applied to the final MV/MF transformer prototype of the SST demonstrator (cf. Subsection 1.7.2 and Chapter 5). The carbon-based coating used for the experimental verification, which was applied in form of an aerosol spray, features adhesion problems on the polycarbonate coil former. This is especially problematic near the cable terminations, which show a complex geometry. Therefore, an industrial coating process should be used or, alternatively, the carbon powder could be directly mixed with the coil former material (injection moulding). For reducing the electric field without a shield, the realized prototype features 1 mm additional insulation thickness compared to the simulation model considered in this chapter. This allows a reduction of the peak electric field at the surface of the insulation to 19 kV/cm, which is below the critical field in air (ca. 25 kV/cm).

7

Dielectric Losses with PWM

Chapter Abstract

Newly available MV SiC semiconductors are setting new limits for the design space of MV converters. Unprecedented blocking voltages, higher switching frequencies, higher commutation speeds, lower losses, and high temperature operation can be reached, which, however, create new challenges for the electrical insulation. In particular, the dielectric losses can become significant for MV converters operated at higher switching frequencies. Moreover, the evaluation of the dielectric losses is a key element for assessing the insulation stress and for insulation diagnostics. Therefore, this chapter analyzes the modeling and the computation of dielectric losses with PWM voltages. After a review of the dielectric loss mechanisms occurring in polymeric insulation materials, scalable analytical expressions are proposed for the losses produced by PWM voltages. Afterwards, the dielectric losses of the MV/MF transformer (± 3.5 kV to ± 400 V, 48 kHz, 25 kW) used in the DC-DC converter of the considered SST demonstrator are analyzed and measured in detail. With epoxy resin, the insulation losses represent a significant share, i.e. up to 17%, of the total transformer losses. As shown, the transformer performance can be significantly improved with a silicone elastomer insulation. Finally, design guidelines are provided for the selection of MV/MF insulation materials.

7.1 Introduction

According to [312], insulation failures, in grid-connected magnetic components, are already challenging in MV/LF systems. In [147–149, 270], it is shown that the fast voltage transients generated by power converters further increase the stresses applied to a dry-type insulation system, leading to increased failure rates. In this context, the usage of new SiC switches, which

show higher voltage capabilities (up to 15 kV), higher switching speeds (up to 100 kV/ μ s), and higher switching frequencies (up to 200 kHz), is particularly critical [82, 111, 112, 143, 156]. Moreover, due to the high power density, elevated operating temperatures are usually occurring inside power converters. Additionally, the emergence of converter topologies featuring complex voltage waveforms, such as multi-level output voltages [94, 105] or multiple galvanically insulated ports [96, 97, 313], is creating new challenges for the design of the electrical insulation. For these reasons, the insulation used in such power converters requires a careful examination in order to obtain a solution which accommodates the opposing requirements for compactness, long-term reliability, thermal management, and EMI performance [25, 64, 143, 205].

Literature related to the evaluation of insulation stresses and insulation diagnostics proposes the examination of partial discharges, breakdown voltages, leakage currents, field distributions, dielectric losses, etc. [105, 146, 148–150, 192, 279, 282, 283]. Among these methods, the inspection of the dielectric losses is of particular interest:

- ▶ The dielectric loss densities (or changes thereof) are found to be related to the lifetime and the reliability of insulation systems, especially for MV/MF components [105, 151, 152, 192, 193].
- ▶ The quantitative calculation of dielectric losses is possible. In contrast, the partial discharge activities or breakdown voltages are difficult to predict without extensive measurements.
- ▶ The online or offline monitoring of the insulation losses allows the detection of insulation degradation and represents a valuable diagnostic tool (e.g., quality control and preventive maintenance) [144, 145, 147, 193].
- ▶ Even if the dielectric losses are usually small compared to the total losses of a converter, this may not be the case for converters simultaneously operated at MV and MF [83, 105, 151, 198].
- ▶ The insulation temperature increase, due to the converter losses, can drive the dielectric itself into a high-loss regime, with a subsequent thermal breakdown of the insulation [151, 287].

It should be noted that, even if the presented analysis is conducted for MV/MF applications, the same problem can appear for LV/HF converters operated with fast-switching GaN HEMTs (above 10 MHz) [314, 315]. In such systems, due to the extreme switching frequencies, even reduced voltages (below 1 kV) can also produce significant insulation stresses. Accordingly, the

theoretical analysis proposed in this chapter is also directly applicable to LV systems operated at HF.

To the knowledge of the author, the exact impact of the harmonics contained in PWM voltages (compared to purely sinusoidal voltages) on the dielectric losses, up to now, has not been studied in detail. Therefore, this chapter examines the computation of insulation losses in converters and is organized as follows. After recalling the definition of the dielectric losses in time and frequency domain in Section 7.2, simple and scalable expressions are derived in Section 7.3 for their evaluation with PWM waveforms. The frequency and temperature dependences of the dielectric material properties are discussed in detail. In Section 7.4, the presented analysis methods are applied to a specific MV/MF transformer design. The predicted dielectric losses are successfully compared with measurements conducted on the constructed prototype. Finally, Section 7.5 presents guidelines for choosing appropriate insulation materials for MV/MF applications.

7.2 Dielectric Polarization Losses

The electrical and dielectric response of a solid insulation material depends on various microphysical processes such as polarization (e.g., electronic, atomic, and dipolar), leakage current (surface and bulk DC conductivity), charge trapping, partial discharges, etc. [192, 193, 316]. The losses occurring inside insulation materials of MV power converters are mostly linked with dielectric polarization effects [151, 192]. The nonlinearities and additional losses which appear above the partial discharge inception voltage and at very low-frequencies (e.g., space charge migration and leakage current) are usually negligible and, therefore, not considered in this work [270, 287, 317]. For typical materials, operating frequencies, and electric field strengths used in power converters, the polarization effects are linear with respect to the electric field [287, 316, 318]. Non-linear polarization effects are mostly occurring in ferroelectric materials (e.g., ceramic capacitors), which are not used as insulation materials due to their high permittivity [287, 316]. With these assumptions, the mathematical models used for calculating the dielectric losses are presented in this section.

7.2.1 Time Domain

As known from linear system theory, the dielectric response of a linear isotropic material is fully described with the polarization response to an elec-

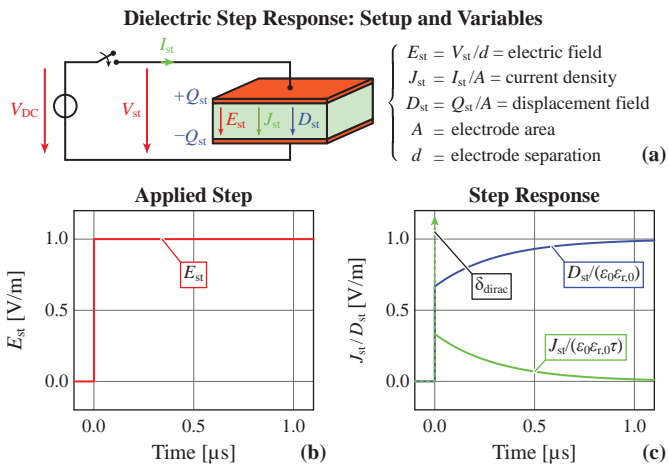


Fig. 7.1: (a) Variables describing the polarization response of a dielectric material to an electric field unit step. (b) Applied electric field unit step. (c) Obtained displacement field and current density responses. A Debye relaxation model (exponential charging model) is used for describing the considered exemplary material ($\epsilon_{r,0} = 3.0$, $\epsilon_{r,\infty} = 2.0$, $\tau = 320$ ns) [192, 317].

tric field unit step [317, 319, 320]. This process is shown in Fig. 7.1 for a simple exemplary dielectric (Debye relaxation model, no leakage current) [192, 317]. The derivative of the step response (displacement field) is the impulse response (current density). At $t = 0$, the impulse response goes to infinity (Dirac delta), which corresponds to an instantaneous charging of the vacuum capacitance of the considered electrode arrangement. The polarization mechanisms occurring at extreme frequencies (e.g., polarization at optical frequencies) can also be included in this quasi-instantaneous response (Dirac delta), at least for power electronics applications. It should be noted that, with the step and impulse responses, only the total losses can be determined. Without additional information on the physical nature of the polarization mechanisms (e.g., transfer dynamics between the dipoles and their molecular environment), an instantaneous dielectric loss rate cannot be specified.

The polarization response to an arbitrary voltage excitation can be obtained by convoluting the applied electric field with the impulse response [192, 320]:

$$D(t) = \int_0^{\infty} J_{st}(t') E(t - t') dt', \quad J(t) = \frac{\partial D(t)}{\partial t}, \quad (7.1)$$

where E is the applied electric field, J_{st} the impulse response, D the obtained displacement field, and J the obtained current density. Then, the input power per unit volume (p) and the supplied energy density (w) can be written as

$$p(t) = E(t) J(t), \quad w(t) = \int_0^t p(t') dt'. \quad (7.2)$$

The time domain convolution is illustrated in Fig. 7.2 for trapezoidal electric field pulses, as resulting from PWM voltages. The dielectric response (D , J , p , and w) contains contributions from the vacuum permittivity (instantaneous response and lossless) and from the material polarization (linked to the dielectric susceptibility, delayed response, and lossy). The dielectric losses can be obtained by making the energy balance between the supplied energy and the energy stored in the field, cf. Fig. 7.2(e). In analogy to magnetic losses, the dielectric losses can also be extracted from the area between the electric field and the displacement field, i.e. the hysteresis curve, cf. Fig. 7.2(f).

Despite its conceptual clarity, the computation of dielectric losses in time domain is often problematic since it involves a convolution integral. Also, the step and impulse responses of the insulation materials are often not directly

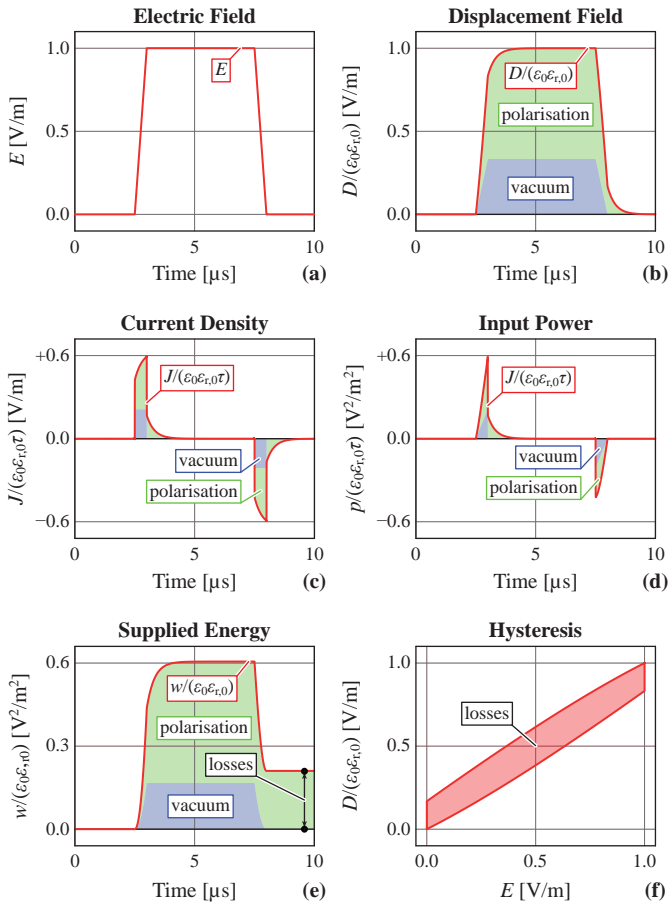


Fig. 7.2: Material response to (a) electric field pulses: (b) displacement field, (c) current density, (d) input power, (e) supplied energy, and (f) hysteresis cycle. The different variables are, whenever possible, split into two distinct parts: vacuum permittivity and material polarization. A Debye relaxation model (exponential charging model) is used for describing the considered exemplary material ($\epsilon_{r,0} = 3.0$, $\epsilon_{r,\infty} = 2.0$, $\tau = 320$ ns) [192, 317].

available (e.g., datasheets). Moreover, the numerical simulation of the electric field in time domain is computationally intensive (e.g., FEM simulations). For these reasons, it is preferable, especially for periodic excitations, to compute the dielectric losses in frequency domain.

7.2.2 Frequency Domain

The response of a linear isotropic dielectric can be described with its complex permittivity and conductivity. The following relationships can be defined [192]:

$$J(f) = J_c(f) + J_d(f) = \sigma E(f) + j2\pi f \varepsilon(f) E(f), \quad (7.3)$$

$$\varepsilon(f) = \varepsilon_0 \varepsilon_r(f) = \varepsilon_0 (\varepsilon'_r(f) - j\varepsilon''_r(f)), \quad (7.4)$$

where f is the frequency, J the current density (due to both free and bound charges), E the electric field, σ the conductivity, and $\varepsilon(f)$ the permittivity. The permittivity is obtained by the following Fourier transform [192, 320]:

$$\varepsilon_r(f) = \varepsilon_r(\infty) + \frac{1}{\varepsilon_0 E_0} \int_0^{\infty} J_{st}(t) e^{-j2\pi f t} dt, \quad (7.5)$$

where J_{st} is the displacement current density response to an electric field unit step (cf. Fig. 7.1). The fact that the frequency domain permittivity is the Fourier transform of a real function imposes some restrictions on $\varepsilon_r(f)$. Moreover, the polarization step response respects causality (equal to zero for $t < 0$). These conditions are expressed by the Kramers-Kronig relations which link the real and imaginary parts of the permittivity [192, 317]:

$$\varepsilon'_r(f) = \varepsilon'_r(\infty) + \frac{2}{\pi} \mathcal{P} \int_0^{\infty} \frac{f' \varepsilon''_r(f')}{f'^2 - f^2} df', \quad (7.6)$$

$$\varepsilon''_r(f) = -\frac{2}{\pi} \mathcal{P} \int_0^{\infty} \frac{f' (\varepsilon'_r(f') - \varepsilon'_r(\infty))}{f'^2 - f^2} df', \quad (7.7)$$

where \mathcal{P} denotes the Cauchy principal value of an integral (handling of the singularity). If the variation of $\varepsilon_r(f)$ is moderate (in a given frequency range), the following approximation of (7.7) can be derived [317, 320]:

$$\varepsilon''_r(f) \approx -\frac{\pi}{2} \frac{\partial \varepsilon'_r(f)}{\partial \ln(f)}. \quad (7.8)$$

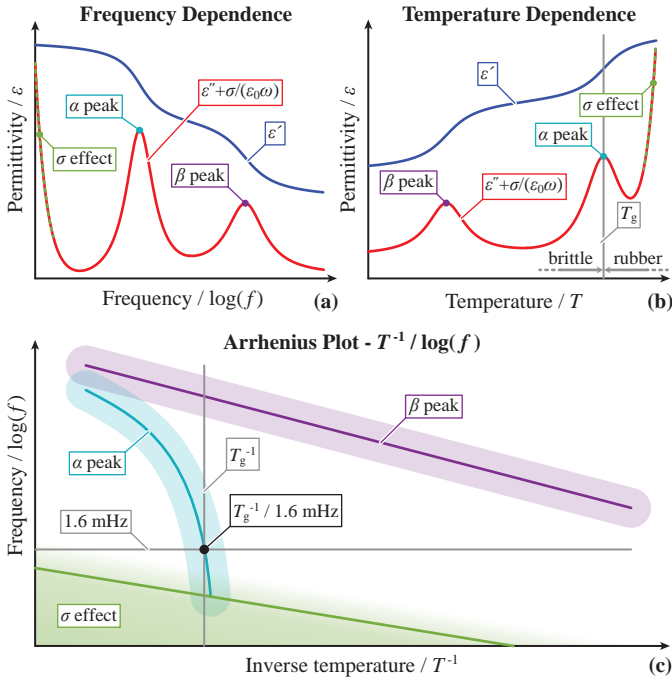


Fig. 7.3: (a) Frequency and (b) temperature dependences of the complex permittivity for an exemplary polymeric insulation material. (c) Arrhenius plot showing the frequency and temperature dependences of the loss peaks. The effects of the α relaxation, β relaxation, and conductivity (σ) are shown, as well as the definition of the glass transition temperature, T_g .

This equation states that a decrease of the real part of the permittivity in a given frequency range will produce a loss peak (imaginary part) in the same frequency range. Compared to (7.7), this approximation is much simpler: no integral over the complete spectrum, no singularity, and applicable locally.

Fig. 7.3(a) depicts the frequency dependence (at a fixed temperature) of the complex permittivity for an exemplary polymeric insulation material. With increasing frequency, the dipoles successively lose their ability to follow the external electric field and the real part (and magnitude) of the permittivity drops [192, 300, 316]. It can be seen that the derivative of the real part (in a logarithmic frequency scale) is approximately proportional to the imaginary part (cf. (7.8)). Two typical loss peaks, corresponding to different types of re-

laxing dipoles, are shown: segmental motion of polymer chains (α relaxation) and orientation of local dipoles (β relaxation). Other loss peaks may occur (e.g., γ relaxation and MWS mode) but are less relevant for the frequency range used by power electronic converters [300, 316]. Towards the lower end of the frequency spectrum (typically well below 50 Hz), the loss due to the DC conductivity (leakage current) begins to dominate the imaginary part of the (effective) permittivity (cf. (7.3)).

Fig. 7.3(b) shows a typical temperature dependence (at a fixed frequency) of the complex permittivity. The real part of the permittivity increases with temperature due to the higher dipole mobility [300, 316]. Again, contributions from discrete relaxation modes (α and β relaxations) and DC conductivity are present (in reverse order compared to the frequency dependence). The α relaxation peak defines the glass transition temperature of the material, T_g , where the material is going from a brittle glassy state to a viscoelastic rubbery state, with a characteristic drop in the polymer's elastic modulus [300]. The glass transition temperature is typically measured at very low-frequencies, where $f = 1.6$ mHz represents the prevalent choice [300].

Fig. 7.3(c) shows the corresponding Arrhenius plot where the frequency and temperature dependences of the loss peaks are simultaneously illustrated. Usually, the α and β peaks merge into a single peak at HF [300]. At low-frequencies or high temperatures, the leakage current dominates over the polarization current.

It should be noted that the AC losses can be arbitrarily split between σ and ϵ_r'' while the DC losses can only be represented with σ (cf. (7.3)). Moreover, with typical AC dielectric spectroscopy measurements, only the total losses are measured and the conduction and polarization losses cannot be split [144, 193]. Usually, σ is set with the DC conductivity and is accepted to be frequency-independent. Then, ϵ_r'' is chosen such that $\sigma + 2\pi f \epsilon_0 \epsilon_r''$ matches the measured AC losses. However, the conduction losses in the insulation of power converters are usually negligible (compared to the polarization losses). Therefore, only the polarization losses are considered in this work.

7.2.3 Loss Computation

With the help of the complex permittivity, it is straightforward to express the time-averaged losses of an insulation system excited with a periodic electric

field as

$$P = \iiint_V \left(\sum_{n=1}^{\infty} \varepsilon_0 \varepsilon_r''(nf_s) (2\pi n f_s) E_{n,\text{RMS}}^2 \right) dV, \quad (7.9)$$

where V is the insulation volume, f_s the fundamental frequency, and $E_{n,\text{RMS}}$ the RMS Fourier series coefficients of the electric field norm. In case of a homogeneous and isothermal dielectric placed between an arbitrary number of electrodes, the expression for the losses can be simplified to

$$P = \sum_{n=1}^{\infty} \varepsilon_r''(nf_s) (2\pi n f_s) \varphi_{n,\text{RMS}}^T C_0 \varphi_{n,\text{RMS}}, \quad (7.10)$$

where C_0 is the vacuum capacitance matrix (describing the geometry) and $\varphi_{n,\text{RMS}}$ is a vector containing the RMS Fourier series coefficients of the potentials applied to the different electrodes. The matrix is computed with ε_0 such that $Q = C_0 \varphi$, where Q and φ are vectors containing the charges and the potentials (with respect to the reference potential 0 V) of the different electrodes.

The aforementioned formulas make use of the complex permittivity. However, for a given material, the absolute value of the permittivity (ε_r) is often given (e.g., norms and datasheets) together with the loss tangent or dissipation factor ($\tan \delta$). Equivalent circuits consisting of the series (C_{ESR} and R_{ESR}) or parallel (C_{EPR} and R_{EPR}) connection of a capacitor and a resistor are also common. These quantities are related to the real and imaginary part of the complex permittivity as follows:

$$\tan \delta = \frac{\varepsilon_r''}{\varepsilon_r'}, \quad (7.11)$$

$$C_{\text{ESR}} = \frac{\varepsilon_r''^2 + \varepsilon_r'^2}{\varepsilon_r'} C_0 \quad \varepsilon_r' \gg \varepsilon_r'' \approx \varepsilon_r' C_0, \quad (7.12)$$

$$R_{\text{ESR}} = \frac{\varepsilon_r''}{\varepsilon_r'^2 + \varepsilon_r'^2} \frac{1}{2\pi f C_0} \quad \varepsilon_r' \gg \varepsilon_r'' \approx \frac{\varepsilon_r''}{\varepsilon_r'} \frac{1}{2\pi f C_{\text{ESR}}}, \quad (7.13)$$

$$C_{\text{EPR}} = \varepsilon_r' C_0, \quad (7.14)$$

$$R_{\text{EPR}} = \frac{1}{\varepsilon_r'} \frac{1}{2\pi f C_0} = \frac{\varepsilon_r'}{\varepsilon_r''} \frac{1}{2\pi f C_{\text{EPR}}}. \quad (7.15)$$

The loss tangent is a figure of merit for capacitors (losses compared to the stored energy). Since energy storage is not a desirable property of electrical

insulation, the loss tangent is not a figure of merit for insulation materials. Models based on the series or parallel equivalent circuits are massively frequency-dependent even for a constant complex permittivity. The approximation of a frequency-independent equivalent circuit, which is common for the computation of capacitor losses in case of constant frequency sinusoidal operation, is invalid for the dielectric losses of insulation materials with PWM voltages (due to the broad voltage spectrum). This would lead to a massive overestimation (C_{ESR} and R_{ESR}) or underestimation (C_{EPR} and R_{EPR}) of the dielectric losses. It should also be noted that the instantaneous losses obtained with the series or parallel equivalent circuits do not feature any physical meaning (only the average losses should be considered). For these reasons, the complex permittivity representation in frequency domain is used in this work.

7.3 Dielectric Losses with PWM Voltages

In steady state operation, typical power converters generate PWM voltages which are also applied to the insulation. Expression (7.10) allows the calculation of the dielectric losses by means of numerical computations. It is, however, very difficult to separate the influence of the different parameters since the frequency-dependent material parameter $\epsilon_r''(f)$ and the amplitude of the voltage harmonic components appear in the product term of the infinite sum.

In order to find a closed-form expression for the losses produced by PWM voltages, a constant value of $\epsilon_r''(f)$ is first considered in Subsection 7.3.1, which, according to [318] is an admissible assumption for certain insulation materials. This holds true for low-loss polymeric materials (e.g., PTFE and PP) for which no significant relaxation peaks occur within the frequency band excited by typical PWM voltages. With this assumption, $\epsilon_r''(f)$ can be taken out of the sum (7.10), allowing the decoupling of the impact of the material properties from the applied excitation. Afterwards, in Subsection 7.3.2, the frequency dependence of the permittivity is analyzed. Finally, Subsection 7.3.3 and Subsection 7.3.4 explain the implications of such frequency dependences on the dielectric losses.

7.3.1 PWM with Frequency-Independent Materials

An insulation system with two electrodes is considered and a PWM voltage is applied, as illustrated in Fig. 7.4(a). The switching transitions are shown in

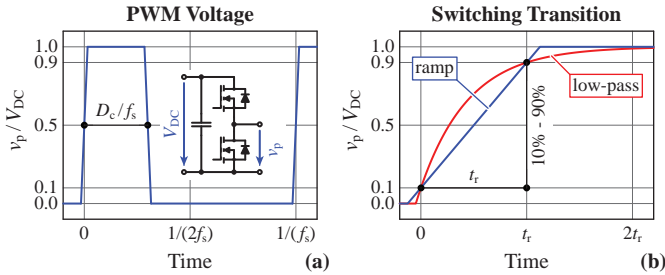


Fig. 7.4: (a) PWM signal with a constant duty cycle. (b) Two different approximations of the switching transition (rise time t_r): the ramp function and the step response of a first-order low-pass filter.

Fig. 7.4(b). The commonly used ramp function generates a spectrum with side lobes ($\sin(x)/x$ shaped harmonics) and, therefore, is complex to analyze in frequency domain. However, the step response of a first-order low-pass filter features a similar spectrum which can be described with a simpler formula. For this reason, the step response of the following low-pass filter is used:

$$G_{lp}(f) = \frac{1}{1 + j\frac{f}{f_c}}, \quad f_c = \frac{\ln\left(\frac{0.9}{0.1}\right)}{2\pi t_r}, \quad (7.16)$$

where t_r is the 10% – 90% rise time, cf. Fig. 7.4(b). The associated harmonic components (Fourier series, without DC component) of the PWM voltage can be computed as

$$V_{n,\text{RMS}} = \left(\frac{\sqrt{2}}{\pi} \frac{|\sin(\pi n D_c)|}{n} V_{DC} \right) |G_{lp}(n f_s)|, \quad (7.17)$$

where D_c is the duty cycle and V_{DC} the voltage pulse amplitude. With the voltage harmonics, the spectral components of the losses (cf. (7.10)) and the total (time averaged) losses can be computed:

$$P_n = (\epsilon_1'' C_0) (2\pi n f_s) V_{n,\text{RMS}}^2, \quad (7.18)$$

$$P_{n,c} = \sum_{n'=1}^n P_{n'}, \quad (7.19)$$

$$P = \lim_{n \rightarrow \infty} P_{n,c} = \sum_{n'=1}^{\infty} P_{n'}, \quad (7.20)$$

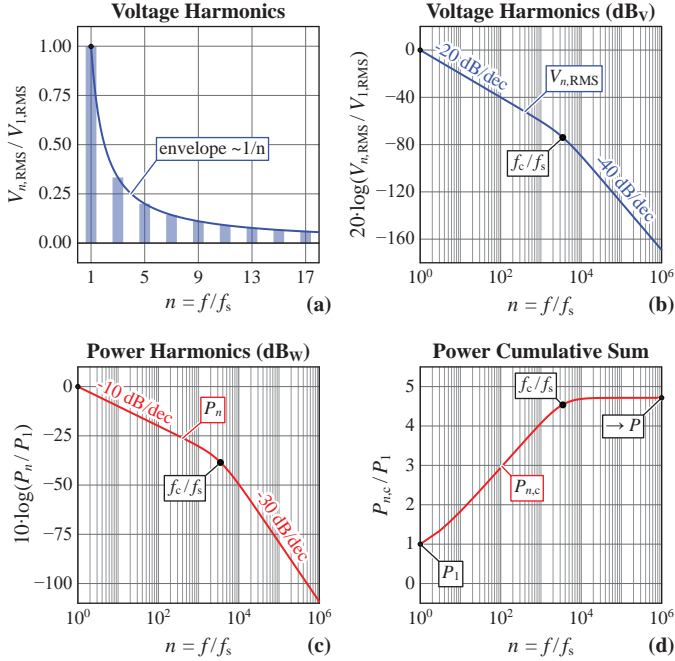


Fig. 7.5: (a) Voltage harmonics for a PWM signal with a constant duty cycle (representation limited to the first harmonics), (b) envelope of the voltage harmonics (in dB_V), (c) envelope of the power loss harmonics (in dB_W), and (d) cumulative sum of the power harmonics. The following parameters are used: $f_s = 1$ kHz, $t_r = 100$ ns, and $D_c = 50\%$. With the chosen duty cycle, no even harmonics are present. All the values are normalized with respect to the fundamental harmonic.

where f_s is the switching frequency, P_n the spectral losses, $P_{n,c}$ the partial losses of the first n harmonics, and P the total losses. The assumption $\epsilon_r''(f) = \text{const.}$ is made.

Fig. 7.5 depicts the voltage harmonics (cf. (7.17)), the loss spectral components (cf. (7.18)), and the cumulative sum of the losses (cf. (7.19)). The voltage and power harmonics are proportional to $1/n$ for frequencies below the corner frequency of the low-pass filter. Above the corner frequency, the voltage and power harmonics are proportional to $1/n^2$ and $1/n^3$, respectively. Therefore, the sum (7.20) only converges above the corner frequency [321].

This implies that an infinitesimally short switching transition would lead to infinite losses. However, this is only true with the assumption of a frequency-independent complex permittivity, which is nonphysical for very large frequency ranges (cf. (7.8)). Nevertheless, the aforementioned results indicate that a model of the switching transition is required for evaluating the dielectric losses with PWM voltages (cf. (7.16)). Moreover, the sum P is much greater than the fundamental harmonic P_1 , showing that a fundamental frequency analysis is invalid.

The calculation of (7.20) is computationally intensive since it requires the summation of many harmonics (cf. Fig. 7.5(d)). This holds especially true for the cases where the electric field patterns are obtained from numerical simulations and the summation is performed on a meshed geometry. Therefore, a closed-form approximation is proposed (with the assumption $\epsilon_r''(f) = \text{const.}$):

$$P \approx \lambda P_1, \quad (7.21)$$

$$P_1 = (\epsilon_r'' C_0) (2\pi f_s) \left(\frac{\sqrt{2}}{\pi} V_{\text{DC}} \right)^2, \quad (7.22)$$

$$\lambda = \frac{1}{2} \ln \left(2e^\gamma \frac{f_c}{f_s} \sin(\pi D_c) \right), \quad (7.23)$$

where P_1 expresses the losses at the fundamental frequency (with $D_c = 50\%$). The correction factor λ takes into account the duty cycle and the harmonics. The constant $\gamma \approx 0.58$ is the Euler-Mascheroni constant. The derivation of (7.21) requires elaborate calculations, which are given in Appendix B.1. The accuracy of the approximation is evaluated in Appendix B.5 for different frequencies, duty cycles, and switching speeds. It is found that the approximation is highly accurate (1% error). The error is also small (4% error) if a ramp function is used instead of the low-pass filter step response for modeling the switching transition (cf. Fig. 7.4(b)). This indicates that an exact model of the switching transition is not necessary and that the model used in (7.16) is sufficient. Moreover, this approximation can be applied to PWM signals with variable duty cycle (e.g., sinusoidal modulation and multi-level inverters) by means of local duty cycle averaging, as shown in [153].

Fig. 7.6 depicts the results obtained with (7.21) for different rise times, switching frequencies, and duty cycles for typical values encountered in MV converters. It can be seen that the impact of the voltage ($P \sim V_{\text{DC}}^2$) and frequency ($P \sim f_s \ln(\text{const.}/f_s)$) are very strong while the losses increase only logarithmically with respect to the reciprocal of the rise time ($P \sim$

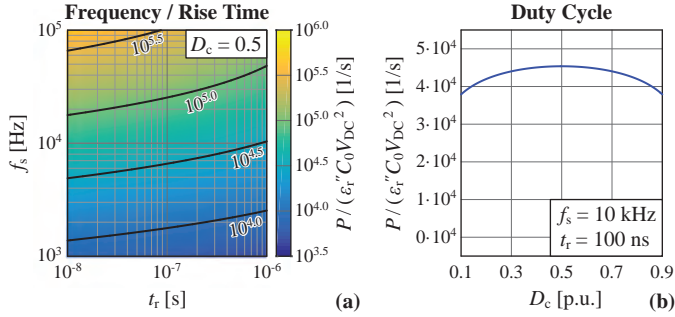


Fig. 7.6: (a) Impact of the switching frequency, the rise time, and (b) the duty cycle on the dielectric losses. The excitation is a PWM signal with a constant duty cycle. All the power values are normalized with respect to $\epsilon_r'' C_0 V_{DC}^2$ while the used parameters are given in the figures.

$\ln(\text{const.}/t_r)$. The influence of the duty cycle on the losses is almost negligible in the practically relevant range ($D_c \in [10\%, 90\%]$).

7.3.2 Frequency-Dependent Materials

In the previous subsection, a constant $\epsilon_r''(f)$ has been assumed. However, due to the coupling between the real and imaginary part of the permittivity (Kramers-Kronig relations, cf. (7.8)), this approximation cannot be accurate in a wide frequency range. The fact that the insulation of power converters is subject to a wide range of operating temperatures and frequencies increases the probability of encountering loss peaks (cf. Fig. 7.3).

In this work, at first, an epoxy resin is considered since this a common insulation material for potting MV components. This resin is an unfilled epoxy ("vonRoll Damisol 3418") with a high glass transition temperature ($T_g = 136^\circ\text{C}$) [145, 323]. Due to the high glass transition temperature, this epoxy features low losses in a wide temperature range (cf. Fig. 7.3).

The complex permittivity is typically measured with a dielectric spectroscopy setup. A voltage is applied to the dielectric and the current is measured. Then, the complex impedance is computed and the complex permittivity can be extracted. Such measurements are intrinsically ill-conditioned due to the low dissipation factor, i.e. the phase shift between the voltage and the current is almost 90° . Therefore, highly accurate impedance measurement setups, which are optimized and/or calibrated for capacitive loads, are

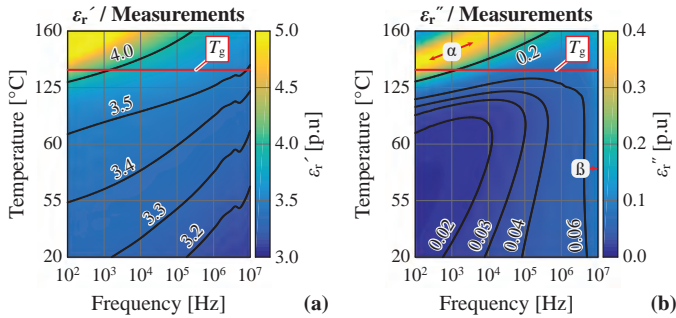


Fig. 7.7: (a) Measured values of $\epsilon_r'(f, T)$ and (b) $\epsilon_r''(f, T)$ for the epoxy resin “vonRoll Damisol 3418” [322]. The glass transition temperature ($T_g = 136\text{ }^\circ\text{C}$) is indicated. The α relaxation peak and the beginning of the β relaxation are shown.

required [144, 145]. Fig. 7.7 shows the measured complex permittivity for the selected resin. The measurements are done with a disc-shaped specimen using a “Novocontrol Alpha-A” high precision dielectric spectroscopy system [322].

The α relaxation peak (at the glass transition temperature) and the beginning of the β relaxation peak (peak above 10 MHz) can be identified (cf. Fig. 7.3). The α relaxation peak is very large and corresponding large losses result if the epoxy resin is operated near the glass transition temperature. It is, therefore, obvious that the approximation of a constant complex permittivity can only be valid in a limited frequency and temperature range.

The Kramers-Kronig relations can be applied to the measured data. Between the relaxation peaks, where the permittivity curve is flat, the approximation (7.8) of the Kramers-Kronig integral (7.7) can be used. Fig. 7.8 shows the correlation between the real and imaginary part of the permittivity and the curves reconstructed with (7.8). A detailed analysis of the accuracy of the approximation of the Kramers-Kronig relations is presented in Appendix B.4 and it is found that the approximation is valid between the loss peaks (9% error).

7.3.3 Upper Bound on the Dielectric Losses

In Subsection 7.3.1, it has been shown that the model of a frequency-independent permittivity diverges for infinite switching speeds. With the results presented in Subsection 7.3.2, this problem can be eliminated and an upper bound for the dielectric losses can be derived.

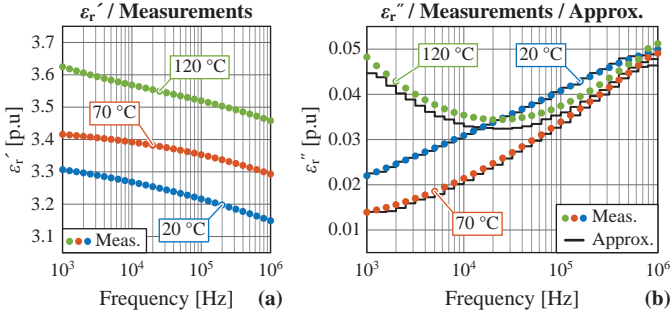


Fig. 7.8: (a) Measured $\varepsilon_r'(f)$ and (b) $\varepsilon_r''(f)$ at different temperatures for the epoxy resin “vonRoll Damisol 3418” [322]. An approximation of $\varepsilon_r''(f)$, computed with the Kramers-Kronig approximation (7.8), is also shown. The selected frequencies and temperatures are located below the α and β peaks (cf. Fig. 7.7).

A single (non-periodic) voltage transition (step response of a first-order low-pass filter, cf. Fig. 7.4(b)) is considered. With the Fourier transformation, the dissipated energy can be calculated in frequency domain:

$$W = C_0 V_{\text{DC}}^2 \left(\frac{1}{\pi} \int_0^{\infty} \varepsilon_r''(f) \frac{1}{f} \frac{f_c^2}{f^2 + f_c^2} df \right). \quad (7.24)$$

The derivation of (7.24) is given in Appendix B.2. For slow switching transition (cf. (7.16)), the integral converges to zero:

$$\lim_{t_r \rightarrow \infty} W = 0. \quad (7.25)$$

With the Kramers-Kronig relations (cf. (7.6)), the expression (7.24) can be rewritten as

$$W = C_0 V_{\text{DC}}^2 \left(\frac{\varepsilon_r'(0) - \varepsilon_r'(\infty)}{2} - \frac{1}{\pi} \int_0^{\infty} \varepsilon_r''(f) \frac{f}{f^2 + f_c^2} df \right). \quad (7.26)$$

The derivation of (7.26) is also given in Appendix B.2. For a switching transition with an infinite switching speed (cf. (7.16)), the integral converges to zero. This implies that the first term of the equation represents an upper bound for the dielectric losses [320]:

$$W_{\text{max}} = \lim_{t_r \rightarrow 0} W = C_0 V_{\text{DC}}^2 \frac{\varepsilon_r'(0) - \varepsilon_r'(\infty)}{2}. \quad (7.27)$$

However, with periodic PWM voltages, this upper bound is usually not reached due to the limited switching speed of the semiconductors. Additionally, a periodic PWM signal does not excite frequencies below the switching frequency, which is not the case for a single (non-periodic) switching transition. Therefore, this upper bound is only of theoretical interest and cannot be used for computing the dielectric losses of insulation systems. An approximation taking into account the finite switching speed and the presence of a finite fundamental period is presented in the next subsection.

7.3.4 PWM with Frequency-Dependent Materials

The approaches considered in Subsection 7.3.1 and Subsection 7.3.2 can be combined for extracting a closed-form approximation of the dielectric losses produced by frequency-dependent materials under PWM voltages:

$$P = (\lambda_1 + \lambda_2) P_1, \quad (7.28)$$

$$P_1 = (\varepsilon_r''(f_s) C_0) (2\pi f_s) \left(\frac{\sqrt{2}}{\pi} V_{\text{DC}} \right)^2, \quad (7.29)$$

$$\lambda_1 = \frac{1}{2} \ln(2e^\gamma \sin(\pi D_c)). \quad (7.30)$$

$$\lambda_2 = \frac{1}{2\varepsilon_r''(f_s)} \underbrace{\int_{\ln(f_s)}^{\ln(f_c)} \varepsilon_r''(f) d(\ln(f))}_{\varepsilon_{r,\text{int}}''}, \quad (7.31)$$

where P_1 represents the losses at the fundamental frequency. The correction factors λ_1 and λ_2 describe the impact of the duty cycle, the harmonics, and the frequency dependence of the material parameters. The derivation of (7.28) is given in Appendix B.3. The proposed formula requires the measurement of $\varepsilon_r''(f)$ for $f \in [f_s, f_c]$ (cf. (7.16) and (7.17)), which is not always available and difficult to perform (due to $\varepsilon_r' \gg \varepsilon_r''$) [144, 193, 324]. However, with the Kramers-Kronig relations (cf. (7.8)), the approximation (7.31) can be simplified

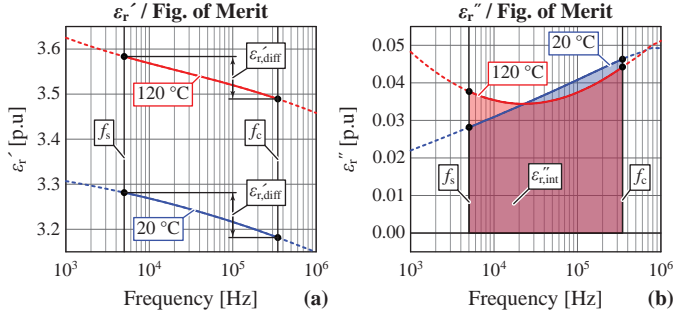


Fig. 7.9: (a) Measured $\epsilon'_r(f)$ and (b) $\epsilon''_r(f)$ for the epoxy resin “vonRoll Damisol 3418”. The difference $\epsilon'_{r,diff}$ (cf. (7.35)) and the area $\epsilon''_{r,int}$ (cf. (7.31)), which are figures of merit for the losses, are shown.

and rewritten as

$$P = (\lambda_1 + \lambda_2) P_1, \quad (7.32)$$

$$P_1 = \left(\left(-\frac{\pi}{2} \frac{\partial \epsilon'_r(f)}{\partial \ln(f)} \Big|_{f_s} \right) C_0 \right) (2\pi f_s) \left(\frac{\sqrt{2}}{\pi} V_{DC} \right)^2, \quad (7.33)$$

$$\lambda_1 = \frac{1}{2} \ln(2e^Y \sin(\pi D_c)). \quad (7.34)$$

$$\lambda_2 = \frac{\pi}{4\epsilon''_r(f_s)} \underbrace{(\epsilon'_r(f_s) - \epsilon'_r(f_c))}_{\epsilon'_{r,diff}}. \quad (7.35)$$

The area $\epsilon''_{r,int}$ (cf. (7.31)) approximates the summation over frequencies of the dielectric losses (cf. (7.20)) and, therefore, is a figure of merit for the losses generated by a dielectric material with PWM voltages. The integral can be combined with the derivative term present of the Kramers-Kronig approximation (cf. (7.8)) leading to an even simpler figure of merit: the difference $\epsilon'_{r,diff}$ (cf. (7.35)). Fig. 7.9 illustrates how these figures of merit can be used for comparing the losses at different temperatures. In addition, they are useful for comparing the losses between different materials.

The accuracy of the approximations is evaluated in Appendix B.5 for different frequencies, duty cycles, switching speeds, and temperatures. The approximations are found to be valid for the selected resin: 8 % error with (7.28) and 16 % error with (7.32). If the frequency dependence of the material parameters is neglected (cf. (7.21)), the error is greater than 100 %, indicating

that the frequency dependence of the permittivity must be considered for accurate computations.

7.4 Case Study: MV/MF Transformer

With the help of the proposed approximations, the dielectric losses of different components can be examined. Since it has been identified that the stresses are particularly high for MV/MF transformers operated inside MV DC-DC converters, such a transformer has been selected for this case study [64, 82, 105, 142, 143, 153, 154].

7.4.1 Transformer Design

The SST demonstrator presented in Subsection 1.7.2 is considered. This 25 kW SST includes a single-cell SRC-DCX operated at 48 kHz between a 7 kV DC bus and a 400 V DC bus. The MV/MF transformer of the considered SST is subject to all identified critical aspects with respect to dielectric losses: MF operation, high switching speed, large CM voltages, and large DM voltages. The design of the MV/MF transformer is described in Chapter 5.

It should be noted that a small difference exists between the system simulated in this chapter and the constructed demonstrator prototype. A simplified version of the AC-DC stage is considered since the AC-DC stage only affects the CM voltages applied to the MV/MF transformer. In this chapter, a full-bridge operated at 48 kHz is considered for the AC-DC rectifier, even if the demonstrator prototype has been operated with a ZVS triangular current mode modulation, featuring a variable switching frequency (between 35 kHz and 75 kHz) [197]. Nevertheless, the exact modulation scheme of the AC-DC stage is no a critical parameter for examining the dielectric losses of the MV/MF transformer.

Fig. 7.10 shows the circuit topology and the constructed transformer prototype (cf. Chapter 5). The stray inductance of the transformer, together with the series capacitor located on the LV side, is used as a resonant tank [83, 143]. The DC-DC converter is operated at the resonance frequency and ZVS is achieved with the magnetizing current of the transformer (cf. Chapter 8) [88, 198]. This implies that the switched current is nearly load-independent (quasi-ZCS) and that the switching transitions feature a limited speed, which is beneficial for the dielectric losses (cf. Fig. 7.6) [111, 112, 143]. Due to the split DC-bus half-bridge configuration, the DM voltage applied to the MV winding

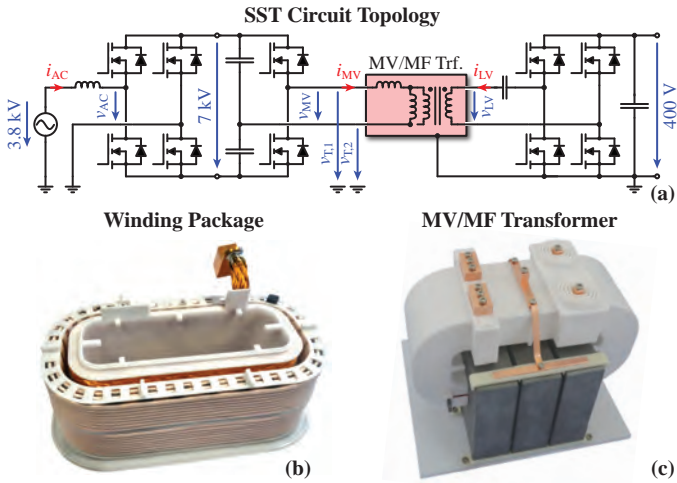


Fig. 7.10: (a) Considered SST (AC-DC converter and isolated DC-DC converter) where the MV/MF transformer is highlighted. (b) MV/MF transformer windings (before vacuum potting). (c) Constructed MV/MF transformer prototype.

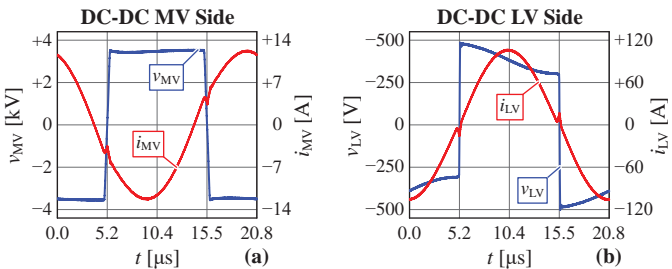


Fig. 7.11: Measured voltages and currents for the (a) MV side and (b) LV side of the MV/MF transformer. The series-resonant DC-DC converter is operated at the switching frequency.

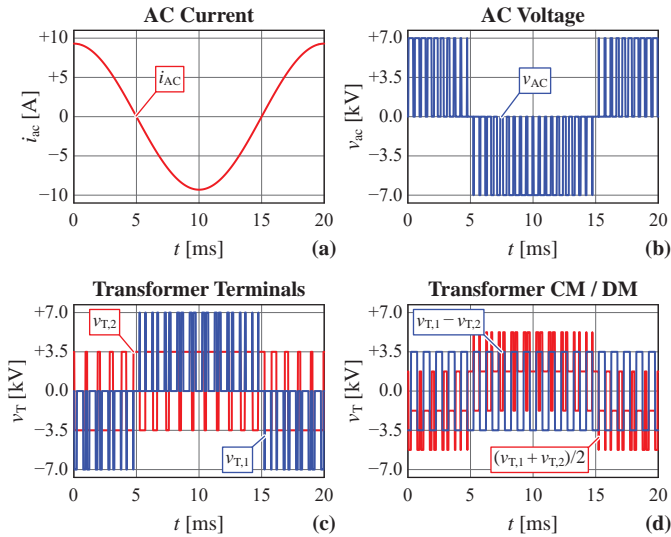


Fig. 7.12: Currents and voltages created by the MV side of the SST: (a) AC grid current, (b) AC PWM voltage, (c) MV/MF transformer terminal voltages, and (d) MV/MF transformer CM and DM voltages. For illustration purposes, a switching frequency of 1 kHz is selected for the AC-DC and DC-DC stages (instead of 48 kHz).

is ± 3.5 kV. Fig. 7.11 shows the measured voltages applied to the transformer and the corresponding currents [198]

In addition to the DM voltage applied to the transformer by the DC-DC stage, the AC-DC stage is creating an extra CM voltage. Fig. 7.12 illustrates the total voltages applied to the MV side of the transformer, given that the system is grounded with respect to the AC grid (solid-earthing) on the MV side and with respect to the DC-bus negative rail on the LV side (cf. Fig. 7.10(a)). The first component of the CM voltage is generated by the AC-DC stage, i.e. the negative rail of the MV DC-bus is jumping between -7 kV and 0 kV with respect to earth (at 48 kHz, with a sinusoidal modulation). The second component of the CM voltage is created by the split DC-bus half-bridge configuration of the DC-DC stage, which is adding a constant CM voltage of 3.5 kV [105]. The total CM voltage has an average value of 0 kV over a complete grid period [105]. Altogether, a CM LF AC voltage, a CM MF PWM voltage, and a DM MF PWM voltage are applied to the transformer insulation and the peak voltage is 7 kV.

Tab. 7.1: Electric Field and Dielectric Losses

| Parameter | Epoxy | Silicone |
|--|--------------|-----------------|
| Maximum electric field inside the insulation | | |
| RMS field | 14.9 kV/cm | 15.0 kV/cm |
| Peak field | 22.4 kV/cm | 22.6 kV/cm |
| Maximum electric field at the surface of the insulation | | |
| RMS field | 12.4 kV/cm | 12.5 kV/cm |
| Peak field | 18.6 kV/cm | 18.7 kV/cm |
| Capacitive reactive power and dielectric losses | | |
| Capacitive reactive power | 1.0 kVar | 1.2 kVar |
| Total dielectric losses | 14.1 W | 8.4 W |
| Max. dielectric loss density | 405 W/l | 273 W/l |

7.4.2 Transformer Simulation

The design and simulation procedure of the MV/MF transformer is described in detail in Chapter 5. The waveforms applied to the transformer by the SRC-DCX are described in Chapter 8. The losses are computed locally based on the applied stress (magnetic flux, electric field, or current density) and temperature. The consideration of a non-uniform loss distribution is required for modeling eventual thermal runaways, which are occurring locally. This is especially critical for the dielectric losses, which are confined to restricted regions of the transformer and, therefore, can lead to very local temperature hot spots. The dielectric material parameters are measured with small-signal frequency domain measurements of the complex permittivity with disc-shaped specimens. The frequency and temperature dependences of the dielectric, electric, and magnetic material parameters are considered. The electric field pattern is extracted from frequency-dependent FEM simulations and the dielectric losses are then computed with (7.9) in frequency domain [228].

7.4.3 Epoxy Resin Insulation

In a first step, the transformer is insulated with the aforementioned “vonRoll Damisol 3418” unfilled epoxy resin (cf. Fig. 7.7) [323]. Figs. 7.13(a)-(b) show the simulated losses and the corresponding temperature distribution for different load conditions. As expected, the voltage related losses (core, cooling, and

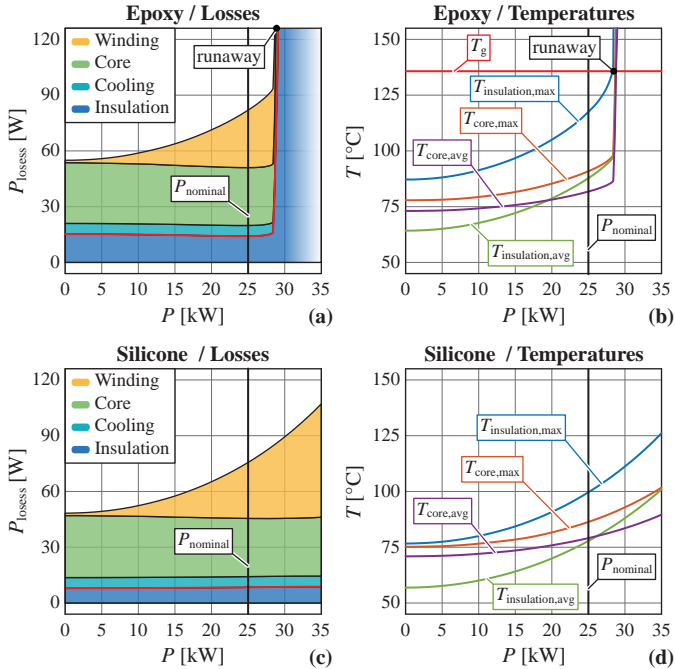


Fig. 7.13: (a) Simulated loss breakdown and (b) temperatures (averaged and hot spot) for the MV/MF transformer with an epoxy resin insulation (“vonRoll Damisol 3418”). (c) Simulated loss breakdown and (d) temperature (averaged and hot spot) for the MV/MF transformer with a silicone elastomer insulation (“Dow Corning TC4605 HLV”). For the epoxy resin, the glass transition temperature ($T_g = 136$ °C) and the associated thermal runaway (α peak) are also indicated. The ambient temperature is set to 40 °C

insulation) are approximately load-independent. Only the winding losses, which are related to the current, are (quadratically) load-dependent.

The key parameters (electric field and dielectric losses) are summarized in Tab. 7.1 for nominal load operation (25 kW). The maximum peak electric field in the insulation is 22.6 kV/cm, which is low for a dry-type insulation material [142,325,326]. However, the total capacitive reactive power, computed as the sum of the reactive power of the different harmonics, is 1.0 kVar. This implies that, even with a low dissipation factor, the dielectric losses represent 27 % of the transformer losses at no-load operation and 17 % at the nominal load.

For loads exceeding 28 kW (12 % overload), a thermal runaway occurs in the insulation (inside the core window, between the windings). The mechanism of the thermal runaway can be explained as follows. The hot spot temperature of the transformer increases when evaluated over the load. This temperature increase is mainly produced by the winding losses which are strongly load-dependent. When the hot spot temperature reaches the glass transition temperature of the insulation material ($T_g = 136\text{ }^\circ\text{C}$ for the considered epoxy resin), a massive increase of the dielectric losses occurs (α peak, cf. Fig. 7.7). According to these results, the considered epoxy resin, which is a typical resin employed for LF systems, is less suitable at MF.

The considered unfilled resin features low-losses (cf. Fig. 7.7) and a high glass transition temperature ($T_g = 136\text{ }^\circ\text{C}$) at the cost of a low thermal conductivity (0.3 W/mK). Unfortunately, this problem is likely to appear with most epoxy resins. Filled epoxy resins will typically feature higher thermal conductivities but also higher losses and lower glass transition temperatures [193,318]. Hence, the transformer prototype has not been insulated with epoxy resin.

7.4.4 Silicone Elastomer Insulation

Materials with significantly lower or higher glass transition temperatures (compared to the operating temperature) would be better suited for the insulation of MF transformers. Therefore, silicone elastomers which feature a low glass-transition temperature (below $0\text{ }^\circ\text{C}$ in the relevant frequency range) are considered, such that the loss peak associated with the glass transition temperature is not critical [301]. Furthermore the β relaxation, which is much smaller than the α relaxation is occurring in the MHz range, i.e. above the corner frequency defined by the switching speed (cf. (7.16)). Therefore, over the complete operating range, no resonance peaks are encountered (cf. Fig. 7.3). The relatively high cost of silicones (as compared to epoxies) is not a

Tab. 7.2: Properties of the “Dow Corning TC4605 HLV” Silicone

| Property | Value |
|------------------------|--|
| Thermal conductivity | 1.0 W/mK |
| Maximum temperature | 200 °C |
| Electrical resistivity | 10^{13} Ω m |
| Dielectric strength | 24 kV/mm |
| Real permittivity | $\epsilon'_r < 4.1$ ($f > 50$ kHz \wedge $T < 120$ °C) |
| Imaginary permittivity | $\epsilon''_r < 0.033$ ($f > 50$ kHz \wedge $T < 120$ °C) |
| Dissipation factor | $\tan \delta < 0.8\%$ ($f > 50$ kHz \wedge $T < 120$ °C) |

disqualifier for MF applications since the insulation volume is relatively small due to the high power densities.

For the considered transformer, the silicone elastomer “Dow Corning TC4605 HLV” has been chosen [268]. This elastomer features a relatively high breakdown strength, moderate permittivity, low dielectric losses, high thermal conductivity (the silicone is mixed with a filler), high temperature stability, low flammability, low viscosity (before curing), good mechanical stability (after curing), and good surface adhesion. The key properties of the material are summarized in Tab. 7.2.

Figs. 7.13(c)-(d) show the simulated losses and the corresponding temperature distribution. The key parameters (electric field and dielectric losses) are again summarized in Tab. 7.1 at the nominal load (25 kW). Compared to the epoxy insulation, the maximum RMS electric field, maximum peak electric field, and the capacitive reactive power are similar. However, the dielectric losses are lower: 16 % of the transformer losses at no-load operation and 11 % at the nominal load. The simulation shows that with silicone insulation, the transformer could be operated at 35 kW (40 % overload) without experiencing excessive temperature or a thermal runaway.

Fig. 7.14 depicts the RMS electric field and the insulation losses. Due to the split DC-bus half-bridge configuration, the electric field pattern is slightly asymmetric between the two halves of the core sets (cf. Fig. 7.12) [105]. As expected, the electric field is most pronounced between the MV and LV windings and inside the MV winding. Since the insulation losses are proportional to the square of the electric field, the dielectric losses are only significant near the surface of the MV winding. Due to the permittivity mismatch between

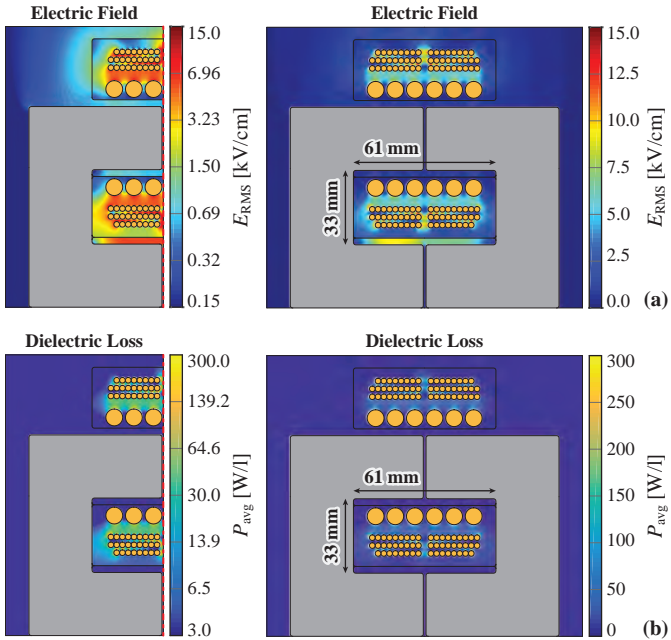


Fig. 7.14: (a) RMS value of the electric field and (b) dielectric loss density in the insulation (logarithmic and linear scales). The simulations are conducted at rated conditions (25 kW) with the silicone elastomer “Dow Corning TC4605 HLV” as insulation material. Due to the permittivity mismatch between the silicone and the air, the electric field is pushed towards the air ducts, given that the magnetic core is grounded.

the silicone and the air, the electric field in the air ducts is particularly large, but below the ionization electric field in air (cf. Chapter 6) [142, 143].

7.4.5 Dielectric Loss Measurements

From the aforementioned considerations and simulations, the silicone elastomer “Dow Corning TC4605 HLV” appears to be superior to epoxy resins and, therefore, has been chosen for insulating the transformer prototype. The LV and MV windings are wound on a polycarbonate coil former, potted with a vacuum potting process, and cured in an oven (cf. Section 5.3).

Due to the low dissipation factor, dielectric losses are only accounting for a small part of the total transformer losses, i.e. 16 % at no-load operation and 11 % at the nominal load. Therefore, the extraction of the dielectric losses during rated operation is intrinsically ill-conditioned and, therefore, inaccurate. For this reason, the measurement of the insulation losses is done with pure CM excitations between the MV and LV windings (the core is grounded with respect to the LV side). With such an excitation, no core or winding losses are occurring and the presented dielectric loss computation methods can be validated. The following excitations are considered:

- ▶ S_{50k} - A MV/MF sinusoidal voltage with a frequency of 50 kHz and a peak amplitude of ± 3.6 kV.
- ▶ S_{100k} - A MV/MF sinusoidal voltage with a frequency of 100 kHz and a peak amplitude of ± 3.6 kV.
- ▶ P_{890n} - A MV/MF PWM voltage with a switching frequency of 50 kHz, a duty cycle of 50 %, a rise time (10 % – 90 %) of 890 ns, and an amplitude of ± 3.5 kV.
- ▶ P_{480n} - A MV/MF PWM voltage with a switching frequency of 50 kHz, a duty cycle of 50 %, a rise time (10 % – 90 %) of 480 ns, and an amplitude of ± 3.5 kV.

Fig. 7.15 shows the measured voltages and the associated CM current through the insulation ($C_{CM} = 139.3$ pF, cf. Subsection 5.4.2). The sinusoidal voltages are generated with a series-resonant circuit fed by a linear amplifier. The PWM voltages are generated by a 10 kV SiC MOSFETs bridge (MV bridge of the SRC-DCX, cf. Subsection 1.7.2) [111, 112, 198]. The switching speed of the MOSFETs is adjusted with the ZVS current, which is provided by a parallel inductor featuring an adjustable air gap.

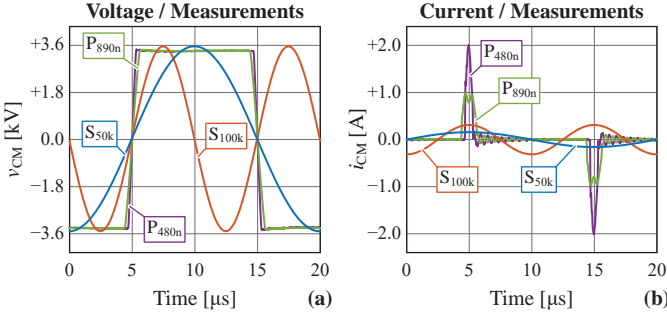


Fig. 7.15: (a) Measured CM voltages applied between the MV winding and the LV winding (the core is grounded with respect to the LV side). (b) CM charging current flowing through the MV winding.

The electrical measurement of the dielectric losses is difficult since most dielectric measurement systems are working with small-signal sinusoidal waveforms and cannot deal with MV/MF sinusoidal or MV/MF PWM voltages. Therefore, the following measurement methods are considered (at an ambient temperature of 22 °C):

- ▶ *Meas. / LV frequency* - The transformer is measured with small signal excitation and the spectral components of the dielectric losses are extracted. The LF measurements (below 150 kHz) are done with the setup described in [144, 145] and the HF measurements (above 150 kHz) are obtained with a precision impedance analyzer [236]. Both measurement setups are carefully calibrated with a quasi-lossless gas reference capacitor [327]. Afterwards, the losses associated with the aforementioned excitations are reconstructed using (7.10) with the hypothesis that the dielectric polarization of the insulation material behaves linearly with respect to the electric field. The peak voltage applied to the insulation varies, depending on the used setup, between 1.4 V and 140 V. Since the dielectric losses are proportional to the square of the voltage, this implies that the measured losses are between 10^2 and 10^7 times smaller than the unscaled values.
- ▶ *Meas. / MV calorimetric* - The transformer is measured with the MV signals and the losses are extracted with transient calorimetric measurements [111, 112]. The windings are equipped with four NTC thermistors (two at the surface of the potted windings and two inside the wind-

ings) and the complete transformer (without the fan) is brought in a thermally insulated polystyrene box. In a first step, the relations between the measured temperatures and the losses are extracted by injecting DC currents in the MV winding (between 1 W and 10 W of losses). Afterwards, the transformer is fed with the MV CM voltages (cf. Fig. 7.15) and the temperatures are recorded. Then, it is straightforward to extract the dielectric losses from the calibration data. The duration of the calibrations and measurements is set to 18 minutes and the time constant of the system is 35 minutes (without the fan). This implies that the measurement is done during the temperature transient. The temperature elevation remains under 3 °C, implying that the temperature dependence of the permittivity can be neglected. This measurement method does not rely on the linearity of the insulation material. The only hypothesis is that the temperature distribution is similar during calibrations and measurements, which is confirmed by the comparison of the measured time constants and temperatures.

The computation of the losses is done with the CM electric field obtained from FEM ($C_{CM} = 149.8$ pF, cf. Subsection 5.4.2) [228]. The insulation material properties are obtained with small-signal frequency domain measurements of the complex permittivity on a disc-shaped specimen. Then the following methods are used for computing the losses (cf. Section 7.3):

- ▶ *Sim. / Infinite Summation* - The dielectric losses are obtained with an infinite summation over the harmonics (cf. (7.10)). For the sinusoidal voltages, only one term is non-zero.
- ▶ *Sim. / Imag. Eps. Approx.* - The approximations based on the imaginary part of the permittivity are used for extracting the losses (cf. (7.28), (7.29), (7.30), and (7.31)). This method is only applicable to PWM voltages (and not to sinusoidal voltages).
- ▶ *Sim. / Real Eps. Approx.* - The approximations based on the real part of the permittivity are used for extracting the losses (cf. (7.32), (7.33), (7.34), (7.35)). This method is only applicable to PWM voltages (and not to sinusoidal voltages).

Tab. 7.3 depicts the calculated and measured losses. The maximum error between the two measurement methods is below 9 % and the maximum error between the measurements and the computations is below 13 %. These deviations are matching with the estimated measurement uncertainties. For

Tab. 7.3: Measured and Simulated Transformer CM Losses

| Meas. / Sim. Method | S_{50k} | S_{100k} | P_{890n} | P_{480n} |
|----------------------------|-----------|------------|------------|------------|
| Meas. / LV Frequency | 1.30 W | 2.35 W | 3.05 W | 3.63 W |
| Meas. / MV Calorimetric | 1.23 W | 2.49 W | 3.02 W | 3.98 W |
| Sim. / Infinite Summation | 1.33 W | 2.54 W | 3.37 W | 4.07 W |
| Sim. / Imag. Eps. Approx. | n/a | n/a | 3.36 W | 3.91 W |
| Sim. / Real Eps. Approx. | n/a | n/a | 3.26 W | 3.78 W |

the MV calorimetric measurements, the total estimated uncertainty is $\pm 16\%$, where the temperature measurement ($\pm 6\%$, datasheet of the NTC thermistors and ADCs) and the error due to the discrepancies between the calibration and the measurements ($\pm 10\%$, estimated with thermal FEM simulations) are considered. Hence, the following hypotheses are verified by the aforementioned measurements:

- ▶ The dielectric response is linear with the electric field and, therefore, the losses of the different harmonics can be determined based on small signal excitations and combined. This point is proven by comparing the small and large signal measurements (both for sinusoidal and PWM voltages).
- ▶ The electric field pattern computed with FEM simulations is sufficiently accurate for computing the losses. This is verified by comparing the measured CM capacitance and losses to the simulated values. This implies that the dielectric loss simulations done for the transformer during rated conditions (with CM and DM voltages, cf. Subsection 7.4.2) are valid.
- ▶ The proposed approximations (cf. Subsection 7.3.4) can be used to avoid the summation of the spectral losses. This greatly facilitates the computation of the dielectric losses from FEM simulations since no computationally intensive summations on FEM meshes are required.

7.5 Design Guidelines

The presented approaches and results can be combined in order to extract design guidelines for choosing appropriate MV/MF (dry-type) insulation materials and computing the corresponding dielectric losses:

- ▶ First, the relevant frequency and temperature ranges should be identified for the insulation system. The frequency range spans from the switching frequency to the corner frequency defined by the switching speed of the semiconductors (cf. (7.16)). The obtained switching speed depends on the used semiconductors and the switching conditions (e.g., ZVS and hard-switching). The usage of converter topologies featuring multiple levels (e.g., flying capacitor, ISOP structures, and MMLC) [92–94, 105] and/or ZVS (e.g., DAB and SRC) [44, 56, 83, 198] reduces the stress applied to the insulation due to the smaller voltage steps and the reduced switching speeds, respectively.
- ▶ The insulation material should be chosen such that no large loss peak occurs in the aforementioned operating range (cf. Fig. 7.3). Particularly, the α relaxation (glass transition temperature) puts a constraint on the temperature range. The β relaxation is less critical but the associated superlinear increase of the dielectric losses as a function of operating frequency should be taken into account. For most insulation materials, the permittivity and dissipation factor provided in the datasheets do not cover the required frequency and temperature ranges. Depending on the required accuracy, the missing information can be extrapolated, taken from available material databases, or measured with a dielectric spectroscopy setup [144, 318, 322].
- ▶ If the permittivity curve is almost constant over the considered spectrum (absence of loss peaks), the approximation (7.21) applies. If the frequency dependence of the permittivity is moderate (absence of loss peaks), the approximations (7.28) and (7.32) can be used. For other cases, the computationally intensive summation (7.10) is required.
- ▶ In power converter insulations, the dielectric materials are usually not the primary source of losses (e.g., compared against core, winding, and semiconductor losses). If the external losses (e.g., winding losses and core losses) are dominating, the dielectric losses can be neglected for computing the temperature distribution. If the external losses and the dielectric losses are in the same range, the impact of the dielectric losses on the temperature distribution should be taken into account with an iterative process. This iterative process is also required for detecting thermal runaways.
- ▶ The dielectric losses with MV excitations can be measured with calorimetric methods. However, due to the linearity of dry-type polymeric

insulation materials, small-signal frequency domain spectroscopy can also be used. Such measurements can be conducted with complete prototypes or material samples. The latter is particularly useful during design phases. Moreover, some capacitances (e.g., DM capacitance of transformers) cannot be measured with complete prototypes without exciting non-dielectric effects (e.g., conduction losses and magnetic losses).

The measurements conducted on the MV/MF transformer prototype prove that the dielectric losses are a critical parameter for MV/MF insulation. However, the choice of a MV/MF insulation material cannot be reduced solely to the dielectric losses. Many other factors influence the suitability of a material for a specific application:

- ▶ *High Voltage* - The breakdown voltage, the bulk conductivity, and the resistance against partial discharges are important properties for MV/MF insulation materials [146, 148–150, 270, 282, 283]. The DC conductivity is particularly important for determining the DC electric field distribution (cf. Chapter 6) [143, 143, 278, 287, 299, 300].
- ▶ *Permittivity* - Even if the dielectric losses are proportional to the imaginary part of the permittivity (cf. (7.10)), the real part is also an important design parameter since it is responsible for the capacitive reactive power in the insulation. Relatively large displacement currents may create losses in the grounding system, oscillations, and EMI issues (cf. Chapter 6) [143, 159, 160, 171].
- ▶ *Thermal* - The thermal conductivity of the insulation is critical since it directly defines the thermal performance of the system. However, materials with high thermal conductivity often feature poor (di)electric performance [300, 318]. Furthermore, the maximum operating temperature (thermal aging) and the flammability of the material should be taken into account.
- ▶ *Chemical* - The resistance to moisture and corrosion, as well as the chemical compatibility with other materials (e.g., glue, windings, and coil formers), has to be considered. The aging of the material is also an important issue [148, 270].
- ▶ *Mechanical* - The mechanical properties (e.g., flexible, rigid, brittle, viscosity before curing, surface adhesion, thermal expansion, and the potential presence of cavities or defects), as well as the processing

capabilities (e.g., milling, injection moulding, and potting), should also be investigated [285, 287, 300].

Trade-offs are required between these properties. The unfilled epoxy resin (“vonRoll Damisol 3418”) considered in this work features a high glass transition temperature, relatively low losses, a moderate permittivity, and a good mechanical stability. However, this material has a low thermal conductivity, is brittle, and exhibits high losses near the glass transition temperature. An unfilled silicone elastomer, compared to the selected filled silicone elastomer (“Dow Corning TC4605 HLV”), would feature lower losses but also lower thermal conductivity and a reduced mechanical stability [301]. Generally, the adjunction of a thermally conductive filler (e.g., SiO_2 and Al_2O_3) increases the permittivity, degrades the (di)electric performance, and increases the viscosity of the polymer (before curing).

Non-pottable and/or non-polymeric insulation materials, such as mica, ceramic (e.g., AlN and AlSiC), aramid (e.g., Nomex), polyimide (e.g., Kapton) also feature interesting properties, i.e. high breakdown strength (especially for thin layers), good resistance to partial discharges, and low losses [318, 328]. These materials are typically combined with potted polymeric materials (e.g., epoxy, silicone, and polyurethane) or oils, in order to avoid the presence of air near the electric field hot spots, which can lead to partial discharges [61, 105, 325].

7.6 Summary

This chapter examines the dielectric losses in the insulation of MV converters. The dielectric losses are a quantitative indicator for the MF insulation stress, which is useful for design and diagnostic processes. First, the modeling of dielectric losses in time and frequency domain is reviewed. Afterwards, the impact of PWM voltages generated by typical power converters on the dielectric losses is studied. Analytical expressions for calculating the dielectric losses of the frequency-dependent materials used in dry-type insulation systems are derived. It is shown that fundamental frequency analysis inaccurately determines the dielectric losses with PWM voltages. For obtaining the correct spectrum, a model of the switching transitions is also required. The proposed approximations are verified with permittivity measurements conducted for a typical MV insulation epoxy resin at different frequencies and temperatures (less than 16 % error). It is shown that, for accurate loss predic-

tions, the frequency and temperature dependences of the material parameters should be considered.

The described computation techniques are applied to the MV/MF transformer (± 3.5 kV to ± 400 V, 48 kHz, 25 kW) used in the DC-DC converter of the considered SST demonstrator (cf. Subsection 1.7.2 and cf. Chapter 5). With the considered epoxy resin, the insulation losses reach 17 % of the total transformer losses at the rated power. Moreover, a thermal runaway, associated with the loss peak at the glass transition temperature, limits the achievable power rating. The usage of a high performance silicone elastomer mitigates the aforementioned problems. The realized prototype, which features a silicone elastomer insulation, is measured with small-signal spectroscopy and with MV large-signal calorimetric methods. It is shown that the deviations between the measurements and the proposed computation methods are below 13 %. Finally, guidelines are given for selecting suitable insulation materials for MV/MF applications.

8

MV DC-DC Converter Prototype

Chapter Abstract

The DC-DC LLC SRC is one of the most popular galvanically isolated DC-DC converters since it provides ZVS, reduced RMS currents, and tightly couples the input and output voltages, when it is operated at (or below) the resonance frequency, and, therefore, acts as DCX without requiring closed-loop voltage control. Hence, this topology has been selected for the bidirectional DC-DC converter (7 kV to 400 V, 48 kHz, 25 kW) of the considered SST demonstrator. This chapter first highlights the limitations of passive (or synchronous) rectification (e.g., oscillations, current distortion, and load-dependent voltage transfer ratio) for bridges employing semiconductors with large output capacitances. Afterwards, a modulation scheme (MCS-ZVS), which allows an active sharing of the magnetizing current between the primary-side and secondary-side MOSFET-based bridges, is analyzed. It is shown that the ZVS mechanism is acting equivalent to a controller, allowing for a robust open-loop operation of the converter. The proposed modulation scheme features a load-independent voltage transfer ratio, load-independent ZVS for both bridges, and quasi-sinusoidal currents. Finally, the modulation scheme is experimentally verified on the realized SRC-DCX prototype and the following performance is achieved: 99.0 % full-load efficiency with a power density of 3.8 kW/l (62 W/in³, 2.9 kW/kg, and 1.3 kW/lb).

8.1 Introduction

Two main circuit topologies have emerged for the realization of high-power DC-DC converters: the DAB [44, 56, 78] and the LLC SRC [42, 61, 81–84]:

- *DAB* - The DC-DC DAB features extended voltage and power flow control capabilities [78]. Furthermore, ZVS and/or ZCS can be achieved [78].

However, the trapezoidal currents in a DAB exhibit large harmonic contents and the semiconductors have to typically switch the full-load current. Nevertheless, a closed-loop voltage control of the converter is required [44, 56, 78].

- ▶ *SRC* - The DC-DC SRC features several advantages such as quasi-sinusoidal currents and the ability to achieve ZVS and/or ZCS [61, 83, 84, 86, 99]. Nevertheless, the control of the power flow and/or output voltage requires frequency and/or duty cycle modulation in a wide range [81, 85, 87]. However, the SRC, operated at (or below) the resonance frequency, i.e. in half-cycle discontinuous current mode, provides a constant voltage transfer ratio without requiring any closed-loop voltage control. Therefore, this operating mode of the SRC is sometimes referred to as DCX and is widely used for MV high-power DC-DC converters [61, 82, 84, 86, 89, 90].

For the aforementioned reasons, the DC-DC SRC topology is selected for the DC-DC converter (7 kV to 400 V, 48 kHz, 25 kW) of the SST demonstrator presented in Subsection 1.7.2. For this DC-DC converter, power flow and voltage control are not required since these functionalities are provided by the input-side AC-DC stage. Hence, the converter is operated at the resonance frequency as DCX. The SRC-DCX is realized with SiC MOSFETs and commutated at 48 kHz. Due to the high switching frequency (considering the high input voltage), complete ZVS should be achieved for all semiconductors for all load conditions [111, 112, 202].

In the literature, the modulation of IGBT-based SRC-DCXs, which feature ZCS has been analyzed in detail [61, 84, 90]. Several MOSFET-based SRC-DCXs, which feature ZVS have also been presented [82, 83, 86, 87, 99, 329]. However, to the knowledge of the author, no detailed and comprehensive analysis of the ZVS mechanism (considering non-ideal switching transitions) has been published for MOSFET-based SRC-DCXs. The consideration of non-instantaneous switching transitions is especially critical for converters using the newly available MV SiC MOSFETs, which feature large semiconductor output capacitances. Therefore, this chapter analyzes the ZVS of SRC-DCXs, including the impact of the parasitic semiconductor capacitances of the inverter and rectifier bridges.

The chapter is organized as follows. Section 8.2 defines the parameters of the considered SRC-DCX. Section 8.3 presents the standard modulation scheme of SRC-DCXs, where the rectifier bridge is operated as passive (or synchronous) rectifier. The limitations of this modulation scheme (e.g., os-

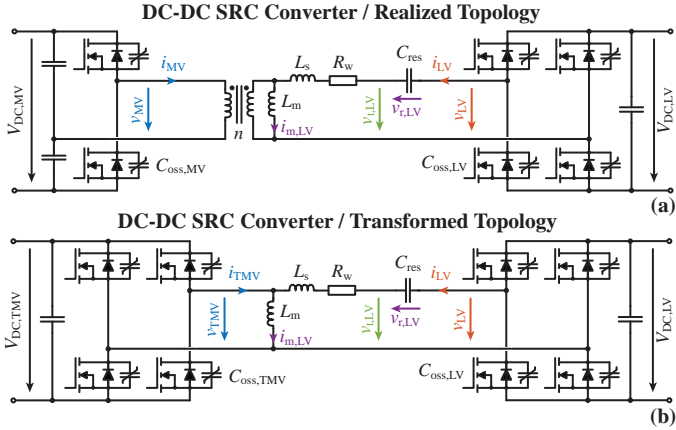


Fig. 8.1: (a) SRC-DCX operated at the resonance frequency, acting as bidirectional DCX. (b) SRC-DCX topology with scaled voltages. The MV half-bridge is transformed into a full-bridge and the complete circuit is referred to the LV side with the voltage transfer ratio of the transformer (n).

cillations, current distortion, and load-dependent voltage transfer ratio) are highlighted for bridges with large semiconductor output capacitances. Therefore, Section 8.4 proposes an alternative MCS-ZVS modulation scheme, which is based on an active phase shift modulation between the bridges. Section 8.5 verifies the stability and robustness of the MCS-ZVS modulation scheme. Finally, Section 8.6 presents experimental results obtained with the aforementioned system, including efficiency measurements.

8.2 Considered SRC-DCX

The bidirectional SRC-DCX of the SST demonstrator presented in Subsection 1.7.2 is considered. Fig. 8.1(a) and Tab. 8.1 depict the circuit topology and the parameter values. This all-SiC 25 kW converter operates between a 7 kV and a 400 V DC-bus at 48 kHz. The design and realization of the semiconductor bridges, which is not a part of this thesis, are described in [111, 112, 198, 200]. More details on the design and construction of the MV/MF transformer can be found in Chapter 5.

In order to reduce the number of switches and for reducing the voltage transfer ratio of the transformer, the combination of a half-bridge on the MV

Tab. 8.1: Parameters of the SRC-DCX

| Variable | Value | Variable | Value |
|--------------|---------------|--------------|-------------|
| $V_{DC,MV}$ | 7 kV | $V_{DC,LV}$ | 400 V |
| P | 25 kW | f_s | 48 kHz |
| R_w | 30 m Ω | L_s | 2.9 μ H |
| L_m | 50.0 μ H | n | 8.8 |
| C_{res} | 3.8 μ F | f_{res} | 48 kHz |
| $C_{oss,MV}$ | 150 pF | $C_{oss,LV}$ | 1700 pF |

side (with a split DC-bus) and a full-bridge on the LV side is used [61, 90]. However, the presented results also apply for any combination of full-bridges and half-bridges. The output capacitance (per switch) of the SiC MOSFETs is represented with a linearized charge-equivalent capacitance ($C_{oss,MV}$ and $C_{oss,LV}$) [202, 330]. The DC-bus voltage ripples, which are small, have no impact on the modulation scheme and are neglected [90, 198].

The transformer equivalent circuit is described with an ideal transformer, a magnetizing inductance, and a leakage inductance (n , L_m , and L_s) [125]. It should be noted that the equivalent circuit of the transformer is slightly different from the values measured in Chapter 5. These differences are due to the inductance of the busbars utilized for connecting the transformer and the bridges. The stray capacitances of the transformer (cf. Chapter 5), which slightly reduce the current available for ZVS, are neglected [156, 331]. The capacitor (C_{res}) is placed in series with the transformer on the LV side, which simplifies the electrical insulation design. Additionally, LV ceramic capacitors with high energy density and low losses can be used.

It should be noted that different equivalent circuits can be chosen for the transformer (cf. Chapter 3) [125]. The equivalent circuit with an ideal transformer and series-parallel inductors (referred to the LV side) has been selected since it allows for a simplified analysis of the circuit. The magnetizing current is a virtual current which does not feature a unique definition and physical interpretation [123, 125]. However, for transformers with high magnetic coupling factors (97% for the considered design), the magnetizing current (related to the LV side) can be described with $i_{m,LV}$ [125].

The resonant capacitor (C_{res}) and the leakage inductance of the transformer (L_s) are chosen such that the desired resonance frequency (f_{res}) is achieved. The transformer voltage transfer ratio (n) is chosen considering the desired voltage transfer ratio between the DC-buses. The magnetizing

inductance of the transformer (L_m) is selected with respect to the MOSFET output capacitances ($C_{oss,MV}$ and $C_{oss,LV}$) in order to obtain a sufficiently large magnetizing current (and stored energy) to achieve ZVS within a reasonable time interval [111, 112, 202].

The load-dependent losses of the converter are represented by a single series resistor (R_w), which represents the conduction losses of the MOSFETs (MV and LV bridges) and the winding losses of the transformer (at the switching frequency). The load-independent losses (i.e. the switching losses of the MOSFETs and the core losses) could be represented by a parallel resistor. However, the current flowing in this resistor would be negligible compared to the magnetizing current. Therefore, the parallel resistor is neglected for the analysis of the modulation scheme.

In order to simplify the circuit and to allow for a direct comparison between the MV and LV sides, the following transformations are made: the MV half-bridge is transformed into a full-bridge and the complete circuit is referred to the LV side with the voltage transfer ratio of the ideal transformer (n). The obtained circuit is depicted in Fig. 8.1(b) and the Transformed Medium-Voltage (TMV) parameters can be expressed as

$$V_{DC, TMV} = \frac{V_{DC, MV}}{2n}, \quad (8.1)$$

$$v_{TMV} = \frac{v_{MV}}{n}, \quad (8.2)$$

$$i_{TMV} = ni_{MV}, \quad (8.3)$$

$$C_{oss, TMV} = 2n^2 C_{oss, MV}. \quad (8.4)$$

It can be observed that the transformed capacitance of the MV MOSFETs is more than ten times larger than the capacitance of the LV MOSFETs ($C_{oss, TMV} \gg C_{oss, LV}$, cf. Tab. 8.1).

With the defined parameters, the modulation scheme of the SRC can be examined aiming for the following properties: load-independent voltage transfer ratio, load-independent ZVS (and quasi-ZCS) for both bridges, quasi-sinusoidal currents (low distortion), DCX behavior in open-loop, and robustness against model non-idealities and production tolerances. Moreover, the modulation scheme should work at partial-load for both power flow directions.

8.3 Passive Rectifier

In this section, the standard modulation scheme for SRC-DCXs is examined [61, 82, 84, 86, 90]. The SRC is operated at (or below) the resonance frequency with an active inverter bridge (50 % duty cycle) and a passive rectifier bridge (diode rectifier). The power flow is directed from the active to the passive bridge. Alternatively, synchronous rectification can be used for reducing the losses of the rectifier bridge [82, 83, 87, 99, 329].

8.3.1 Operating Principle

For explaining the operating principle of SRC-DCXs, the switching frequency is first set to $f_s = 40$ kHz (instead of $f_s = 48$ kHz) in order to operate the converter below the resonance frequency ($f_{res} = 48$ kHz). The converter is operated with an active LV bridge and a passive MV rectifier. As shown later, this power flow direction and switching frequency represent the critical case, which includes all the non-idealities.

Fig. 8.2 depicts the simulated waveforms. The switching period can be decomposed in several operating modes and/or time intervals and the corresponding equivalent circuits are shown in Fig. 8.3. The operation of the converter can be explained as follows:

- ▶ *Resonant Pulse (“RP”)* - The MV and LV bridge voltages cancel each other and the resonant tank (between L_s and C_{res}) is excited by the initial resonant capacitor (C_{res}) voltage. This results in a sinusoidal resonant current flowing between the bridges at the resonance frequency (f_{res}). Simultaneously, the active bridge (LV side) is providing the triangular current flowing in the magnetizing inductance (L_m).
- ▶ *Discontinuous Conduction Mode (“DCM”)* - As soon as the resonant current returns to zero (on the MV side), the diode rectifier stops conducting. However, the semiconductor output capacitances of the rectifier ($C_{oss, TMV}$) oscillate with the leakage inductance (L_s) of the transformer. Simultaneously, the active bridge (LV side) is still providing the current flowing in the magnetizing inductance (L_m) and the voltage of the resonant capacitor (C_{res}) remains approximately unchanged.
- ▶ *ZVS LV Side (“ZLV”)* - The switches of the active bridge (LV side) are turned off (dead time) and the magnetizing inductance (L_m) is providing current for obtaining a fast ZVS transition, i.e. charging and discharging the MOSFET output capacitances ($C_{oss, LV}$). During this very short

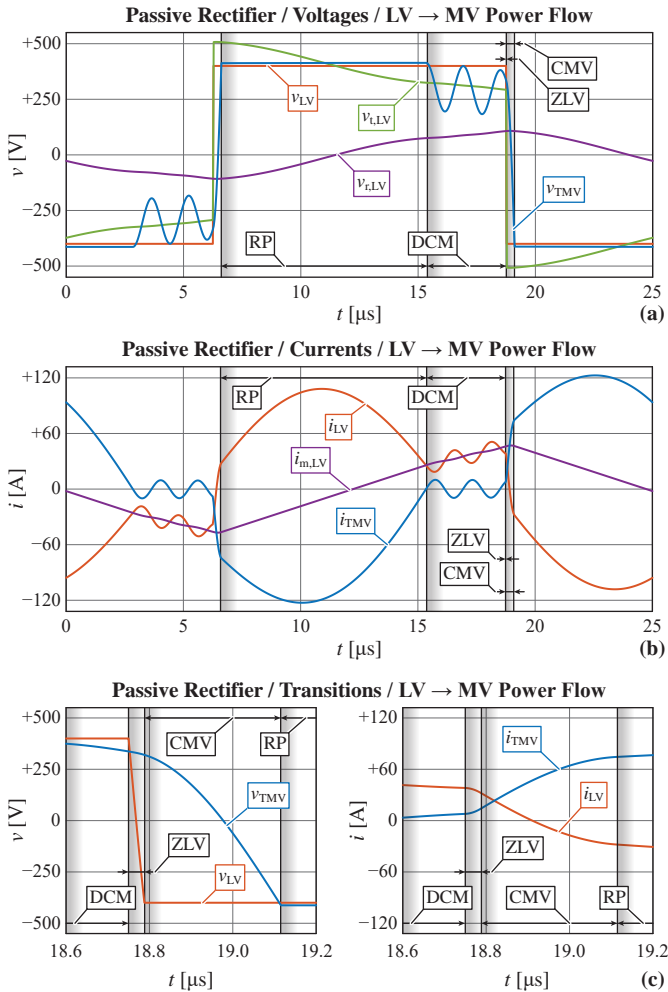


Fig. 8.2: Simulated (a) voltages and (b) currents with an active LV bridge and a passive MV rectifier ($f_s = 40$ kHz, $P = 25$ kW, and power flow from the LV to the MV side). (c) Voltages and currents during the ZVS switching transition. The different operating modes and/or time intervals occurring in one switching cycle are indicated.

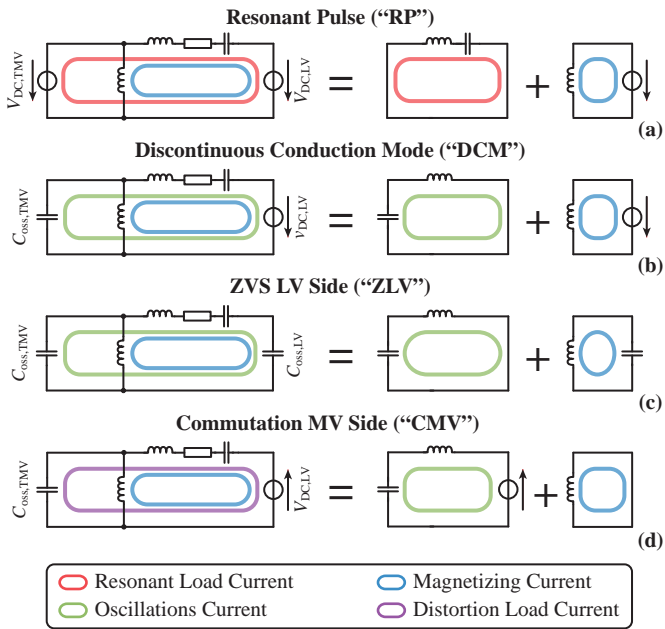


Fig. 8.3: Equivalent circuits during the different operating modes and/or time intervals occurring in one switching cycle (cf. Fig. 8.2): (a) Resonant Pulse ("RP"), (b) Discontinuous Conduction Mode ("DCM"), (c) ZVS LV side ("ZLV"), and (d) Commutation MV side ("CMV").

interval, the oscillation current (between L_s and $C_{\text{oss, TMV}}$) continues to flow but remains approximately unchanged.

- ▶ *Commutation MV Side (“CMV”)* - The difference between the MV and LV bridge voltages is applied to the leakage inductance (L_s) causing a rapid change of the current, which distorts the sinusoidal resonant current. This current is charging the semiconductor output capacitances of the rectifier bridge ($C_{\text{oss, TMV}}$), which slowly commutates the diodes (resonance between $C_{\text{oss, TMV}}$ and L_s). During this short interval, the current flowing in the magnetizing inductance (L_m) continues to flow but remains approximately unchanged.

Ideally, the SRC-DCX would only feature the resonant (load-dependent) current which is transferring the energy from the active bridge to the passive bridge. This current is flowing at the resonance frequency (f_{res}), which cancels the series impedance (except R_w) between the bridges. This implies that, ideally, the voltage transfer ratio of the SRC-DCX is almost load-independent.

However, in addition to the resonant current, a magnetizing (load-independent) current is required to achieve ZVS of the active bridge [83, 86, 329]. With a passive rectifier, the magnetizing current exclusively flows in the active bridge [84]. The magnetizing current cannot flow in the rectifier bridge due to the unidirectional nature of the diodes and/or the fact that a passive rectifier is not able to provide reactive power.

The amplitude of the voltage oscillation, occurring during the discontinuous conduction interval, is related to the peak-to-peak voltage of the resonant capacitor (C_{res}). The amplitude of the current oscillation is proportional to the output capacitances of the rectifier bridge ($C_{\text{oss, TMV}}$). These oscillations produce additional losses (conduction losses and switching losses) [84, 99, 111, 112]. Moreover, the oscillations can disturb the initial condition of the next resonant pulse.

The commutation of the passive rectifier would ideally occur instantaneously as soon as the next resonant pulse is starting, i.e. after the ZVS transition of the active bridge. However, due to the semiconductor output capacitances of the rectifier bridge ($C_{\text{oss, TMV}}$), the voltage of the diodes cannot change instantaneously. The mismatch between the MV and LV bridge voltages is applied to L_s , causing a rapid change of the currents. This distorts the ideal sinusoidal current shape and also contributes to the energy transfer (as known for SRCs operated above the resonance frequency) [81, 87]. One has note that during this time interval, the SRC is shortly operated as a DAB [44, 78]. Additionally, as shown in [87], the reverse recovery of the

diodes (or body diodes) can create further distortions during the commutation of the rectifier bridge.

The amplitude of the oscillations can be reduced by a proper choice of the impedance of the resonant tank (ratio between L_s and C_{res}), i.e. a design with a small leakage inductance and a large resonant capacitor. On the other hand, a reduction of the leakage inductance (L_s) would increase the current distortion occurring during the commutation of the passive rectifier. For a rectifier bridge realized with diodes or IGBTs, the semiconductor output capacitances are small and the current distortion is often negligible [61, 90]. However, if the semiconductor output capacitances are large (e.g., for a synchronous rectifier realized with MOSFETs), the current distortion is critical and the leakage inductance cannot be further reduced [111, 112]. Additionally, the leakage inductance of the transformer cannot be reduced below a certain threshold, especially for a MV design (due to geometrical, electric, and magnetic constraints).

8.3.2 Simulated Waveforms

From the aforementioned example, an appropriate modulation scheme for SRC-DCXs can be derived. SRC-DCXs using bipolar semiconductors (e.g., IGBT) are typically operated with a discontinuous conduction interval, i.e. below the resonance frequency, for achieving ZCS. A small magnetizing current can be added for removing the charge carriers and reducing the switching losses [61, 84, 90]. For SRC-DCXs using unipolar semiconductors (e.g., MOSFET), the usage a discontinuous conduction interval is not necessary and would only increase the RMS currents and, therefore, the losses [90]. Hence, such SRC-DCXs are operated at the resonance frequency with a significant magnetizing current in order to achieve ZVS [83, 86, 329]. Therefore, the considered converter, which is MOSFET-based, is operated at the resonance frequency ($f_s = f_{res} = 48$ kHz).

Fig. 8.4(a) shows the obtained waveforms for a power flow directed from the LV to the MV side. The magnetizing current is flowing on the LV side and significant oscillations and distortions are observed. The current distortion during the commutation of the passive MV rectifier (cf. Fig. 8.2) is considerable since the output capacitance of the MV MOSFETs is large ($C_{oss, TMV} \gg C_{oss, LV}$, cf. Tab. 8.1). This current distortion is contributing to the energy transfer and, therefore, is impacting the shape and the amplitude of the resonant current. This implies that, even if the converter is operated at the resonance frequency ($f_s = f_{res}$), a discontinuous conduction interval exists and oscillations can be

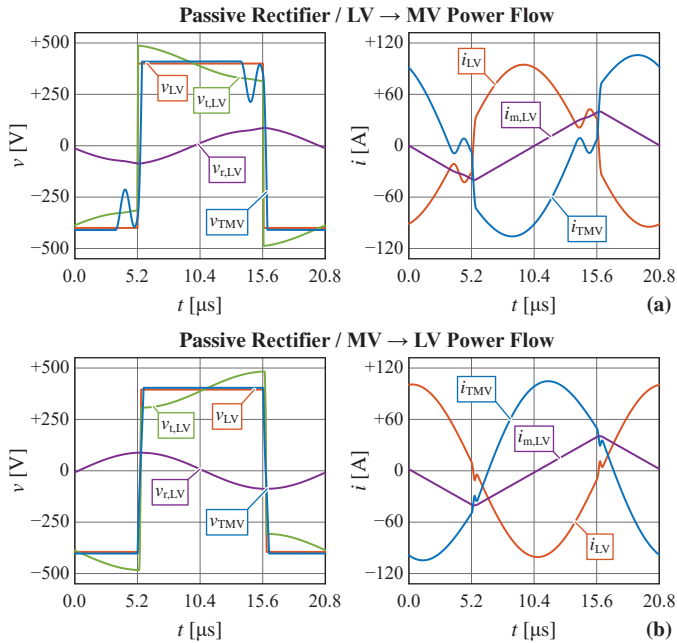


Fig. 8.4: Simulated voltages and currents with a passive rectifier bridge ($f_s = 48$ kHz and $P = 25$ kW). (a) The power flow is directed from the LV bridge (active) to the MV bridge (passive). (b) The power flow is directed from the MV bridge (active) to the LV bridge (passive).

observed. An increased switching frequency ($f_s > f_{res}$) would suppress the oscillations, but the current distortions due to the parasitic DAB operation would become larger.

Fig. 8.4(b) shows the obtained waveforms for a power flow directed from the MV to the LV side. The currents are almost sinusoidal, the magnetizing current is flowing on the MV side, and no significant oscillations or distortions occur. The current distortion during the commutation of the passive LV rectifier (cf. Fig. 8.2) is extremely small since the output capacitance of the LV MOSFETs is small ($C_{oss, TMV} \gg C_{oss, LV}$, cf. Tab. 8.1) and allows for a fast commutation of the rectifier. The oscillations are not present since the converter is operated at the resonance frequency (no discontinuous conduction interval).

8.3.3 Partial-Load Operation

The modulation scheme should also work for partial-load operation. In order to evaluate the achieved performance, different figures of merit are introduced. The voltage transfer ratio (r) is defined as

$$r = \frac{V_{DC, TMV}}{V_{DC, LV}}, \quad (8.5)$$

where the DC-bus voltages ($V_{DC, TMV}$ and $V_{DC, LV}$) are considered. Ideally, the voltage transfer ratio should be load-independent and approximately equal to $r \approx 1$, given that the voltage transformation is only provided by the transformer and by the combination between the half-bridge and the full-bridge (cf. (8.1)). As a second figure of merit, the power factor (λ) is defined as

$$\lambda = \frac{|P|}{\frac{1}{2}(V_{LV}I_{LV} + V_{TMV}I_{TMV})}, \quad (8.6)$$

where the RMS currents and voltages of the bridges (V_{LV} , I_{LV} , V_{TMV} , and I_{TMV}), and the transferred power (P) are considered. For an ideal SRC-DCX operated at the resonance frequency with a purely sinusoidal current (no oscillations, no distortions, and no magnetizing current), the obtained power factor is $\lambda = \sqrt{8}/\pi \approx 0.90$, which represents the theoretical maximum [90].

Fig. 8.5(a) shows the obtained voltage transfer ratio for different load conditions and power flow directions. For a power flow directed from the MV to the LV side, the voltage transfer ratio is, as expected, load-independent. For the reverse power flow direction, i.e. from the LV to the MV side, the voltage

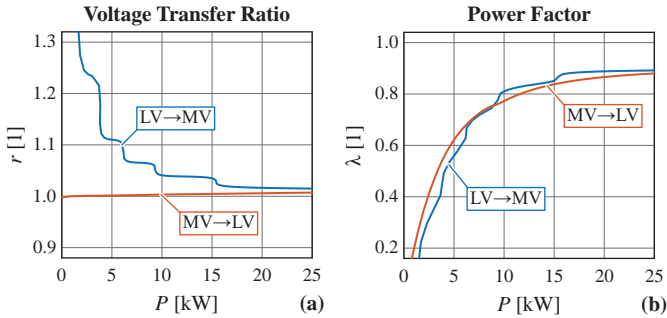


Fig. 8.5: (a) Voltage transfer ratio (cf. (8.5)) and (b) power factor (cf. (8.6)). The SRC-DCX is operated with a passive rectifier bridge ($f_s = 48$ kHz) at different load conditions and for both power flow directions.

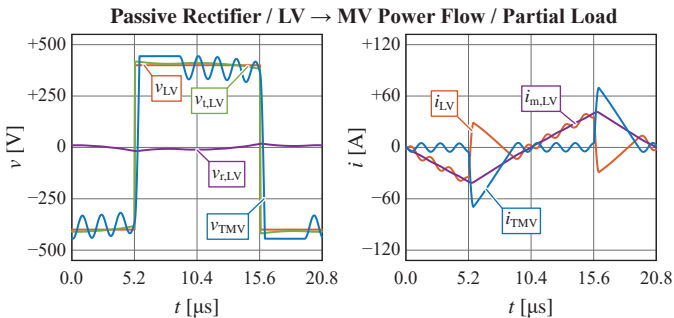


Fig. 8.6: Simulated voltages and currents at partial-load with a passive rectifier bridge ($f_s = 48$ kHz and $P = 5$ kW). The power flow is directed from the LV bridge (active) to the MV bridge (passive).

transfer ratio is not load-independent and is increasing as the load is reduced. Fig. 8.6 illustrates this last case with a power flow of 5 kW, where the MV DC bus voltage reaches 7.8 kV (instead of 7 kV). This increased voltage transfer ratio can be explained by the distortion of the resonant current occurring during the commutation of the MV diodes (cf. Fig. 8.2). This current distortion transfers additional energy to the MV DC-bus during partial-load operation and, therefore, causes a drift of the MV DC-bus voltage until the transferred current matches the load current.

Fig. 8.5(b) depicts the obtained power factor for different load conditions and power flow directions. The power factor at the nominal load (0.88) is close to the theoretical maximum (0.90) of the SRC-DCX. At partial-load, the power factor is dropping, mostly due to the constant magnetizing current. Hence, complete ZVS of the active bridge is achieved for all load conditions.

For a power flow directed from the LV to the MV side, the curves shown in Fig. 8.5 are not smooth in function of the power flow. This is explained by the oscillations occurring during the discontinuous conduction interval which lead to varying initial conditions for the resonant pulses.

It can be concluded that the operation of the SRC-DCX with a passive (or synchronous) rectifier stage is problematic in case of a rectifier bridge with large semiconductor output capacitances and/or large mismatches between the semiconductor output capacitances of both bridges ($C_{oss, TMV}$ and $C_{oss, LV}$). Oscillations, current distortions, and a load-dependent voltage transfer ratio are occurring. The load-dependent voltage transfer ratio could be eliminated with duty cycle and frequency modulation of the active bridge, at the cost of an increased control complexity [81, 85, 87]. However, with a closed-loop voltage control, the SRC cannot be anymore considered to show DCX functionalities. Another solution is to actively switch the rectifier bridge in order to share the magnetizing current, used for ZVS, between the bridges.

8.4 Active Rectifier / Analytical Model

In this section, both bridges are actively operated. This solution has already been examined in order to extend the power flow and voltage control capabilities of SRCs [85, 332, 333]. Nevertheless, these results cannot be directly used since the goal of this work is to examine the DCX operating mode, which should not require any closed-loop voltage control. Therefore, the proposed MCS-ZVS modulation scheme offers a DCX behavior with an active phase shift modulation between the bridges. In this section the power flow is exclusively directed from the LV to the MV side since this has been identified

as the critical case (cf. Section 8.3). However, all the presented results are valid for both power flow directions.

8.4.1 Considered Model

Both bridges are actively operated with a duty cycle of 50 % and a constant phase shift is actively applied between the bridge voltages. For the analytical model, the switching transition durations of the MV bridge and the LV bridge are first neglected and perfect rectangular voltage waveforms are considered. The SRC-DCX is operated at the resonance frequency for achieving sinusoidal currents:

$$f_s \approx f_{\text{res}} = \frac{1}{2\pi} \frac{1}{\sqrt{L_s C_{\text{res}}}}. \quad (8.7)$$

The rectangular PWM voltages produced by the MV bridge and the LV bridge can be described by the following functions:

$$v_{\text{TMV}} = -V_{\text{DC, TMV}} \operatorname{sgn}(\cos(2\pi f_s(t + t_p))), \quad (8.8)$$

$$v_{\text{LV}} = -V_{\text{DC, LV}} \operatorname{sgn}(\cos(2\pi f_s t)), \quad (8.9)$$

where t_p represents the phase shift between the bridges. The mismatch between the DC-bus voltages (ΔV_{LV}) can be defined as

$$\Delta V_{\text{LV}} = V_{\text{DC, LV}} - V_{\text{DC, TMV}}. \quad (8.10)$$

Fig. 8.7(a) depicts the resulting equivalent circuit, the applied voltages, and the obtained currents, which can be decomposed into three distinct parts: the resonant current, a circulating current, and the magnetizing current.

8.4.2 Resonant Current

The equivalent circuit for the resonant current is shown in Fig. 8.7(b). Only the fundamental frequency of the voltages (first Fourier harmonic) is considered. The other harmonics are filtered out by the band-pass characteristic of the series resonant circuit. The phase shift (t_p) is neglected but the mismatch (ΔV_{LV}) between the DC-bus voltages is considered:

$$v_{\text{I, TMV}} = -\frac{4}{\pi} V_{\text{DC, TMV}} \cos(2\pi f_s t), \quad (8.11)$$

$$v_{\text{I, LV}} = -\frac{4}{\pi} V_{\text{DC, LV}} \cos(2\pi f_s t). \quad (8.12)$$

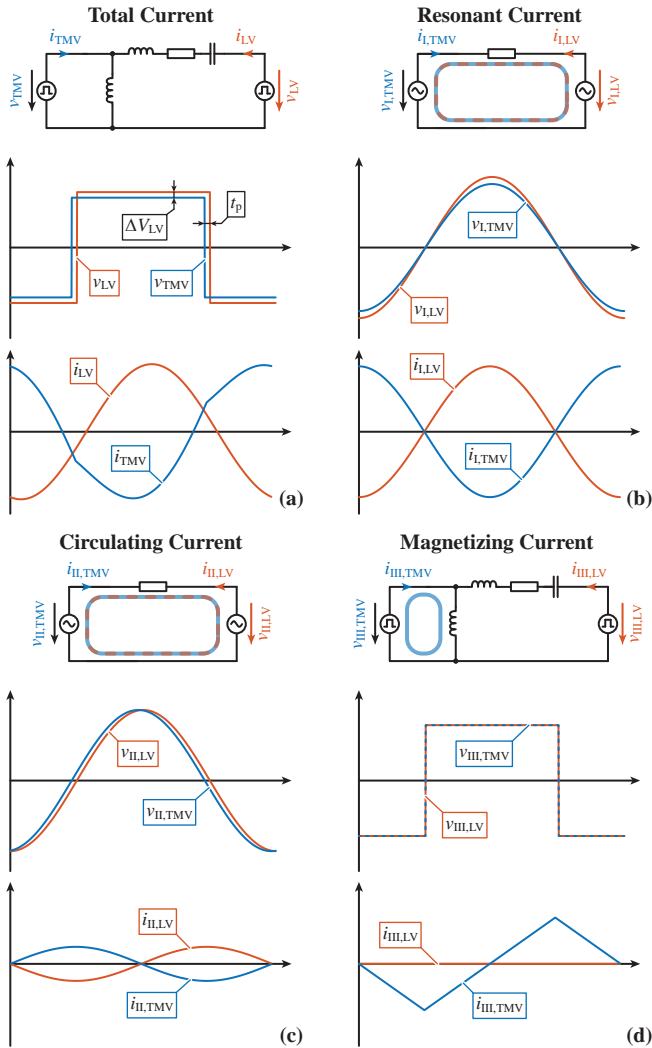


Fig. 8.7: (a) Equivalent circuit of the SRC-DCX (with a schematic view of the waveforms) operated with MCS-ZVS modulation (phase shifted PWM voltages with 50 % duty cycle). The total current in the SRC-DCX can be decomposed into three parts: (b) the resonant current, (c) a circulating current, and (d) the magnetizing current. A power flow from the LV to the MV side is considered.

The magnetizing inductance (L_m) is neglected and, at the resonance frequency, the impedances of the leakage inductance (L_s) and the resonance capacitor (C_{res}) cancel each other out. Accordingly, only the resistance (R_w) remains. The currents in the equivalent circuit can be expressed as

$$I_{I,pk} = \frac{4}{\pi} \frac{\Delta V_{LV}}{R_w}, \quad (8.13)$$

$$i_{I, TMV} = +I_{I,pk} \cos(2\pi f_s t), \quad (8.14)$$

$$i_{I, LV} = -I_{I,pk} \cos(2\pi f_s t). \quad (8.15)$$

As expected, the resonant current is sinusoidal and is created by the small mismatch (ΔV_{LV}) between the DC-bus voltages required due to the losses (R_w). The transferred power (positive for the considered power flow) can be expressed as

$$P = \frac{8}{\pi^2} \frac{V_{DC,LV} \Delta V_{LV}}{R_w}. \quad (8.16)$$

Since R_w is small, both bridges are operated in a quasi-short-circuit, resulting in a nearly load-independent voltage transfer ratio. This implies that a small mismatch (ΔV_{LV}) between the DC-bus voltages will create a large power flow, given that the side where the source is located (LV side) features a slightly higher voltage than the side where the load is located (MV side).

8.4.3 Circulating Current

The equivalent circuit for the reactive circulating current is shown in Fig. 8.7(c). Again, only the fundamental frequency of the voltages (first Fourier harmonic) is considered. The other harmonics are filtered out by the resonant tank. The mismatch (ΔV_{LV}) between the DC-bus voltages is neglected but the phase shift (t_p) is considered:

$$v_{II, TMV} = -\frac{4}{\pi} V_{DC,LV} \cos(2\pi f_s (t + t_p)), \quad (8.17)$$

$$v_{II, LV} = -\frac{4}{\pi} V_{DC,LV} \cos(2\pi f_s t). \quad (8.18)$$

The magnetizing inductance (L_m) is neglected and, due to the operation at the resonance frequency, only the resistance (R_w) has to be considered. The

currents in the equivalent circuit can be then expressed as

$$I_{II,pk} = \frac{8f_s t_p V_{DC,LV}}{R_w}, \quad (8.19)$$

$$i_{II,TMV} = +I_{I,LV,pk} \sin(2\pi f_s t), \quad (8.20)$$

$$i_{II,LV} = -I_{I,LV,pk} \sin(2\pi f_s t). \quad (8.21)$$

The phase shift between the bridges creates a circulating current, which is also sinusoidal. This current is orthogonal (90° phase shift) to the resonant current and, therefore, purely reactive.

8.4.4 Magnetizing Current

The equivalent circuit for the magnetizing current is shown in Fig. 8.7(d). The rectangular voltages formed by the bridges are considered but the phase shift (t_p) and the mismatch between the DC-bus voltages (ΔV_{LV}) are neglected:

$$v_{III,TMV} = -V_{DC,LV} \operatorname{sgn}(\cos(2\pi f_s t)), \quad (8.22)$$

$$v_{III,LV} = -V_{DC,LV} \operatorname{sgn}(\cos(2\pi f_s t)). \quad (8.23)$$

With this operating condition, no voltage is applied to the series elements (L_s , C_{res} , and R_w) and, therefore, no current is flowing between the bridges. Hence, the current flowing in the magnetizing inductance (L_m) is provided by the MV bridge:

$$I_{III,pk} = \frac{V_{DC,LV}}{4f_s L_m}, \quad (8.24)$$

$$i_{III,TMV} = -I_{III,pk} \frac{2}{\pi} \arcsin(\sin(2\pi f_s t)), \quad (8.25)$$

$$i_{III,LV} = 0. \quad (8.26)$$

As expected, the magnetizing current is triangular (integral of the applied rectangular voltage). This current is also orthogonal to the resonant current and, therefore, purely reactive.

8.4.5 Choice of the Equivalent Circuit

The considered equivalent circuit features an important assumption: the series resistance of the transformer and of the MOSFETs (R_w) is placed on the LV side. In reality, this resistance would be shared between the MV and

LV sides. The choice of a lumped resistance on the LV side has been made to simplify the model. Moreover, in the considered SRC-DCX, the resonant capacitor (C_{res}) is placed on the LV side. However, the resonant capacitor could be also placed on the MV side or be shared between both sides.

The fact that the magnetizing current is solely provided by the MV bridge results from the positions of the resonant capacitor (C_{res}) and the series resistance (R_w). In reality, the magnetizing current will be shared between the bridges (cf. Chapter 3) [123, 125]. However, the presented model, which features a simple analytical interpretation, is sufficient for explaining the fundamental working principle of the SRC-DCX with MCS-ZVS modulation.

8.4.6 Current Waveforms

The three currents shown in Figs. 8.7(b)-(d) can be superimposed in order to obtain an approximation of the total current shown in Fig. 8.7(a). This approximation is extremely accurate, i.e. shows less than 8 % RMS error for the current waveforms for the complete operating range.

The resonant current is only dependent on the mismatch between the DC-bus voltages (ΔV_{LV}), which is, therefore, determining the power flow. The circulating current is only dependent on the phase shift (t_p) and is purely reactive. The magnetizing current is independent of both the mismatch between the DC-bus voltages (ΔV_{LV}) and the phase shift (t_p). This implies that the active and reactive power flow can be controlled independently.

Fig. 8.8 shows the obtained waveforms. Since both bridges are operated at the resonance frequency with a duty cycle of 50 %, no discontinuous conduction interval can be observed. The superposition of the resonant current and the reactive currents is highlighted.

8.4.7 ZVS Currents

Without loss of generality, only the switching transitions near $t \approx 1/(4f_s)$ are considered (half-wave symmetry of the waveforms). At the switching instant, the resonant current is zero and only the circulating and magnetizing currents are contributing to ZVS (cf. Fig. 8.7). The ZVS currents in the LV bridge ($I_{ZVS,LV}$) and MV bridge ($I_{ZVS,TMV}$) can be computed as

$$I_{ZVS,TMV} = +I_{II,pk} - I_{III,pk}, \quad (8.27)$$

$$I_{ZVS,LV} = -I_{II,pk}. \quad (8.28)$$

The signs are chosen such that ZVS is achieved for negative $I_{ZVS,LV}$ and $I_{ZVS,TMV}$. The applied phase shift introduces the reactive circulating current

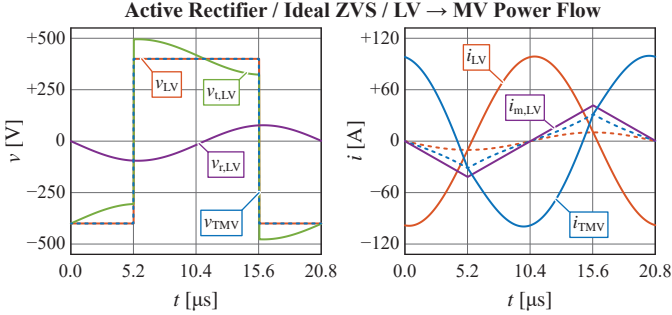


Fig. 8.8: Calculated voltages and currents with MCS-ZVS modulation ($f_s = 48$ kHz, $t_p = 2$ ns, $P = 25$ kW, and power flow from the LV to the MV side). The reactive currents ($i_{TM,V} - i_{L,TM,V}$ and $i_{LV} - i_{L,LV}$) are indicated with dashed lines for both bridges. For the calculation, the semiconductor output capacitances of the bridges are neglected and perfect switching transitions are considered.

($I_{II,pk}$), which effectively is equivalent to a sharing of the magnetizing current ($I_{III,pk}$) between both bridges. Nevertheless, the total current available for ZVS for both bridges is limited by the magnetizing current ($I_{III,pk}$). The switching durations of the LV bridge ($t_{r,LV}$) and MV bridge ($t_{r,TM,V}$) can be computed as

$$t_{r,TM,V} = -C_{oss,TM,V} \frac{2V_{DC,TM,V}}{I_{ZVS,TM,V}}, \quad (8.29)$$

$$t_{r,LV} = -C_{oss,LV} \frac{2V_{DC,LV}}{I_{ZVS,LV}}. \quad (8.30)$$

These expressions are only valid if complete ZVS is achieved (negative $I_{ZVS,LV}$ and $I_{ZVS,TM,V}$). It should again be noted, that the impact of the ZVS transition durations on the currents is not considered with the presented analytical model since the currents are derived with perfect rectangular PWM voltages.

Fig. 8.9 shows the ZVS currents and the ZVS transition durations for different phase shifts. As expected, for all phase shifts, the sum of both ZVS currents ($I_{ZVS,TM,V}$ and $I_{ZVS,LV}$) is limited by the magnetizing current ($I_{III,pk}$). The ZVS transitions are much faster for the LV bridge than for the MV bridge ($C_{oss,TM,V} \gg C_{oss,LV}$, cf. Tab. 8.1).

The ZVS currents are negative for both bridges for $t_p \in [0, +8]$ ns. However, the ZVS currents should be sufficiently negative for obtaining complete ZVS within a reasonable dead time [202, 330]. Complete ZVS is calculated as achievable within a reasonable dead time for $I_{ZVS,TM,V} < -20$ A and

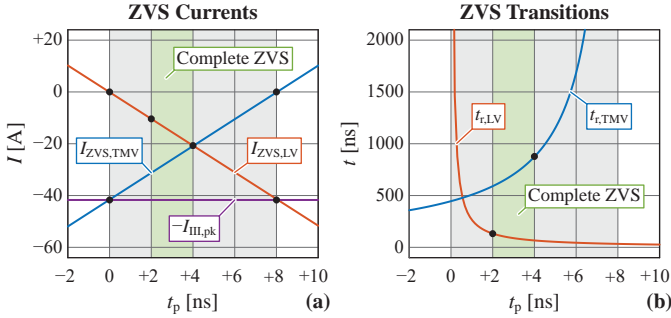


Fig. 8.9: Calculated (a) ZVS currents and (b) ZVS transition durations obtained for the SRC-DCX operated with MCS-ZVS modulation ($f_s = 48$ kHz, $t_p \in [-2, +10]$ ns). Complete ZVS is calculated as achievable within a reasonable dead time for $I_{ZVS, LV} < -10$ A and $I_{ZVS, TMV} < -20$ A. For the calculation of the currents, the semiconductor output capacitances of the bridges are neglected and ideal instantaneous switching transitions are considered.

$I_{ZVS, LV} < -10$ A. The phase shift window, where complete ZVS is achievable, is reduced to $t_p \in [+2, +4]$ ns. In Fig. 8.8, a phase shift of $t_p = 2$ ns (minimum value) has been chosen to minimize the mismatch between the switching transition durations of both bridges. The phase shift window, where complete ZVS is achievable, is so small that the robustness of the modulation scheme should be further analyzed with a more detailed ZVS model.

8.5 Active Rectifier / Simulations

In this section, both bridges are actively operated with a duty cycle of 50% and a constant delay (t_d) is actively applied between the gate signals of the MV and LV bridges, resulting in a phase shift (t_p) between the bridge voltages (MCS-ZVS, cf. Section 8.4). The ZVS transitions are now simulated with the output capacitances of the MOSFETs, which implies that the coupling between the ZVS currents and the ZVS transition durations is considered [202, 330]. For the following analysis, the power flow is exclusively directed from the LV to the MV side since this has been identified as the critical case (cf. Section 8.3). However, all the presented results are valid for both power flow directions.

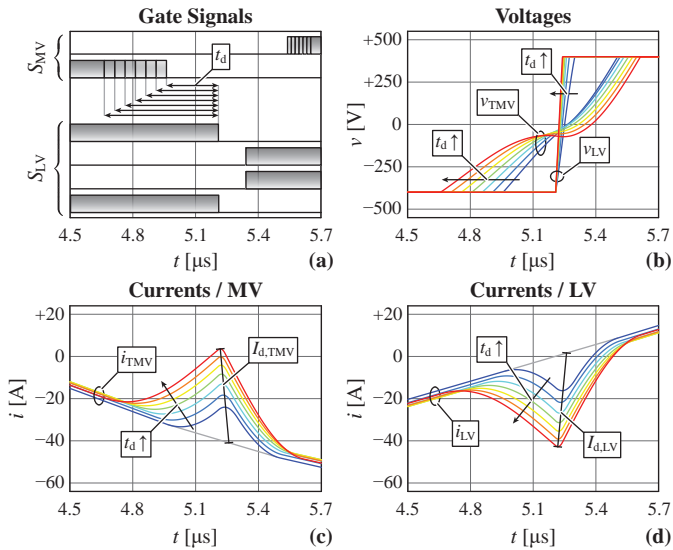


Fig. 8.10: Simulated ZVS transition with MCS-ZVS modulation for different time delays ($f_s = 48$ kHz, $P = 25$ kW, $t_d \in [+250, +550]$ ns, and power flow from the LV to the MV side). (a) Applied gate signals, (b) bridge voltages, (c) MV currents, and (d) LV currents.

8.5.1 Phase Shift Operation

The obtained phase shift (t_p) between the bridge voltages depends on the applied delay (t_d) between the gating of the bridges and the ZVS switching transition durations ($t_{r, TMV}$ and $t_{r, LV}$), which are determined by the ZVS currents ($I_{ZVS, TMV}$ and $I_{ZVS, LV}$). The coupling between the ZVS currents and the ZVS transition durations implies that only an indirect relation exists between t_p and t_d .

This effect is illustrated in Fig. 8.10, where the voltages and the currents are simulated for different time delays. It can be seen that the complete ZVS is achieved for both bridges in a wide range of time delays ($t_d \in [+250, +550]$ ns). This is astonishing, considering the results obtained in Fig. 8.9, where the switching transitions have been assumed as infinitely fast and ZVS could only be achieved in a very narrow range of time delays (t_d). This difference between the analytical model and the simulations is due to the ZVS mechanism, which is automatically aligning the voltages, such that the phase shift (t_p) between the bridge voltages is always close to zero. The aforementioned analytical model (cf. Section 8.4) can be used for explaining this alignment effect for a fixed time delay (t_d):

$$t_p \uparrow \Rightarrow I_{ZVS, TMV} \uparrow \wedge I_{ZVS, LV} \downarrow, \quad (8.31)$$

$$I_{ZVS, TMV} \uparrow \wedge I_{ZVS, LV} \downarrow \Rightarrow t_{r, TMV} \uparrow \wedge t_{r, LV} \downarrow, \quad (8.32)$$

$$t_{r, TMV} \uparrow \wedge t_{r, LV} \downarrow \Rightarrow t_p \downarrow. \quad (8.33)$$

This self-alignment effect is stabilizing the modulation scheme, ensuring that large tolerances are acceptable for the time delay between the gating of the bridges (t_d). It appears that, as expected, the ZVS currents and the ZVS transition durations can be controlled by adjusting the time delay (t_d). The following approximations can be made (assuming $C_{oss, TMV} \gg C_{oss, LV}$, cf. Tab. 8.1):

$$t_{r, TMV} \approx 2t_d, \quad (8.34)$$

$$t_{r, LV} \approx 0. \quad (8.35)$$

$$t_p \approx 0. \quad (8.36)$$

Due to the mismatch of the switching transition durations of the MV and LV bridges, the SRC is shortly operated as a DAB causing a current distortion during the switching transitions, as explained in Section 8.3. The amplitude

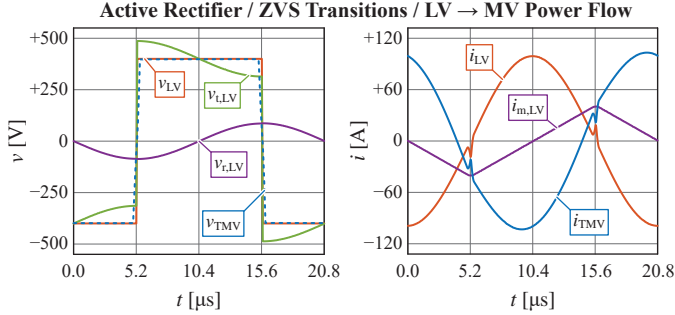


Fig. 8.11: Simulated voltages and currents with MCS-ZVS modulation ($f_s = 48$ kHz, $t_d = 270$ ns, and $P = 25$ kW, and power flow from the LV to the MV side). The reactive currents (circulating current and magnetizing current) are almost exclusively flowing in the MV bridge (cf. (8.27)) and the LV bridge is switched with the current distortion (cf. (8.38)).

of the current spikes ($I_{d, TMV}$ and $I_{d, LV}$) can be expressed as (cf. Fig. 8.10)

$$I_{d, TMV} \approx + \frac{V_{DC, TMV} t_d}{2L_s}, \quad (8.37)$$

$$I_{d, LV} \approx - \frac{V_{DC, LV} t_d}{2L_s}. \quad (8.38)$$

Since the phase shift (t_p) between the bridge voltages is almost zero, these spikes are only causing local distortions and are not changing the global shape of the currents. Nevertheless, these current distortions have an impact on the ZVS currents (cf. (8.28) and (8.27)). The current $I_{d, LV}$ is negative and increases the LV ZVS current. The current $I_{d, TMV}$ is positive and decreases the MV ZVS current, slowing down the switching speed of the MV bridge, especially in the middle of the switching transition (cf. Fig. 8.10).

For large time delays ($t_d > 550$ ns), the MV ZVS current becomes (partially) positive and the MV bridge starts to oscillate back in the middle of the transition. For small time delays ($t_d < 250$ ns), the LV ZVS current is not sufficient to obtain complete ZVS, implying that matching the switching transition durations of both bridges ($t_{r, TMV} = t_{r, LV}$) is not achievable.

The choice of the time delay should be done with two objectives in mind: the minimization of the mismatch between the switching transition durations of both bridges and the mitigation of the switching speed. For the considered converter, a time delay of $t_d = 270$ ns, which is close to the minimum value,

has been chosen in order to minimize the mismatch between the switching transition durations. With this choice, the switching speed is still moderate (below $15 \text{ kV}/\mu\text{s}$), due to the achieved ZVS with quasi-ZCS.

Fig. 8.11 depicts the obtained waveforms. The currents and voltages are very similar to the results obtained with the analytical model (cf. Fig. 8.8), except for the aforementioned small current spikes occurring during the switching transition. With the chosen time delay, the reactive currents (circulating current and magnetizing current) are almost exclusively flowing in the MV bridge (cf. (8.29)) and the LV bridge is switched with the current distortion (cf. (8.38)). Therefore, the maximum possible current (the magnetizing current) is switched by the MV bridge, which exhibits the larger semiconductor output capacitances ($C_{\text{oss, TMV}} \gg C_{\text{oss, LV}}$, cf. Tab. 8.1).

8.5.2 Robustness of the Modulation Scheme

With the aforementioned results, it appears that the modulation scheme is highly robust with respect to the time delay (t_d) between the gating of the bridges. However, the robustness of the modulation scheme should be further examined, particularly with respect to the operating frequency (f_s). Due to model non-idealities (e.g., non-modeled parasitics) and production tolerances (e.g., transformer parameters and capacitor values), the operating frequency (f_s) might not exactly match the resonance frequency (f_{res}) [125, 334].

Fig. 8.12 depicts the voltage transfer ratio, the phase shift between the bridge voltages (computed between the first Fourier harmonics), and the ZVS transition durations for different time delays (t_d) and operating frequencies (f_s). The voltage transfer ratio is almost constant and ZVS is achieved for the complete range. The time delay, as already shown in Fig. 8.10, allows for the sharing of the magnetizing current and, therefore, to choose the ZVS switching durations. If the converter is operated at the resonance frequency, the phase shift between the bridge voltages is almost zero (cf. Fig. 8.10). For operating frequencies close to the resonant frequency (imperfect compensation between C_{res} and L_s), a small phase shift (t_p) is present, which causes a small additional current distortion but does not impact the ZVS capabilities and the voltage transfer ratio.

Therefore, it can be concluded that the proposed modulation scheme is robust in a wide range of time delays and operating frequencies. Model non-idealities or production tolerances (cf. Chapter 3) will only marginally affect the obtained waveforms and complete ZVS can still be achieved [125].

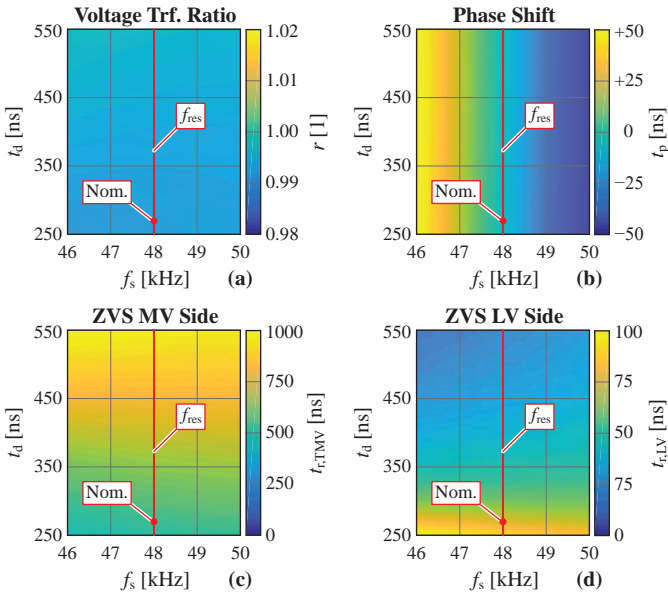


Fig. 8.12: Simulated (a) voltage transfer ratio (cf. (8.5)), (b) phase shift between the bridge voltages (computed between the first Fourier harmonics), (c) MV ZVS switching durations, and (d) LV ZVS switching durations. The SRC-DCX is operated with MCS-ZVS modulation ($P = 25$ kW and power flow from the LV to the MV side). Different time delays (t_d) and operating frequencies (f_s) are considered. The nominal operating point ($f_s = 48$ kHz, $t_d = 270$ ns) is indicated.

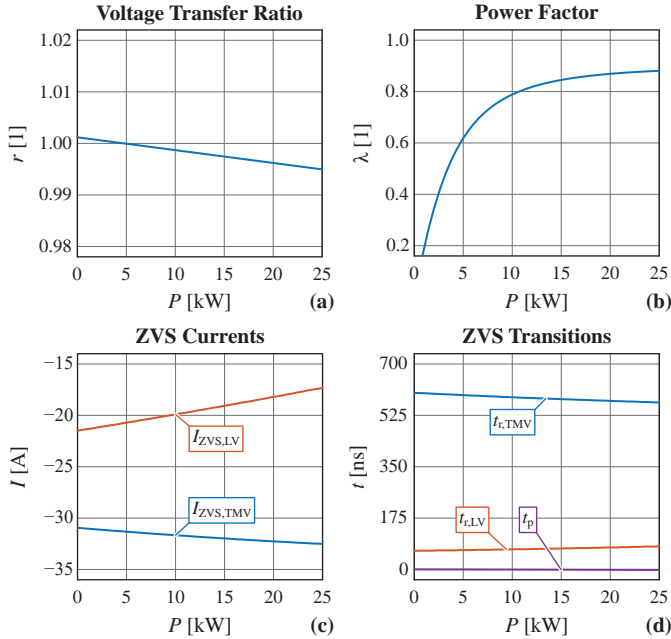


Fig. 8.13: Simulated (a) voltage transfer ratio (cf. (8.5)), (b) power factor (cf. (8.6)), (c) ZVS currents (average over the switching durations), and (d) ZVS transition durations. The phase shift between the bridge voltages is also shown (computed between the first Fourier harmonics). The SRC-DCX is operated with MCS-ZVS modulation ($f_s = 48$ kHz, $t_d = 270$ ns, $P = 25$ kW, and power flow from the LV to the MV side) at different load conditions.

8.5.3 Partial-Load Operation

The modulation scheme should also work for partial-load operation. Fig. 8.13 shows the obtained voltage transfer ratio, power factor, ZVS currents, ZVS switching transition durations, and the phase shift between the bridge voltages. The voltage transfer ratio is almost constant (less than 0.5 % deviation) since no oscillations and no current distortions occur. The power factor at the nominal load (0.88) is close to the theoretical maximum (0.90) of the SRC-DCX. Complete ZVS is achieved for the complete load range. The variation of the ZVS currents (average during the switching transitions) and ZVS switching transition durations is also small (less than 25 % deviation). The phase shift between the bridge voltages is always close to zero, proving that

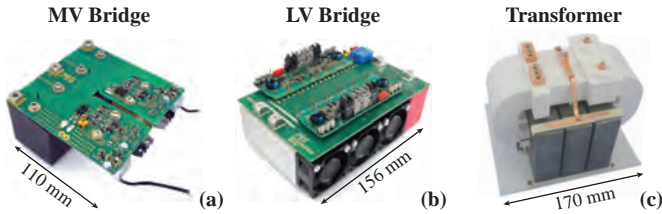


Fig. 8.14: Considered 25 kW SRC-DCX operated at 48 kHz between a 7 kV and a 400 V DC-bus (cf. Fig. 8.1(a) and Tab. 8.1): (a) MV bridge based on 10 kV SiC MOSFETs, (b) LV bridge based on 1200 V SiC MOSFETs, and (c) MV/MF transformer (cf. Chapter 5).

the self-alignment of the PWM signal works for all load conditions without requiring a dynamic regulation of the phase-shift.

Therefore, the goals defined in Section 8.2 are achieved. A robust modulation scheme, featuring a load-independent voltage transfer ratio, bidirectional power flow, load-independent ZVS (and quasi-ZCS), and quasi-sinusoidal currents, has been found. The converter acts as DCX for the complete load range without requiring measurements or closed-loop voltage control.

8.6 Measurements

The considered converter (cf. Fig. 8.1(a) and Tab. 8.1) has been constructed. Fig. 8.14 shows the realized prototype, which features the following power density: 3.8 kW/l (62 W/in³, 2.9 kW/kg, and 1.3 kW/lb). The MV half-bridge is realized with “Cree QPM3-10000-0300” 10 kV SiC MOSFETs [335]. The LV full-bridge employs “Cree C2M0025120D” 1200 V SiC MOSFETs, where three devices are placed in parallel per switch [336]. The design and realization of the semiconductor bridges are described in [111, 112, 198, 200]. More details on the construction and design of the MV/MF transformer (7.4 kW/l, 121 kW/in³, 4.0 kW/kg, and 1.8 kW/lb) can be found in Chapter 5.

8.6.1 Modulation Scheme

The proposed MCS-ZVS modulation scheme is applied. Fig. 8.15 shows the obtained measurements at 25.3 kW (power flow from the LV to the MV side). The measured waveforms are in very good agreement with the simulations (cf. Fig. 8.11). This implies that the underlying assumptions are valid: linearized charge-equivalent semiconductor output capacitances ($C_{oss, TMV}$ and $C_{oss, LV}$),

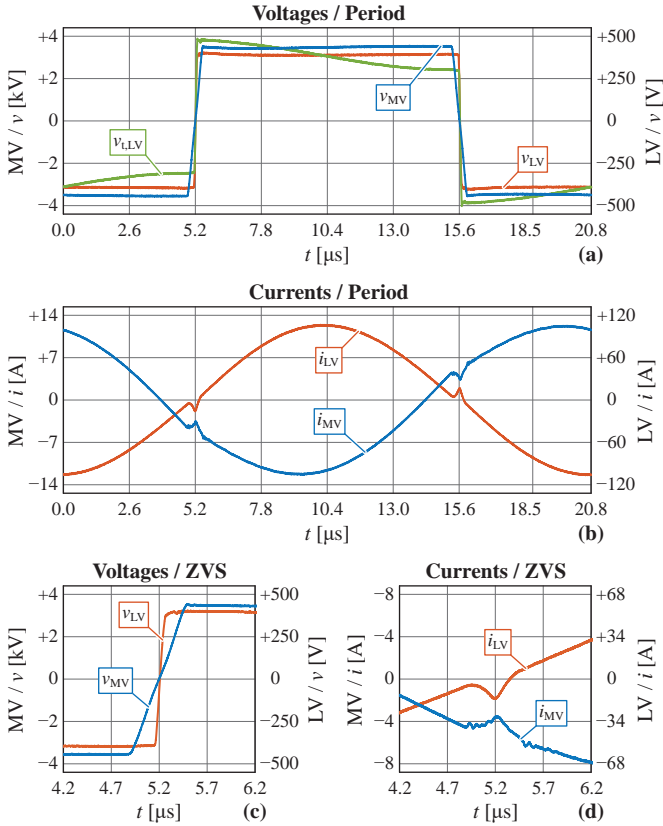


Fig. 8.15: Measured (a) voltages and (b) currents for a complete switching period. Measured (c) voltages and (d) currents during the ZVS transitions. The MCS-ZVS modulation ($f_s = 48$ kHz, $t_d = 270$ ns, $P = 25.3$ kW, and power flow from the LV to the MV side) is used.

lumped series resistance placed on the LV side (R_w), neglected DC-bus voltage ripples, and neglected stray capacitances of the transformer.

The measured currents are almost perfectly sinusoidal (no oscillations or significant distortions) and ZVS is achieved for both bridges. As expected (cf. Fig. 8.10), the phase shift between the bridge voltages is very small. The time delay (t_d) between the MV and LV bridge gate signals is chosen such that (cf. Fig. 8.11) the magnetizing current is almost exclusively flowing in the MV bridge (cf. (8.29)) and the LV bridge is switched with the current distortion (cf. (8.38)). However, the magnetizing current, which is a virtual current, cannot directly be measured in a prototype, and therefore, is not shown (cf. Chapter 3) [123, 125]. At full-load operation, the measured power factor (0.87) is close to the theoretical maximum (0.90) of the SRC-DCX.

The converter has been tested for $P \in [0, 25]$ kW with a power flow from the LV to the MV side. In the complete range, ZVS is achieved, no oscillations are observed, and the voltage transfer ratio is almost constant (less than 0.8 % deviation). Therefore, it can be concluded that the proposed MCS-ZVS modulation scheme is working as expected from the simulation model.

For the sake of completeness, the converter has also been successfully tested with a power flow from the MV to the LV side. In this case (cf. Section 8.3), the converter can be operated with the typical synchronous rectification modulation scheme or with the proposed MCS-ZVS modulation scheme. The MCS-ZVS modulation scheme has been preferred since it does not require a zero-crossing detection of the current.

8.6.2 Efficiency Measurements

The comparatively low RMS currents (high power factor), associated with the quasi-sinusoidal current shapes, allow for an efficient operation of the transformer as already shown in Chapter 5. The simulated full-load efficiency of the transformer is 99.69 % and the measured efficiency is 99.65 ± 0.07 %. The achieved complete ZVS with quasi-ZCS leads to reduced semiconductor losses, even for the comparatively high switching frequency (48 kHz) for a MV converter [111, 112]. The losses of the semiconductors have been measured calorimetrically as explained in [198]. Finally, the losses of the fans (transformer and bridges) and of the auxiliary circuits are measured electrically. All these measured losses (transformer, MV bridge, LV bridge, fans, and auxiliary circuits) are compiled and added up for calculating the total efficiency of the DC-DC converter. Fig. 8.16 shows the obtained efficiency, measurement uncertainties, and the loss breakdown [198]. The losses of the resonant capacitor

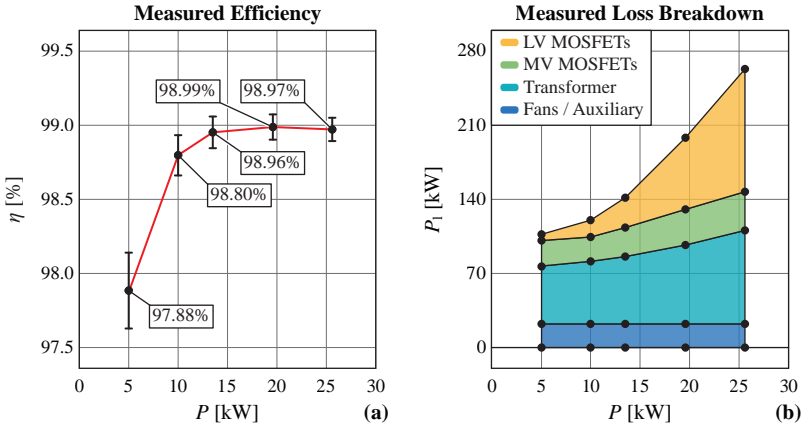


Fig. 8.16: (a) Measured efficiency of the DC-DC converter with the corresponding measurement tolerance. (b) Measured loss breakdown between the different components. More details on the measurement of the semiconductor losses can be found in [198]. The measurement of the transformer losses is described in Chapter 5. The black dots represent the measured operating points of the SRC-DCX, for which the different loss components are evaluated.

(2 W) are small and, therefore, integrated into the transformer losses. The losses of DC-bus capacitors are also negligible (2 W) and integrated into the losses of the bridges. The losses of the fan of the transformer are integrated in the fan and auxiliary losses and, accordingly, removed from the transformer losses measured in Chapter 5.

The full-load efficiency of the SRC-DCX converter is $98.97 \pm 0.08\%$, implying that the error on the measured losses is 8%. Moreover, the converter achieves an efficiency close to 99.0% between 13.5 kW and 25.6 kW. Therefore, it can be concluded that the converter, despite the additional magnetizing current required for obtaining ZVS, achieves extremely high full-load and partial-load efficiencies. This indicates, together with the measured semiconductor temperatures, that the converter could be operated at higher power [198]. The simulated thermal limit of the transformer should be reached at 35 kW (cf. Chapter 5).

From the loss breakdown, it can be seen that the losses of the LV bridge account for the largest part of the converter losses. By replacing the utilized C2M0025120D 1200 V SiC MOSFETs with the newly available “Cree CPM3-0900-0010” 900 V SiC MOSFETs, the efficiency could be further improved [336,

337]. The 900 V SiC MOSFET, which was not available when the converter was designed, features twice lower conduction losses. With these new MOSFETs, the converter would reach 99.2 % full-load efficiency.

The reasons why the efficiency measurements are done by adding the losses of the different components and not by calculating the difference between the input and output power are explained as follows. For measuring the input and output power, two voltages and two currents measurements are required. For the currents, high precision shunts ($\pm 0.02\%$) could be used [338]. The voltage measurement of the MV bus would require a voltage divider ($\pm 0.05\%$) [339]. Then, all the four voltages (output of the two shunts, output of the MV divider, and LV bus voltage) could be measured with a high precision multimeter [340]. The combination of all measurement errors would give an accuracy of $\pm 0.12\%$. However, this error has been computed with freshly calibrated devices and shunts and voltage dividers with optimal values. Moreover, the thermal coefficients of the different components have been neglected. In practice, the electrical measurements conducted with the prototype were affected by reproducibility issues. For these reasons, the efficiency has been extracted considering the (calorimetrically and/or electrically) measured losses of the different components ($\pm 0.08\%$). Additionally, the chosen measurement method also gives the loss breakdown, which would not be available with the measurement of the difference between the input and output power.

8.7 Summary

This chapter studies the operation of the bidirectional DC-DC converter (7 kV to 400 V, 48 kHz, 25 kW) of the considered SST demonstrator (cf. Subsection 1.7.2). The converter is implemented as a SiC MOSFET-based SRC-DCX topology operating at the resonance frequency. Accordingly, the converter behaves as DCX and features a load-independent voltage transfer ratio in open-loop, quasi-sinusoidal currents, and achieves ZVS with the magnetizing current.

First, the converter operation is analyzed with a passive (or synchronous) rectifier. It is shown that, for rectifier bridges implemented with semiconductors exhibiting large output capacitances (e.g., 10 kV SiC MOSFETs), oscillations, current distortions, and a load-dependent voltage transfer ratio occur. Therefore, the system does not show a DCX behavior and passive (or synchronous) rectification cannot be used.

These problems can be solved with the proposed MCS-ZVS modulation scheme, where a small phase shift is introduced between the gating of the MV and LV bridges. This modulation scheme is analyzed with analytical and numerical models. The magnetizing current, which is available for ZVS, can be actively shared between both bridges with proper phase shift. It is found that the ZVS mechanism is effectively acting as a controller, which is automatically stabilizing the modulation scheme. All in all, the proposed modulation scheme features the following characteristics: load-independent voltage transfer ratio, load-independent ZVS (and quasi-ZCS) for both bridges, quasi-sinusoidal currents (low distortion), and robustness against model non-idealities and tolerances. Therefore, the converter acts as bidirectional DCX for the complete load range without requiring measurements or closed-loop voltage control.

Finally, the described modulation scheme is experimentally verified with the realized prototype. The measured waveforms are in good agreement with the simulations. Due to the achieved complete ZVS and the quasi-sinusoidal currents, a full-load efficiency of 99.0 % is achieved with a power density of 3.8 kW/l (62 W/in³, 2.9 kW/kg, and 1.3 kW/lb). Moreover, the peak efficiency of 99.0 % is maintained between 50 % and 100 % load.

9

Conclusion and Outlook

NEWLY available fast-switching MV SiC semiconductors feature unprecedented blocking voltages (up to 15 kV) and reduced switching and conduction losses [108, 109, 111, 112]. These semiconductors enable the realization of extremely efficient and compact MV converters, where the increased blocking voltages allow for the usage of simple single-cell topologies in place of complex multi-cell systems. Hence, MV SiC semiconductors are interesting for numerous applications such as locomotive traction chains, datacenter power supply chains, collecting grids for renewable energies, high power electrical vehicle chargers, and more-electric aircraft [27, 28, 77].

However, power semiconductors are not the only components of a MV converter. The passive components, especially the MV/MF transformers, should be able to exploit the full potential offered by the MV SiC semiconductors [18, 25, 113]. MV/MF transformers are one of the fundamental building blocks of MV converter systems and offer two critical functionalities: voltage scaling and galvanic isolation [27, 28]. Large voltage scaling ratios are typically required for MV converters in order to interface LV systems. Galvanic isolation is required for safety reasons, for isolating faults (especially with DC voltages), and due to the different earthing policies of the MV, LV, and HV grids [79, 80]. More specifically, the following challenges are appearing for the design of MV/MF transformers operated with MV SiC semiconductors. Firstly, the increased operating frequencies are critical for the magnetic core and are causing HF winding losses [24, 27, 173]. Secondly, MV/MF PWM voltages are creating harmful electric field stresses in the insulation [144–149]. Finally, the MV/MF transformers should feature efficiencies above 99.5 % in order to fully profit from the reduced conduction and switching losses of the MV SiC semiconductors [156, 163].

Motivated by the previous discussion, this thesis proposed a detailed analysis of the design and implementation challenges of highly efficient MV/MF transformers. The derived models and results have been applied for a MV DC-DC converter (7 kV to 400 V, 48 kHz, 25 kW), which is part of a MV AC to LV DC SST [197, 198]. A summary of the important results is given at the end of each chapter. Therefore, only the main conclusions are presented hereunder, followed by a critical analysis of the presented work and suggestions for future research topics.

9.1 MV/MF Transformer Technologies

The design of MF transformers is a complex process involving many different fields of physics and engineering: electromagnetism, thermodynamics, fluid dynamics, material science, and process engineering [17, 91, 114, 115, 191, 287]. First, a theoretical analysis of MF transformers is conducted and, accordingly, several points are identified as critical and are studied in more detail. The following important conclusions can be drawn:

- ▶ *Optimization and scaling laws* - Analytical optima are found for the design of MF transformers and the fundamental performance limitations of such components are extracted. Compact designs are operated at higher frequencies, but feature reduced efficiencies. High power designs are operated with limited operating frequencies and are, intrinsically, highly efficient. The nature of optimal designs is examined and it is found that the optimum operating frequency of a MF transformer can always be divided by two with less than 15 % additional losses, by adapting the number of turns. This indicates that the optima are extremely flat. The mapping between the design space and the performance space is analyzed and it is concluded that very different designs feature similar performances (design space diversity). This fact complicates the design process of MF transformers but also offers additional degrees of freedom.
- ▶ *Equivalent circuit uncertainties* - Different analytical and numerical methods are compared for the extraction of the magnetic parameters of MF transformers. The uncertainties linked to model inaccuracies, geometrical tolerances, and material tolerances are analyzed with statistical methods and the measurement uncertainties are also considered. It is concluded that complex numerical field simulation methods (e.g., FEM simulations) are, due to the model uncertainties and parameter

tolerances, only providing minor benefits compared to analytical methods.

- ▶ *Losses of non-ideal litz wires* - The impacts of imperfections of litz wires (e.g., number of pitches and twisting) on the winding losses is examined. A 2.5D PEEC numerical field simulation method is proposed and implemented, for computing the current sharing and the losses of non-ideal litz wires. Imperfect twisting schemes, which are commonly observed in commercially available litz wires, can lead to a massive increase of the eddy current losses (up to 100 % increase). Simple analytical expressions are also proposed to quickly evaluate the impact of imperfect twisting schemes on the losses.
- ▶ *Electrical insulation with PWM voltages* - MV/MF transformers are subject to large PWM voltages with fast switching transitions and, eventually to LF AC voltages or DC voltages. This implies that DC, MF, and HF electric fields are present inside the insulation, at the surface of the insulation, and in the surrounding air. Such electric fields are critical for the insulation design and can create capacitively coupled disturbances. A resistive shield, which confines the electric field without creating additional losses, is proposed for mitigating the aforementioned problems. Afterwards, the critical impact of the insulation requirements on the achievable efficiencies and power densities (up to a factor of two) is highlighted. Finally, the practical process used for realizing a high quality dry-type insulated winding package (vacuum potting) is described in detail.
- ▶ *Dielectric losses with PWM voltages* - The dielectric losses represent a valuable quantitative indicator for evaluating the MF insulation stress. The exact impact of the harmonics contained in PWM voltages (compared to sinusoidal voltages) on the dielectric losses is examined for typical dry-type polymeric insulation materials. Scalable analytical expressions are proposed for the losses produced by PWM voltages, taking into account the frequency and temperature dependences of the material parameters. It is found that the dielectric losses can represent a significant share of the losses of a MV/MF transformer (more than 15 %) and can be responsible for thermal runaways. Different materials are evaluated and it is found that silicone elastomers are better suited for MV/MF insulation than typical epoxy resins.

- ▶ *Measurements of MF transformers* - Many different measurements (short-circuit, saturation, impedances, resonances, insulation test, thermal model, core losses, winding losses, and dielectric losses) are presented for the realized MV/MF transformer. It appears that the electric measurement of the losses is particularly difficult for highly efficient (above 99.0 %) MF transformers. A tolerance analysis shows that the measurement of the difference between the input and output power is impossible for highly efficient MF transformers. Therefore, the prototype is measured during open-circuit and short-circuit operation, which is also challenging due to the low power factor. Calorimetric measurements are performed and successfully compared with different electrical measurement methods. From the tolerance analysis, it can be concluded that calorimetric measurements are the most accurate.

9.2 DC-DC Demonstrator System

A SST demonstrator system has been built in order to demonstrate that MV/MF transformers can profit from the advantages offered by the new MV SiC MOSFETs [108–110]. In this context, a 25 kW SST, which interfaces a MV AC grid (3.8 kV phase-to-neutral RMS voltage and 6.6 kV phase-to-phase RMS voltage) to a LV DC bus (400 V) is considered [197, 198]. This SST, which features an AC-DC and an isolated DC-DC converter, is aimed to supply future datacenters directly from the MV grid [59, 196].

More particularly, the 25 kW bidirectional isolated DC-DC converter, which operates between a MV DC bus (7 kV) and a LV DC bus (400 V), is considered. The usage of 10 kV SiC MOSFETs allows for the realization of the converter with a single-cell structure [108, 109]. This implies that the complexity of the system is significantly lower than for state-of-the-art multi-cell systems [60, 61, 82, 103, 104, 196]. A DC-DC SRC topology is selected and is operated at the resonance frequency, as DCX. In order to reduce the number of switches and for reducing the voltage transfer ratio of the transformer, the combination of a half-bridge on the MV side and a full-bridge on the LV side is used. The converter is operated at 48 kHz, which is significantly above the frequencies used for typical MV converters [61, 64, 83, 99, 196].

The realized MV/MF transformer prototype (± 3.5 kV to ± 400 V, 48 kHz, 25 kW) features the following characteristics: U-core shape, shell-type arrangement, ferrite material, litz wires, forced air cooling, and silicone dry-type insulation. A special focus has been brought on the electrical insulation, where the electric field pattern, dielectric losses, and vacuum potting process have

been examined in detail. The prototype features a power density of 7.4 kW/l (121 kW/in³, 4.0 kW/kg, and 1.8 kW/lb) and achieves a simulated full-load efficiency of 99.69 %, whereas the measured full-load efficiency is 99.65 %.

In next step, the MV/MF transformer prototype was integrated into the SRC-DCX. Due to the high switching frequency (for a MV converter), complete ZVS should be achieved for all semiconductors for all load conditions [111, 112, 202]. It is shown that the typical ZVS modulation scheme of high power SRC-DCXs (operation at or below the resonance frequency, passive or synchronous rectification, and ZVS achieved with the magnetizing current) is problematic with MV SiC MOSFETs, due to the large output capacitances of the semiconductors. Voltage oscillations, current distortions, and a load-dependent voltage transfer ratio are appearing. Therefore, an alternative MCS-ZVS modulation scheme, which features an active sharing of the magnetizing current available for ZVS between the bridges, is proposed, analyzed in detail, and successfully implemented.

Finally, the complete DC-DC converter is tested at the rated power. Due to the achieved complete ZVS and the quasi-sinusoidal currents, a full-load system efficiency of 99.0 % is achieved with a power density of 3.8 kW/l (62 W/in³, 2.9 kW/kg, and 1.3 kW/lb). Moreover, the partial-load efficiency is also close to 99.0 % between 50 % and 100 % load. Given that state-of-the-art isolated MV DC-DC converters employing single-cell or multi-cell topologies with Si, GaN, or SiC semiconductors usually feature efficiencies around 98.0 %, the realized converter features unprecedented low losses [61, 64, 82, 83, 99, 196, 203, 205].

9.3 Outlook and Future Research Areas

In the framework of this thesis, it has been shown that MV SiC MOSFETs are enabling the realization of extremely efficient and compact isolated MV DC-DC converters. Based on the results obtained during this thesis, different aspects could be further studied for improving the performance of isolated MV DC-DC converters and for allowing the commercialization of industrial products based on MV SiC MOSFETs. Accordingly, the following topics are proposed for future work:

- ▶ *Resonance frequencies* - The resonance frequencies (open-circuit, short-circuit, or CM) of high power MV/MF transformers can be close to the operating frequencies of the converters (cf. Chapter 5) [143, 156, 159–161, 276]. Such oscillations can disturb the modulation scheme, produce

additional losses, EMI issues, and insulation overvoltages (uneven voltage sharing between the turns) [155, 156]. This is particularly critical with fast switching SiC MOSFETs [108, 109, 111, 112]. Therefore, better models are required for predicting and, finally, mitigating the impact of the resonance frequencies [155, 156, 341].

- ▶ *Efficiency measurements* - It has been shown (cf. Chapter 5) that the measurement of the losses of highly efficient (above 99.0 %) MF transformers is a challenging task [198]. The measurement of MF transformers, during rated operation, with calorimetric methods (transient or steady state) should be further examined [111, 112, 290, 291]. Alternatively, the accuracy of back-to-back converter efficiency measurements should be evaluated, with the drawback that the semiconductor losses must be subtracted in order to obtain the transformer losses [27, 115, 209]
- ▶ *Lightning surges* - The insulation of MV/MF transformers should be tested with respect to lightning surges [142, 271–273]. This test is necessary to guarantee the integrity of galvanic isolation during fault conditions [79, 80]. More particularly, the MV cable terminations should be designed to be able to withstand surge voltages [142, 307].
- ▶ *Partial discharges* - The critical impact of MF PWM voltages on partial discharges has been highlighted in many publications [148, 149, 270, 282, 283]. Therefore, during nominal conditions, MV/MF transformers should be free of partial discharges [149, 270]. Hence, the partial discharge activity should be carefully measured with LF AC, MF AC, and MF PWM voltages. The partial discharge resistance of the different insulation materials at MF should also be examined, as well as MF partial discharge measurement setups [280, 282].
- ▶ *DC field stress* - The simulation of the DC field distribution inside the insulation is a difficult problem. The surface conductivity of the insulation is not clearly defined (e.g., pollution and moisture) [278]. Moreover, the conductivity of dry-type insulation materials features extreme temperature dependences and can exhibit non-linear effects (space charge migration) [287, 300]. Therefore, this problem should be studied in order to guarantee a homogeneous electric field distribution inside MV/MF transformers subject to large CM DC voltages.
- ▶ *Oil insulation* - MV/MF transformers with large power ratings often feature oil insulation, which is also advantageous for the cooling of

the device [15, 61, 62, 140]. However, the presence of MF PWM or DC voltages is also critical for liquid insulation systems. Therefore, dry-type and oil-based insulation concepts should be compared in order to extract the optimal solution for the different voltage and power ratings.

- ▶ *Alternative transformer concepts* - Next to the classical shell-type MF transformers, many different concepts can be studied: planar transformer [117–119], coaxial transformers [63, 120, 121], air-core transformers [75, 342], multi-winding transformers [97, 98], or matrix transformers [343, 344]. Additionally, advanced materials could be used for the magnetic core, insulation, or cooling system [191, 345–347].
- ▶ *Optimization* - The Pareto optimization of MV transformer and MV converters leads to a multi-variable, multi-constrained, mixed-integer, and non-linear optimization problem [91, 163, 165, 172]. As highlighted in Chapter 2, the optima are very flat and very different designs feature similar performances (design space diversity) [22, 113]. Brute force optimization algorithms are widely used but cannot efficiently solve large problem [91, 163, 172]. Therefore, the ability of advanced algorithms (e.g., genetic algorithm, pattern search, and particle swarm) to cover the design space should be further studies [165, 223]. Next to the efficiency and the power density, other figures of merit, that are important for industrial systems, such as reliability, robustness, and cost, should also be analyzed [91, 103, 104, 163].
- ▶ *Model tolerances* - For highly efficient MV transformer and MV converters, the impact of model tolerances can be critical [25, 165, 172, 175]. The analysis conducted in Chapter 3 for the magnetic parameters can be extended to the other transformer parameters and, more particularly, to the loss models and thermal models. Identifying the accuracy limit of the models is fundamental to further improve the models and, therefore, the performance of MF transformers and MV converters [125]. Moreover, the knowledge of the tolerances and sensitivities is also critical for performing multi-objective optimizations of complete converter systems including MF transformers [91, 163].
- ▶ *Converter topologies* - The different isolated DC-DC converter topologies (e.g., SRC and DAB) and converter structures (e.g., NPC, flying capacitor, ISOP structures, and MMLC) [88, 92, 93, 103, 104, 107] should be examined for each application in order to select the optimal solution. More specifically, single-cell converters using MV SiC MOSFETs

(e.g., 10 kV and 15 kV) should be compared with modular structures using semiconductors with lower blocking voltages (e.g., 1200 V, 1700 V, and 3300 V) [27, 94, 103, 104, 106, 107]. For extreme DC-link voltages, the series connection of MV SiC MOSFETs should also be considered, as, e.g., achieved using NPC, flying capacitor, ISOP structures, and MMLC [92, 348].

Appendices



Equivalent Circuit Comparison

Chapter Abstract

This appendix extends Chapter 3. The theoretical background behind transformer magnetic equivalent circuits is reviewed. Section A.1 analyzes, compares, and highlights the pitfalls of the different equivalent circuits. Afterwards, Section A.2 and Section A.3 present the procedures for extracting equivalent circuits from analytical and numerical computations, respectively. Finally, Section A.4, gives some approximations for transformers with high magnetic coupling factors.

A.1 Transformer Equivalent Circuits

The magnetic equivalent circuit of a (lossless) linear transformer with two windings is fully described by the following inductance matrix, cf. Fig. 3.1(b) [17, 123, 238]:

$$\begin{bmatrix} v_p \\ v_s \end{bmatrix} = \begin{bmatrix} \frac{\partial \Psi_p}{\partial t} \\ \frac{\partial \Psi_s}{\partial t} \end{bmatrix} = \begin{bmatrix} L_p & M \\ M & L_s \end{bmatrix} \begin{bmatrix} \frac{\partial i_p}{\partial t} \\ \frac{\partial i_s}{\partial t} \end{bmatrix}, \quad (\text{A.1})$$

where L_p is the primary self-inductance, L_s the secondary self-inductance, and M the mutual inductance. The inductance matrix features three independent parameters. The energy, W , stored in the transformer (quadratic form of the inductance matrix) can be computed as

$$W = \frac{1}{2}L_p i_p^2 + \frac{1}{2}L_s i_s^2 + M i_p i_s. \quad (\text{A.2})$$

The energy stored in the transformer is always positive (i.e. the inductance matrix is positive definite), which leads to the condition $M^2 < L_p L_s$. Therefore, the mutual inductance can be expressed with a normalized parameter, the magnetic coupling:

$$k = \frac{M}{\sqrt{L_p L_s}}, \quad \text{with } k \in [0, 1]. \quad (\text{A.3})$$

During open-circuit operation, the inductance matrix has the following physical interpretation. The self-inductances (L_p and L_s) represent flux linkages of the two windings themselves (defined as magnetizing flux linkages). The mutual inductance (M) describes the flux linkage between the windings (defined as coupled flux linkage). The differences between the self inductances and the mutual inductance ($L_p - M$ and $L_s - M$) represent the flux linkage differences (defined as leakage flux linkages), which can, for some designs, be negative (especially if $N_p \neq N_s$).

With the aforementioned inductance matrix, the inductances, voltage transfer ratios, and current transfer ratios can be expressed for short-circuit and open-circuit operations (cf. Fig. 3.2(b)):

$$L_{oc,p} = L_p, \quad \frac{v_s}{v_p} = +k \sqrt{\frac{L_s}{L_p}}, \quad \text{with } i_s = 0, \quad (\text{A.4})$$

$$L_{oc,s} = L_s, \quad \frac{v_p}{v_s} = +k \sqrt{\frac{L_p}{L_s}}, \quad \text{with } i_p = 0, \quad (\text{A.5})$$

$$L_{sc,p} = (1 - k^2) L_p, \quad \frac{i_s}{i_p} = -k \sqrt{\frac{L_p}{L_s}}, \quad \text{with } v_s = 0, \quad (\text{A.6})$$

$$L_{sc,s} = (1 - k^2) L_s, \quad \frac{i_p}{i_s} = -k \sqrt{\frac{L_s}{L_p}}, \quad \text{with } v_p = 0. \quad (\text{A.7})$$

The terminal behavior (cf. (A.1)) and the stored energy (cf. (A.2)) of the transformer can be represented with different equivalent circuits. The circuits shown in Fig. 3.1(b) are directly related to the inductance matrix. Contrary, Fig. A.1 depicts equivalent circuits, which do not provide a direct insight on the magnetic flux linkages. The following important remarks can be given about the different equivalent circuits of transformers:

- All the presented equivalent circuits (cf. Fig. 3.1(b) and Fig. A.1) model perfectly the terminal behavior and the stored energy.

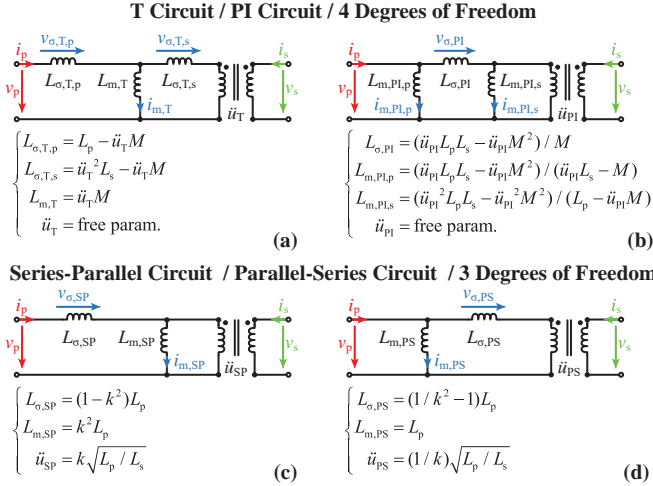


Fig. A.1: Transformer (lossless) linear equivalent circuits. (a) T circuit, (b) PI circuit, (c) series-parallel circuit, and (d) parallel-series circuit. The circuits are referred to the primary-side of the transformer.

- ▶ The equivalent circuits with more than three degrees of freedom (cf. Figs. A.1(a)-(b)) are underdetermined and do not have a physical meaning, without accepting restrictive assumptions [123].
- ▶ The turns ratio of the transformer, $N_p : N_s$, is not clearly defined for some transformer geometries (e.g., inductive power transfer coils) [342, 349]. This implies that the turns ratio is not always directly related to the flux linkages and to the magnetic parameters.
- ▶ The magnetizing and leakage fluxes cannot be spatially separated. In other words, it is not always possible to sort the magnetic field lines into leakage and magnetizing field lines [342].
- ▶ In a transformer, a phase shift is present between the primary and secondary currents, which originates from the modulation scheme, the load, the limited magnetic coupling, and/or the losses. This implies that the distribution of the magnetic field lines is time-dependent [123, 342]. Therefore, the leakage and magnetizing flux linkages only have a clear and obvious interpretation for a lossless transformer during open-circuit and short-circuit operation [342].

- The magnetizing and leakage inductances are usually defined as the parallel and series inductances in the equivalent circuit, respectively. However, the values of these inductances depend on the chosen equivalent circuit (cf. Fig. A.1) and, therefore, do not have a clear and/or unique physical interpretation. This also implies that the associated magnetizing current (i_m) and leakage voltage (v_σ) only represent virtual parameters, which are not directly measurable [123].

It can be concluded that only the equivalent circuit shown in Fig. 3.1(b) features a clear physical interpretation and, therefore, should be preferred. The circuits with more than three degrees of freedom (cf. Figs. A.1(a)-(b)) should be avoided since they are unnecessarily complex. The circuits depicted in Figs. A.1(c)-(d) are interesting for designing transformers with high magnetic coupling factors as explained in Section A.4.

A.2 Analytical Computations

The analytical methods are based on several assumptions (cf. Section 3.3). The inductances are accepted to scale quadratically with the number of turns. The inductances are extracted for $i_p = 0 \vee i_s = 0$ (the energy is confined inside the core and air gaps) and for $+N_p i_p = -N_s i_s$ (the energy is confined inside the winding window). Then, the following inductances can be extracted for a virtual 1 : 1 transformer:

$$L'_m = 2 \frac{W}{i_p^2 N_p^2} = 2 \frac{W}{i_s^2 N_s^2}, \quad \text{with } i_s = 0 \vee i_p = 0, \quad (\text{A.8})$$

$$L'_\sigma = 2 \frac{W}{i_p^2 N_p^2} = 2 \frac{W}{i_s^2 N_s^2}, \quad \text{with } +N_p i_p = -N_s i_s. \quad (\text{A.9})$$

The equivalent circuit (cf. (A.1) and (A.3)) of the transformer is extracted such that the stored energy (cf. (A.2)) matches with the considered excitations, which leads to

$$L_p = N_p^2 L'_m, \quad L_s = N_s^2 L'_m, \quad (\text{A.10})$$

$$M = N_p N_s \left(L'_m - \frac{1}{2} L'_\sigma \right), \quad k = 1 - \frac{1}{2} \frac{L'_\sigma}{L'_m}. \quad (\text{A.11})$$

Afterwards, the following expressions can be extracted for the open-circuit and short-circuit operation of the transformer:

$$L_{oc,p} = N_p^2 L'_m, \quad \frac{v_s}{v_p} = +k \frac{N_s}{N_p}, \quad \text{with } i_s = 0, \quad (\text{A.12})$$

$$L_{oc,s} = N_s^2 L'_m, \quad \frac{v_p}{v_s} = +k \frac{N_p}{N_s}, \quad \text{with } i_p = 0, \quad (\text{A.13})$$

$$L_{sc,p} = N_p^2 \left(\frac{1+k}{2} \right) L'_\sigma, \quad \frac{i_s}{i_p} = -k \frac{N_p}{N_s}, \quad \text{with } v_s = 0, \quad (\text{A.14})$$

$$L_{sc,s} = N_s^2 \left(\frac{1+k}{2} \right) L'_\sigma, \quad \frac{i_p}{i_s} = -k \frac{N_s}{N_p}, \quad \text{with } v_p = 0. \quad (\text{A.15})$$

A.3 FEM Simulations

Different methods exist for extracting the magnetic equivalent circuit of a transformer from numerical simulations (e.g., FEM simulations): integration of the magnetic flux, computation of the induced voltages, extraction of the energy, etc. The energy represents a numerically stable parameter which is easy to extract. Therefore, the energy is extracted for the following cases: $i_p \neq 0 \wedge i_s = 0$, $i_p = 0 \wedge i_s \neq 0$, and $+N_p i_p = -N_s i_s$. This last solution can be obtained by the superposition of the two first solutions. This leads to

$$L_p = 2 \frac{W}{i_p^2}, \quad \text{with } i_p \neq 0 \wedge i_s = 0, \quad (\text{A.16})$$

$$L_s = 2 \frac{W}{i_s^2}, \quad \text{with } i_p = 0 \wedge i_s \neq 0, \quad (\text{A.17})$$

$$M = \frac{W}{i_p i_s} - \frac{1}{2} L_p \frac{i_p}{i_s} - \frac{1}{2} L_s \frac{i_s}{i_p}, \quad \text{with } +N_p i_p = -N_s i_s. \quad (\text{A.18})$$

It should be noted that these expressions are general since no assumptions are required for the geometry, the turns ratio, the coupling factor, etc.

A.4 Designs with High Coupling Factors

For a transformer with a high magnetic coupling factor ($k > 0.95$), the parameters of the equivalent circuits shown in Fig. A.1 are converging together.

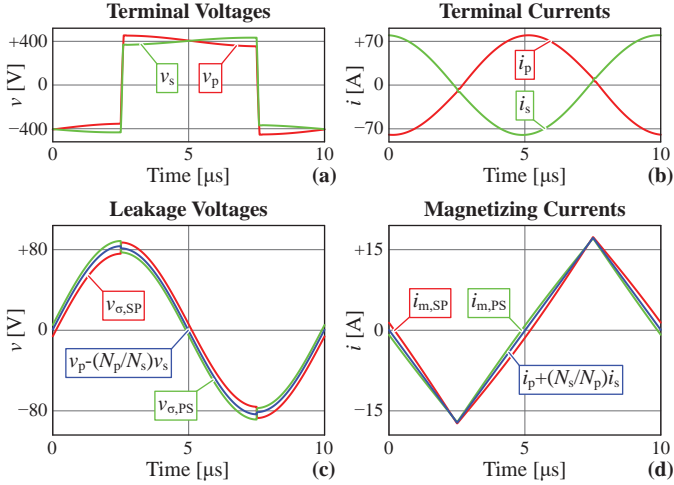


Fig. A.2: Voltage and current waveforms for the considered MF transformer ($k = 0.986$, SRC-DCX, cf. Fig. 3.2). (a) Terminal voltages, (b) terminal currents, (c) voltage across the leakage inductance, and (d) current through the magnetizing inductance. The equivalent circuits shown in Figs. A.1(c)-(d) are considered and compared.

Then, it is possible to define the transformer with the following parameters:

$$L_{\sigma} \approx N_p^2 L'_{\sigma} \approx L_{sc,p} \approx L_{sc,s} \frac{N_p^2}{N_s^2}, \quad (\text{A.19})$$

$$\approx L_{\sigma,T,p} + L_{\sigma,T,s} \approx L_{\sigma,PI} \approx L_{\sigma,SP} \approx L_{\sigma,PS},$$

$$L_m \approx N_p^2 L'_m \approx L_{oc,p} \approx L_{oc,s} \frac{N_p^2}{N_s^2}, \quad (\text{A.20})$$

$$\approx L_{m,T} \approx \frac{L_{m,PI,p} L_{m,PI,s}}{L_{m,PI,p} + L_{m,PI,s}} \approx L_{m,SP} \approx L_{m,PS},$$

$$\ddot{u} \approx \frac{N_p}{N_s} \approx \ddot{u}_T \approx \ddot{u}_{PI} \approx \ddot{u}_{SP} \approx \ddot{u}_{PS}, \quad (\text{A.21})$$

where L_{σ} is the leakage inductance, L_m the magnetizing inductance, and \ddot{u} the voltage transfer ratio. These three parameters, which are nearly independent of the chosen equivalent circuit, are typically used for the design process of transformers.

Fig. A.2 illustrates the leakage voltage and magnetizing current obtained with the equivalent circuits depicted in Figs. A.1(c)-(d) for the considered

MF transformer ($k = 0.986$, SRC-DCX, cf. Fig. 3.2). It can be seen that the aforementioned approximations (cf. (A.19), (A.20), and (A.21)) are valid.

With these assumptions, a clear and unique definition of the leakage and magnetizing fluxes is achieved for transformers with high magnetic coupling factors. The leakage field, which is linked to the leakage inductance (L_σ and v_σ) and to the load current (series inductance), is located inside the winding window and winding heads (cf. Figs. 3.4(a)-(c)). The magnetizing field, which is linked to the magnetizing inductance (L_m and i_m) and to the applied voltage (parallel inductance), is located inside the core and air gaps (cf. Fig. 3.4(d)). During rated operating condition (with a resistive load), the leakage and magnetizing magnetic fields feature 90° phase shift (cf. Fig. A.2).

B

Approximations of Dielectric Losses

Chapter Abstract

This appendix extends Chapter 7. The derivations and the corresponding accuracy analysis are shown for the formulas proposed for computing the dielectric losses. Section B.1 shows the derivation of the approximation of the dielectric losses produced by frequency-independent materials under PWM voltages. Section B.2 proposes an expression for the losses produced by frequency-dependent materials subject to a single (non-periodic) switching transition. Section B.3 shows the derivation of the approximation of the dielectric losses produced by frequency-dependent materials with PWM voltages. Afterwards, Section B.4 tests the validity of the approximation of the Kramers-Kronig equations for the complex permittivity. Finally, Section B.5 analyzes the accuracy of the proposed approximations for computing dielectric losses with PWM voltages.

B.1 Frequency-Independent Materials

An approximation of the dielectric losses produced by frequency-independent materials under PWM voltages (cf. (7.21), (7.22), and (7.23)) is derived in the following. From (7.18) and (7.20), the normalized losses P' can be written as (with the assumption $\epsilon_r''(f) = \text{const.}$)

$$P' = \frac{P}{\epsilon_r'' C_0 V_{\text{DC}}^2} = \sum_{n=1}^{\infty} \frac{4f_s}{\pi} \frac{\sin^2(\pi n D_c)}{n} \frac{1}{1 + \left(n \frac{f_s}{f_c}\right)^2}. \quad (\text{B.1})$$

The infinite summation can be approximated by a finite summation (until the corner frequency of the first-order low-pass filter, cf. (7.16)). The following

expression is derived (using the double angle trigonometric formula):

$$P' \approx \sum_{n=1}^{\lceil f_c/f_s \rceil} \frac{4f_s}{\pi} \frac{1 - \cos(2\pi D_c n)}{2n}, \quad (\text{B.2})$$

which can be rewritten as

$$P' \approx \frac{2f_s}{\pi} \left(\sum_{n=1}^{\lceil f_c/f_s \rceil} \frac{1}{n} - \sum_{n=1}^{\lceil f_c/f_s \rceil} \frac{(-1)^n \cos(2\pi n D_c - n\pi)}{n} \right). \quad (\text{B.3})$$

An approximation exists for the partial sum of the first term, which is a harmonic series [321]. The second term converges quickly such that the finite sum can be approximated with the infinite sum, for which a closed-form solution exists [350]. This leads to

$$P' \approx \frac{2f_s}{\pi} \left(\ln\left(\frac{f_c}{f_s}\right) + \gamma + \frac{1}{2} \ln(2 + 2 \cos(2\pi D_c - \pi)) \right). \quad (\text{B.4})$$

This last expression can be further simplified with the double angle trigonometric formula:

$$P' \approx \frac{2f_s}{\pi} \ln\left(2e^\gamma \frac{f_c}{f_s} \sin(\pi D_c)\right), \quad (\text{B.5})$$

which is equivalent, after some trivial algebraic operations, to the expressions proposed in (7.21), (7.22), and (7.23).

B.2 Upper Bound on the Dielectric Losses

In the following, the proposed expression for the losses produced by frequency-dependent materials subject to a single (non-periodic) switching transition (cf. (7.24) and (7.26)) is derived. The transition is modeled as the step response of a first-order low-pass filter, cf. Fig. 7.4(b)). First, the Fourier transform of the applied signal is considered:

$$V(f) = \int_0^{\infty} \left(1 - e^{-2\pi f_c t}\right) e^{-j2\pi f t} dt. \quad (\text{B.6})$$

This Fourier transform features an analytical solution:

$$V(f) = \frac{1}{2\pi} \left(\frac{1}{jf} + \frac{1}{jf + jf_c} + \pi\delta(f) \right), \quad (\text{B.7})$$

where δ is the Dirac delta function. Then, the normalized losses can be computed from the integration of the spectral losses (Parseval's theorem):

$$W' = \frac{W}{C_0 V_{\text{DC}}^2} = 2 \int_0^{\infty} \varepsilon_r''(2\pi f) |V(f)|^2 df, \quad (\text{B.8})$$

which can be rewritten as

$$W' = \frac{1}{\pi} \int_0^{\infty} \varepsilon_r''(f) \frac{1}{f} \frac{f_c^2}{f^2 + f_c^2} df, \quad (\text{B.9})$$

which is equivalent to (7.24). This equation can be expanded as

$$W' = \frac{1}{2} \varepsilon_r'(0) - \frac{1}{2} \varepsilon_r'(\infty) + \frac{1}{\pi} \int_0^{\infty} \varepsilon_r''(f) \frac{1}{f} \frac{f_c^2}{f^2 + f_c^2} df. \quad (\text{B.10})$$

This last expression can be transformed by introducing the Kramers-Kronig relation for the real part of the permittivity (cf. (7.6)). This leads to

$$W' = \frac{\varepsilon_r'(0) - \varepsilon_r'(\infty)}{2} + \frac{1}{\pi} \int_0^{\infty} \varepsilon_r''(f) \frac{1}{f} \left(\frac{f_c^2}{f^2 + f_c^2} - 1 \right) df, \quad (\text{B.11})$$

which is equivalent to the expression (7.26).

B.3 Frequency-Dependent Materials

An approximation of the dielectric losses produced by frequency-dependent materials under PWM voltages (cf. (7.28), (7.29), (7.30), and (7.31)) is derived in the following. First, the duty cycle is fixed to $D_c = 50\%$. From (7.18) and (7.20), the normalized losses P' can be written as

$$P' = \frac{P}{C_0 V_{\text{DC}}^2} = \sum_{n=1}^{\infty} \frac{4f_s}{\pi} \frac{\varepsilon_r''(nf_s) \cdot \sin^2\left(\frac{\pi}{2}n\right)}{n} \frac{1}{1 + \left(n\frac{f_s}{f_c}\right)^2}. \quad (\text{B.12})$$

With the chosen duty cycle, only the odd harmonics are non-zero. As shown in Section B.1, the summation can be truncated at the corner frequency:

$$P' \approx \sum_{n=1(\text{odd})}^{\lceil f_c/f_s \rceil} \frac{4f_s}{\pi} \frac{\varepsilon_r''(nf_s)}{n}. \quad (\text{B.13})$$

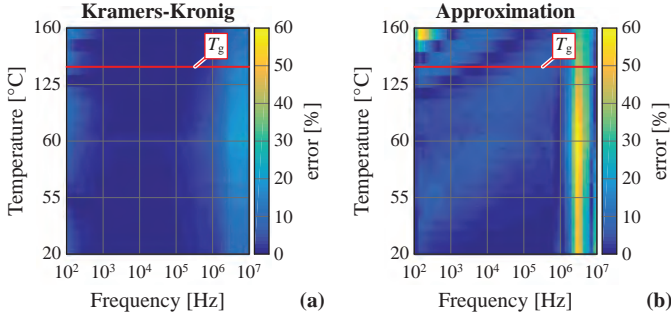


Fig. B.1: Relative error between the measured values of $\varepsilon_r''(f, T)$ and the values computed with (a) the formula (7.7) and (b) the approximation (7.8). The epoxy resin “vonRoll Damisol 3418” is considered and the glass transition temperature ($T_g = 136$ °C) is indicated. The measured complex permittivity is shown in Fig. 7.7.

This summation can be approximated with an integral [351]. The inaccuracy of this approximation near the fundamental frequency is compensated by an additional term P'_{add} :

$$P' \approx P'_{\text{add}} + \frac{1}{2} \frac{4f_s}{\pi} \int_{\ln(f_s)}^{\ln(f_c)} \varepsilon_r''(f) d(\ln(f)), \quad (\text{B.14})$$

where the factor $1/2$ results from the fact that only odd values of n are considered. The term P'_{add} is chosen such that the approximation is equivalent to (B.5) for the special case of a frequency-independent $\varepsilon_r''(f)$. This leads to

$$P'_{\text{add}} = \frac{2f_s}{\pi} \ln(2e^\gamma \sin(\pi D_c)) \varepsilon_r''(f_s), \quad (\text{B.15})$$

which, together with (B.14), after some trivial algebraic operations, is equal to the expressions proposed in (7.28), (7.29), (7.30), and (7.31).

B.4 Kramers-Kronig Approximations

The Kramers-Kronig relations (cf. (7.7)) are compared with the approximation (cf. (7.8)). For the comparison, the epoxy resin “vonRoll Damisol 3418”, which presents the typical characteristics of a polymeric insulation material, is used (cf. Fig. 7.7) [323].

Tab. B.1: PWM with Frequency-Independent Materials

| Considered parameter combinations (cf. Fig. 7.4) | | |
|---|-----------------|-------------|
| $f_s \in [1, 100] \text{ kHz} / t_r \in [10, 1000] \text{ ns} / D_c \in [10 \%, 90 \%]$ | | |
| $t_r f_s < 0.2 D_c / t_r f_s < 0.2 (1 - D_c)$ | | |
| Reference values are obtained with (7.10) | | |
| Equations | Low-pass | Ramp |
| (7.22) | 78.8 % | 78.6 % |
| (7.21), (7.22), (7.23) | 0.6 % | 4.0 % |

Fig. B.1(a) shows the relative error between the measured values of $\varepsilon_r''(f, T)$ and the values computed with (7.7). Due to the presence of singularities, the numerical integration of (7.7) is challenging. In this work, the Maclaurin's formula has been used, as described in [352]. The error between the two curves can be explained by several factors [353]: the accuracy of the measurements, the presence of non-linearities (especially for reduced frequencies), and the fact that (7.7) requires the permittivity for the complete spectrum (from 0 Hz to ∞ Hz). Therefore, the computation is less accurate at the boundaries of the measured frequency range. Nevertheless, the deviation is below 17 % for the complete range and below 7 % for frequencies and temperatures located outside the relaxation peaks (below 1 MHz and below 120 °C).

Fig. B.1(b) depicts the relative error between the measured values of $\varepsilon_r''(f, T)$ and the values computed with (7.8). The local approximation is accurate (less than 9 % error) for frequencies and temperatures located outside the relaxation peaks (below 1 MHz and below 120 °C). For the complete range, the maximum error reaches 60 %, indicating that the approximation of the Kramers-Kronig relations should not be used around the loss peaks.

B.5 Accuracies of the Approximations

The proposed approximations for the computation of the dielectric losses are compared to the summation (7.10). For the summation, two approximations of the switching transitions are used: the ramp function ("ramp") and the step response of a first-order low-pass filter ("low-pass"), cf. Fig. 7.4(b)). The considered parameter ranges are based on typical values used for MV converters. The obtained maximum relative errors over all the possible combinations are

Tab. B.2: PWM with Frequency-Dependent Materials

| Considered parameter combinations (cf. Fig. 7.4) | | |
|--|-----------------|-------------|
| $f_s \in [1, 100] \text{ kHz} / t_r \in [100, 1000] \text{ ns} / D_c \in [10 \%, 90 \%]$ | | |
| $t_r f_s < 0.2 D_c / t_r f_s < 0.2 (1 - D_c)$ | | |
| $T \in [20, 160] \text{ }^\circ\text{C} / \text{“vonRoll Damisol 3418” epoxy resin}$ | | |
| Reference values are obtained with (7.10) | | |
| Equations | Low-pass | Ramp |
| (7.22) | 90.4 % | 90.0 % |
| (7.21), (7.22), (7.23) | 109.4 % | 111.6 % |
| (7.28), (7.29), (7.30), (7.31) | 7.1 % | 7.6 % |
| (7.32), (7.33), (7.34), (7.35) | 16.1 % | 10.6 % |

considered. A condition is set on the duty cycle, switching frequency, and switching speed in order to avoid quasi-triangular pulses.

Tab. B.1 contains the results for the losses of frequency-independent materials subject to PWM voltages (cf. Subsection 7.3.1). It appears that the proposed approximation is valid. A fundamental frequency analysis of PWM voltages is invalid (78 % error).

Tab. B.2 shows the errors for the losses with frequency and temperature dependent materials subject to PWM voltages (cf. Subsection 7.3.4). For the analysis, the epoxy resin “vonRoll Damisol 3418”, which presents the typical characteristics of a polymeric insulation material, is considered (cf. Fig. 7.7) [323]. The proposed approximations are valid. It appears that the frequency dependence of the permittivity cannot be neglected (111 % error).

Bibliography

- [1] M. Faraday, *Faraday's Diary*. G. Bell and Sons, Ltd., 1936, vol. 7.
- [2] P. A. David, "Heroes, Herds and Hysteresis in Technological History: Thomas Edison and 'The Battle of the Systems' Reconsidered," *Industrial and Corporate Change*, vol. 1, no. 1, pp. 129–180, 1992, DOI: [10.1093/icc/1.1.129](https://doi.org/10.1093/icc/1.1.129).
- [3] P. Yablochkov, "Disposition de Courants, Destinée à l'Eclairage par la Lumière Electrique (in French)," French Patent 112 024, 1876 (filed 1876).
- [4] A. Ben-Menahem, *Historical Encyclopedia of Natural and Mathematical Sciences*. Springer, Berlin, Heidelberg, 2009, vol. 3.
- [5] D. J. Allan, "Power Transformers – The Second Century," *Power Engineering Journal*, vol. 5, no. 1, pp. 5–14, 1991, DOI: [10.1049/pe:19910004](https://doi.org/10.1049/pe:19910004).
- [6] J. W. Coltman, "The Transformer [Historical Overview]," *IEEE Ind. Appl. Mag.*, vol. 8, no. 1, pp. 8–15, 2002, DOI: [10.1109/2943.974352](https://doi.org/10.1109/2943.974352).
- [7] M. von Dolivo-Dobrowolsky, "Electrical Induction Apparatus or Transformer," U.S. Patent 422 746, 1890 (filed 1890).
- [8] J. Steen, M. Scholdei-Klie, and A. Junker, *Eine neue Zeit: Die Internationale Elektrotechnische Ausstellung 1891 (in German)*. Historisches Museum Frankfurt am Main, 1991.
- [9] V. Smil, *Creating the Twentieth Century: Technical Innovations of 1867-1914 and their Lasting Impact*. Oxford University Press, 2005.
- [10] G. Neidhofer, "50 Hz Frequency [History]," *IEEE Power & Energy Mag.*, vol. 9, no. 4, pp. 66–81, 2011, DOI: [10.1109/MPE.2011.941165](https://doi.org/10.1109/MPE.2011.941165).
- [11] E. L. Owen, "The Origins of 60 Hz as a Power Frequency," *IEEE Ind. Appl. Mag.*, vol. 3, no. 6, pp. 8–14, 1997, DOI: [10.1109/2943.628099](https://doi.org/10.1109/2943.628099).
- [12] T. J. Blalock and C. A. Woodworth, "25 Hz at Niagara Falls [History]," *IEEE Power & Energy Mag.*, vol. 6, no. 1, pp. 84–89, 2008, DOI: [10.1109/MPE.2007.915180](https://doi.org/10.1109/MPE.2007.915180).
- [13] R. J. Hill, "Electric Railway Traction. Part 3. Traction Power Supplies," *Power Engineering Journal*, vol. 8, no. 6, pp. 275–286, 1994, DOI: [10.1049/pe:19940604](https://doi.org/10.1049/pe:19940604).

- [14] A. Palaz, *Cours d'Electricité Industrielle (in French)*. Rouge, 1892.
- [15] S. V. Kulkarni and S. A. Khaparde, *Transformer Engineering: Design and Practice*. CRC press, 2004.
- [16] J. A. Ferreira, *Electromagnetic Modelling of Power Electronic Converters*. Springer, Science & Business Media, 2013.
- [17] V. C. Valchev and A. Van den Bossche, *Inductors and Transformers for Power Electronics*. Taylor & Francis, 2005.
- [18] M. Leibl, “Three-Phase PFC Rectifier and High-Voltage Generator,” Ph.D. dissertation, ETH Zürich, 2017.
- [19] J. Mühlethaler, “Modeling and Multi-Objective Optimization of Inductive Power Components,” Ph.D. dissertation, ETH Zürich, 2012.
- [20] W. J. Gu and R. Liu, “A Study of Volume and Weight vs. Frequency for High-Frequency Transformers,” in *Proc. of the IEEE Power Electronics Specialists Conf. (PESC)*, Jun. 1993, DOI: [10.1109/PESC.1993.472059](https://doi.org/10.1109/PESC.1993.472059).
- [21] Metglas, “Magnetic Alloy 2605SA1 (Iron-Based),” Jun. 2011.
- [22] T. Guillod and J. W. Kolar, “Medium-Frequency Transformer Scaling Laws: Derivation, Verification, and Critical Analysis,” *Springer Electrical Engineering*, (under review), 2019.
- [23] W. G. Hurley, W. H. Wölfle, and J. G. Breslin, “Optimized Transformer Design: Inclusive of High-Frequency Effects,” *IEEE Trans. Power Electron.*, vol. 13, no. 4, pp. 651–659, 1998, DOI: [10.1109/63.704133](https://doi.org/10.1109/63.704133).
- [24] W. G. Hurley, T. Merkin, and M. Duffy, “The Performance Factor for Magnetic Materials Revisited: The Effect of Core Losses on the Selection of Core Size in Transformers,” *IEEE Power Electron. Mag.*, vol. 5, no. 3, pp. 26–34, 2018, DOI: [10.1109/MPEL.2018.2848738](https://doi.org/10.1109/MPEL.2018.2848738).
- [25] M. Leibl, G. Ortiz, and J. W. Kolar, “Design and Experimental Analysis of a Medium Frequency Transformer for Solid-State Transformer Applications,” *IEEE Trans. Emerg. Sel. Topics Power Electron.*, vol. 5, no. 1, pp. 110–123, 2017, DOI: [10.1109/JESTPE.2016.2623679](https://doi.org/10.1109/JESTPE.2016.2623679).
- [26] C. Grawinkel and K. Strecker, *Hilfsbuch für die Elektrotechnik*. Springer, Berlin, Heidelberg, 1893.

-
- [27] G. Ortiz, “High-Power DC-DC Converter Technologies for Smart-Grid and Traction Applications,” Ph.D. dissertation, ETH Zürich, 2013.
- [28] J. W. Kolar and J. E. Huber, “Solid-State Transformers,” in *Leistungselektronische Schaltungen: Funktion, Auslegung und Anwendung (in German)*, D. Schröder, Ed. Springer, Berlin Heidelberg, 2018.
- [29] T. J. Blalock, “The Frequency Changer Era - Interconnecting Systems of Varying Cycles,” *IEEE Power & Energy Mag.*, vol. 99, no. 5, pp. 72–79, 2003, DOI: [10.1109/MPAE.2003.1231697](https://doi.org/10.1109/MPAE.2003.1231697).
- [30] T. J. Blalock, “The Rotary Era, Part 1: Early AC-to-DC Power Conversion [History],” *IEEE Power & Energy Mag.*, vol. 11, no. 5, pp. 82–92, 2013, DOI: [10.1109/MPE.2013.2265791](https://doi.org/10.1109/MPE.2013.2265791).
- [31] T. J. Blalock, “The Rotary Era, Part 2: AC-to-DC Power Conversion, Continued [History],” *IEEE Power & Energy Mag.*, vol. 11, no. 6, pp. 96–105, 2013, DOI: [10.1109/MPE.2013.2276199](https://doi.org/10.1109/MPE.2013.2276199).
- [32] M. Guarnieri, “Solidifying Power Electronics [Historical],” *IEEE Ind. Electron. Mag.*, vol. 12, no. 1, pp. 36–40, 2018, DOI: [10.1109/MIE.2018.2791062](https://doi.org/10.1109/MIE.2018.2791062).
- [33] E. F. W. Alexanderson and E. L. Phillipi, “History and Development of the Electronic Power Converter,” *Electrical Engineering*, vol. 63, no. 9, pp. 654–657, 1944, DOI: [10.1109/T-AIEE.1944.5058993](https://doi.org/10.1109/T-AIEE.1944.5058993).
- [34] E. L. Owen, M. M. Morack, C. C. Herskind, and A. S. Grimes, “AC Adjustable-Speed Drives with Electronic Power Converters – The Early Days,” *IEEE Trans. Ind. Appl.*, vol. IA-20, no. 2, pp. 298–308, 1984, DOI: [10.1109/TIA.1984.4504412](https://doi.org/10.1109/TIA.1984.4504412).
- [35] D. Prince, “The Direct Current Transformer Utilizing Thyatron Tubes,” *General Electric Review*, vol. 31, no. 7, pp. 347–350, 1928.
- [36] A. Wydts and G. Weissmann, “Continuous-Current Transformer,” U.S. Patent 645 774, 1900 (filed 1899).
- [37] P. M. J. Boucherot, “Transformer of Continuous Current,” U.S. Patent 1 206 662, 1916 (filed 1913).
- [38] H. J. Van der Bijl, “Direct-Current Transformer,” U.S. Patent 1 448 583, 1923 (filed 1916).

- [39] W. McMurray, "Power Converter Circuits Having a High Frequency Link," U.S. Patent 3 517 300, 1970 (filed 1968).
- [40] W. McMurray, "Multipurpose Power Converter Circuits," U.S. Patent 3 487 289, 1969 (filed 1968).
- [41] W. McMurray, "The Thyristor Electronic Transformer: A Power Converter Using a High-Frequency Link," *IEEE Trans. Ind. Appl.*, vol. 7, no. 4, pp. 451–457, 1971, DOI: [10.1109/TIGA.1971.4181326](https://doi.org/10.1109/TIGA.1971.4181326).
- [42] F. C. Schwarz, "A Method of Resonant Current Pulse Modulation for Power Converters," *IEEE Trans. Ind. Electron.*, vol. 17, no. 3, pp. 209–221, 1970, DOI: [10.1109/TIECI.1970.230769](https://doi.org/10.1109/TIECI.1970.230769).
- [43] R. W. De Doncker, D. M. Divan, and M. H. Kheraluwala, "A Three-Phase Soft-Switched High Power Density DC/DC Converter for High Power Applications," in *Proc. of the IEEE Industry Applications Society Annual Meeting (IAS)*, Oct. 1988.
- [44] R. W. De Doncker, D. M. Divan, and M. H. Kheraluwala, "A Three-Phase Soft-Switched High-Power-Density DC/DC Converter for High-Power Applications," *IEEE Trans. Ind. Appl.*, vol. 27, no. 1, pp. 63–73, 1991, DOI: [10.1109/28.67533](https://doi.org/10.1109/28.67533).
- [45] R. W. De Doncker, M. H. Kheraluwala, and D. M. Divan, "Power Conversion Apparatus for DC/DC Conversion Using Dual Active Bridges," U.S. Patent 5 027 264, 1991 (filed 1989).
- [46] H. A. B. Siddique and R. W. De Doncker, "Evaluation of DC Collector-Grid Configurations for Large Photovoltaic Parks," *IEEE Trans. Power Del.*, vol. 33, no. 1, pp. 311–320, 2018, DOI: [10.1109/TPWRD.2017.2702018](https://doi.org/10.1109/TPWRD.2017.2702018).
- [47] T. Jimichi, M. Kaymak, and R. W. De Doncker, "Design and Loss Analysis of a Medium-Voltage DC-DC Converter Intended for Offshore Wind Farms," in *Proc. of the IEEE Int. Conf. on Renewable Energy Research and Applications (ICRERA)*, Nov. 2016, DOI: [10.1109/ICRERA.2016.7884517](https://doi.org/10.1109/ICRERA.2016.7884517).
- [48] R. W. De Doncker, "Power Electronic Technologies for Flexible DC Distribution Grids," in *Proc. of the IEEE Energy Conversion Congr. and Expo. (ECCE Asia)*, May 2014, DOI: [10.1109/IPEC.2014.6869670](https://doi.org/10.1109/IPEC.2014.6869670).
- [49] Q. Xun, B. Xun, Z. Li, P. Wang, and Z. Cai, "Application of SiC Power Electronic Devices in Secondary Power Source for Aircraft," *Renewable*

- and Sustainable Energy Reviews*, vol. 70, no. 1, pp. 1336–1342, 2017, DOI: [10.1016/j.rser.2016.12.035](https://doi.org/10.1016/j.rser.2016.12.035).
- [50] J. E. Huber, “Conceptualization and Multi-Objective Analysis of Multi-Cell Solid-State Transformers,” Ph.D. dissertation, ETH Zürich, 2016.
- [51] A. Q. Huang, M. L. Crow, G. T. Heydt, J. P. Zheng, and S. J. Dale, “The Future Renewable Electric Energy Delivery and Management (FREEDM) System: The Energy Internet,” *Proc. IEEE*, vol. 99, no. 1, pp. 133–148, 2011, DOI: [10.1109/JPROC.2010.2081330](https://doi.org/10.1109/JPROC.2010.2081330).
- [52] “EcoDry: Ultra-Efficient Dry-Type Transformers,” ABB, Feb. 2010.
- [53] J. E. Huber and J. W. Kolar, “Volume/Weight/Cost Comparison of a 1 MVA 10 kV/400 V Solid-State Against a Conventional Low-Frequency Distribution Transformer,” in *Proc. of the IEEE Energy Conversion Congr. and Expo. (ECCE USA)*, Sep. 2014, DOI: [10.1109/ECCE.2014.6954023](https://doi.org/10.1109/ECCE.2014.6954023).
- [54] J. Wang, A. Q. Huang, W. Sung, Y. Liu, and B. Baliga, “Smart Grid Technologies,” *IEEE Ind. Electron. Mag.*, vol. 3, no. 2, pp. 16–23, 2009, DOI: [10.1109/MIE.2009.932583](https://doi.org/10.1109/MIE.2009.932583).
- [55] J. E. Huber and J. W. Kolar, “Applicability of Solid-State Transformers in Today’s and Future Distribution Grids,” *IEEE Trans. Smart Grid*, vol. 10, no. 1, pp. 317–326, 2019, DOI: [10.1109/TSG.2017.2738610](https://doi.org/10.1109/TSG.2017.2738610).
- [56] A. Tripathi, S. Madhusoodhanan, K. Mainali, K. Vechalapu, R. Chattopadhyay, and S. Bhattacharya, “Enabling DC Microgrids with Direct MV DC Interfacing DAB Converter Based on 15 kV SiC IGBT and 15 kV SiC MOSFET,” in *Proc. of the IEEE Energy Conversion Congr. and Expo. (ECCE USA)*, Sep. 2016, DOI: [10.1109/ECCE.2016.7855078](https://doi.org/10.1109/ECCE.2016.7855078).
- [57] A. Remaci, C. Merlo, O. Curea, A. Hacala, and V. Guerre, “Renewable Electricity Conversion and Storage: Focus on Power to Gas Process, EMR Modelling and Simulation,” in *Proc. of the Int. Exhib. and Conf. for Power Electronics, Intelligent Motion, Renewable Energy and Energy Management (PCIM Europe)*, May 2016.
- [58] D. Rothmund, G. Ortiz, and J. W. Kolar, “SiC-Based Unidirectional Solid-State Transformer Concepts for Directly Interfacing 400 V DC to Medium-Voltage AC Distribution Systems,” in *Proc. of the IEEE Telecommunications Energy Conf. (INTELEC)*, Sep. 2014, DOI: [10.1109/INTELEC.2014.6972199](https://doi.org/10.1109/INTELEC.2014.6972199).

- [59] B. Hafez, H. S. Krishnamoorthy, P. Enjeti, S. Ahmed, and I. J. Pitel, "Medium Voltage Power Distribution Architecture with Medium Frequency Isolation Transformer for Data Centers," in *Proc. of the IEEE Applied Power Electronics Conf. and Expo. (APEC)*, Mar. 2014, DOI: [10.1109/APEC.2014.6803810](https://doi.org/10.1109/APEC.2014.6803810).
- [60] M. Glinka, "Prototype of Multiphase Modular-Multilevel-Converter with 2 MW Power Rating and 17-Level-Output-Voltage," in *Proc. of the IEEE Power Electronics Specialists Conf. (PESC)*, Jun. 2004, DOI: [10.1109/PESC.2004.1355234](https://doi.org/10.1109/PESC.2004.1355234).
- [61] C. Zhao, D. Dujic, A. Mester, J. K. Steinke, M. Weiss, S. Lewdeni-Schmid, T. Chaudhuri, and P. Stefanutti, "Power Electronic Traction Transformer - Medium Voltage Prototype," *IEEE Trans. Ind. Electron.*, vol. 61, no. 7, pp. 3257–3268, 2014, DOI: [10.1109/TPEL.2013.2248756](https://doi.org/10.1109/TPEL.2013.2248756).
- [62] M. Steiner and H. Reinold, "Medium Frequency Topology in Railway Applications," in *Proc. of the European Conf. Power Electronics and Applications (EPE-ECCE Europe)*, Sep. 2007, DOI: [10.1109/EPE.2007.4417570](https://doi.org/10.1109/EPE.2007.4417570).
- [63] L. Heinemann, "An Actively Cooled High Power, High Frequency Transformer with High Insulation Capability," in *Proc. of the IEEE Applied Power Electronics Conf. and Expo. (APEC)*, Mar. 2002, DOI: [10.1109/APEC.2002.989270](https://doi.org/10.1109/APEC.2002.989270).
- [64] F. Kieferndorf, U. Drofenik, F. Agostini, and F. Canales, "Modular PET, Two-Phase Air-Cooled Converter Cell Design and Performance Evaluation with 1.7 kV IGBTs for MV Applications," in *Proc. of the IEEE Applied Power Electronics Conf. and Expo. (APEC)*, Mar. 2016, DOI: [10.1109/APEC.2016.7467914](https://doi.org/10.1109/APEC.2016.7467914).
- [65] J. Kuseian, T. J. McCoy, and K. M. McCoy, "Naval Power Systems Technology Development Roadmap PMS 320," U.S. Naval Sea Systems Command, Electric Ships Office, Mar. 2013.
- [66] U. Javaid, D. Dujic, and W. Van der Merwe, "MVDC Marine Electrical Distribution: Are We Ready?" in *Proc. of the IEEE Industrial Electronics Society Conf. (IECON)*, Nov. 2015, DOI: [10.1109/IECON.2015.7392201](https://doi.org/10.1109/IECON.2015.7392201).
- [67] B. Zahedi and L. E. Norum, "Efficiency Analysis of Shipboard DC Power Systems," in *Proc. of the IEEE Industrial Electronics Society Conf. (IECON)*, Nov. 2013, DOI: [10.1109/IECON.2013.6699218](https://doi.org/10.1109/IECON.2013.6699218).

- [68] “Shore-to-Ship Power and Smart Port Solutions,” ABB, Oct. 2016.
- [69] H. Devold, “Subsea High Power Long Offset Electrical Power Systems,” in *Proc. of the US-Norway Oil & Gas Technology Partnership Conf. (NOR-WEP)*, Mar. 2014.
- [70] J. Paul Guyer, *An Introduction to 400 Hz Electrical Distribution Systems*. Createspace Independent Pub., 2016.
- [71] B. Sarlioglu and C. T. Morris, “More Electric Aircraft: Review, Challenges, and Opportunities for Commercial Transport Aircraft,” *IEEE Trans. Transport. Electrific.*, vol. 1, no. 1, pp. 54–64, 2015, DOI: [10.1109/TTE.2015.2426499](https://doi.org/10.1109/TTE.2015.2426499).
- [72] A. S. Gohardani, G. Doulgeris, and R. Singh, “Challenges of Future Aircraft Propulsion: A Review of Distributed Propulsion Technology and its Potential Application for the All Electric Commercial Aircraft,” *Progress in Aerospace Sciences*, vol. 47, no. 5, pp. 369–391, 2011, DOI: [10.1016/j.paerosci.2010.09.001](https://doi.org/10.1016/j.paerosci.2010.09.001).
- [73] A. Lücken, J. Brombach, and D. Schulz, “Design and Protection of a High Voltage DC Onboard Grid with Integrated Fuel Cell System on More Electric Aircraft,” in *Proc. of the IEEE Electrical Systems for Aircraft, Railway and Ship Propulsion Conf. (ESARS)*, Oct. 2010, DOI: [10.1109/ESARS.2010.5665245](https://doi.org/10.1109/ESARS.2010.5665245).
- [74] N. Madavan, “NASA Investments in Electric Propulsion Technologies for Large Commercial Aircraft,” in *Proc. of the Electric and Hybrid Aerospace Technology Symp.*, Nov. 2016.
- [75] P. Czyz, T. Guillod, F. Krismer, and J. W. Kolar, “Exploration of the Design and Performance Space of a High Frequency 166 kW/10 kV SiC Solid-State Air-Core Transformer,” in *Proc. of the IEEE Energy Conversion Congr. and Expo. (ECCE Asia)*, May 2018, DOI: [10.23919/IPEC.2018.8507746](https://doi.org/10.23919/IPEC.2018.8507746).
- [76] J. W. Kolar and G. Ortiz, “Solid-State-Transformers: Key Components of Future Traction and Smart Grid Systems,” in *Proc. of the IEEE Energy Conversion Congr. and Expo. (ECCE Asia)*, May 2014.
- [77] J. E. Huber and J. W. Kolar, “Solid-State Transformers: On the Origins and Evolution of Key Concepts,” *IEEE Ind. Electron. Mag.*, vol. 10, no. 3, pp. 19–28, 2016, DOI: [10.1109/MIE.2016.2588878](https://doi.org/10.1109/MIE.2016.2588878).

- [78] F. Krismer, “Modeling and Optimization of Bidirectional Dual Active Bridge DC-DC Converter Topologies,” Ph.D. dissertation, ETH Zürich, 2010.
- [79] T. Guillod, F. Krismer, R. Färber, C. M. Franck, and J. W. Kolar, “Protection of MV/LV Solid-State Transformers in the Distribution Grid,” in *Proc. of the IEEE Industrial Electronics Society Conf. (IECON)*, Nov. 2015, DOI: [10.1109/IECON.2015.7392648](https://doi.org/10.1109/IECON.2015.7392648).
- [80] T. Guillod, F. Krismer, and J. W. Kolar, “Protection of MV Converters in the Grid: The Case of MV/LV Solid-State Transformers,” *IEEE J. Emerg. Sel. Topics Power Electron.*, vol. 5, no. 1, pp. 393–408, 2017, DOI: [10.1109/JESTPE.2016.2617620](https://doi.org/10.1109/JESTPE.2016.2617620).
- [81] V. Vorperian and S. Cuk, “A Complete DC Analysis of the Series Resonant Converter,” in *Proc. of the IEEE Power Electronics Specialists Conf. (PESC)*, Apr. 1982, DOI: [10.1109/PESC.1982.7072398](https://doi.org/10.1109/PESC.1982.7072398).
- [82] S. Zhao, Q. Li, F. C. Lee, and B. Li, “High-Frequency Transformer Design for Modular Power Conversion from Medium-Voltage AC to 400 V DC,” *IEEE Trans. Power Electron.*, vol. 33, no. 9, pp. 7545–7557, 2018, DOI: [10.1109/TPEL.2017.2774440](https://doi.org/10.1109/TPEL.2017.2774440).
- [83] L. Wang, Q. Zhu, W. Yu, and A. Q. Huang, “A Medium-Voltage Medium-Frequency Isolated DC-DC Converter Based on 15 kV SiC MOSFETs,” *IEEE J. Emerg. Sel. Topics Power Electron.*, vol. 5, no. 1, pp. 100–109, 2017, DOI: [10.1109/JESTPE.2016.2639381](https://doi.org/10.1109/JESTPE.2016.2639381).
- [84] L. Lindenmüller, R. Alvarez, and S. Bernet, “Optimization of a Series Resonant DC/DC Converter for Traction Applications,” in *Proc. of the IEEE Energy Conversion Congr. and Expo. (ECCE USA)*, Sep. 2012, DOI: [10.1109/ECCE.2012.6342442](https://doi.org/10.1109/ECCE.2012.6342442).
- [85] X. Li and A. K. S. Bhat, “Analysis and Design of High-Frequency Isolated Dual-Bridge Series Resonant DC/DC Converter,” *IEEE Trans. Power Electron.*, vol. 25, no. 4, pp. 850–862, 2010, DOI: [10.1109/TPEL.2009.2034662](https://doi.org/10.1109/TPEL.2009.2034662).
- [86] B. Yang, F. C. Lee, A. J. Zhang, and G. Huang, “LLC Resonant Converter for Front End DC/DC Conversion,” in *Proc. of the IEEE Applied Power Electronics Conf. and Expo. (APEC)*, Mar. 2002, DOI: [10.1109/APEC.2002.989382](https://doi.org/10.1109/APEC.2002.989382).

- [87] F. Dianbo, L. Ya, F. C. Lee, and X. Ming, "An Improved Novel Driving Scheme of Synchronous Rectifiers for LLC Resonant Converters," in *Proc. of the IEEE Applied Power Electronics Conf. and Expo. (APEC)*, Feb. 2008, DOI: [10.1109/APEC.2008.4522769](https://doi.org/10.1109/APEC.2008.4522769).
- [88] T. Guillod, D. Rothmund, and J. W. Kolar, "Active Magnetizing Current Splitting ZVS Modulation of a 7 kV/400 V DC Transformer," *IEEE Trans. Power Electron.* (early access), 2019, DOI: [10.1109/TPEL.2019.2918622](https://doi.org/10.1109/TPEL.2019.2918622).
- [89] J. E. Huber, J. Miniböck, and J. W. Kolar, "Generic Derivation of Dynamic Model for Half-Cycle DCM Series Resonant Converters," *IEEE Trans. Power Electron.*, vol. 33, no. 4-7, pp. 8063–8067, 2018, DOI: [10.1109/TPEL.2017.2703300](https://doi.org/10.1109/TPEL.2017.2703300).
- [90] D. Rothmund, J. E. Huber, and J. W. Kolar, "Operating Behavior and Design of the Half-Cycle Discontinuous-Conduction-Mode Series-Resonant-Converter with Small DC Link Capacitors," in *Proc. of the Workshop on Control and Modeling for Power Electronics (COMPEL)*, Jun. 2013, DOI: [10.1109/COMPEL.2013.6626447](https://doi.org/10.1109/COMPEL.2013.6626447).
- [91] R. Burkart, "Advanced Modeling and Multi-Objective Optimization of Power Electronic Converter Systems," Ph.D. dissertation, ETH Zürich, 2016.
- [92] A. Nabae, I. Takahashi, and H. Akagi, "A New Neutral-Point-Clamped PWM Inverter," *IEEE Trans. Ind. Appl.*, vol. 17, no. 5, pp. 518–523, 1981, DOI: [10.1109/TIA.1981.4503992](https://doi.org/10.1109/TIA.1981.4503992).
- [93] T. A. Meynard and H. Foch, "Multi-Level Conversion: High Voltage Choppers and Voltage-Source Inverters," in *Proc. of the IEEE Power Electronics Specialists Conf. (PESC)*, Jun. 1992, DOI: [10.1109/PESC.1992.254717](https://doi.org/10.1109/PESC.1992.254717).
- [94] F. Zhang, F. Z. Peng, and Z. Qian, "Study of the Multilevel Converters in DC-DC Applications," in *Proc. of the IEEE Power Electronics Specialists Conf. (PESC)*, Jun. 2004, DOI: [10.1109/PESC.2004.1355682](https://doi.org/10.1109/PESC.2004.1355682).
- [95] P. Cxyz, P. Papamanolis, F. Krismer, T. Guillod, and J. W. Kolar, "New 40 kV/300 kVA Quasi-2-Level Operated 5-Level Flying Capacitor SiC "Super-Switch" IPM," in *Proc. of the IEEE Energy Conversion Congr. and Expo. (ECCE Asia)*, May 2019.
- [96] L. F. Costa, G. Buticchi, and M. Liserre, "Quad-Active-Bridge DC-DC Converter as Cross-Link for Medium-Voltage Modular Inverters,"

- IEEE Trans. Ind. Appl.*, vol. 53, no. 2, pp. 1243–1253, 2017, DOI: [10.1109/TIA.2016.2633539](https://doi.org/10.1109/TIA.2016.2633539).
- [97] H. Krishnaswami and N. Mohan, “Three-Port Series-Resonant DC–DC Converter to Interface Renewable Energy Sources with Bidirectional Load and Energy Storage Ports,” *IEEE Trans. Power Electron.*, vol. 24, no. 10, pp. 2289–2297, 2009, DOI: [10.1109/TPEL.2009.2022756](https://doi.org/10.1109/TPEL.2009.2022756).
- [98] C. Meyer and R. W. De Doncker, “Design of a Three-Phase Series Resonant Converter for Offshore DC Grids,” in *Proc. of the IEEE Industry Applications Society Annual Meeting (IAS)*, Sep. 2007, DOI: [10.1109/07IAS.2007.40](https://doi.org/10.1109/07IAS.2007.40).
- [99] Q. Zhu, L. Wang, L. Zhang, and A. Q. Huang, “A 10 kV DC Transformer (DCX) Based on Current Fed SRC and 15 kV SiC MOSFETs,” in *Proc. of the IEEE Applied Power Electronics Conf. and Expo. (APEC)*, Mar. 2018, DOI: [10.1109/APEC.2018.8341001](https://doi.org/10.1109/APEC.2018.8341001).
- [100] W. McMurray, “Fast Response Stepped-Wave Switching Power Converter Circuit,” U.S. Patent 3 581 212, 1971 (filed 1969).
- [101] M. Steiner and H. Reinold, “Antriebssystem für ein Schienenfahrzeug und Ansteuerverfahren hierzu (in German),” German Patent 19 630 284, 1998 (filed 1996).
- [102] M. Steiner and H. Reinold, “Antriebsschaltung für ein Schienenfahrzeug (in German),” German Patent 19 827 872, 1999 (filed 1998).
- [103] J. E. Huber and J. W. Kolar, “Optimum Number of Cascaded Cells for High-Power Medium-Voltage Multilevel Converters,” in *Proc. of the IEEE Energy Conversion Congr. and Expo. (ECCE USA)*, Sep. 2013, DOI: [10.1109/ECCE.2013.6646723](https://doi.org/10.1109/ECCE.2013.6646723).
- [104] J. E. Huber and J. W. Kolar, “Optimum Number of Cascaded Cells for High-Power Medium-Voltage AC–DC Converters,” *IEEE J. Emerg. Sel. Topics Power Electron.*, vol. 5, no. 1, pp. 213–232, 2017, DOI: [10.1109/JESTPE.2016.2605702](https://doi.org/10.1109/JESTPE.2016.2605702).
- [105] T. Guillod, J. E. Huber, G. Ortiz, A. De, C. M. Franck, and J. W. Kolar, “Characterization of the Voltage and Electric Field Stresses in Multi-Cell Solid-State Transformers,” in *Proc. of the IEEE Energy Conversion Congr. and Expo. (ECCE USA)*, Sep. 2014, DOI: [10.1109/ECCE.2014.6954048](https://doi.org/10.1109/ECCE.2014.6954048).

- [106] J. Zhang, Z. Wang, and S. Shao, "A Three-Phase Modular Multilevel DC–DC Converter for Power Electronic Transformer Applications," *IEEE J. Emerg. Sel. Topics Power Electron.*, vol. 5, no. 1, pp. 140–150, 2017, DOI: [10.1109/JESTPE.2016.2609936](https://doi.org/10.1109/JESTPE.2016.2609936).
- [107] S. Kenzelmann, A. Rufer, D. Dujic, F. Canales, and Y. R. de Novaes, "Isolated DC/DC Structure Based on Modular Multilevel Converter," *IEEE Trans. Power Electron.*, vol. 30, no. 1, pp. 89–98, 2015, DOI: [10.1109/TPEL.2014.2305976](https://doi.org/10.1109/TPEL.2014.2305976).
- [108] J. B. Casady, V. Pala, D. J. Lichtenwalner, E. V. Brunt, B. Hull, G. Wang, J. Richmond, S. T. Allen, D. Grider, and J. W. Palmour, "New Generation 10 kV SiC Power MOSFET and Diodes for Industrial Applications," in *Proc. of the Int. Exhib. and Conf. for Power Electronics, Intelligent Motion, Renewable Energy and Energy Management (PCIM Europe)*, May 2015.
- [109] J. Wang, T. Zhao, J. Li, A. Q. Huang, R. Callanan, F. Husna, and A. Agarwal, "Characterization, Modeling, and Application of 10 kV SiC MOSFET," *IEEE Trans. Electron Devices*, vol. 55, no. 8, pp. 1798–1806, 2008, DOI: [10.1109/TED.2008.926650](https://doi.org/10.1109/TED.2008.926650).
- [110] J. W. Palmour, L. Cheng, V. Pala, E. V. Brunt, D. J. Lichtenwalner, G. Wang, J. Richmond, M. O'Loughlin, S. Ryu, S. T. Allen, A. A. Burk, and C. Scozzie, "Silicon Carbide Power MOSFETs: Break-through Performance from 900 V up to 15 kV," in *Proc. of the IEEE Int. Symp. on Power Semiconductor Devices and ICs (ISPSD)*, Jun. 2014, DOI: [10.1109/ISPSD.2014.6855980](https://doi.org/10.1109/ISPSD.2014.6855980).
- [111] D. Rothmund, D. Bortis, and J. W. Kolar, "Accurate Transient Calorimetric Measurement of Soft-Switching Losses of 10 kV SiC MOSFETs and Diodes," *IEEE Trans. Power Electron.*, vol. 33, no. 6, pp. 5240–5250, 2018, DOI: [10.1109/TPEL.2017.2729892](https://doi.org/10.1109/TPEL.2017.2729892).
- [112] D. Rothmund, D. Bortis, and J. W. Kolar, "Accurate Transient Calorimetric Measurement of Soft-Switching Losses of 10 kV SiC MOSFETs," in *Proc. of the IEEE Symp. on Power Electronics for Distributed Generation Systems (PEDG)*, Jun. 2016, DOI: [10.1109/PEDG.2016.7527030](https://doi.org/10.1109/PEDG.2016.7527030).
- [113] J. W. Kolar, D. Bortis, and D. Neumayr, "The Ideal Switch is Not Enough," in *Proc. of the IEEE Int. Symp. on Power Semiconductor Devices and ICs (ISPSD)*, Jun. 2016, DOI: [10.1109/ISPSD.2016.7520767](https://doi.org/10.1109/ISPSD.2016.7520767).

- [114] I. Villar, “Multiphysical Characterization of Medium-Frequency Power Electronic Transformers,” Ph.D. dissertation, EPFL, 2010.
- [115] M. Mogorovic and D. Dujic, “100 kW, 10 kHz Medium Frequency Transformer Design Optimization and Experimental Verification,” *IEEE Trans. Power Electron.*, vol. 34, no. 2, pp. 1696–1708, 2019, DOI: [10.1109/TPEL.2018.2835564](https://doi.org/10.1109/TPEL.2018.2835564).
- [116] I. Villar, L. Mir, I. Etxeberria-Otadui, J. Colmenero, X. Agirre, and T. Nieva, “Optimal Design and Experimental Validation of a Medium-Frequency 400 kVA Power Transformer for Railway Traction Applications,” in *Proc. of the IEEE Energy Conversion Congr. and Expo. (ECCE USA)*, Sep. 2012, DOI: [10.1109/ECCE.2012.6342754](https://doi.org/10.1109/ECCE.2012.6342754).
- [117] Z. Ouyang, O. C. Thomsen, and M. A. E. Andersen, “Optimal Design and Tradeoff Analysis of Planar Transformer in High-Power DC–DC Converters,” *IEEE Trans. Ind. Electron.*, vol. 59, no. 7, pp. 2800–2810, 2012, DOI: [10.1109/TIE.2010.2046005](https://doi.org/10.1109/TIE.2010.2046005).
- [118] G. Cerri, S. A. Kovyryalov, and V. M. Primiani, “Modelling of a Litz-Wire Planar Winding Geometry for an Accurate Reactance Evaluation,” *IET Science, Measurement & Technology*, vol. 4, no. 4, pp. 214–219, 2010, DOI: [10.1049/iet-smt.2009.0118](https://doi.org/10.1049/iet-smt.2009.0118).
- [119] C. Quinn, K. Rinne, T. O’Donnell, M. Duffy, and C. O. Mathuna, “A Review of Planar Magnetic Techniques and Technologies,” in *Proc. of the IEEE Applied Power Electronics Conf. and Expo. (APEC)*, Mar. 2001, DOI: [10.1109/APEC.2001.912514](https://doi.org/10.1109/APEC.2001.912514).
- [120] K. W. Klontz, D. M. Divan, and D. W. Novotny, “An Actively Cooled 120 kW Coaxial Winding Transformer for Fast Charging Electric Vehicles,” *IEEE Trans. Ind. Appl.*, vol. 31, no. 6, pp. 1257–1263, 1995, DOI: [10.1109/28.475695](https://doi.org/10.1109/28.475695).
- [121] S. Baek and S. Bhattacharya, “Analytical Modeling and Implementation of a Coaxially Wound Transformer with Integrated Filter Inductance for Isolated Soft-Switching DC–DC Converters,” *IEEE Trans. Ind. Electron.*, vol. 65, no. 3, pp. 2245–2255, 2018, DOI: [10.1109/TIE.2017.2740855](https://doi.org/10.1109/TIE.2017.2740855).
- [122] L. Heinemann, H. Reinold, and M. Steiner, “Transformator mit koaxialer Wicklungsanordnung (in German),” German Patent 19 717 554, 1998 (filed 1997).

- [123] H. Kleinrath, "Ersatzschaltbilder für Transformatoren und Asynchronmaschinen (in German)," *e&i*, vol. 110, no. 1, p. 68–74, 1993.
- [124] J. Mühlethaler, J. W. Kolar, and A. Ecklebe, "A Novel Approach for 3D Air Gap Reluctance Calculations," in *Proc. of the IEEE Energy Conversion Congr. and Expo. (ECCE Asia)*, May 2011, DOI: [10.1109/ICPE.2011.5944575](https://doi.org/10.1109/ICPE.2011.5944575).
- [125] T. Guillod, F. Krismer, and J. W. Kolar, "Magnetic Equivalent Circuit of MF Transformers: Modeling and Parameters Uncertainties," *Springer Electrical Engineering*, vol. 100, no. 4, pp. 2261–2275, 2018, DOI: [10.1007/s00202-018-0701-0](https://doi.org/10.1007/s00202-018-0701-0).
- [126] M. Mogorovic and D. Dujic, "Medium Frequency Transformer Leakage Inductance Modeling and Experimental Verification," in *Proc. of the IEEE Energy Conversion Congr. and Expo. (ECCE USA)*, Oct. 2017, DOI: [10.1109/ECCE.2017.8095813](https://doi.org/10.1109/ECCE.2017.8095813).
- [127] B. Cougo, A. Tüysüz, J. Mühlethaler, and J. W. Kolar, "Increase of Tape Wound Core Losses Due to Interlamination Short Circuits and Orthogonal Flux Components," in *Proc. of the IEEE Industrial Electronics Society Conf. (IECON)*, Nov. 2011, DOI: [10.1109/IECON.2011.6119508](https://doi.org/10.1109/IECON.2011.6119508).
- [128] K. Venkatachalam, C. R. Sullivan, T. Abdallah, and H. Tacca, "Accurate Prediction of Ferrite Core Loss with Nonsinusoidal Waveforms Using only Steinmetz Parameters," in *Proc. of the IEEE Workshop on Computers in Power Electronics (CIPE)*, Jun. 2002, DOI: [10.1109/CIPE.2002.1196712](https://doi.org/10.1109/CIPE.2002.1196712).
- [129] W. G. Hurley, E. Gath, and J. G. Breslin, "Optimizing the AC Resistance of Multilayer Transformer Windings with Arbitrary Current Waveforms," *IEEE Trans. Power Electron.*, vol. 15, no. 2, pp. 369–376, 2000, DOI: [10.1109/63.838110](https://doi.org/10.1109/63.838110).
- [130] Z. Ouyang, O. C. Thomsen, and M. A. E. Andersen, "The Analysis and Comparison of Leakage Inductance in Different Winding Arrangements for Planar Transformer," in *Proc. of the IEEE Conf. Power Electronics and Drive Systems (PEDS)*, Nov. 2009, DOI: [10.1109/PEDS.2009.5385844](https://doi.org/10.1109/PEDS.2009.5385844).
- [131] A. M. Urling, V. A. Niemela, G. R. Skutt, and T. G. Wilson, "Characterizing High-Frequency Effects in Transformer Windings - A Guide to Several Significant Articles," in *Proc. of the IEEE Applied Power Electronics Conf. and Expo. (APEC)*, Mar. 1989, DOI: [10.1109/APEC.1989.36989](https://doi.org/10.1109/APEC.1989.36989).

- [132] D. Leuenberger and J. Biela, "Accurate and Computationally Efficient Modeling of Flyback Transformer Parasitics and their Influence on Converter Losses," in *Proc. of the European Conf. on Power Electronics and Applications (EPE-ECCE Europe)*, Sep. 2015, DOI: [10.1109/EPE.2015.7309194](https://doi.org/10.1109/EPE.2015.7309194).
- [133] C. R. Sullivan and R. Y. Zhang, "Simplified Design Method for Litz Wire," in *Proc. of the IEEE Applied Power Electronics Conf. and Expo. (APEC)*, Mar. 2014, DOI: [10.1109/APEC.2014.6803681](https://doi.org/10.1109/APEC.2014.6803681).
- [134] N. Xi and C. R. Sullivan, "An Equivalent Complex Permeability Model for Litz-Wire Windings," *IEEE Trans. Ind. Appl.*, vol. 45, no. 2, pp. 854–860, 2009, DOI: [10.1109/IAS.2005.1518758](https://doi.org/10.1109/IAS.2005.1518758).
- [135] T. Guillod, J. Huber, F. Krismer, and J. W. Kolar, "Litz Wire Losses: Effects of Twisting Imperfections," in *Proc. of the Workshop on Control and Modeling for Power Electronics (COMPEL)*, Jul. 2017, DOI: [10.1109/COMPEL.2017.8013327](https://doi.org/10.1109/COMPEL.2017.8013327).
- [136] J. Mühlethaler and J. W. Kolar, "Optimal Design of Inductive Components Based on Accurate Loss and Thermal Models," in *Tutorial at the IEEE Applied Power Electronics Conf. and Expo. (APEC)*, Feb. 2012.
- [137] C. Gammeter, F. Krismer, and J. W. Kolar, "Comprehensive Conceptualization, Design, and Experimental Verification of a Weight-Optimized All-SiC 2 kV/700 V DAB for an Airborne Wind Turbine," *IEEE J. Emerg. Sel. Topics Power Electron.*, vol. 4, no. 2, pp. 638–656, 2016, DOI: [10.1109/JESTPE.2015.2459378](https://doi.org/10.1109/JESTPE.2015.2459378).
- [138] I. Villar, A. Garcia-Bediaga, U. Viscarret, I. Etxeberria-Otadui, and A. Rufer, "Proposal and Validation of Medium-Frequency Power Transformer Design Methodology," in *Proc. of the IEEE Energy Conversion Congr. and Expo. (ECCE USA)*, Sep. 2011, DOI: [10.1109/ECCE.2011.6064284](https://doi.org/10.1109/ECCE.2011.6064284).
- [139] M. Mogorovic and D. Dujic, "Thermal Modeling and Experimental Verification of an Air Cooled Medium Frequency Transformer," in *Proc. of the European Conf. Power Electronics and Applications (EPE-ECCE Europe)*, Sep. 2017, DOI: [10.23919/EPE17ECCEurope.2017.8099176](https://doi.org/10.23919/EPE17ECCEurope.2017.8099176).
- [140] S. Isler, T. Chaudhuri, D. Aguglia, and X. A. Bonnin, "Development of a 100 kW, 12.5 kV, 22 kHz and 30 kV Insulated Medium Frequency

- Transformer for Compact and Reliable Medium Voltage Power Conversion,” in *Proc. of the European Conf. Power Electronics and Applications (EPE-ECCE Europe)*, Sep. 2017, DOI: [10.23919/EPE17ECCEEurope.2017.8099196](https://doi.org/10.23919/EPE17ECCEEurope.2017.8099196).
- [141] S. B. Y. Du, G. Wang, and S. Bhattacharya, “Design Considerations of High Voltage and High Frequency Transformer for Solid State Transformer Application,” in *Proc. of the IEEE Industrial Electronics Society Conf. (IECON)*, Nov. 2010, DOI: [10.1109/IECON.2010.5674991](https://doi.org/10.1109/IECON.2010.5674991).
- [142] T. B. Gradinger, U. Drogenik, and S. Alvarez, “Novel Insulation Concept for a MV Dry-Cast Medium-Frequency Transformer,” in *Proc. of the European Conf. Power Electronics and Applications (EPE-ECCE Europe)*, Sep. 2017, DOI: [10.23919/EPE17ECCEEurope.2017.8099006](https://doi.org/10.23919/EPE17ECCEEurope.2017.8099006).
- [143] T. Guillod, F. Krismer, and J. W. Kolar, “Electrical Shielding of MV/MF Transformers Subjected to High dv/dt PWM Voltages,” in *Proc. of the IEEE Applied Power Electronics Conf. and Expo. (APEC)*, Mar. 2017, DOI: [10.1109/APEC.2017.7931050](https://doi.org/10.1109/APEC.2017.7931050).
- [144] R. Färber and C. M. Franck, “Modular High-Precision Dielectric Spectrometer for Quantifying the Aging Dynamics in (Sub-) Picofarad Polymeric Specimens,” *IEEE Trans. Dielectr. Electr. Insul.*, vol. 25, no. 3, pp. 1056–1063, 2018, DOI: [10.1109/TDEI.2018.006898](https://doi.org/10.1109/TDEI.2018.006898).
- [145] R. Färber and C. Franck, “Modular Arbitrary Waveform Dielectric Spectrometer for Aging Diagnostics of Recessed Specimens,” in *Proc. of the IEEE Electrical Insulation and Dielectric Phenomena (CEIDP)*, Oct. 2016, DOI: [10.1109/CEIDP.2016.7785614](https://doi.org/10.1109/CEIDP.2016.7785614).
- [146] M. Birle and C. Leu, “Breakdown of Polymer Dielectrics at High Direct and Alternating Voltages Superimposed by High Frequency High Voltages,” in *Proc. of the IEEE Conf. on Solid Dielectrics (ICSD)*, Jun. 2013, DOI: [10.1109/ICSD.2013.6619851](https://doi.org/10.1109/ICSD.2013.6619851).
- [147] K. Niayesh and E. Gockenbach, “On the Aging Mechanism of Solid Insulating Materials Exposed to Repetitive High Voltage Pulses,” *IEEE Trans. Dielectr. Electr. Insul.*, vol. 21, no. 1, pp. 304–310, 2014, DOI: [10.1109/TDEI.2013.004055](https://doi.org/10.1109/TDEI.2013.004055).
- [148] P. Wang, A. Cavallini, and G. Montanari, “The Influence of Repetitive Square Wave Voltage Parameters on Enameled Wire Endurance,” *IEEE*

- Trans. Dielectr. Electr. Insul.*, vol. 21, no. 3, pp. 1276–1284, 2014, DOI: [10.1109/TDEI.2014.6832275](https://doi.org/10.1109/TDEI.2014.6832275).
- [149] D. Konig, N. Hardt, and V. Scherb, “Comparative Insulation Tests with DC and AC at 50 Hz and 50 kHz,” in *Proc. of the IEEE Conf. on Electrical Insulation and Dielectric Phenomena (CEIDP)*, Oct. 1998, DOI: [10.1109/CEIDP.1998.732994](https://doi.org/10.1109/CEIDP.1998.732994).
- [150] R. Färber, T. Guillod, F. Krismer, J. W. Kolar, and C. M. Franck, “Endurance of Polymeric Insulation under Mixed-Frequency Medium-Voltage Stress,” *IEEE Trans. Dielectr. Electr. Insul.*, (under review), 2019.
- [151] B. Sonerud, T. Bengtsson, J. Blennow, and S. M. Gubanski, “Dielectric Heating in Insulating Materials Subjected to Voltage Waveforms with High Harmonic Content,” *IEEE Trans. Dielectr. Electr. Insul.*, vol. 16, no. 4, pp. 926–933, 2009, DOI: [10.1109/TDEI.2009.5211835](https://doi.org/10.1109/TDEI.2009.5211835).
- [152] L. Paulsson, B. Ekehov, S. Halen, T. Larsson, L. Palmqvist, A. A. Edris, D. Kidd, A. J. F. Keri, and B. Mehraban, “High-Frequency Impacts in a Converter-Based Back-to-Back Tie; The Eagle Pass Installation,” *IEEE Trans. Power Del.*, vol. 18, no. 4, pp. 1410–1415, 2003, DOI: [10.1109/TPWRD.2003.817724](https://doi.org/10.1109/TPWRD.2003.817724).
- [153] T. Guillod, R. Färber, F. Krismer, C. M. Franck, and J. W. Kolar, “Computation and Analysis of Dielectric Losses in MV Power Electronic Converter Insulation,” in *Proc. of the IEEE Energy Conversion Congr. and Expo. (ECCE USA)*, Sep. 2016, DOI: [10.1109/ECCE.2016.7854952](https://doi.org/10.1109/ECCE.2016.7854952).
- [154] T. Guillod, R. Färber, F. Krismer, C. M. Franck, and J. W. Kolar, “Dielectric Losses in Dry-Type Insulation of Medium-Voltage Power Electronic Converters,” *IEEE J. Emerg. Sel. Topics Power Electron.* (early access), 2019, DOI: [10.1109/JESTPE.2019.2914997](https://doi.org/10.1109/JESTPE.2019.2914997).
- [155] L. Dalessandro, F. da Silveira Cavalcante, and J. W. Kolar, “Self-Capacitance of High-Voltage Transformers,” *IEEE Trans. Power Electron.*, vol. 22, no. 5, pp. 2081–2092, 2007, DOI: [10.1109/TPEL.2007.904252](https://doi.org/10.1109/TPEL.2007.904252).
- [156] D. Rothmund, G. Ortiz, T. Guillod, and J. W. Kolar, “10 kV SiC-Based Isolated DC-DC Converter for Medium Voltage-Connected Solid-State Transformers,” in *Proc. of the IEEE Applied Power Electronics Conf. and Expo. (APEC)*, Mar. 2015, DOI: [10.1109/APEC.2015.7104485](https://doi.org/10.1109/APEC.2015.7104485).

- [157] D. Bortis, “20 MW Halbleiter-Leistungsmodulator-System (in German),” Ph.D. dissertation, ETH Zürich, 2008.
- [158] P. Wallmeier and H. Grotstollen, “Magnetic Shielding Applied to High-Frequency Inductors,” in *Proc. of the IEEE Industry Applications Society Annual Meeting (IAS)*, Oct. 1997, DOI: [10.1109/IAS.1997.629003](https://doi.org/10.1109/IAS.1997.629003).
- [159] A. Tripathi, K. Mainali, D. Patel, A. Kadavelugu, S. Hazra, S. Bhattacharya, and K. Hatua, “Design Considerations of a 15 kV SiC IGBT Enabled High-Frequency Isolated DC-DC Converter,” in *Proc. of the IEEE Energy Conversion Congr. and Expo. (ECCE Asia)*, May 2014, DOI: [10.1109/IPEC.2014.6869673](https://doi.org/10.1109/IPEC.2014.6869673).
- [160] S. Madhusoodhanan, A. Tripathi, D. Patel, K. Mainali, A. Kadavelugu, S. Hazra, S. Bhattacharya, and K. Hatua, “Solid-State Transformer and MV Grid Tie Applications Enabled by 15 kV SiC IGBTs and 10 kV SiC MOSFETs Based Multilevel Converters,” *IEEE Trans. Ind. Appl.*, vol. 51, no. 4, pp. 3343–3360, 2015, DOI: [10.1109/TIA.2015.2412096](https://doi.org/10.1109/TIA.2015.2412096).
- [161] A. K. Tripathi, K. Mainali, D. C. Patel, A. Kadavelugu, S. Hazra, S. Bhattacharya, and K. Hatua, “Design Considerations of a 15 kV SiC IGBT-Based Medium-Voltage High-Frequency Isolated DC-DC Converter,” *IEEE Trans. Ind. Appl.*, vol. 51, no. 4, pp. 3284–3294, 2015, DOI: [10.1109/TIA.2015.2394294](https://doi.org/10.1109/TIA.2015.2394294).
- [162] C. R. Paul, *Introduction to Electromagnetic Compatibility*. Wiley, 2006.
- [163] R. M. Burkart and J. W. Kolar, “Comparative η - ρ - σ Pareto Optimization of Si and SiC Multilevel Dual-Active-Bridge Topologies with Wide Input Voltage Range,” *IEEE Trans. Power Electron.*, vol. 32, no. 7, pp. 5258–5270, 2017, DOI: [10.1109/TPEL.2016.2614139](https://doi.org/10.1109/TPEL.2016.2614139).
- [164] P. Shuai and J. Biela, “Design and Optimization of Medium Frequency, Medium Voltage Transformers,” in *Proc. of the European Conf. Power Electronics and Applications (EPE-ECCE Europe)*, Sep. 2013, DOI: [10.1109/EPE.2013.6634423](https://doi.org/10.1109/EPE.2013.6634423).
- [165] A. Garcia-Bediaga, I. Villar, A. Rujas, L. Mir, and A. Rufer, “Multi-objective Optimization of Medium-Frequency Transformers for Isolated Soft-Switching Converters Using a Genetic Algorithm,” *IEEE Trans. Power Electron.*, vol. 32, no. 4, pp. 2995–3006, 2017, DOI: [10.1109/TPEL.2016.2574499](https://doi.org/10.1109/TPEL.2016.2574499).

- [166] M. A. Bahmani, T. Thiringer, and M. Kharezy, "Optimization and Experimental Validation of Medium-Frequency High Power Transformers in Solid-State Transformer Applications," in *Proc. of the IEEE Applied Power Electronics Conf. and Expo. (APEC)*, Mar. 2016, DOI: [10.1109/APEC.2016.7468297](https://doi.org/10.1109/APEC.2016.7468297).
- [167] M. Pavlovsky, S. W. H. de Haan, and J. A. Ferreira, "Reaching High Power Density in Multikilowatt DC–DC Converters with Galvanic Isolation," *IEEE Trans. Power Electron.*, vol. 24, no. 3, pp. 603–612, 2009, DOI: [10.1109/TPEL.2008.2008650](https://doi.org/10.1109/TPEL.2008.2008650).
- [168] A. Pereira, F. Sixdenier, M. A. Rault, B. Lefebvre, and N. Burais, "Comparison Between Numerical and Analytical Methods of AC Resistance Evaluation for Medium-Frequency Transformers: Validation on a Prototype and Thermal Impact Analysis," *Canadian J. Elect. Comput. Eng.*, vol. 40, no. 2, pp. 101–109, 2017, DOI: [10.1109/CJECE.2016.2594118](https://doi.org/10.1109/CJECE.2016.2594118).
- [169] Y. Du, S. Baek, S. Bhattacharya, and A. Q. Huang, "High-Voltage High-Frequency Transformer Design for a 7.2 kV to 120 V/240 V 20 kVA Solid State Transformer," in *Proc. of the IEEE Industrial Electronics Society Conf. (IECON)*, Nov. 2010, DOI: [10.1109/IECON.2010.5674828](https://doi.org/10.1109/IECON.2010.5674828).
- [170] M. Birle, "Beanspruchung von Polymeren durch höherfrequente Anteile einer Mischspannung (in German)," Ph.D. dissertation, TU Ilmenau, 2015.
- [171] J. E. Huber and J. W. Kolar, "Common-Mode Currents in Multi-Cell Solid-State Transformers," in *Proc. of the IEEE Energy Conversion Congr. and Expo. (ECCE Asia)*, May 2014, DOI: [10.1109/IPEC.2014.6869674](https://doi.org/10.1109/IPEC.2014.6869674).
- [172] M. Mogorovic and D. Dujic, "Sensitivity Analysis of Medium Frequency Transformer Design," in *Proc. of the IEEE Energy Conversion Congr. and Expo. (ECCE Asia)*, May 2018, DOI: [10.23919/IPEC.2018.8507855](https://doi.org/10.23919/IPEC.2018.8507855).
- [173] W. G. Odendaal and J. A. Ferreira, "Effects of Scaling High-Frequency Transformer Parameters," *IEEE Trans. Ind. Appl.*, vol. 35, no. 4, pp. 932–940, 1999, DOI: [10.1109/28.777203](https://doi.org/10.1109/28.777203).
- [174] L. M. R. Oliveira and A. J. M. Cardoso, "Leakage Inductances Calculation for Power Transformers Interturn Fault Studies," *IEEE Trans. Power Del.*, vol. 30, no. 3, pp. 1213–1220, 2015, DOI: [10.1109/TPWRD.2014.2371877](https://doi.org/10.1109/TPWRD.2014.2371877).

- [175] N. Dai and F. C. Lee, "Edge Effect Analysis in a High-Frequency Transformer," in *Proc. of the IEEE Power Electronics Specialists Conf. (PESC)*, Jun. 1994, DOI: [10.1109/pesc.1994.373778](https://doi.org/10.1109/pesc.1994.373778).
- [176] M. Meinhardt, M. Duffy, T. O'Donnell, S. O'Reilly, J. Flannery, and C. O. Mathuna, "New Method for Integration of Resonant Inductor and Transformer – Design, Realisation, Measurements," in *Proc. of the IEEE Applied Power Electronics Conf. and Expo. (APEC)*, Mar. 1999, DOI: [10.1109/APEC.1999.750516](https://doi.org/10.1109/APEC.1999.750516).
- [177] W. T. McLyman, *Transformer and Inductor Design Handbook*. CRC Press, 2004.
- [178] Z. Ouyang, J. Zhang, and W. G. Hurley, "Calculation of Leakage Inductance for High-Frequency Transformers," *IEEE Trans. Power Electron.*, vol. 30, no. 10, pp. 5769–5775, 2015, DOI: [10.1109/TPEL.2014.2382175](https://doi.org/10.1109/TPEL.2014.2382175).
- [179] R. Doebbelin, M. Benecke, and A. Lindemann, "Calculation of Leakage Inductance of Core-Type Transformers for Power Electronic Circuits," in *Proc. of the IEEE Int. Power Electronics and Motion Control Conf. (PEMC)*, Sep. 2008, DOI: [10.1109/EPEPEMC.2008.4635445](https://doi.org/10.1109/EPEPEMC.2008.4635445).
- [180] A. L. Morris, "The Influence of Various Factors Upon the Leakage Reactance of Transformers," *Journal of the Institution of Electrical Engineers*, vol. 86, no. 521, pp. 485–495, 1940, DOI: [10.1049/jiee-1.1940.0068](https://doi.org/10.1049/jiee-1.1940.0068).
- [181] R. Doebbelin, C. Teichert, M. Benecke, and A. Lindemann, "Computerized Calculation of Leakage Inductance Values of Transformers," *Piers Online*, vol. 5, no. 8, pp. 721–726, 2009.
- [182] J. Acero, R. Alonso, J. M. Burdio, L. A. Barragan, and D. Puyal, "Frequency-Dependent Resistance in Litz-Wire Planar Windings for Domestic Induction Heating Appliances," *IEEE Trans. Power Electron.*, vol. 21, no. 4, pp. 856–866, 2006, DOI: [10.1109/TPEL.2006.876894](https://doi.org/10.1109/TPEL.2006.876894).
- [183] R. Y. Zhang, J. K. White, J. G. Kassakian, and C. R. Sullivan, "Realistic Litz Wire Characterization Using Fast Numerical Simulations," in *Proc. of the IEEE Applied Power Electronics Conf. and Expo. (APEC)*, Mar. 2014, DOI: [10.1109/APEC.2014.6803390](https://doi.org/10.1109/APEC.2014.6803390).
- [184] D. C. Meeker, "An Improved Continuum Skin and Proximity Effect Model for Hexagonally Packed Wires," *Journal of Computational*

- and Applied Mathematics*, vol. 236, no. 18, pp. 4635–4644, 2012, DOI: [10.1016/j.cam.2012.04.009](https://doi.org/10.1016/j.cam.2012.04.009).
- [185] C. R. Sullivan, “Optimal Choice for Number of Strands in a Litz-Wire Transformer Winding,” *IEEE Trans. Power Electron.*, vol. 14, no. 2, pp. 283–291, 1999, DOI: [10.1109/63.750181](https://doi.org/10.1109/63.750181).
- [186] H. Rossmanith, M. Doebroenti, M. Albach, and D. Exner, “Measurement and Characterization of High Frequency Losses in Nonideal Litz Wires,” *IEEE Trans. Power Electron.*, vol. 26, no. 11, pp. 3386–3394, 2011, DOI: [10.1109/TPEL.2011.2143729](https://doi.org/10.1109/TPEL.2011.2143729).
- [187] R. Scapolan, “Modélisation Electromagnétique 3D d’Inducteurs Multibrins - Développement d’une Méthode Intégrale Parallélisée (in French),” Ph.D. dissertation, Université de Grenoble, 2014.
- [188] P. B. Reddy, T. M. Jahns, and T. P. Bohn, “Transposition Effects on Bundle Proximity Losses in High-Speed PM Machines,” in *Proc. of the IEEE Energy Conversion Congr. and Expo. (ECCE USA)*, Sep. 2009, DOI: [10.1109/ECCE.2009.5316037](https://doi.org/10.1109/ECCE.2009.5316037).
- [189] A. Roskopf, E. Baer, C. Joffe, and C. Bonse, “Calculation of Power Losses in Litz Wire Systems by Coupling FEM and PEEC Method,” *IEEE Trans. Power Electron.*, vol. 31, no. 9, pp. 6442–6449, 2016, DOI: [10.1109/TPEL.2015.2499793](https://doi.org/10.1109/TPEL.2015.2499793).
- [190] C. Hewson and W. R. Ray, “The Effect of Electrostatic Screening of Rogowski Coils Designed for Wide-Bandwidth Current Measurement in Power Electronic Applications,” in *Proc. of the IEEE Power Electronics Specialists Conf. (PESC)*, Jun. 2004, DOI: [10.1109/PESC.2004.1355583](https://doi.org/10.1109/PESC.2004.1355583).
- [191] N. Soltau, M. Kaymak, S. Cui, and R. W. De Doncker, “Materials, Devices and Components for Flexible Electrical Networks of the Future,” in *Proc. of the Int. ETG Congress*, Nov. 2015.
- [192] W. S. Zaengl, “Dielectric Spectroscopy in Time and Frequency Domain for HV Power Equipment I. Theoretical Considerations,” *IEEE Elect. Insul. Mag.*, vol. 19, no. 5, pp. 5–19, 2003, DOI: [10.1109/MEI.2003.1238713](https://doi.org/10.1109/MEI.2003.1238713).
- [193] R. Bartnikas, *Engineering Dielectrics: Measurement Techniques. Electrical Properties of Solid Insulating Materials*. ASTM, 1987.

- [194] G. AlLee and W. Tschudi, "Edison Redux: 380 V DC Brings Reliability and Efficiency to Sustainable Data Centers," *IEEE Power & Energy Mag.*, vol. 10, no. 6, pp. 50–59, 2012, DOI: [10.1109/MPE.2012.2212607](https://doi.org/10.1109/MPE.2012.2212607).
- [195] A. Pratt, P. Kumar, and T. V. Aldridge, "Evaluation of 400 V DC Distribution in Telco and Data Centers to Improve Energy Efficiency," in *Proc. of the IEEE Telecommunications Energy Conf. (INTELEC)*, Oct. 2007, DOI: [10.1109/INTELEC.2007.4448733](https://doi.org/10.1109/INTELEC.2007.4448733).
- [196] Y. Kashihara, Y. Nemoto, W. Qichen, S. Fujita, R. Yamada, and Y. Okuma, "An Isolated Medium-Voltage AC/DC Power Supply Based on Multi-Cell Converter Topology," in *Proc. of the IEEE Applied Power Electronics Conf. and Expo. (APEC)*, Mar. 2017, DOI: [10.1109/APEC.2017.7931002](https://doi.org/10.1109/APEC.2017.7931002).
- [197] D. Rothmund, T. Guillod, D. Bortis, and J. W. Kolar, "99.1 % Efficient 10 kV SiC-Based Medium Voltage ZVS Bidirectional Single-Phase PFC AC/DC Stage," *IEEE J. Emerg. Sel. Topics Power Electron.*, vol. 7, no. 2, pp. 779–797, 2019, DOI: [10.1109/JESTPE.2018.2886140](https://doi.org/10.1109/JESTPE.2018.2886140).
- [198] D. Rothmund, T. Guillod, D. Bortis, and J. W. Kolar, "99 % Efficient 10 kV SiC-Based 7 kV/400 V DC-Transformer for Future Data Centers," *IEEE J. Emerg. Sel. Topics Power Electron.*, vol. 7, no. 2, pp. 753–767, 2019, DOI: [10.1109/JESTPE.2018.2886139](https://doi.org/10.1109/JESTPE.2018.2886139).
- [199] D. Wang, C. Ren, A. Sivasubramaniam, B. Urgaonkar, and H. Fathy, "Energy Storage in Datacenters: What, Where, and How Much?" in *Proc. of the ACM SIGMETRICS/PERFORMANCE Joint Int. Conf. on Measurement and Modeling of Computer Systems*, Jun. 2012, DOI: [10.1145/2254756.2254780](https://doi.org/10.1145/2254756.2254780).
- [200] D. Rothmund, "10 kV SiC-Based Medium Voltage Solid-State Transformer Concepts for 400 V DC Distribution Systems," Ph.D. dissertation, ETH Zürich, 2018.
- [201] D. Rothmund, T. Guillod, D. Bortis, and J. W. Kolar, "Design and Experimental Analysis of a 10 kV SiC MOSFET Based 50 kHz Soft-Switching Single-Phase 3.8 kV AC/400 V DC Solid-State Transformer," in *Proc. of the IEEE Energy Conversion Congr. and Expo. (ECCE USA)*, Sep. 2018.
- [202] M. Kasper, R. M. Burkart, G. Deboy, and J. W. Kolar, "ZVS of Power MOSFETs Revisited," *IEEE Trans. Power Electron.*, vol. 31, no. 12, pp. 8063–8067, 2016, DOI: [10.1109/TPEL.2016.2574998](https://doi.org/10.1109/TPEL.2016.2574998).

- [203] H. Fan and H. Li, "High-Frequency Transformer Isolated Bidirectional DC-DC Converter Modules with High Efficiency Over Wide Load Range for 20 kVA Solid-State Transformer," *IEEE Trans. Power Electron.*, vol. 26, no. 12, pp. 3599–3608, 2011, DOI: [10.1109/TPEL.2011.2160652](https://doi.org/10.1109/TPEL.2011.2160652).
- [204] H. Fan and H. Li, "High Frequency High Efficiency Bidirectional DC-DC Converter Module Design for 10 kVA Solid State Transformer," in *Proc. of the IEEE Applied Power Electronics Conf. and Expo. (APEC)*, Feb. 2010, DOI: [10.1109/APEC.2010.5433670](https://doi.org/10.1109/APEC.2010.5433670).
- [205] M. Stojadinović and J. Biela, "Modelling and Design of a Medium Frequency Transformer for High Power DC-DC Converters," in *Proc. of the IEEE Energy Conversion Congr. and Expo. (ECCE Asia)*, May 2018, DOI: [10.23919/IPEC.2018.8507864](https://doi.org/10.23919/IPEC.2018.8507864).
- [206] U. Badstübner, J. Biela, and J. W. Kolar, "An Optimized, 99 % Efficient, 5 kW, Phase-Shift PWM DC-DC Converter for Data Centers and Telecom Applications," in *Proc. of the IEEE Energy Conversion Congr. and Expo. (ECCE Asia)*, Jun. 2010, DOI: [10.1109/IPEC.2010.5543337](https://doi.org/10.1109/IPEC.2010.5543337).
- [207] T. Yang, C. O'Loughlin, R. Meere, T. O'Donnell, N. Wang, and Z. Pavlovic, "Investigation of Modularity in DC-DC Converters for Solid State Transformers," in *Proc. of the IEEE Symp. on Power Electronics for Distributed Generation Systems (PEDG)*, Jun. 2014, DOI: [10.1109/PEDG.2014.6878694](https://doi.org/10.1109/PEDG.2014.6878694).
- [208] J. E. Huber, G. Ortiz, F. Krismer, N. Widmer, and J. W. Kolar, " η - ρ Pareto Optimization of Bidirectional Half-Cycle Discontinuous-Conduction-Mode Series-Resonant DC/DC Converter with Fixed Voltage Transfer Ratio," in *Proc. of the IEEE Applied Power Electronics Conf. and Expo. (APEC)*, Mar. 2013, DOI: [10.1109/APEC.2013.6520484](https://doi.org/10.1109/APEC.2013.6520484).
- [209] H. Akagi, S. Kinouchi, and Y. Miyazaki, "Bidirectional Isolated Dual-Active-Bridge (DAB) DC-DC Converters Using 1.2 kV 400 A SiC-MOSFET Dual Modules," *CPSS Trans. Power Electron. and Appl.*, vol. 1, no. 1, pp. 33–40, 2016, DOI: [10.24295/CPSSTPEA.2016.00004](https://doi.org/10.24295/CPSSTPEA.2016.00004).
- [210] M. Kasper, D. Bortis, G. Deboy, and J. W. Kolar, "Design of a Highly Efficient (97.7 %) and Very Compact (2.2 kW/dm³) Isolated AC-DC Telecom Power Supply Module Based on the Multicell ISOP Converter Approach," *IEEE Trans. Power Electron.*, vol. 32, no. 10, pp. 7750–7769, 2017, DOI: [10.1109/TPEL.2016.2633334](https://doi.org/10.1109/TPEL.2016.2633334).

-
- [211] R. Ramachandran and M. Nymand, “A 98.8 % Efficient Bidirectional Full-Bridge Isolated DC-DC GaN Converter,” in *Proc. of the IEEE Applied Power Electronics Conf. and Expo. (APEC)*, Mar. 2016, DOI: [10.1109/APEC.2016.7467934](https://doi.org/10.1109/APEC.2016.7467934).
- [212] R. Ramachandran and M. Nymand, “Experimental Demonstration of a 98.8 % Efficient Isolated DC-DC GaN Converter,” *IEEE Trans. Ind. Electron.*, vol. 64, no. 11, pp. 9104–9113, 2017, DOI: [10.1109/TIE.2016.2613930](https://doi.org/10.1109/TIE.2016.2613930).
- [213] H. Akagi, “A Bidirectional Isolated DAB DC-DC Converter Using 1.2 kV 400 A SiC-MOSFET Modules Without SBD,” in *Proc. of the IEEE Energy Conversion Congr. and Expo. (ECCE USA)*, Sep. 2018.
- [214] “Verteiltransformatoren (in German),” Deutsches Kupferinstitut, Feb. 2007.
- [215] ThyssenKrupp, “Grain Oriented Electrical Steel Powercore,” May 2017.
- [216] TDK, “SIFERRIT Material N97,” May 2017.
- [217] Vacuumschmelze, “VITROPERM 500F / VITROVAC 6030F,” Apr. 2003.
- [218] TDK, “SIFERRIT Material N27,” May 2017.
- [219] TDK, “SIFERRIT Material N49,” May 2017.
- [220] TDK, “SIFERRIT Material N87,” Sep. 2017.
- [221] TDK, “SIFERRIT Material N95,” May 2017.
- [222] A. Quarteroni and F. Saleri, *Scientific Computing with MATLAB*. Springer, Berlin, Heidelberg, 2004.
- [223] MathWorks, “Global Optimization Toolbox - User’s Guide,” Mar. 2019.
- [224] J. Yang, W. Peng, M. O. Ward, and E. A. Rundensteiner, “Interactive Hierarchical Dimension Ordering, Spacing and Filtering for Exploration of High Dimensional Datasets,” in *Proc. of the IEEE Conf. on Information Visualization. (INFOVIS)*, Oct. 2003, DOI: [10.1109/INFVIS.2003.1249015](https://doi.org/10.1109/INFVIS.2003.1249015).
- [225] A. Van den Bossche, V. C. Valchev, and R. Filchev, “Improved Approximation for Fringing Permeances in Gapped Inductors,” in *Proc. of the IEEE Industry Applications Society Annual Meeting (IAS)*, Oct. 2002, DOI: [10.1109/IAS.2002.1042670](https://doi.org/10.1109/IAS.2002.1042670).

- [226] M. Eslamian and B. Vahidi, “New Methods for Computation of the Inductance Matrix of Transformer Windings for Very Fast Transients Studies,” *IEEE Trans. Power Del.*, vol. 27, no. 4, pp. 2326–2333, 2012, DOI: [10.1109/TPWRD.2012.2204905](https://doi.org/10.1109/TPWRD.2012.2204905).
- [227] M. Lambert, F. Sirois, M. Martinez-Duro, and J. Mahseredjian, “Analytical Calculation of Leakage Inductance for Low-Frequency Transformer Modeling,” *IEEE Trans. Power Del.*, vol. 28, no. 1, pp. 507–515, 2013, DOI: [10.1109/TPWRD.2012.2225451](https://doi.org/10.1109/TPWRD.2012.2225451).
- [228] COMSOL, “COMSOL Multiphysics 5.1 - Reference Manual,” Apr. 2015.
- [229] K. J. Binns and P. J. Lawrenson, *Analysis and Computation of Electric and Magnetic Field Problems*. Elsevier, 1973.
- [230] G. Skutt, F. C. Lee, R. Ridley, and D. Nicol, “Leakage Inductance and Termination Effects in a High-Power Planar Magnetic Structure,” in *Proc. of the IEEE Applied Power Electronics Conf. and Expo. (APEC)*, Feb. 1994, DOI: [10.1109/APEC.1994.316385](https://doi.org/10.1109/APEC.1994.316385).
- [231] I. J. Bahl, *Lumped Elements for RF and Microwave Circuits*. Artech House, 2003.
- [232] S. S. Rao, *The Finite Element Method in Engineering*. Elsevier, 2011.
- [233] I. M. Sobol, *A Primer for the Monte Carlo Method*. CRC Press, 1994.
- [234] F. Scholz, “Tolerance Stack Analysis Methods,” Boeing, Dec. 1995.
- [235] L. C. Andrews, *Special Functions of Mathematics for Engineers*. SPIE Optical Engineering Press, 1997.
- [236] Agilent Technologies, “Agilent 4294A Precision Impedance Analyzer, Operation Manual,” Feb. 2003.
- [237] ed-k, “Power Choke Tester DPG10 – Series,” Jul. 2014.
- [238] J. G. Hayes, N. O’Donovan, M. G. Egan, and T. O’Donnell, “Inductance Characterization of High-Leakage Transformers,” in *Proc. of the IEEE Applied Power Electronics Conf. and Expo. (APEC)*, Feb. 2003, DOI: [10.1109/APEC.2003.1179361](https://doi.org/10.1109/APEC.2003.1179361).
- [239] omicron lab, “Bode 100, User Manual,” Jul. 2010.
- [240] omicron lab, “B-WIC & B-SMC, Impedance Test Adapters,” Feb. 2014.

- [241] A. Rosskopf, "Calculation of Frequency Dependent Power Losses in Inductive Systems with Litz Wire Conductors by a Coupled Numeric Approach," Ph.D. dissertation, Universität Erlangen-Nürnberg, 2018.
- [242] A. Rosskopf, E. Bar, and C. Joffe, "Influence of Inner Skin- and Proximity Effects on Conduction in Litz Wires," *IEEE Trans. Power Electron.*, vol. 29, no. 10, pp. 5454–5461, 2014, DOI: [10.1109/TPEL.2013.2293847](https://doi.org/10.1109/TPEL.2013.2293847).
- [243] X. Tang and C. R. Sullivan, "Stranded Wire with Uninsulated Strands as a Low-Cost Alternative to Litz Wire," in *Proc. of the IEEE Power Electronics Specialist Conf. (PESC)*, Jun. 2003, DOI: [10.1109/PESC.2003.1218308](https://doi.org/10.1109/PESC.2003.1218308).
- [244] C. R. Sullivan and R. Y. Zhang, "Analytical Model for Effects of Twisting on Litz-Wire Losses," in *Proc. of the IEEE Control and Modeling for Power Electronics Conf. (COMPEL)*, Jun. 2014, DOI: [10.1109/COMPEL.2014.6877187](https://doi.org/10.1109/COMPEL.2014.6877187).
- [245] M. Leibl, O. Knecht, and J. W. Kolar, "Inductive Power Transfer Efficiency Limit of a Flat Half-Filled Disc Coil Pair," *IEEE Trans. Power Electron.*, vol. 33, no. 11, pp. 9154–9162, 2018, DOI: [10.1109/TPEL.2018.2797366](https://doi.org/10.1109/TPEL.2018.2797366).
- [246] A. E. Ruehli, G. Antonini, and L. Jiang, *Circuit Oriented Electromagnetic Modeling Using the PEEC Techniques*. Wiley, 2017.
- [247] B. A. Reese and C. R. Sullivan, "Litz Wire in the MHz Range: Modeling and Improved Designs," in *Proc. of the IEEE Control and Modeling for Power Electronics Conf. (COMPEL)*, Jul. 2017, DOI: [10.1109/COMPEL.2017.8013391](https://doi.org/10.1109/COMPEL.2017.8013391).
- [248] A. E. Ruehli, "Partial Element Equivalent Circuit (PEEC) Method and its Application in the Frequency and Time Domain," in *Proc. of the IEEE Symposium on Electromagnetic Compatibility (ISEMC)*, Aug. 1996, DOI: [10.1109/ISEMC.1996.561214](https://doi.org/10.1109/ISEMC.1996.561214).
- [249] A. E. Ruehli, "Equivalent Circuit Models for Three-Dimensional Multi-conductor Systems," *IEEE Trans. Microw. Theory Tech.*, vol. 22, no. 3, pp. 216–221, 1974, DOI: [10.1109/TMTT.1974.1128204](https://doi.org/10.1109/TMTT.1974.1128204).
- [250] I. Kovačević-Badstübner, R. Burkart, C. Dittli, J. W. Kolar, and A. Müsing, "A Fast Method for the Calculation of Foil Winding Losses," in *Proc. of the European Conf. Power Electronics and Applications (EPE-ECCE Europe)*, Sep. 2015, DOI: [10.1109/EPE.2015.7309151](https://doi.org/10.1109/EPE.2015.7309151).

- [251] New England Wire Technologies, “Litz & Winding Wires,” Nov. 2009.
- [252] Yokogawa, “WT3000 Precision Power Analyzer, User’s Manual,” Feb. 2014.
- [253] W. Shen, F. Wang, D. Boroyevich, and C. W. Tipton, “Loss Characterization and Calculation of Nanocrystalline Cores for High-Frequency Magnetics Applications,” *IEEE Trans. Power Electron.*, vol. 23, no. 1, pp. 475–484, 2008, DOI: [10.1109/TPEL.2007.911881](https://doi.org/10.1109/TPEL.2007.911881).
- [254] G. Calderon-Lopez, Y. Wang, and A. J. Forsyth, “Mitigation of Gap Losses in Nanocrystalline Tape-Wound Cores,” *IEEE Trans. Power Electron.*, vol. 34, no. 5, pp. 4656–4664, 2019, DOI: [10.1109/TPEL.2018.2863665](https://doi.org/10.1109/TPEL.2018.2863665).
- [255] J. Szynowski, R. Kolano, A. Kolano-Burian, and M. Polak, “Reduction of Power Losses in the Tape-Wound FeNiCuNbSiB Nanocrystalline Cores Using Interlaminar Insulation,” *IEEE Trans. Magn.*, vol. 50, no. 4, pp. 1–4, 2014, DOI: [10.1109/TMAG.2013.2285406](https://doi.org/10.1109/TMAG.2013.2285406).
- [256] BLINZINGER, “Ferrite Core U93/76/20,” Oct. 2014.
- [257] J. W. Kolar, F. Krismer, Y. Lobsiger, J. Mühlethaler, T. Nussbaumer, and J. Miniböck, “Extreme Efficiency Power Electronics,” in *Proc. of the IEEE Int. Conf. on Integrated Power Electronics Systems (CIPS)*, Mar. 2012.
- [258] *Industrial, Scientific and Medical Equipment - Radio-Frequency Disturbance Characteristics - Limits and Methods of Measurement*, IEC Std. CISPR 11, Jun. 2015.
- [259] F. G. Brockman, P. H. Dowling, and W. G. Steneck, “Dimensional Effects Resulting from a High Dielectric Constant Found in a Ferromagnetic Ferrite,” *Phys. Rev.*, vol. 77, pp. 85–93, 1950, DOI: [10.1103/PhysRev.77.85](https://doi.org/10.1103/PhysRev.77.85).
- [260] G. R. Skutt, “High-Frequency Dimensional Effects in Ferrite-Core Magnetic Devices,” Ph.D. dissertation, Virginia Polytechnic Institute and State University, 1996.
- [261] MG Chemicals, “Silver Conductive Epoxy Adhesive 8331,” Mar. 2016.
- [262] NMB, “NMB 11925SA,” May 2018.
- [263] Stratasys, “PC (Polycarbonate) for Fortus 3D Production Systems,” Aug. 2015.

- [264] vonRoll, “Winding Wires and Litz Wires,” Sep. 2018.
- [265] Vishay, “Vishay NTCS0805E3,” Jul. 2017.
- [266] PACK Feindrähte, “RUPALIT Hochfrequenzlitzten (in German),” Oct. 2018.
- [267] RS Pro, “MSS08/011, Formex GK-30,” Sep. 2018.
- [268] Dow Corning, “TC4605 HLV, Thermally Conductive Encapsulant,” Feb. 2015.
- [269] *Information Technology Equipment - Safety - General Requirements*, IEC Std. 60 950-1, Jun. 2015.
- [270] D. Fabiani, G. C. Montanari, and A. Contin, “Aging Acceleration of Insulating Materials for Electrical Machine Windings Supplied by PWM in the Presence and in the Absence of Partial Discharges,” in *Proc. of the IEEE Conf. on Solid Dielectrics (ICSD)*, Jun. 2001, DOI: [10.1109/ICSD.2001.955625](https://doi.org/10.1109/ICSD.2001.955625).
- [271] J. Carr, Z. Wang, S. Bhattacharya, and D. Patel, “Transient Overvoltage Rating and BIL of the Transformerless Intelligent Power Substation,” in *Proc. of the IEEE Power and Energy Society General Meeting (PESMG)*, Jul. 2013, pp. 1–5, DOI: [10.1109/PESMG.2013.6672424](https://doi.org/10.1109/PESMG.2013.6672424).
- [272] *Power Transformers – Insulation Levels, Dielectric Tests and External Clearances in Air*, IEC Std. 60 076-3, Jul. 2013.
- [273] *Safety Requirements for Power Electronic Converter Systems and Equipment – Power Electronic Converters from 1000 V AC or 1500 V DC up to 36 kV AC or 54 kV DC*, IEC Std. 62 477-2, Jun. 2018.
- [274] Quantum Silicones, “Addition Cure Silicones Guide: Identifying Chemicals that Cause Inhibition,” Aug. 2014.
- [275] Loctite, “Loctite 3090,” Sep. 2012.
- [276] M. Popov, L. Van der Sluis, G. C. Paap, and H. De Herdt, “Computation of Very Fast Transient Overvoltages in Transformer Windings,” *IEEE Trans. Power Del.*, vol. 18, no. 4, pp. 1268–1274, 2003, DOI: [10.1109/TPWRD.2003.817738](https://doi.org/10.1109/TPWRD.2003.817738).
- [277] Megger, “MIT400 Series - Insulation and Continuity Testers,” Jun. 2006.

- [278] Megger, “A Guide to Diagnostic Insulation Testing Above 1kV,” Oct. 2002.
- [279] *IEEE Recommended Practice for Testing Insulation Resistance of Electric Machinery*, IEEE Std. 43-2013, Mar. 2014.
- [280] *High-Voltage Test Techniques – Partial Discharge Measurements*, IEC Std. 60 270, Dec. 2000.
- [281] D. A. Nattrass, “Partial Discharge Measurement and Interpretation,” *IEEE Elect. Insul. Mag.*, vol. 4, no. 3, pp. 10–23, 1988, DOI: [10.1109/57.830](https://doi.org/10.1109/57.830).
- [282] J. Jiang, M. Zhao, C. Zhang, M. Chen, H. Liu, and R. Albarracín, “Partial Discharge Analysis in High-Frequency Transformer Based on High-Frequency Current Transducer,” *Energies*, vol. 11, no. 8, p. 1997, 2018, DOI: [10.3390/en11081997](https://doi.org/10.3390/en11081997).
- [283] P. Wang, G. C. Montanari, and A. Cavallini, “Partial Discharge Phenomenology and Induced Aging Behavior in Rotating Machines Controlled by Power Electronics,” *IEEE Trans. Ind. Electron.*, vol. 61, no. 12, pp. 7105–7112, 2014, DOI: [10.1109/TIE.2014.2320226](https://doi.org/10.1109/TIE.2014.2320226).
- [284] B. W. Hoff, S. S. Maestas, S. C. Hayden, D. J. Harrigan, R. O. Grudt, M. L. Ostraat, J. C. Horwath, and S. Leontsev, “Dielectric Strength Heterogeneity Associated with Printing Orientation in Additively Manufactured Polymer Materials,” *Additive Manufacturing*, vol. 22, no. 1, pp. 21–30, 2018, DOI: [10.1016/j.dib.2018.07.070](https://doi.org/10.1016/j.dib.2018.07.070).
- [285] A. Küchler, *Hochspannungstechnik: Grundlagen – Technologie - Anwendungen (in German)*. Springer, Berlin, Heidelberg, 2009.
- [286] M. Aguet and M. Ianoz, *Haute Tension (in French)*. Presses Polytechniques et Universitaires Romandes, 2001.
- [287] R. Eichhorn, *Engineering Dielectrics: Electrical Properties of Solid Insulating Materials: Molecular Structure and Electrical Behavior*. ASTM, 1983.
- [288] A. Christe, E. Coulinge, and D. Dujic, “Insulation Coordination for a Modular Multilevel Converter Prototype,” in *Proc. of the European Conf. Power Electronics and Applications (EPE-ECCE Europe)*, Sep. 2016, DOI: [10.1109/EPE.2016.7695527](https://doi.org/10.1109/EPE.2016.7695527).
- [289] Wima, “Wima FKP 1,” Jan. 2019.

- [290] D. Christen, U. Badstübner, J. Biela, and J. W. Kolar, “Calorimetric Power Loss Measurement for Highly Efficient Converters,” in *Proc. of the IEEE Energy Conversion Congr. and Expo. (ECCE Asia)*, Jun. 2010, DOI: [10.1109/IPEC.2010.5544503](https://doi.org/10.1109/IPEC.2010.5544503).
- [291] Enertronics, “Precise Calorimetric Power Loss Measurement Setup,” May 2013.
- [292] M. Mu, “High Frequency Magnetic Core Loss Study,” Ph.D. dissertation, Virginia Polytechnic Institute and State University, 2013.
- [293] M. Mu, Q. Li, D. J. Gilham, F. C. Lee, and K. D. T. Ngo, “New Core Loss Measurement Method for High-Frequency Magnetic Materials,” *IEEE Trans. Power Electron.*, vol. 29, no. 8, pp. 4374–4381, 2014, DOI: [10.1109/TPEL.2013.2286830](https://doi.org/10.1109/TPEL.2013.2286830).
- [294] ZES Zimmer, “LMG671 - Precision Power Analyzer,” Feb. 2019.
- [295] ZES Zimmer, “HST - Wideband Precision High Voltage Divider,” Jul. 2012.
- [296] D. Rothmund, D. Bortis, and J. W. Kolar, “Highly Compact Isolated Gate Driver with Ultrafast Overcurrent Protection for 10 kV SiC MOSFETs,” *CPSS Trans. Power Electron. and Appl.*, vol. 3, no. 4, pp. 278–291, 2018, DOI: [10.24295/CPSSTPEA.2018.00028](https://doi.org/10.24295/CPSSTPEA.2018.00028).
- [297] A. Roberts, “Stress Grading for High Voltage Motor and Generator Coils,” *IEEE Elect. Insul. Mag.*, vol. 11, no. 4, pp. 26–31, 1995, DOI: [10.1109/57.400761](https://doi.org/10.1109/57.400761).
- [298] Hitachi Metals, “FINEMET, Nanocrystalline Soft Magnetic Material,” Apr. 2016.
- [299] H. R. Carlon, *Electrical Properties of Atmospheric Moist Air: A Systematic Experimental Study*. U.S. Army Munitions Chemical Command, 1988.
- [300] J. D. Menczel and R. B. Prime, *Thermal Analysis of Polymers: Fundamentals and Applications*. John Wiley & Sons, 2014.
- [301] C. Johansson and M. Robertsson, “Broadband Dielectric Characterization of a Silicone Elastomer,” *Journal of Electronic Materials*, vol. 36, no. 9, pp. 1206–1210, 2007, DOI: [10.1007/s11664-007-0124-6](https://doi.org/10.1007/s11664-007-0124-6).

- [302] M. Sato, A. Kumada, K. Hidaka, K. Yamashiro, Y. Hayase, and T. Takano, “Dynamic Potential Distributions of Surface Discharge in Silicone Gel,” *IEEE Trans. Dielectr. Electr. Insul.*, vol. 22, no. 3, pp. 1733–1738, 2015, DOI: [10.1109/TDEI.2015.7116371](https://doi.org/10.1109/TDEI.2015.7116371).
- [303] R. Steiner, P. K. Steimer, F. Krismer, and J. W. Kolar, “Contactless Energy Transmission for an Isolated 100 W Gate Driver Supply of a Medium Voltage Converter,” in *Proc. of the IEEE Industrial Electronics Society Conf. (IECON)*, Nov. 2009, DOI: [10.1109/IECON.2009.5414939](https://doi.org/10.1109/IECON.2009.5414939).
- [304] F. P. Espino-Cortes, E. A. Cherney, and S. H. Jayaram, “Impact of Inverter Drives Employing Fast-Switching Devices on Form-Wound AC Machine Stator Coil Stress Grading,” *IEEE Elect. Insul. Mag.*, vol. 23, no. 1, pp. 16–28, 2007, DOI: [10.1109/MEI.2007.288451](https://doi.org/10.1109/MEI.2007.288451).
- [305] M. Farahani, H. Borsi, E. Gockenbach, and M. Kaufhold, “Partial Discharge and Dissipation Factor Behavior of Model Insulating Systems for High Voltage Rotating Machines under Different Stresses,” *IEEE Elect. Insul. Mag.*, vol. 21, no. 5, pp. 5–19, 2005, DOI: [10.1109/MEI.2005.1513425](https://doi.org/10.1109/MEI.2005.1513425).
- [306] F. Lü, D. Li, Y. Guo, C. Fu, and H. Wang, “Optimal Design of Compact Main Insulation Structure of PETT,” in *Proc. of the Electrical Machines and Systems Conf. (ICEMS)*, Oct. 2015, DOI: [10.1109/ICEMS.2015.7385047](https://doi.org/10.1109/ICEMS.2015.7385047).
- [307] C. Zachariades, S. M. Rowland, I. Cotton, V. Peesapati, and D. Chambers, “Development of Electric-Field Stress Control Devices for a 132 kV Insulating Cross-Arm Using Finite-Element Analysis,” *IEEE Trans. Power Del.*, vol. 31, no. 5, pp. 2105–2113, 2016, DOI: [10.1109/TPWRD.2015.2499795](https://doi.org/10.1109/TPWRD.2015.2499795).
- [308] T. Bengtsson, F. Dijkhuizen, L. Ming, F. Sahlen, L. Liljestränd, D. Bormann, R. Papazyan, and M. Dahlgren, “Repetitive Fast Voltage Stresses – Causes and Effects,” *IEEE Elect. Insul. Mag.*, vol. 25, no. 4, pp. 26–39, 2009, DOI: [10.1109/MEI.2009.5191414](https://doi.org/10.1109/MEI.2009.5191414).
- [309] *Standard Test Methods for DC Resistance or Conductance of Insulating Materials*, ASTM Std. D257, Jun. 2007.
- [310] M. H. Holmes, *Introduction to Perturbation Methods*. Springer, New York, 2012.
- [311] Kontakt Chemie, “GRAPHIT 33, Technical Data Sheet,” Jun. 2013.

- [312] J. Jagers and S. Tenbohlen, "Evaluation of Transformer Reliability Data Based on National and Utility Statistics," in *Proc. of the Int. Symp. on High Voltage Engineering (ISH)*, Aug. 2009.
- [313] M. Neubert, A. Gorodnichev, J. Gottschlich, and R. W. De Doncker, "Performance Analysis of a Triple-Active Bridge Converter for Interconnection of Future DC-Grids," in *Proc. of the IEEE Energy Conversion Congr. and Expo. (ECCE USA)*, Sep. 2016, DOI: [10.1109/ECCE.2016.7855337](https://doi.org/10.1109/ECCE.2016.7855337).
- [314] W. Liang, L. Raymond, L. Gu, and J. Rivas, "27.12 MHz GaN Resonant Power Converter with PCB Embedded Resonant Air Core Inductors and Capacitors," in *Proc. of the IEEE Energy Conversion Congr. and Expo. (ECCE USA)*, Sep. 2015, DOI: [10.1109/ECCE.2015.7310260](https://doi.org/10.1109/ECCE.2015.7310260).
- [315] J. Choi, D. Tsukiyama, Y. Tsuruda, and J. Rivas, "13.56 MHz 1.3 kW Resonant Converter with GaN FET for Wireless Power Transfer," in *Proc. of the IEEE Wireless Power Transfer Conf. (WPTC)*, May 2015, DOI: [10.1109/WPT.2015.7140167](https://doi.org/10.1109/WPT.2015.7140167).
- [316] K. C. Kao, *Dielectric Phenomena in Solids*. Academic Press, 2004.
- [317] C. J. F. Böttcher and P. Bordewijk, *Theory of Electric Polarization, Dielectrics in Time-Dependent Fields, Vol. II*. Elsevier, 1978.
- [318] W. B. Westphal and A. Sils, *Dielectric Constant and Loss Data*. Air Force Materials Laboratory, Air Force Systems Command, 1972.
- [319] W. Wasylkiwskyj, *Signals and Transforms in Linear Systems Analysis*. Springer, New York, 2013.
- [320] A. K. Jonscher, "Dielectric Loss under Transient Excitation," *Journal of Physics C: Solid State Physics*, vol. 11, no. 14, pp. 601–606, 1978, DOI: [10.1088/0022-3719/11/14/009](https://doi.org/10.1088/0022-3719/11/14/009).
- [321] G. H. Hardy and E. M. Wright, *An Introduction to the Theory of Numbers*. Oxford University Press, 1979, Ch. 18.
- [322] Novocontrol Technologies, "Alpha-A, Technical Specification," Mar. 2010.
- [323] von Roll, "Damisol 3418 API," Nov. 2013.
- [324] F. Kremer and A. Schönhal, *Broadband Dielectric Spectroscopy*. Springer, Berlin, Heidelberg, 2012.

- [325] A. Wichmann, “Two Decades of Experience and Progress in Epoxy Mica Insulation Systems for Large Rotating Machines,” *IEEE Trans. Power App. Syst.*, vol. 102, no. 1, pp. 74–82, 1983, DOI: [10.1109/TPAS.1983.318000](https://doi.org/10.1109/TPAS.1983.318000).
- [326] B. Hofmann, “Distribution Transformers and EMC,” Siemens, Nov. 2012.
- [327] IET Labs, “Primary Standard Capacitors, 1404 Series,” Oct. 2013.
- [328] C. Neusel, H. Jelitto, D. Schmidt, R. Janssen, F. Felten, and G. A. Schneider, “Thickness-Dependence of the Breakdown Strength: Analysis of the Dielectric and Mechanical Failure,” *Journal of the European Ceramic Society*, vol. 35, no. 1, pp. 113–123, 2015, DOI: [10.1016/j.jeurceram-soc.2014.08.028](https://doi.org/10.1016/j.jeurceram-soc.2014.08.028).
- [329] J. Jung, H. Kim, M. Ryu, and J. Baek, “Design Methodology of Bidirectional CLLC Resonant Converter for High-Frequency Isolation of DC Distribution Systems,” *IEEE Trans. Power Electron.*, vol. 28, no. 4, pp. 1741–1755, 2013, DOI: [10.1109/TPEL.2012.2213346](https://doi.org/10.1109/TPEL.2012.2213346).
- [330] R. Elferich, “General ZVS Half Bridge Model Regarding Nonlinear Capacitances and Application to LLC Design,” in *Proc. of the IEEE Energy Conversion Congr. and Expo. (ECCE USA)*, Sep. 2012, DOI: [10.1109/ECCE.2012.6342223](https://doi.org/10.1109/ECCE.2012.6342223).
- [331] D. Fu, S. Wan, P. Kong, F. C. Lee, and D. Huang, “Novel Techniques to Suppress the Common-Mode EMI Noise Caused by Transformer Parasitic Capacitances in DC–DC Converters,” *IEEE Trans. Ind. Electron.*, vol. 60, no. 11, pp. 4968–4977, 2013, DOI: [10.1109/TIE.2012.2224071](https://doi.org/10.1109/TIE.2012.2224071).
- [332] T. Jiang, J. Zhang, X. Wu, K. Sheng, and Y. Wang, “A Bidirectional LLC Resonant Converter with Automatic Forward and Backward Mode Transition,” *IEEE Trans. Power Electron.*, vol. 30, no. 2, pp. 757–770, 2015, DOI: [10.1109/TPEL.2014.2307329](https://doi.org/10.1109/TPEL.2014.2307329).
- [333] H. Song, X. Li, and A. K. S. Bhat, “A Comparative Study of Phase-Shift Control Schemes in a Bidirectional Series Resonant Converter,” in *Proc. of the IEEE Int. Future Energy Electronics Conf. (IFEEEC)*, Jun. 2017, DOI: [10.1109/IFEEEC.2017.7992155](https://doi.org/10.1109/IFEEEC.2017.7992155).
- [334] W. Feng, P. Mattavelli, and F. C. Lee, “Pulsewidth Locked Loop (PWLL) for Automatic Resonant Frequency Tracking in LLC DC–DC Transformer (LLC -DCX),” *IEEE Trans. Power Electron.*, vol. 28, no. 4, pp. 1862–1869, 2013, DOI: [10.1109/TPEL.2012.2210912](https://doi.org/10.1109/TPEL.2012.2210912).

- [335] Cree/Wolfspeed, “QPM3-10000-0300, Z-FET Silicon Carbide MOSFET,” Oct. 2017.
- [336] Cree/Wolfspeed, “C2M0025120D, Silicon Carbide Power MOSFET,” Oct. 2015.
- [337] Cree/Wolfspeed, “CPM3-0900-0010A, Silicon Carbide Power MOSFET,” Jan. 2017.
- [338] Burster, “Precision High Capacity Resistors, Model 1282,” May 2019.
- [339] nicrom electronic, “High Voltage Dividers Series 300,” Jan. 2016.
- [340] Keysight Technologies, “Digital Multimeters, 34470A (7.5 Digit),” May 2019.
- [341] J. Smajic, T. Steinmetz, M. Rüegg, Z. Tanasic, R. Obrist, J. Tepper, B. Weber, and M. Carlen, “Simulation and Measurement of Lightning-Impulse Voltage Distributions Over Transformer Windings,” *IEEE Trans. Magn.*, vol. 50, no. 2, pp. 553–556, 2014, DOI: [10.1109/TMAG.2013.2283061](https://doi.org/10.1109/TMAG.2013.2283061).
- [342] R. Bosshard, T. Guillod, and J. W. Kolar, “Electromagnetic Field Patterns and Energy Flux of Efficiency Optimal Inductive Power Transfer Systems,” *Springer Electrical Engineering*, vol. 99, no. 3, pp. 969–977, 2017, DOI: [10.1007/s00202-016-0461-7](https://doi.org/10.1007/s00202-016-0461-7).
- [343] D. Huang, S. Ji, and F. C. Lee, “LLC Resonant Converter with Matrix Transformer,” in *Proc. of the IEEE Applied Power Electronics Conf. and Expo. (APEC)*, Mar. 2014, DOI: [10.1109/APEC.2014.6803447](https://doi.org/10.1109/APEC.2014.6803447).
- [344] G. Ortiz, J. Biela, D. Bortis, and J. W. Kolar, “1 Megawatt, 20 kHz, Isolated, Bidirectional 12 kV to 1.2 kV DC-DC Converter for Renewable Energy Applications,” in *Proc. of the IEEE Energy Conversion Congr. and Expo. (ECCE Asia)*, Jun. 2010, DOI: [10.1109/IPEC.2010.5542018](https://doi.org/10.1109/IPEC.2010.5542018).
- [345] J. Bourdon, P. Asfaux, and A. M. Etayo, “Review of Power Electronics Opportunities to Integrate in the More Electrical Aircraft,” in *Proc. of the IEEE Electrical Systems for Aircraft, Railway and Ship Propulsion Conf. (ESARS)*, Mar. 2015, DOI: [10.1109/ESARS.2015.7101425](https://doi.org/10.1109/ESARS.2015.7101425).
- [346] Y. Du, Y. Lv, C. Li, M. Chen, Y. Zhong, J. Zhou, X. Li, and Y. Zhou, “Effect of Semiconductive Nanoparticles on Insulating Performances of Transformer Oil,” *IEEE Trans. Dielectr. Electr. Insul.*, vol. 19, no. 3, pp. 770–776, Jun. 2012, DOI: [10.1109/TDEL.2012.6215079](https://doi.org/10.1109/TDEL.2012.6215079).

- [347] X. C. Tong, *Advanced Materials for Thermal Management of Electronic Packaging*. Springer, New York, 2011.
- [348] K. Vechalapu, A. Negi, and S. Bhattacharya, “Comparative Performance Evaluation of Series Connected 15 kV SiC IGBT Devices and 15 kV SiC MOSFET Devices for MV Power Conversion Systems,” in *Proc. of the IEEE Energy Conversion Congr. and Expo. (ECCE USA)*, Sep. 2016, DOI: [10.1109/ECCE.2016.7855343](https://doi.org/10.1109/ECCE.2016.7855343).
- [349] W. G. Hurley, M. C. Duffy, J. Zhang, I. Lope, B. Kunz, and W. H. Wölfle, “A Unified Approach to the Calculation of Self- and Mutual-Inductance for Coaxial Coils in Air,” *IEEE Trans. Power Electron.*, vol. 30, no. 11, pp. 6155–6162, 2015, DOI: [10.1109/TPEL.2015.2413493](https://doi.org/10.1109/TPEL.2015.2413493).
- [350] H. B. Dwight, *Tables of Integrals and Other Mathematical Data*. Macmillan Company, 1964, Eqn. 418.
- [351] F. B. Hildebrand, *Introduction to Numerical Analysis*. McGraw-Hill, New York, 1974, Ch. 5.8.
- [352] K. Ohta and H. Ishida, “Comparison Among Several Numerical Integration Methods for Kramers-Kronig Transformation,” *Applied Spectroscopy*, vol. 42, no. 6, pp. 952–957, 1988, DOI: [10.1366/0003702884430380](https://doi.org/10.1366/0003702884430380).
- [353] B. Hirschorn and M. E. Orazem, “On the Sensitivity of the Kramers-Kronig Relations to Nonlinear Effects in Impedance Measurements,” *Journal of The Electrochemical Society*, vol. 156, no. 10, pp. 345–351, 2009, DOI: [10.1560/10.11491.3190160](https://doi.org/10.1560/10.11491.3190160).

Curriculum Vitae

Personal Information

| | |
|---------------|------------------------|
| Name | Thomas Guillod |
| Date of birth | September 9, 1989 |
| Nationality | Swiss |
| Citizen of | Bas-Vully, Switzerland |
| Contact | guillod@lem.ee.ethz.ch |

Education

| | |
|-------------|---|
| 2013 – 2018 | Doctorate, ETH Zurich Power Electronic Systems Laboratory (PES) |
| 2011 – 2013 | MSc ETH (with distinction), ETH Zurich Information Technology and Electrical Engineering |
| 2007 – 2011 | BSc ETH, ETH Zurich Information Technology and Electrical Engineering |
| 2004 – 2007 | High School, La Chaux-de-Fonds Physics and Applied Mathematics |

Work Experience

| | |
|-------------|---|
| 2013 – 2018 | Research Assistant, ETH Zurich Power Electronic Systems Laboratory (PES) |
| 2013 – 2013 | Research Assistant, ETH Zurich High Voltage Laboratory (HVL) |
| 2011 – 2011 | Internship at Bombardier Transport, Zurich |
| 2008 – 2009 | Substitute teacher at CIFOM-ET, Le Locle (part time) |